5-2017

Comparison of As-built FEA Simulations and Experimental Results for Additively Manufactured Dogbone Geometries.

Prathamesh Baikerikar
Clemson University, prathameshbaikerikar@gmail.com

COMPARISON OF AS-BUILT FEA SIMULATIONS AND EXPERIMENTAL RESULTS FOR ADDITIVELY MANUFACTURED DOGBONE GEOMETRIES

A Thesis
Presented to
the Graduate School of
Clemson University

In Partial Fulfillment
of the Requirements for the Degree
Master of Science
Mechanical Engineering

---

by
Prathamesh J. Baikerikar
May 2017

Accepted by:
Dr. Cameron Turner, Committee Chair
Dr. Georges Fadel, Committee Member
Dr. Gang Li, Committee Member

ABSTRACT

Additive manufacturing (AM) is increasingly used in new product development: from prototyping to functional part testing, tooling and manufacturing. The flexibility of AM results in the ability to develop a geometrically complex part with reduced effort by moderating some manufacturing constraints while imposing other constraints. However, additively manufactured parts entail a certain amount of ambiguity in terms of material properties, microstructures effects and defects. Due to the intensive energy, rapid cooling and phase changes, parts made by Fused Deposition Modelling (FDM – a branch of AM) and other layer-manufacturing processes may deviate from the designed geometry resulting in inaccuracies such as discontinuities, curling, and delamination, all of which are attributed to the residual stress accumulations during geometry fabrication. Therefore, the FDM part can strongly differ from its design model, in terms of strength and stiffness. In performance critical applications, analyzing and simulating the component is necessary. Identifying appropriate methodologies to simulate and analyze additively manufactured parts accurately, enables better modelling and design of components. The Finite Element Method (FEM) is a widely used analysis tool for various linear and nonlinear engineering problems (structural, vibrational, thermal etc.). Therefore, it is necessary to determine the accuracy of FEA while analyzing the non-continuous, non-linear FDM parts. The goal of this study is to compare Finite Element Analysis (FEA) simulations of the as-built geometry with the experimental tests of actual FDM parts. A dogbone geometry is used as a test specimen for the study, with a set of different infill patterns. A displacement

controlled tensile test is conducted using these specimens to obtain the experimental stress-strain results. Further, as built 3D CAD models of these specimens are developed and a displacement controlled tensile test is simulated using different material models in two FEA solvers. The stress-strain results of the analyses are compared and discussed with the experimental results. The metrics of the comparison are the precision and the accuracy of the results. This study found that FEA results are not always an accurate or reliable means of predicting FDM part behaviors, even when advance experimentally derived material models and as-built geometries are incorporated.

DEDICATION

I dedicate this thesis work to my parents, Shraddha J. Baikerikar and Jayprakash G. Baikerikar, for their unconditional love and support and for encouraging me to work hard for the goals, I aim to achieve. I also dedicate this work to my advisor, Dr. Cameron Turner, for his continued guidance and support.

ACKNOWLEDGEMENTS

I am very fortunate to have conducted my graduate work at Clemson University and want to thank the following people for their help and support.

I would like to express deepest gratitude to my advisor Dr. Cameron Turner, for his continued guidance, support and encouragement. I thank Dr. Turner for his persistent presence and help during the challenges of this work. This journey has been an enlightening experience and I am grateful to have found such a supportive mentor. I appreciate the opportunity given to me.

I would like to thank my committee members, Dr. Georges Fadel and Dr. Gang Li for their contributions and timely guidance. I wish to thank Dr. Garrett Pataky for providing access to the load test equipment in his laboratory.

I would like to gratefully acknowledge the support of the Clemson University Mechanical Engineering Department. I would also like to thank my CEDAR lab mates for their valuable feedback.

I also want to acknowledge and thank my parents, Jayprakash G. Baikerikar and Shraddha J. Baikerikar for their continued love and encouragement. This work would not have been possible without their support.

TABLE OF CONTENTS

LIST OF TABLES

LIST OF FIGURES

CHAPTER 1: INTRODUCTION

1.1 Additive Manufacturing

Additive Manufacturing (AM) or 3D printing has generated a renewed interest of engineering and manufacturing sectors in the recent years. Additive manufacturing is increasingly used in the development of new products: from prototypes to functional parts and tooling [1]. According to an industry report by Wohler's Associates' [2] 'Annual Worldwide Progress Report on 3D printing', by 2019, the sale of AM products and services could reach or exceed $6.5 billion. The dexterity of AM can be related in terms of the moderation of the manufacturability constraints, the ability to develop a geometrically complex part with reduced effort, that otherwise would have been tedious with traditional methods. Adding to this, these parts can be customized for low volume production with economic feasibility. Figure 1 shows use of AM parts in different applications.

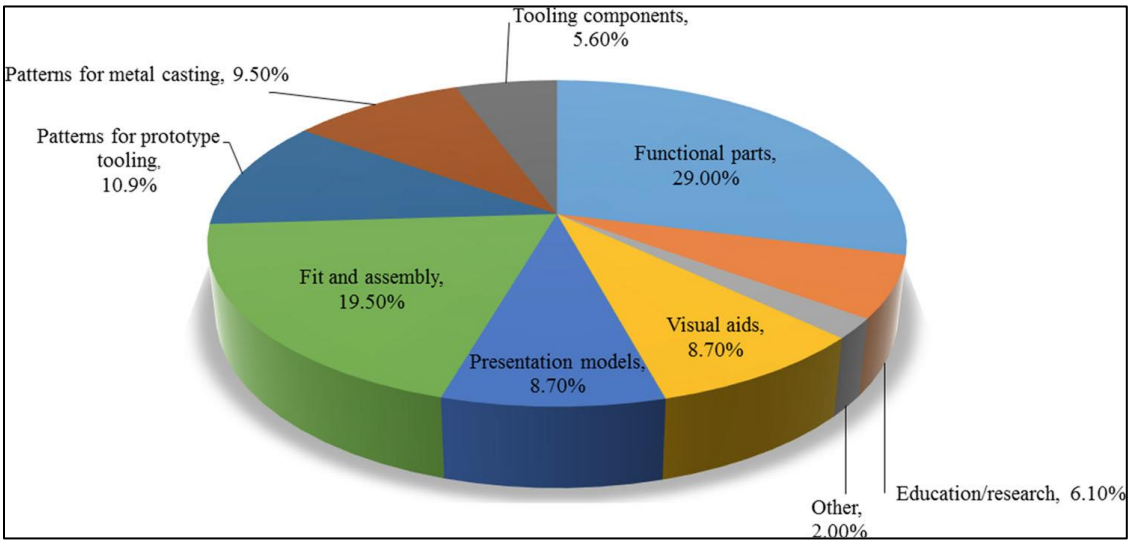

Figure 1: Chart showing applications of AM [2].

AM is the process of creating parts by depositing material in layers, i.e. by adding material. AM usually employs techniques such as extrusion of material as in Fused Deposition Modelling (FDM), Photo Polymerization: Stereo lithography (SLA) and Powder bed techniques like Selective Laser Sintering (SLS). A generic process for fabricating a part by AM starts with generating a 3D CAD (Computer Aided Design) model. This model is converted into an STL (Stereo lithography) file, which transforms the CAD geometry into a triangulated mesh format. Next, slicing software slices the model into horizontal layers. This software also determines an optimized toolpath for the extruder to generate the part boundary and infill pattern; and generates computer numeric control (CNC) commands. This file enables the 3D printing machine to print the final part.

Traditional subtractive manufacturing imposes design constraints upon the geometry and materials of the part. These constraints can be relaxed or even eliminated through AM processes. The strengths of AM lie in the limitations of the traditional means of manufacturing. The principal point is the ability of AM to produce complex geometries for zero added costs. Figure 2 and Figure 3 show complex geometries manufactured from a single process, which is not possible through traditional manufacturing. AM enables materials savings by enabling infill patterns that result in lightweight parts. A high degree of design freedom, coupled with optimization and integration of functional features has resulted in designers increasingly exploiting the strengths of AM.

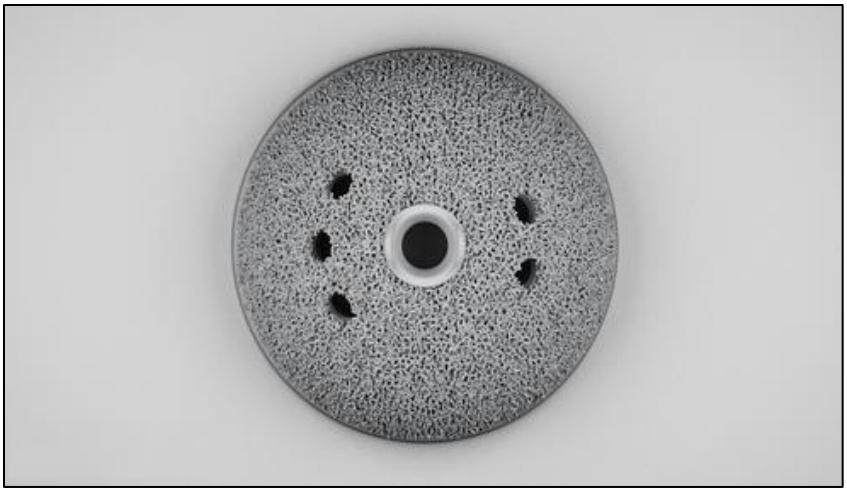

Figure 2: Parts manufactured from metal-laser sintering: Hip Implant with lattice structure [3]

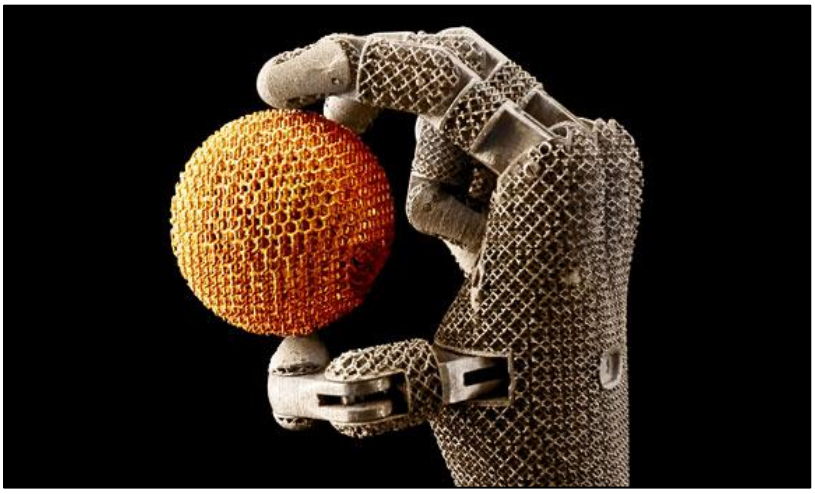

Figure 3: Parts manufactured from metal-laser sintering: handheld ball built bottom-up [4].

1.2 Fused Deposition Modelling

Fused Deposition Modelling (FDM) is used for printing the parts in this study. FDM is an AM technology based on the principle of material extrusion. FDM begins with

the software stage, where a CAD model of the part is created and stored in a STL (Stereo lithography) file format. Next, a slicing software mathematically slices the part into a number of layers and generates a toolpath for the printer nozzle to print the geometry. The software stores this data in a G-code file format for the 3D printer. The part is built from the bottom up, one layer at a time. In FDM, the filament is fed through an extruder nozzle, which heats the filament to a semi-molten state. The filament is then extruded through the nozzle and deposited to form the part geometry on the printer bed. Figure 4 is a diagrammatic representation of the FDM process. Often, the printer bed is heated to enable for better adhesion of the first print layer. Since the material is extruded in a semi-molten state, the newly deposited material fuses with the adjacent material that has previously been deposited. After an entire layer is deposited, the build platform moves downward along the z-axis by an increment equal to the filament height (layer thickness) and the next layer is deposited on top of it [5]. The extruder moves in X-Y plane, whereas the bed moves in Z direction (however, in case of certain printers, the bed moves in the X-Y plane). Even though FDM is quite flexible in printing complex geometries with small overhangs, by the support from lower layers, FDM generally has some restrictions on the slope of the overhang. For slopes greater than 45˚, support material is extruded which can be detached later. The support structure can be printed from the same material or from a different material if a dual-extruder set-up is present. Figure 5 shows a part built using FDM. Since the part is built in a single process, it eliminates the need of assembling individual parts.

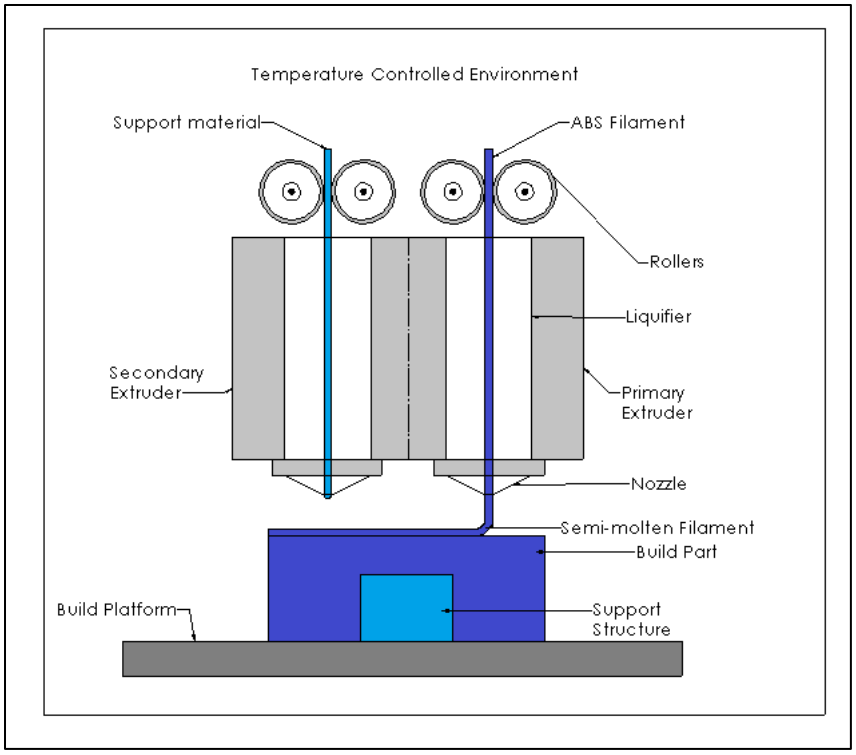

Figure 4: Fused Deposition Modelling process representation.

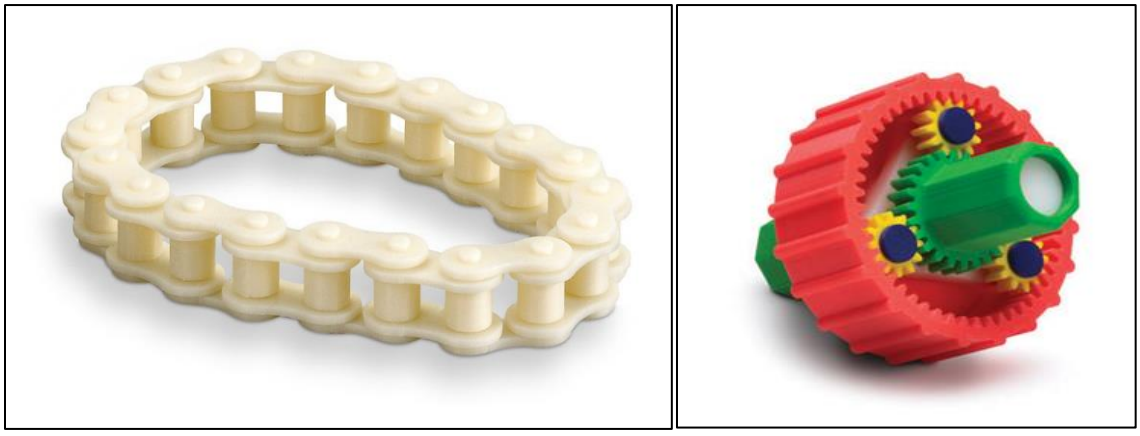

Figure 5: FDM parts: (left) – bicycle chain prototype, (right) – planetary gear system [6].

The quality of the FDM parts largely depends upon the printing parameters used for the build process. A higher layer resolution (i.e. the number of layers) increases the quality of the part and better represents fine geometries. Table 1 shows the list of few of the process parameters affecting the properties of parts. The strength and material properties of the FDM part are dependent on these parameters, majorly on the layer orientation of the filament. Due to the type of manufacture, FDM parts not completely homogeneous and often exhibit voids. Thus, FDM parts have an anisotropic behavior. Different parameters lead to different properties for the same geometries. Figure 6 represents a FDM part from a microstructure perspective. Table 1 lists some of the parameters that affect the properties of the FDM part.

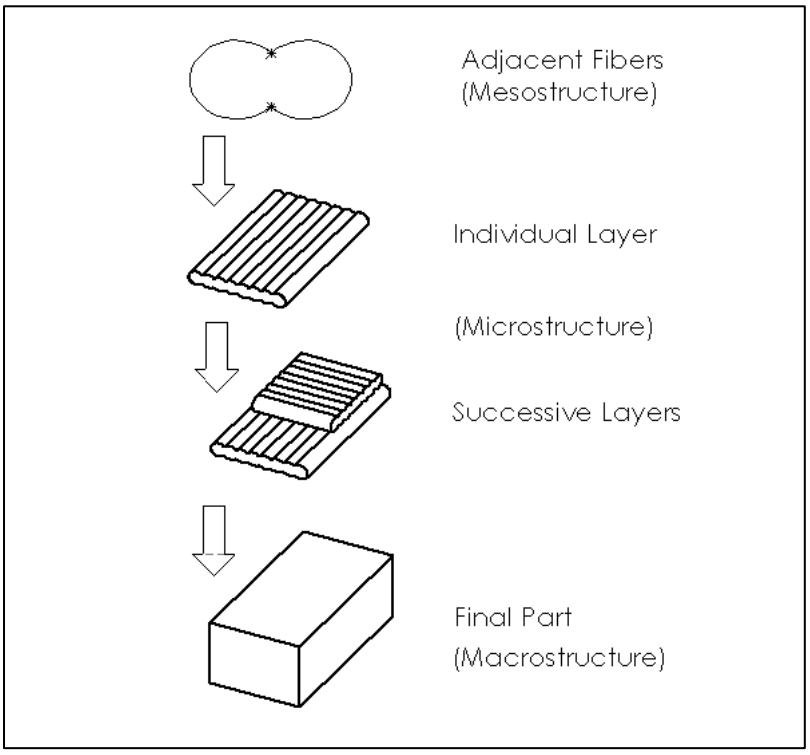

Figure 6: Multiscale levels of FDM part.

Table 1: Process Parameters affecting the final part.

Process Parameters affecting the final part	
Extruder Temperature	Layer Height
Layer Orientation	Percentage Infill
Filament Width	Extrusion rate
Filament Overlap	Bed Temperature
Time between bonding	Movement speed
Infill Pattern	Number of shells

In addition, each of these processes result in certain amount of inaccuracy. Creating the STL files preserves only the approximate geometric information of the original model [7] resulting in an imperfect geometry. In addition, the final product is largely dependent on the precision and accuracies of the slicers as well as the machine. Figure 7 shows the errors (ε) introduced in each of the stages of manufacturing the part. Thus, the additively manufactured part is not in perfect rendition of its 3D model. Additive manufacturing provides flexibility in terms of material, microstructures and layer thickness, but it also entails certain amount of ambiguity in terms of material properties, microstructures [8], etc. Owing to the intensive energy, rapid cooling, and phase changes, parts made by FDM and other layer-manufacturing processes may deviate from the designed geometry; and exhibit inaccuracies such as curling, warping, and delamination which are attributed to the residual stress accumulations during prototype fabrications [9].

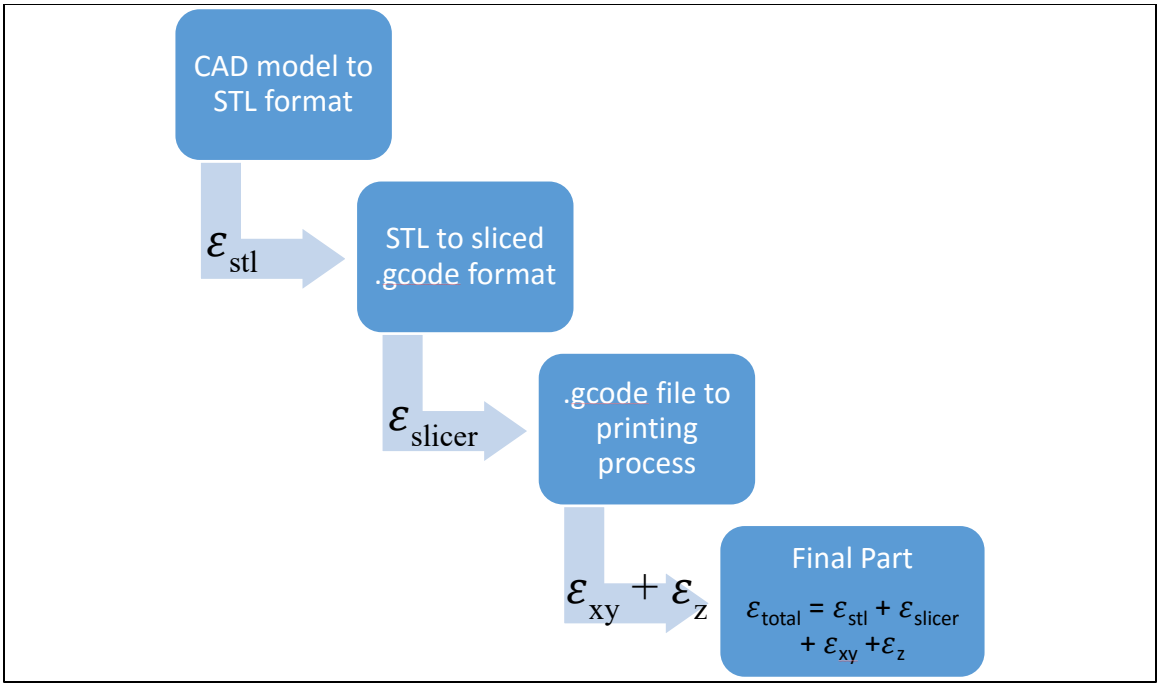

Figure 7: FDM processes introducing error at different stages.

Since the material is built up in layers of fibers, the directional orientation of fibers leads to an anisotropic behavior. Therefore, even though the material of FDM parts is not anisotropic, the FDM part as a whole behaves as an anisotropic part. The mechanical properties of the FDM parts are generally inferior to those of the parts made from the traditional methods due the structure of FDM parts. The presence of voids at the mesostructural level accounts for some of the decreases in strength. They do result in a lightweight part and provide an opportunity for tailoring the mechanical performance via control of void geometry and layer distribution. However, the mechanical properties and strength of FDM parts are generally weaker as compared to traditionally manufactured parts, and therefore, should be analyzed.

1.3 Material Models

With FDM parts exhibiting an anisotropic behavior, even though, the material being isotropic, it is necessary to understand the material models related to the isotropic and anisotropic behaviors. In a general form, Hooke's Law states that the strain applied is proportional to stress induced. This enables us to obtain a general matrix relation between stress and strain for different materials. An isotropic material has uniform material properties in all the directions. The relation between stress and strain for an isotropic material is given in Eq. 1,

$$[\varepsilon] = [C][\sigma] \tag{1}$$

Where, C is the compliance matrix,

σ = Stress,

ε = Strain

Equation 1 can be expanded in matrix form as follows,

$$\begin{bmatrix} \varepsilon_{xx} \\ \varepsilon_{yy} \\ \varepsilon_{zz} \\ \varepsilon_{yz} \\ \varepsilon_{zx} \\ \varepsilon_{xy} \end{bmatrix} = \frac{1}{E} \begin{bmatrix} 1 & -\nu & -\nu & 0 & 0 & 0 \\ -\nu & 1 & -\nu & 0 & 0 & 0 \\ -\nu & -\nu & 1 & 0 & 0 & 0 \\ 0 & 0 & 0 & 2(1+\nu) & 0 & 0 \\ 0 & 0 & 0 & 0 & 2(1+\nu) & 0 \\ 0 & 0 & 0 & 0 & 0 & 2(1+\nu) \end{bmatrix} \begin{bmatrix} \sigma_{xx} \\ \sigma_{yy} \\ \sigma_{zz} \\ \sigma_{yz} \\ \sigma_{zx} \\ \sigma_{xy} \end{bmatrix} \tag{2}$$

Where,

σ_{ij} = stresses in respective planes,

ε_{ij} = strain in respective planes,

E = Young's Modulus,

ν = Poisson' Ratio,

Inverting Eq. 2, we get stress in terms of strain, given in Eq. 3,

$$\begin{bmatrix}\sigma_{xx}\\ \sigma_{yy}\\ \sigma_{zz}\\ \sigma_{yz}\\ \sigma_{zx}\\ \sigma_{xy}\end{bmatrix} = \frac{E}{(1+\nu)(1-2\nu)}\begin{bmatrix} 1-\nu & \nu & \nu & 0 & 0 & 0\\ \nu & 1-\nu & \nu & 0 & 0 & 0\\ \nu & \nu & 1-\nu & 0 & 0 & 0\\ 0 & 0 & 0 & \frac{1-2\nu}{2} & 0 & 0\\ 0 & 0 & 0 & 0 & \frac{1-2\nu}{2} & 0\\ 0 & 0 & 0 & 0 & 0 & \frac{1-2\nu}{2}\end{bmatrix}\begin{bmatrix}\varepsilon_{xx}\\ \varepsilon_{yy}\\ \varepsilon_{zz}\\ \varepsilon_{yz}\\ \varepsilon_{zx}\\ \varepsilon_{xy}\end{bmatrix} \quad (3)$$

This equation enables us to calculate the stresses at a given strain, if the material properties are known. Such material models are used in analytical approaches to calculate stresses and other mechanical variables. The isotropic model thus needs two independent elastic constants i.e. the Young's modulus and Poisson's ratio for a complete analysis.

On the other hand, in case of anisotropic materials, the material properties change with direction along the object. With an anisotropic model however, we need twenty-one independent constants from the compliance matrix to define a material model completely. Deriving all twenty-one constants is not always possible and therefore, a simpler orthotropic material model is resorted to.

An orthotropic material is material whose properties differ along three mutually orthogonal axes. Eq. 4 gives the compliance matrix for orthogonal materials,

$$\begin{bmatrix}\varepsilon_{xx}\\ \varepsilon_{yy}\\ \varepsilon_{zz}\\ \varepsilon_{yz}\\ \varepsilon_{zx}\\ \varepsilon_{xy}\end{bmatrix} = \begin{bmatrix} \frac{1}{E_x} & -\frac{\nu_{yx}}{E_y} & -\frac{\nu_{zx}}{E_z} & 0 & 0 & 0 \\ -\frac{\nu_{xy}}{E_x} & \frac{1}{E_y} & -\frac{\nu_{zy}}{E_z} & 0 & 0 & 0 \\ -\frac{\nu_{xz}}{E_x} & -\frac{\nu_{yz}}{E_y} & \frac{1}{E_z} & 0 & 0 & 0 \\ 0 & 0 & 0 & \frac{1}{G_{yz}} & 0 & 0 \\ 0 & 0 & 0 & 0 & \frac{1}{G_{zx}} & 0 \\ 0 & 0 & 0 & 0 & 0 & \frac{1}{G_{xy}} \end{bmatrix} \begin{bmatrix}\sigma_{xx}\\ \sigma_{yy}\\ \sigma_{zz}\\ \sigma_{yz}\\ \sigma_{zx}\\ \sigma_{xy}\end{bmatrix} \quad (4)$$

ν_{ij} = Poisson's ratio in different orientations,

G_{ij} = Shear Modulus in respective planes,

E_i = Young's Modulus in respective planes.

Inverting Eq. 4, we can solve for stresses analytically. For an orthotropic material model, only nine constants are required to define the material model completely. This not only reduces the amount of experimental data needed, but also reduces the computational time required for analyses.

A special case of orthotropic materials is the transversely isotropic case. Transversely isotropic materials have uniform (same) properties in a given plane (e.g. x and y) and different properties in direction normal to this plane (z). With properties being similar in a given plane, this reduces the independent constants in the compliance matrix to five. Eq. 5 gives the compliance matrix for transversely isotropic materials,

$$\begin{bmatrix} \varepsilon_{xx} \\ \varepsilon_{yy} \\ \varepsilon_{zz} \\ \varepsilon_{yz} \\ \varepsilon_{zx} \\ \varepsilon_{xy} \end{bmatrix} = \begin{bmatrix} \frac{1}{E_p} & -\frac{\nu_p}{E_p} & -\frac{\nu_{zp}}{E_z} & 0 & 0 & 0 \\ -\frac{\nu_p}{E_p} & \frac{1}{E_p} & -\frac{\nu_{zp}}{E_z} & 0 & 0 & 0 \\ -\frac{\nu_{pz}}{E_p} & -\frac{\nu_{pz}}{E_p} & \frac{1}{E_z} & 0 & 0 & 0 \\ 0 & 0 & 0 & \frac{1}{G_{pz}} & 0 & 0 \\ 0 & 0 & 0 & 0 & \frac{1}{G_{zp}} & 0 \\ 0 & 0 & 0 & 0 & 0 & \frac{2(1+\nu_p)}{E_p} \end{bmatrix} \begin{bmatrix} \sigma_{xx} \\ \sigma_{yy} \\ \sigma_{zz} \\ \sigma_{yz} \\ \sigma_{zx} \\ \sigma_{xy} \end{bmatrix} \quad (5)$$

Where,

'p' represents the principle direction of symmetry,

$E_p = E_x = E_y$

The factor 1/2 multiplying the shear moduli in the compliance matrix results from the difference between shear strain and engineering shear strain, where, $\gamma_{xy} = \varepsilon_{xy} + \varepsilon_{yx} = 2\varepsilon_{xy}$. More information can be found in [10]. These material models are used in analytical methods and commercial FEA solvers to define anisotropy and isotropy in different analyses. The material model for composites is discussed in the next section.

1.4 Classical Laminate Theory.

Since the FDM parts are built up layer-by-layer, they are similar to composite materials in the sense that composite is also made up of stacked up laminae. Therefore, a composite theory might be able to lend itself for the analysis of FDM parts. This approach,

adopted in different works, is discussed further in Chapter 2. A composite is made up of a stack of plies or lamina, consisting of individual fibers. Classical Laminate Theory (CLT) is used for analysis of composite materials. In order to extend the CLT towards analysis of FDM parts, it is necessary to understand the assumptions of the theory. Certain important assumptions pertaining to this study are [11]:

- A perfect bonding prevails between each lamina, such that there is no slip in adjacent layers.
- Each lamina is considered as a homogeneous layer of fibers.

A coordinate system is considered for the laminae, shown as follows in Figure 8 [11],

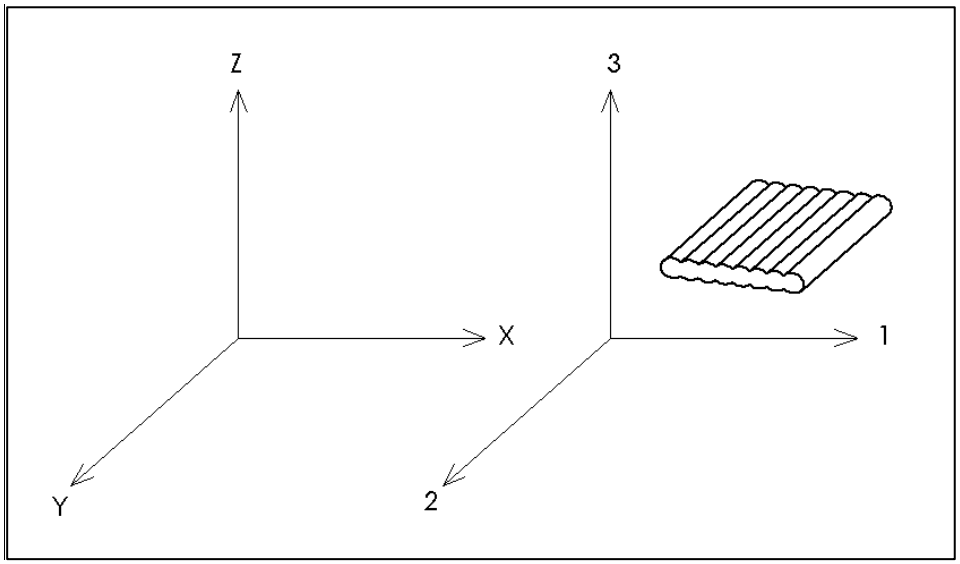

Figure 8: Coordinate system of composites [Adapted from 11].

For a laminate theory, the constitutive model can be described as that for a thin plate (Kirchhoff's Classical Plate Theory). If a lamina is thin and does not carry any out of plane loads, one can assume plane stress conditions for the lamina [11]. Causing $\sigma_3=0$,

$\tau 31 = 0$ and $\tau 23 = 0$. Therefore, equation for orthotropic plane stress can be written as shown in Eq. 6 [12].

$$\begin{bmatrix} \varepsilon_1 \\ \varepsilon_2 \\ \nu_{12} \end{bmatrix} = \begin{bmatrix} S_{11} & S_{12} & 0 \\ S_{21} & S_{22} & 0 \\ 0 & 0 & S_{66} \end{bmatrix} \begin{bmatrix} \sigma_1 \\ \sigma_2 \\ \tau_{12} \end{bmatrix} \tag{6}$$

Inverting the equation gives us the stress values shown in Eq. 7 [12].

$$\begin{bmatrix} \sigma_1 \\ \sigma_2 \\ \tau_{12} \end{bmatrix} = \begin{bmatrix} Q_{11} & Q_{12} & 0 \\ Q_{21} & Q_{22} & 0 \\ 0 & 0 & Q_{66} \end{bmatrix} \begin{bmatrix} \varepsilon_1 \\ \varepsilon_2 \\ \nu_{12} \end{bmatrix} \tag{7}$$

Where Q_{ij} are reduced stiffness coefficients given by [12],

$$Q_{11} = \frac{E_1}{1 - \nu_{12}\nu_{21}}, \qquad Q_{12} = \frac{\nu_{12}E_2}{1 - \nu_{12}\nu_{21}}, \qquad Q_{22} = \frac{E_2}{1 - \nu_{12}\nu_{21}}, \qquad Q_{66} = G_{12}$$

E_1 = Longitudinal Young's Modulus (direction 1)

E_2 = Transverse Young's Modulus (direction 2)

G_{12} = In-plane shear Modulus (direction 1)

ν_{12}= Major Poisson's Ratio

CLT builds on plane stress theory to develop relationships for composite material under loading. Laminate strains can be written as Eq. 8 [12].

$$\begin{bmatrix} \varepsilon_x \\ \varepsilon_y \\ \nu_{xy} \end{bmatrix} = \begin{bmatrix} \varepsilon_x^0 \\ \varepsilon_y^0 \\ \nu_{xy}^0 \end{bmatrix} + z \begin{bmatrix} k_x \\ k_y \\ k_{xy} \end{bmatrix} \tag{8}$$

In addition, Eq. 9 [12] gives the corresponding stress relationship

$$\begin{bmatrix}\sigma_x\\ \sigma_y\\ \tau_{xy}\end{bmatrix}=\begin{bmatrix}Q_{11} & Q_{12} & Q_{16}\\ Q_{21} & Q_{22} & Q_{26}\\ Q_{16} & Q_{26} & Q_{66}\end{bmatrix}\begin{bmatrix}\varepsilon_x^0\\ \varepsilon_y^0\\ \nu_{xy}^0\end{bmatrix}+z\begin{bmatrix}Q_{11} & Q_{12} & Q_{16}\\ Q_{21} & Q_{22} & Q_{26}\\ Q_{16} & Q_{26} & Q_{66}\end{bmatrix}\begin{bmatrix}k_x\\ k_y\\ k_{xy}\end{bmatrix} \tag{9}$$

Equation 10 gives the stresses in each lamina in terms of these unknowns. The stresses in each lamina can be integrated through the laminate thickness to give resultant forces and moments [12]. The resultant forces and moments can be written in terms of mid-plane strains and curvatures.

$$\begin{bmatrix}N\\ M\end{bmatrix}=\begin{bmatrix}A & B\\ B & D\end{bmatrix}\begin{bmatrix}\varepsilon^0\\ k_x\end{bmatrix} \tag{10}$$

[N] = Resultant Forces,

[M] = Resultant Moments,

[A] = Extensional Coupling,

[B] = Cross-coupling Stiffness,

[D] = Bending Stiffness.

These are the basic equations for the analysis of composite laminae.

1.5 Finite Element Analysis

Finite Element Analysis (FEA) is widely used as an analysis tool in engineering problems (structural, vibrational, thermal etc.), that is based on the Finite Element Method

(FEM). FEA was originally developed as a method for stress analysis for aircrafts, but nowadays is extensively used for a range of mechanical and thermal analyses and simulations. FEM is a numerical technique for finding approximate solutions to boundary value problems for partial differential equations. FEM subdivides a large problem into smaller parts, known as finite elements, each represented by a simple set of equations. The simple equations that model these finite elements are then assembled into a larger system of equations that models the entire problem. Using methods from calculus, an approximate solution can be found [13]. Figure 9 depicts the FEA of a part, showing its meshed geometry (larger geometry divided into finite elements). FEA has also been used to analyze AM parts as well as AM processes. However, since in FEA, the part is discretized into a continuum of finite elements, it might not be able to effectively represent discontinuous (AM) components. Due to the microstructure of FDM and the difficulties in representing the material constitutive behavior model, FEA may not be able to predict the behavior of FDM parts effectively. Thus, an FEA technique that takes into account these differences between the ideal and actual conditions relating to anisotropy and microstructure, would be able to represent the behavior of FDM parts accurately. Therefore, there is need to link local structural and bonding differences to a global anisotropic material behavior, in order to develop an accurate FEA model. More information can be found in [14].

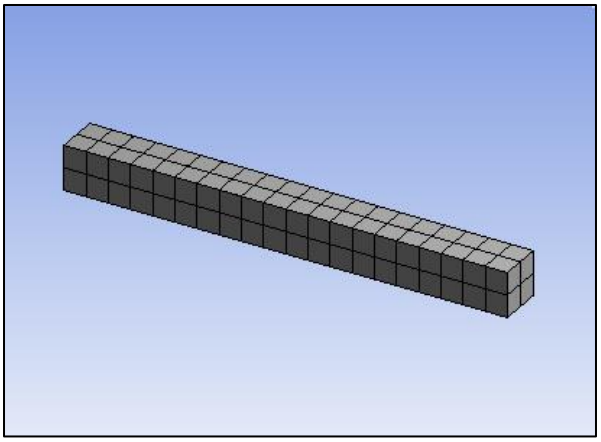

Figure 9: Finite Element Model: Discretization of geometry.

1.6 Objective and Scope

With the differences mentioned above, an additively manufactured component can strongly differ from an ideal model in terms of its strength and stiffness. In performance critical conditions, it is necessary to know the behavior of the FDM parts or to simulate the part under actual application conditions. AM parts with specific infill patterns can be used for function specific purposes making it necessary to analyze AM parts with their infill patterns. With increasing use of AM parts in functional applications, the need for simulating these parts in their actual loading conditions arises. Therefore, identifying methodologies to simulate and analyze additively manufactured parts would enable better understanding, modeling and design of components.

The simplest approach, which is commonly used, represents a FDM part as a continuous part, with a linear isotropic material model. However, FDM parts are neither isotropic nor continuous bodies; therefore, such an FEA would not be the best representation of its behavior. Another approach is to represent the material with an

isotropic material property derived by experimental testing of the specified raster orientation and layer thickness. However, due to vast number of potential parameters, such an analysis would be true for only the specific orientation and layer parameters. The next logical step is to use an orthotropic model, using the derived properties in the three principle directions to build a constitutive model for the part. This should take into consideration the directional orientation of fibers. A similar approach can be found in [15, 16].

Another parallel approach can be to model the parts as they are built, i.e. fiber-by-fiber and layer by layer. In addition, FDM parts are not always manufactured as continuous solids in order to save weight. The infill patterns used in a complex part need to be represented accordingly when an FEA is performed. Modeling additively manufactured components with an as-built model; simulating and analyzing these as-built components enables an understanding the effective material properties and behavior. This in turn enables us to better design FDM parts. The focus of this study is to compare FEA simulations of the as-built geometries in tensile loading with the experimental tests of actual AM parts.

The design statement for this work is:

FEA simulations of as-built geometries in tensile loading, using experimentally derived material models, predict actual behaviors of FDM parts.

For this comparison, a suitable dogbone geometry is designed with different infill patterns for obtaining experimental results. Similarly, to compare the infill patterns with a solid pattern of similar weight, corresponding continuous geometries of equal volume are

also designed and evaluated both in simulation and with a microscale tensile testing machine. Due to a large number of potential parameters affecting the material properties, the printing parameters used for the parts are consistent throughout the study. Therefore, results of the study stand true for parts built with these parameters. A uniaxial tensile test is performed to obtain experimental data and this test is simulated using FEA. A suitable sample size is used to ensure repeatability. The study also uses as-built CAD models of the infill geometries to be analyzed in an FEA software. Initially, the properties of the bulk material are used to carry out the FEA. However, FEA is also performed using derived properties with an isotropic material model and derived properties with orthotropic material model as well as a composite layup model.

Chapter 2 describes a brief background about the differences of the material properties of the additively manufactured parts as compared to the continuous counterparts. Work done on similar platforms is reviewed. Chapter 3 describes the initial part of the study. This includes the methodology; presenting the geometries and infill patterns used for the study. The as-built 3D model and its FE analyses using the bulk properties and derived properties are also discussed. The experimental test results and the FEA simulations are presented; differences in the results of the FEA simulations and experimental tests are studied and discussed. Chapter 4 discusses a few more commonly used infill patterns. We analyze the geometries using orthotropic material model and the composite layup model and discuss the results. In Chapter 5, we conclude by giving remarks regarding the accuracy of FEA simulations with respect to the experimental results for FDM parts and state the scope for future development.

CHAPTER 2: LITERATURE REVIEW

AM has developed as a technology both in process and product. AM, also known as 'Rapid Prototyping', in its initial stages was used for developing prototypes; the technology then not being feasible for producing functional parts. AM manufacturing today is not just limited to prototyping, but is used for a variety of different purposes ranging from concept modeling and modeling aesthetic commodities to creating functional models, end use parts, high heat applications and as components in assemblies [17]. The development in AM technologies has led to many advantages:

- Decrease in the time required for printing.
- Increase in the number of materials that can be used.
- Increase in control of printing parameters.
- Ease of printing complex parts.
- Ability for low volume production with short lead times.

FDM parts are used in varied sectors from aerospace, automobile, industrial, medical etc. FDM technologies today enable manufacturing parts with high mechanical and thermal durability with fast lead times. FDM proves perfect for low volume production for complex end-use products, jig and fixtures and other applications. Further information of applications of FDM parts can be found in [18, 19, and 20]

Due to these reasons, it is necessary to understand the behavior of the FDM parts. Simulating and analyzing these parts in their functional environment is important.

Therefore, understanding the material behavior and structure of FDM parts is required to accurately simulate and analyze them. This would enable us to validate the fidelity of the FEA simulations of FDM parts with their actual behaviors and scenarios.

2.1 Anisotropy in FDM parts.

The FDM parts often fail to match the properties of corresponding parts manufactured by traditional means (i.e. molding and machining). The difference in properties of FDM parts emanates primarily from their structure. FDM parts are manufactured by laying down fibers adjacent to each other to form the geometry of the part. This is done layer by layer for the entire thickness of the part. The absence of ideal bonding conditions and the presence of cooling effects leads to a part that is not completely continuous. This, in addition to the directions of fibers that are laid down, leads to anisotropy in the FDM parts. This anisotropy in FDM parts makes the material properties difficult to determine and the analyses of FDM parts complicated. Understanding the anisotropic behavior would enable us to better simulate FDM parts and predict their mechanical behavior. One of the limitations of additive manufacturing as pointed out in [5], is that if the material properties for the AM parts were known in detail, then AM could be used to fabricate functional parts of a wide variety and complexity. Zieman *et al* [5], Lee *et al* [21] and Upadhyay *et al* [22] discuss the anisotropic properties of FDM parts. Zieman *et al* [5] and Upadhyay *et al* [22] use FDM parts printed with different fiber orientation to derive a range of mechanical properties through tensile, compressive and hardness tests. Both the studies discuss the failure patterns and strengths of each of the

fiber orientations. Figure 10 depicted below shows the fracture patterns under tensile loading of parts with different fiber orientations conducted in [5]. It is important to document these fracture patterns, as these would prove to be a metric for comparison with FEA simulations.

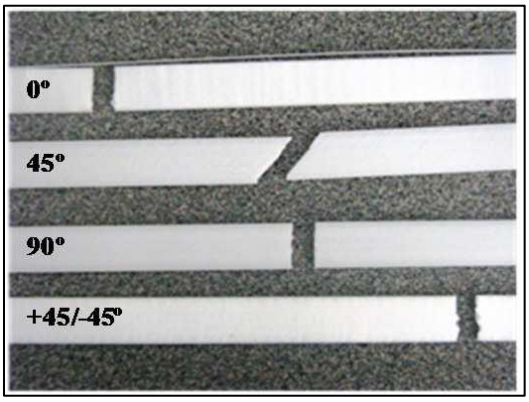

Figure 10: Fracture patterns of specimens with different layer orientations [5].

Upadhyay *et al* [19] conclude that the horizontal arrangement of fibers proves to be the strongest orientation for tensile strength whereas the vertical arrangement of fibers is stronger in a compressive strength test, even though both were weaker than their corresponding injection molded parts. Evidently, the FDM parts should be manufactured considering the application of the parts. Similar work is presented in [23]. Es-Said *et al* [23] develop models which they print and test FDM parts with different layer orientations. Tensile tests, bending tests and impact tests are conducted. The results are similar and in accordance to those mentioned in [5, 22]. Es-Said *et al* [23] further discuss the critical parameters influencing the quality of prototypes in FDM parts.

Li *et al* [24] study the mechanical properties of FDM prototypes by conducting theoretical and experimental analyses to establish constitutive models. Elastic constants of the prototypes are determined using a set of equations and the models are then evaluated by experiments. The authors intend to use this data to develop prototypes with locally controlled properties. With these studies, the fact that the anisotropic properties of FDM parts are influenced by the build parameters becomes apparent. Studying these printing parameters is necessary, so as to determine the material properties of the FDM parts used in this study.

2.2 Effects of Process Parameters on Strength

Owing to the anisotropy, the properties of such parts depend upon the printing parameters specified. Therefore, it is critical to understand the influence of the printing parameters on the part and on its anisotropic behavior. Gajdos *et al* [25] discusses how the processing temperatures affect the structure of FDM parts. The study analyzes the structure of these parts and how varying head and envelope temperatures change the structure of the parts. The results show that higher temperatures lead to a decrease in the percentage of non-filled area in the volume, indicating better bonding. Figure 11 shows how the process temperatures affect the structure of the part. The authors however, conclude that the structure homogeneity of the part is affected more by the geometry and shape of the part than the process temperatures.

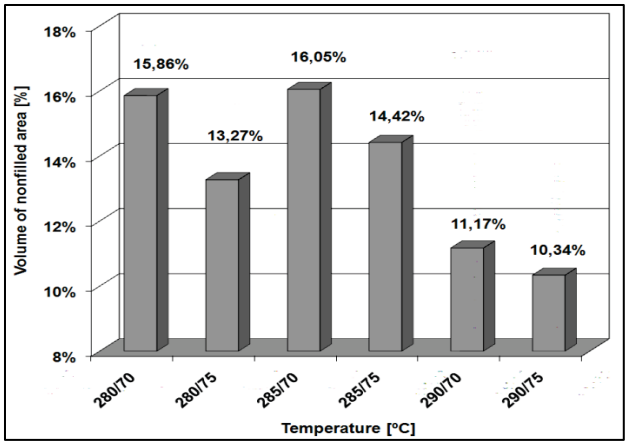

Figure 11: The influence of liquefier and envelope temperatures on the volume of non-filled area in samples with rectangular cross-section [25].

The void area is directly related to how the fibers are laid. These fibers bond to the material surrounding the fibers as they cool and solidify. Effectively the quality of the bonds between the individual neighboring fibers is a determining factor of the mechanical properties of the specimens. The quality of the bonds formed is affected by amount of necking present in adjacent filaments and the relative temperatures of the fibers. Bellehumeur *et al* [26] talk about modeling this bond formation between fibers in a FDM process. The quality of the bond formation determines the strength of the part. The results show that the bond quality is more affected by the extrusion temperature than the envelope temperature. The authors state that the extruded filaments cannot be maintained at high temperatures long enough to enable complete bonding to occur between filaments and therefore, a finer control of the cooling conditions will affect how the bonds are formed in the process and eventually affect the material properties of the part. In a similar work, Sun *et al* [27] investigate the mechanisms controlling the bond formation between filaments.

The authors analyze the mesostructure and bond formation in adjacent polymer filaments and study the temperature profile to state that the process temperature and convection coefficient strongly affect the bond formation and therefore, the quality of the part.

Another important parameter that affects the behavior of FDM models is the raster orientation or the layer orientation. In addition to the literature mentioned before, Bagsik *et al* [28] compares the effect of layer orientation on the mechanical properties of the parts. These parts are built in three orientations representing the three different directions; these parts are tested under tension and compression. Ahn *et al* [29] presents a comprehensive work, which studies the effect of raster orientations, filament width, air gap and temperature of model on the strength of the model. The work also compares these FDM parts with a corresponding injection molded part. Figure 12 shows that the longitudinal fiber orientation (0^o) is the strongest followed by the 45/-45, and both are weaker than the injection molded part. The figure represents parts printed with -0.003 inch air gap (0.003 inch fiber overlap) which yield the strongest parts [29]. The authors also suggest a set of build rules derived from the study to help designers to better utilize the influence of the parameters of build result. In a similar work, Montero *et al* [30] discuss the effect of process parameters on the strength of part, using a Design of Experiments approach. This literature is used to obtain optimum prints results in this study.

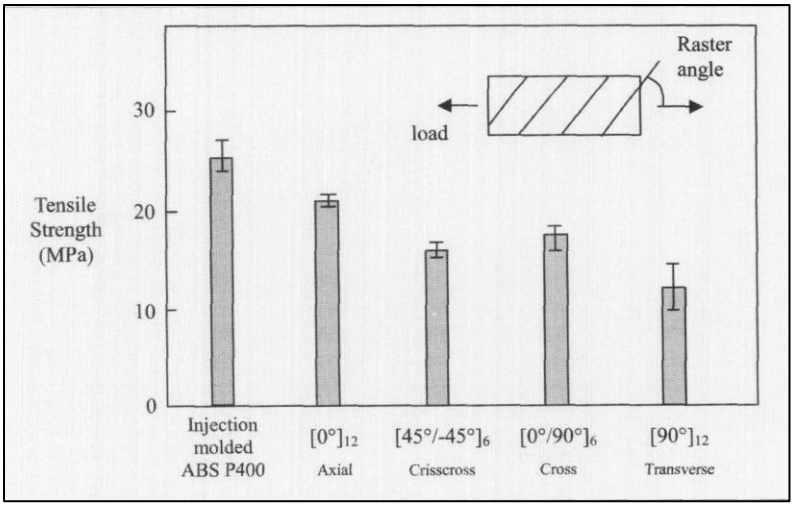

Figure 12: Tensile Strength of specimens with varied raster orientations versus injection molded ABS [29].

Ample literature is available dealing with the influence of process parameters on the outcome of the part. Domingo-Espin *et al* [31] talk about the influence of process parameters on the dynamic mechanical properties of parts. Further information on the influence of process parameters can be found in [32, 33, 34, 35, 36, 37 and 38]. These papers discuss the effect of various process parameters on the final part.

Khan *et al* [39] study the effect of infill pattern on the strength of the part. Wu *et al* [40] discuss the effects of layer thickness on the mechanical properties of the part. The authors report that the layer height of 0.3 mm resulted in a stronger part whereas layer thickness of 0.4 mm resulted in the weakest part. Figure 13 is a summary of the mechanical strengths with varying parameters. Further reading for effect of layer thickness can be found in [41]

Factors		Tensile strength (MPa)	Bending strength (MPa)	Compressive strength (MPa)
Layer Thickness (μm)	200	40.1	52.1	53.6
	300	56.6	56.1	60.9
	400	32.4	48.7	54.1
Raster Angle (°)	0°/90°	56.6	56.1	-
	30°/−60°	41.8	48.5	-
	45°/−45°	43.3	43.2	-

Figure 13: Mechanical properties from different layer thicknesses and raster angles [40].

Table 2: Summary of research pertaining to effect of process parameters.

	Raster / Layer Orientation	Temperature	Filament Width	Air gap	Layer Thickness
Upadhyay *et al* [22] Es-Said *et al* [23], Bagsik *et al* 27],	✓				
Gajdos *et al* [25]		✓			
Sun *et al* [27]	✓	✓			
Ahn *et al* [29], Montero *et al* [30]	✓	✓	✓	✓	
Wu *et al* [40], Syamsuzzaman *et al* [41]	✓				✓

Table 2 categorizes the literature according to the process parameters studied in their work. This knowledge of the effect of process parameters enables us to develop an optimum final part to be used in our study.

2.3 Analytical Approaches

Understanding the material properties or the anisotropic properties of the material is necessary when these parts are analyzed using FEA. The choice of type of material models used in simulations would greatly affect the results of the analyses. Using the properties of the bulk material, would be erroneous since this would treat the part as a continuous isotropic model and may not represent the discontinuous, anisotropic nature of FDM parts. Therefore, Material Characterization or Material modeling of a general FDM part is necessary. This would enable us to derive the material properties of the anisotropic FDM parts and apply these in analysis.

Zou *et al* [42] compare the two types of material models for FDM parts. The first model they use is a transversely isotropic model and then compare it with a completely isotropic model. The directional moduli are calculated using the compliance material matrix equations. The authors however go on to mention that a complete anisotropic model should be used for better precision and accuracy.

Casavola *et al* [43] describe the mechanical behavior of FDM parts using Classical Laminate Theory (CLT). Orthotropic properties are derived using experimental procedures and a CLT compliance matrix is used to derive the stress and strain results. The author then compares the results from the CLT predictions. The results from the CLT predictions are

in accordance with the experimental values of stress for majority of the stress-strain curve; however, CLT results deviate close to 2% strain. Figure 14 shows the stress-strain results. With such results, it can be said that the CLT predictions for elastic modulus were quite accurate for elastic deformations.

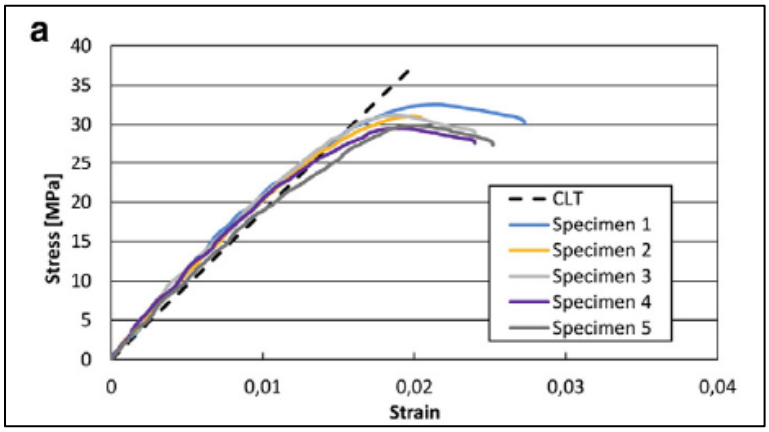

Figure 14: Stress-Strain plot comparing experimental and CLT results [43].

Bertoldi *et al* [44] also uses a similar approach to derive stress results to be further applied using CLT. The compliance matrix is populated using the values determined from the experimental tests and a stiffness matrix is calculated for an orthotropic model. The authors state this model can be used for computational analyses using CLT. Magalhães *et al* [45] too work on similar grounds using CLT to evaluate the stress results. The authors evaluate a part having different raster orientation in each layer, which they call a sandwiched pattern. Experimental values are used to derive the CLT compliance matrix and the results are compared. It is noteworthy that the authors state that the results obtained indicated that the analytical model did not accurately predict the mechanical behavior of parts especially in case of longitudinal layers and therefore suggest the need for a better

analytical model. On the other hand, Alaimo *et al* [46] conducted a similar study to predict mechanical behavior for FDM ABS parts, and they suggest that this orthotropic CLT based model is consistent with the experimental values and should be adopted in analyses of FDM parts. Thus, we see contradicting results while using similar approaches. Kulkarni *et al* [47] examines the differences in strengths of FDM parts resulting from different deposition strategies i.e. layer orientations. Composite material modeling is used to analytically determine the stress results and in this case was also found to be consistent with the experimental results.

Liu *et al* [48] use a different approach to predict mechanical behavior, a homogenization method to compensate for the heterogeneity FDM parts. An implicit representation of the effective mesoscale structure is created and is then homogenized at a macro scale using a solution through an integral equation using Green's function [48]. These models are validated with a FE model and experimental results. The results indicate appreciable agreement with the homogenization model indicating opportunities for effective analyses.

In another study, Croccolo *et al* [49] discuss the experimental characterization and analytical modeling for FDM ABS parts. The procedure adopted is similar to other works discussed in this section. Test parts are used to obtain experimental results and using these, analytical models were developed and compared with the experimental values. A case specific, complex analytical model was developed along with a general model consisting of longitudinal and inclined raster orientations. The general model assumes that the load is shared by both longitudinal and inclined fibers, as if two beams working in parallel.

Therefore, equivalent stiffness and force equations are developed for longitudinal and inclined beams (fibers). In addition to this, the adhesive force between adjacent fibers is also modeled. This information is aggregated to calculate the net effective force acting and to evaluate the results. The results obtained using this model, provides accurate results with reasonable error as compared to the experimental values. Figure 15 depicts a part of the results of the study showing Young's Modulus derived experimentally and analytically for different test specimens. 'Type' in figure means the different types of dogbone geometries used in the study. Further results can be found in [49].

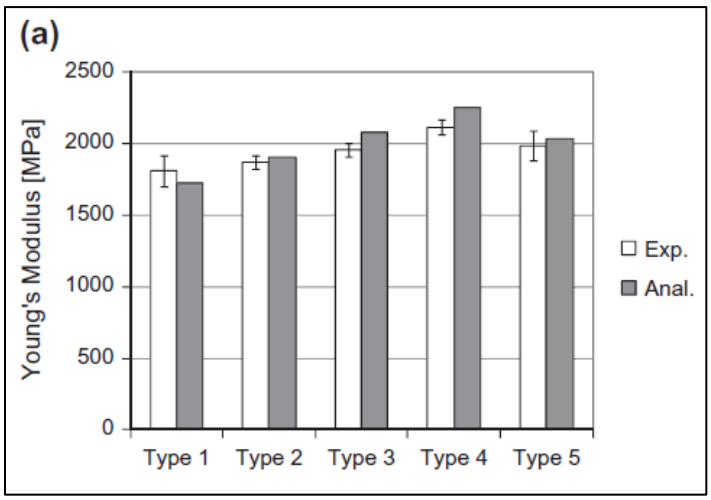

Figure 15: Comparison of experimental and analytical values of Young's Modulus [49].

The results obtained are accurate but the process is computationally intensive. The adhesive forces depend on the build parameters and the raster orientation and pattern varies; consequently, leading to changes in the effective stiffness and force equations i.e.

the model is derived for a specific part. A designer would want to adapt an already existing model rather than developing a new one each time.

Gurrala *et al* [50] develop a mathematical model of neck growth between adjacent filament both in intra-layer and inter-layer situations. These models represent the bonding between each fiber of the FDM parts. Figure 16 shows the schematic used. This theoretical model and the experimental data is used to determine how the bonding between the fibers affects the strength of the overall part. Even though this work is not essentially a comparison between numerical and experimental results, it is important to note that this work presents a new idea for simulating FDM parts; i.e. modeling the part with the actual fiber microstructure. This study determines strong correlation between neck growth between filaments and the strength of parts effectively, using experimental and mathematical models [50]. Such a model would be conducive to analyze actual fracture behavior of FDM parts. Table 3 below summarizes the different material models adopted by different authors.

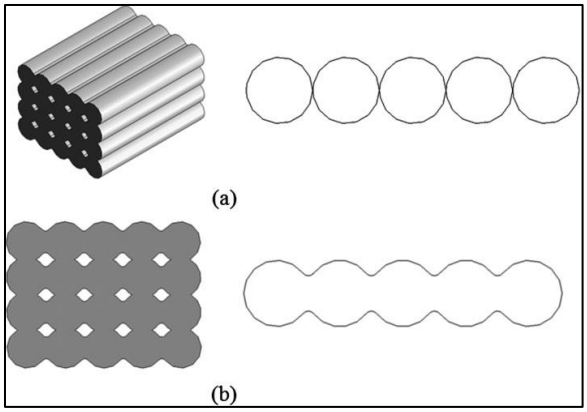

Figure 16: Schematic model of inter-fiber bonding: (a) before bonding, (b) after bonding [50].

Table 3: Summary of literature regarding analytical approaches.

	Material Model Used	Results
Zou *et al* [42]	Isotropic, Transversely Isotropic	2% difference between the 2 models. Recommends using anisotropic model.
Casavola *et al* [43]	Classical Laminate Theory	Results are in accordance with experimental data for majority of the stress-strain curve; Results deviate at 2% strain.
Bertoldi *et al* [44]	Orthotropic model	-
Magalhães *et al* [45]	Classical Laminate Theory	Mechanical Behavior not predicted accurately using CLT; Suggest using a better analytical model.
Alaimo *et al* [46]	Classical Laminate Theory	Results obtained using CLT are consistent with the experimental data.

With analytical approaches, stress calculation of cross-section having continuous, uniform areas is straight-forward. However, in case of complex geometries, stress calculations at different regions of part becomes complicated. A series of FEA algorithms have to be used, which would be cumbersome on part of the designer. Hence simulation

approaches using commercial software is preferred instead of manually generating a FEA solver. General FEA solvers used for mechanical analyses are ANSYS, Abaqus and Hyperworks.

2.4 Simulation Approaches

Simulation of real loading conditions enables us to realize the behavior of the part as a whole. Analytical approaches suggest using material models to analyze FDM parts. The literature below can be segregated in to 3 types: using orthotropic material models with solid parts, using orthotropic material model with mesostructured parts; and composite layup.

Hambali *et al* [51] discusses the effect of build orientation on FDM parts to validate the deformation behavior in FEA. Material properties are derived to be used in an orthotropic model. 3D model is created in the three different orientations and a linear-static FEA is performed to simulate the loading conditions. The results from FEA show close correlation with the experimental results, however, the accuracy of FEA results depend on the build orientation of the part. Moreover, the FEA stress plots are in unison with the fracture modes of the physical test models. The authors conclude that FEA is reliable tool for visualizing the fracture in FDM parts but a non-linear, dynamic FEA should be used for better results. In a similar work, Hambali *et al* [52] determines the effect of build orientation on the strength of parts. In this work, the experimental results are validated by FEA. The experimental results show, change in part strengths with change in part orientation. Even though FEA results show a change in strength with changes in part orientations, the results

are not consistent in magnitude with the respective experimental counterpart. Errors as large as 30% are observed from the results [52]. Figure 17 shows the results from [52].

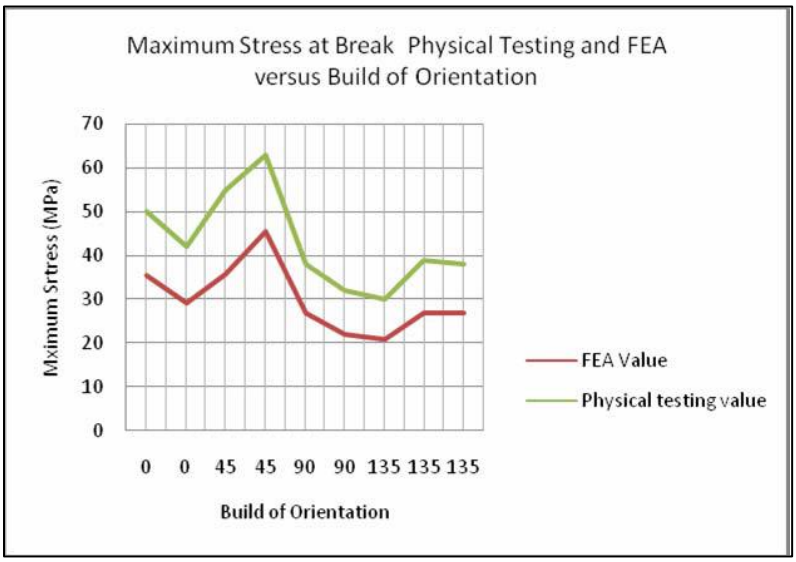

Figure 17: Failure comparison of different orientation of FEA and experimental data [52].

Domingo-Espin *et al* [53] aims to find a simulation approach to analyze FDM parts and to validate the simulation model with experimental results. The authors derive a constitutive orthotropic material model to obtain the stiffness matrix. This matrix would be used as input material properties for simulations. A simple part comprising of L shape is printed and tested to obtain experimental data. This loading condition is simulated using ANSYS using a completely solid CAD model. The simulation results show similarities with the experimental data. The similarity in results however, depend on the building base orientation [53]. A similar simulation is performed using an isotropic model for analysis. Results show similarities in the isotropic model as well, showing similar deviances as the

orthotropic model [53]. The authors suggest that since the isotropic model is easier to set up, it should be used in elastic region only, since errors were similar and acceptable. Whereas, in analyses exceeding the elastic region, orthotropic or anisotropic model should be adopted.

Mamadapur *et al* [16] also discuss a similar methodology. A compliance matrix is derived from experimental results of FDM parts to evaluate the material properties. This characterization is then used with analytical methods as an application of mechanical characterization. Two simple parts are designed to be analyzed under different loading scenarios; angled bar under combined loading and solid bar under bending. A solid model was created and assigned different material orientation as per the actual parts. The orthotropic properties from the material model were used for an FEA. These results are validated using experimental testing and the authors found that the FEA results match experimental results with an acceptable amount of error (4%-10%). However, in case of the solid bar, FEA values were consistent with experimental values only in case of two of the four orientations. This may be possible in case of bending tests due to the composite material behavior of FDM parts [16].

Bellini *et al* [54] developed FEA models without directional orientation and using isotropic properties and then using anisotropic properties. The authors reveal considerable differences in the results obtained from an isotropic model as compared to the experimental results.

Rodriguez *et al* [55] discuss the development of computational models for FDM material stiffness and strengths. These theoretical predictions are validated with experimentally derived values of moduli and strength. A finite element model is used to evaluate the effective elastic moduli using two approaches: a strength of materials approach and a homogenization approach. These are compared to the experimental values of the ABS. The authors state that assuming an orthotropic material model is a good approximation to model the stiffness of the extruded fibers in FDM parts. The properties are largely dependent on the void shape and area; hence, further detail modelling is required [55].

Owing to the non-continuous fibered nature of the FDM parts accurately, representing the model to be analyzed is necessary. Several papers have represented the parts with its mesostructure; i.e. designing the parts in form of fibers and with voids. Cuan-Urquizo *et al* [56] focusses on mechanical characterization of lattice structure of FDM parts. The authors develop a cubed lattice model, using simple elastic elements to form the entire part. These parts are printed and tested to obtain material properties and study the structure-property relationship, which is used in a FEA solver to determine the effective elastic moduli.

Villalpando *et al* [57] compares an FEA approach to experimental data, using models with parametric internal matrix structures under compressive loading. A solid 3D CAD model is created and converted to a shell structure, shown in Figure 18. A primitive modifiable element is used to form internal structures by joining the spherical ends along with specific geometrical constraints to create complex truss-like structures [57]. Different

internal structures are used. An FEA simulation is run using Abaqus©. This model is sliced and printed using FDM to obtain experimental data. Figure 19 shows the results of the FEA simulations and experimental data for the compressive tests conducted on the different models. The load applied is compared and shows consistent similarities between simulation and experimental results. Therefore, it can be assumed that the FEA simulations will provide a reliable estimation in compressive loading cases for parts with similar characteristics as the ones simulated in this CAE model. [57]. A similar compressive analysis is also performed in [58].

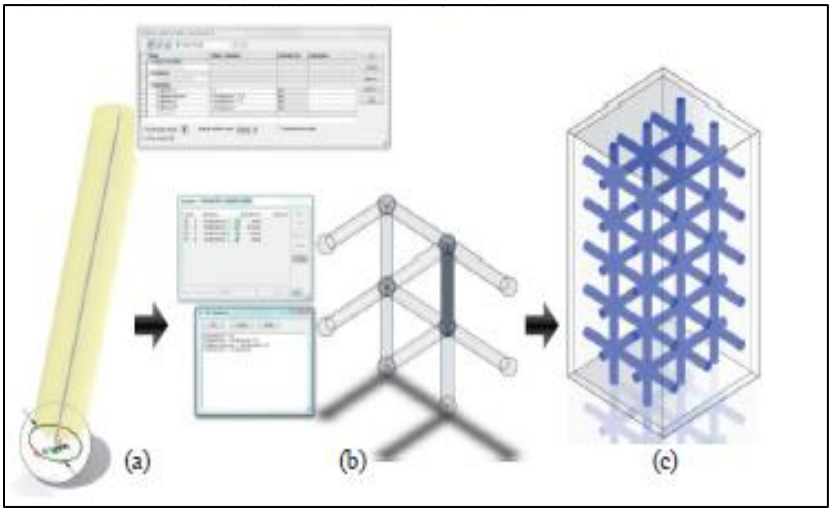

Figure 18: Parametric modeling of the modifiable element structure (a), the parametric web-like structure, and (c) the internally modified shelled part [57].

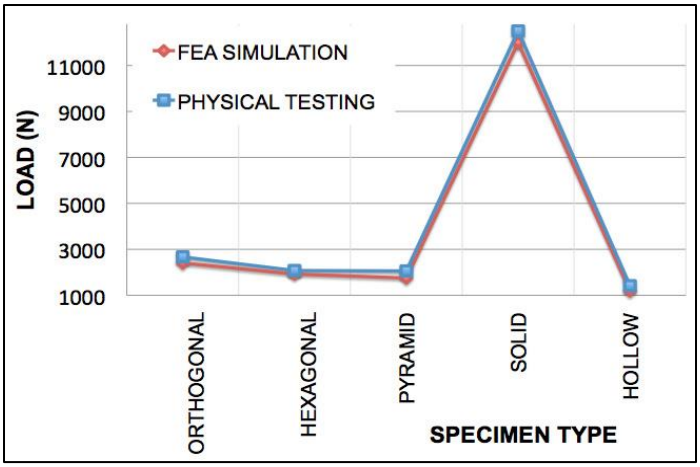

Figure 19: Comparative of FEA simulations and experimental compressive tests [57].

El-Gizawy *et al* [59] present an integrated approach to characterize mechanical properties and internal structure of FDM parts and analyze these using CLT. Experimental data is used to derive the material properties. Image based mesostructure is analyzed using electron microscope based images and these are recreated to represent the cross-section of lamina. A composite layup is used so that the part is represented as composite. The resulting simulations are consistent with the experimental data.

Rezayat *et al* [60] conducts a similar study which studies the macroscopic behavior by modeling the microstructure. An FEA using composite lamina is performed in COMSOL and validated with experimental data. Garg *et al* [61] try to study the failure of FDM parts under tensile loading, using FEA. Parts built in different orientations and with different raster orientations are simulated in FEA and later validated. It is important to note that even this study uses a mesostructure to model FDM parts using microscopic imaging.

Ajoku *et al* [62] replicates compression loading on a Nylon-12 FDM part using FEA and validating with experimental results. This work adopts two approaches to modeling; in the first approach, material data from injection molded and laser sintered parts is used, whereas, the second approach obtains material data from laser sintered parts and translates the degree of porosity into the model. The first approach shows considerable deviance from the experimental values for laser-sintered parts. Even though the second approach shows better predictions than the first approach, authors state that the approach of geometric porosity is not an entirely appropriate method to represent the AM parts.

Since FDM parts are built layer-by-layer, authors argue that a composite lamina theory will enable to better realize the behavior of FDM parts. Martinez *et al* [63] uses a composite laminate layup in FEA using Abaqus to predict the behavior of FDM parts. The orthotropic material properties are derived and used as input in FEA simulations. Two approaches are used; modelling a rigid geometry using orthotropic properties, and secondly, modeling a composite geometry using orthotropic properties. Both the models show remarkable approximation to reality with the rigid model underestimating the failure criterion more than the composite model.

Sayre *et al* [11] performs an FEA on 3D printed part using modifications to the CLT. Two models are created, an isotropic model, based on a part manufactured from traditional means; and a composite FE model, based on a layered FDM part. Tensile, compressive and bending tests are simulated in Abaqus©, and results show considerable difference in the values of the two models; the composite parts yield at a lower load than their isotropic counterparts. The authors however have not compared the FEA models with

experimental results directly. It is important to note that FEA model using a composite configuration tend to exhibit properties of the laminate as a whole rather than exhibiting failure in a single lamina during uniaxial tests [11]. The authors conclude that the FE model with modification of material properties appear to reasonable to mimic the behavior of FDM parts better than isotropic model.

Table 4: Summary of literature regarding simulation of FDM parts.

Approach	References	Work needed.
Orthotropic Material Model	Hambali *et al* [51, 52]	Inconsistency
	Domingo-Espin *et al* [53]	In agreement
	Mamadapur *et al* [16]	Inconsistency
	Bellini *et al* [54]	In disagreement
Mesotructure	Villalpando *et al* [57],	In agreement
	Garg *et al* [61],	-
	Ajoku *et al* [62]	Inconsistency
Composite Laminate Model	Martinez *et al* [63],	In agreement
	Sayre [11]	In agreement

Table 4 summarizes the different simulation approaches used. It is evident that the FEA results for FDM parts have not been consistent. Some models show agreement with a general FEA model of a simple part, whereas other models show inconsistencies. It is evident that a detailed model that takes into account the microstructure and the anisotropy of FDM parts is required for precise and accurate analyses. FDM parts are usually complex with an integral infill pattern, and validating FEA approaches to accurately predict the FDM part behavior is necessary. In the following chapters, FEA is performed on as-built FDM parts and is validated with experimental results. Chapter 3 talks about an isotropic model used for FEA, and its comparison with experimental results.

CHAPTER 3: INTIAL FEA SIMULATIONS AND EXPERIMENTAL RESULTS

The goal of this study is to evaluate approaches that would best represent the AM parts; not as continuous entities but as anisotropic, discrete fibers closely spaced together to form the part. With the properties of FDM in mind, considering a general method of analysis that accounts for all these properties is herculean task. Therefore, a systematic approach is used. This chapter is submitted as a conference paper for ASME IDETC 2017 Conference. Two approaches to represent AM parts better, have been proposed in the following sections. The first approach modifies the CAD model to represent the AM parts better. This approach deals with design the parts as they are built, so that they are closer to their actual structure. The second approach deals with modifications in the analysis process so that a better representation of the AM parts' material model can be achieved. The basic approach for analysis of FDM parts is performed using the bulk isotropic properties of ABS. These properties are the properties of a continuous bulk ABS. The parts are assumed to be continuous and isotropic in nature. Even though this is against the actual behavior of FDM parts, it is important to point the difference in representing FDM parts as continuous isotropic elements. In order to have a basis for comparison, the simulation results are compared with the experimental results. Further, to represent the FDM parts better, derived properties of the FDM parts are used in the simulations. The following sections talk about the approaches mentioned to analyze FDM parts and validate their precision and accuracy with the experimental results. An overview of the methodology, specimen development, comparison metrics and the process of the study is provided in the following subsections.

3.1 Methodology

The approach used in the initial part of the study is to redesign the AM part as it is built to an acceptable extent of precision, accuracy and detail in CAD. A set of geometries is designed, to be printed and tested on a tensile test bed. Once the part is printed, its CAD model was redesigned as an 'as-built' model using the G-code from slicer. A fiber-by-fiber and layer-by-layer model was created that would represent the actual printed parts. This structure should represent the geometry as well as the infill pattern of the part. Thus, the as-built CAD model enables us to represent the FDM parts with their mesostructure: with individual fibers forming the entire part. The G-code was input in Solidworks© to obtain a toolpath in a particular layer to be extruded. Figure 20 shows the G-code sketched in Solidworks©.

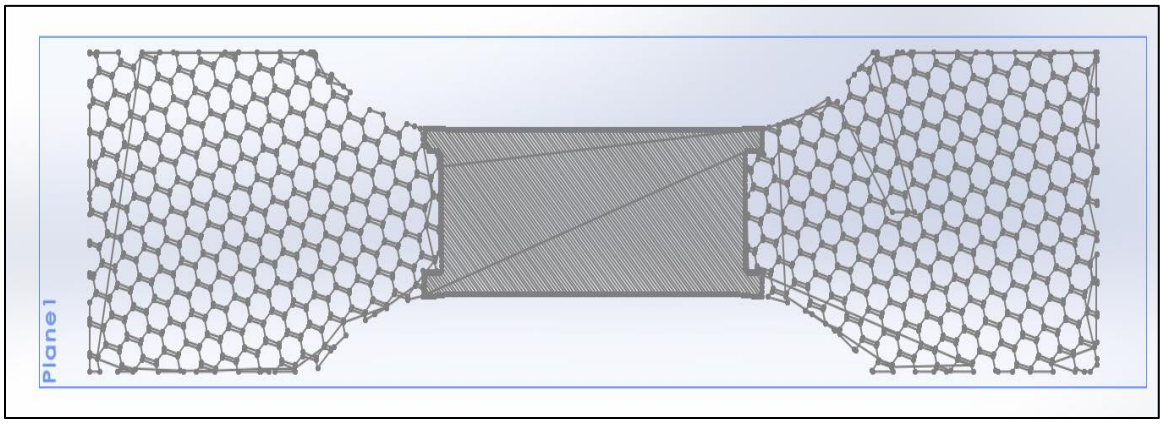

Figure 20: Solidworks© sketch using G-code of the printer toolpath

'Sweep' feature was used to sweep the rectangular shaped filament through the toolpath. Thus, each layer was form built on top of the previous one. However, initial

analyses pointed out the problems faced in using this model. Figure 21 shows the individual filaments along the toolpath.

- As seen from the figure, some of the filaments intersected adjacent features (filaments), whereas some did not. This resulted in intersecting errors within the part, rendering the CAD model useless. In addition, it is not possible to merge adjacent bodies while using the 'Swept' feature in Solidworks© unlike the 'Extrude' feature.

- Secondly, a part without these errors caused meshing problems. The mesh elements were not aligned and caused misalignment between adjacent elements of the mesh.

- The part file was large owing to large features, taking four hours to save. Meshing the part further took nine more hours, and the analysis took forty hours.

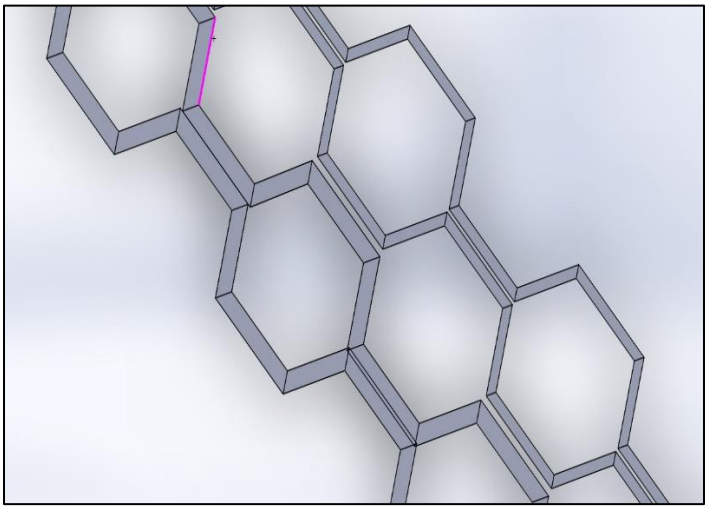

Figure 21: 'Sweep' feature on the G-code toolpath sketch.

This is a fairly simple geometry which took an extensive amount of time and memory to be analyzed and hence using this method to model FDM parts was prohibitive. Therefore, a continuous model depicting the geometry and infill pattern is used. Further details about the geometry and design are discussed in 3.1.1. These parts are then simulated in a FEM solver, first using bulk properties, and then using derived properties. A sample model is used to derive the material properties for the parts. This would enable us to compare the simulations results of the 'as-built' AM parts with the experimental results. In order to efficiently compare both results, appropriate test problems and test metrics are developed. The tensile test conducted on the print specimens are replicated in the simulations and later compared with each other.

3.1.1 Geometry.

The present work primarily includes tensile tests only; therefore, the test specimen used is a dogbone geometry. It has enlarged ends known as shoulders for gripping. The area of concern in the specimen is the gage section. The cross-sectional area of the gage section is reduced relative to that of the shoulders of the specimen so that deformation and failure will be localized in this region [64]. All the measurements of the test sample are carried out over the gage length of the specimen. This geometry was designed as a CAD model in Solidworks© and later converted to the STL format for printing. The design of the geometry is similar to the standard specifications stated in ASTM D638 but not identical due to printing and testing considerations. The final dimensions of the dogbone were a gage area of 50x20x2 mm. Including the shoulders, the specimen was 170 mm in length and was

35 mm wide at the shoulders. The height of the geometry was uniform throughout. The maximum length was dependent on the length of the 3D-printer bed as well as the maximum test frame length of the tensile testing machine. Whereas, the width of the shoulders and the height of the specimen were determined based on the grips of the test machine. Figures 22 through 26 depict the drawings of the different dogbone geometries that were designed for this study using Solidworks©.

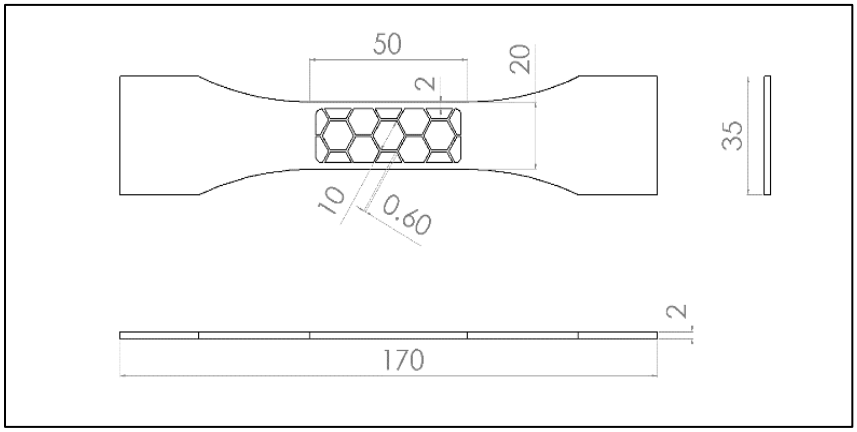

Figure 22: Hexagonal Infill (HI) specimen.

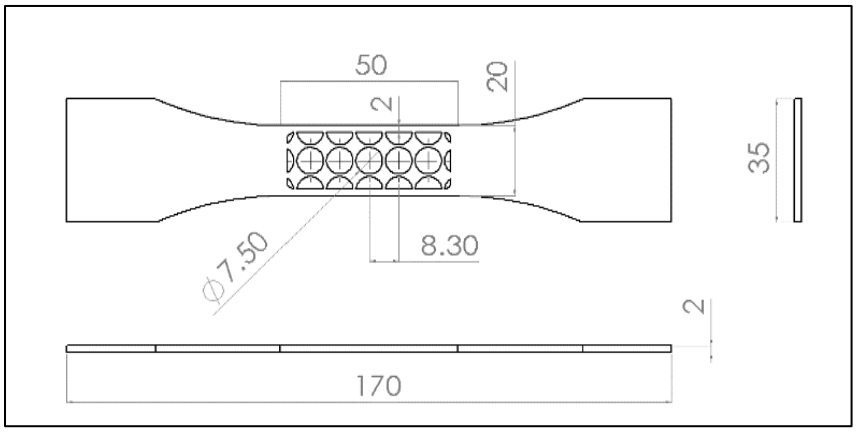

Figure 23: Circular Infill (CS) specimen.

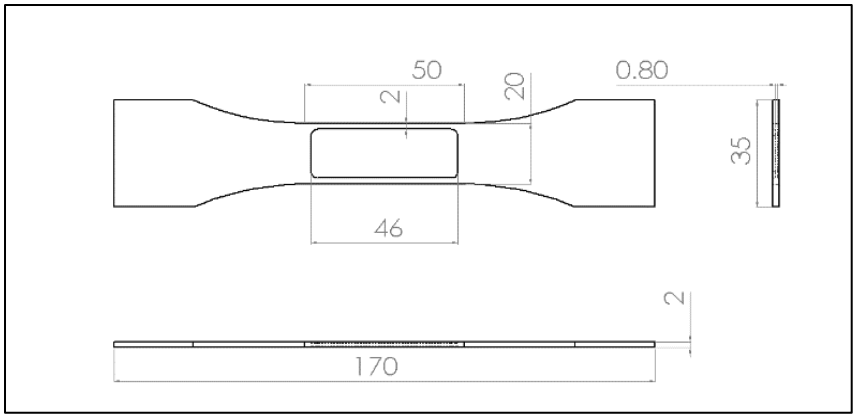

Figure 24: Circular continuous (CCS) specimen.

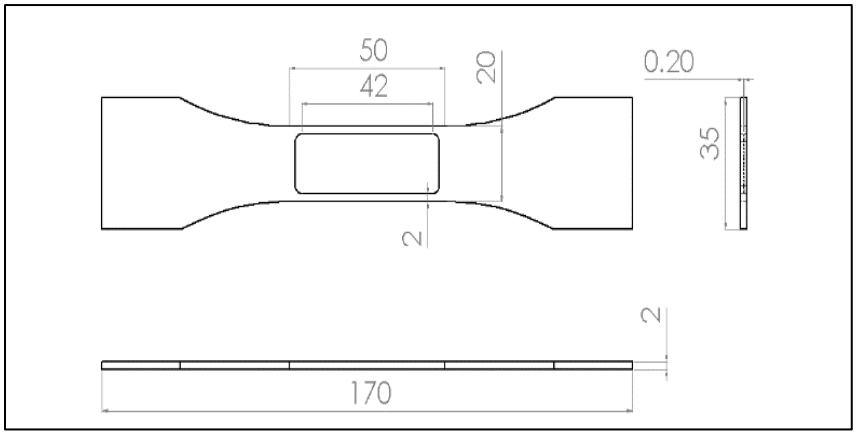

Figure 25: Hexagonal continuous (CHI) specimen.

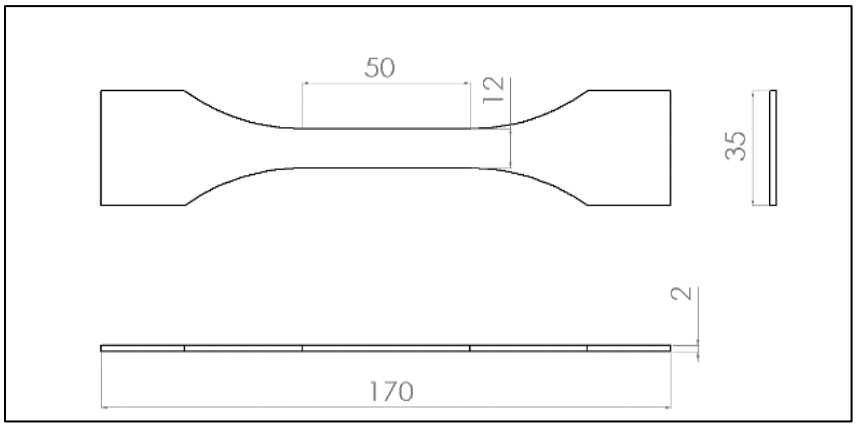

Figure 26: Continuous (C) specimen.

Another important aspect of the AM parts is the infill pattern and the infill percentage. Many times, AM parts are not 100% solid but have a structured mesh inside the model. Infill percentage and pattern influence print weight, material usage, strength, print time and sometimes, decorative properties. Therefore, a number of infill patterns were considered in this study, namely honeycomb and circular. The infill percentage for each of the pattern was different and was decided on basis of the accuracy of the printer. The dimensions of the reduced cross section of the dogbone geometry were decided keeping in mind whether the geometry is able to accommodate the necessary features of all the infill patterns. The patterns are constrained to the gage area only and not over the entire geometry. This would ensure that the specimens would primarily elongate and fracture in the gage area. The rest of the geometry was designed to be continuous so that the results would not be affected by the compressive forces of the grips or the localized stresses due to the change in geometry. The patterns were designed such that each side of a pattern would represent an extruded filament. Therefore, in case of the hexagonal pattern, the sides of each hexagon were 0.6 mm thick. Similarly, each of the infill pattern geometries had a corresponding continuous model. This model was continuous in the gage length with the same width but lesser thickness so that it was equal in volume with the corresponding patterned part. The corners in the gage area for all the geometries were filleted to avoid stress concentrations. To ensure repeatability a sample set of 20 specimens for each pattern were printed and tested.

Additionally, a completely continuous specimen is modelled as shown in Figure 26 to derive the material properties for the FDM parts. This part has a narrower gage section

to ensure fracture in the gage section. To avoid confusion with the names of these specimens, abbreviations are assigned for the sake of this study. The geometries considered for this study are listed below:

- Completely Continuous (C)
- Hexagonal Infill (HI)
- Hexagonal Continuous (CHI)
- Circular Straight Infill (CS)
- Circular Continuous (CCS)

3.1.2 Assumptions

A number of assumptions that were made in the study have been stated below:

- Since different spools of ABS were used for printing the specimens, it is assumed that the material from the different spools is consistent with the material properties.
- The environment is not considered as a significant factor that affects the printing or testing. This is considered since the laboratory operation temperature was consistent throughout the study.
- Any errors in clamping the specimens were considered to be randomly distributed.

3.1.3 Printer

Once a CAD model had been created taking into account the appropriate 3D printing considerations, these files were converted to a STL format. The STL file is processed using the slicer, which creates a G-code file for the 3D printer. The 3D printer

used for this study is the MakerBot© Replicator 2X. The printer is shown in Figure 27. The printer only runs .x3g files unlike other printers, which use G-code files. The process of creating the file remains the same, i.e. we import the STL file in the 'MakerWare Desktop©' software which slices the dogbone geometry and converts it into an .x3g file for the printer. However, initial prints revealed that the 3D printer was not printing consistent specimens. Analysis of the failed prints and print previews from the software suggested that the software was not able to efficiently slice the models and subsequently the printer could not replicate the models as required.

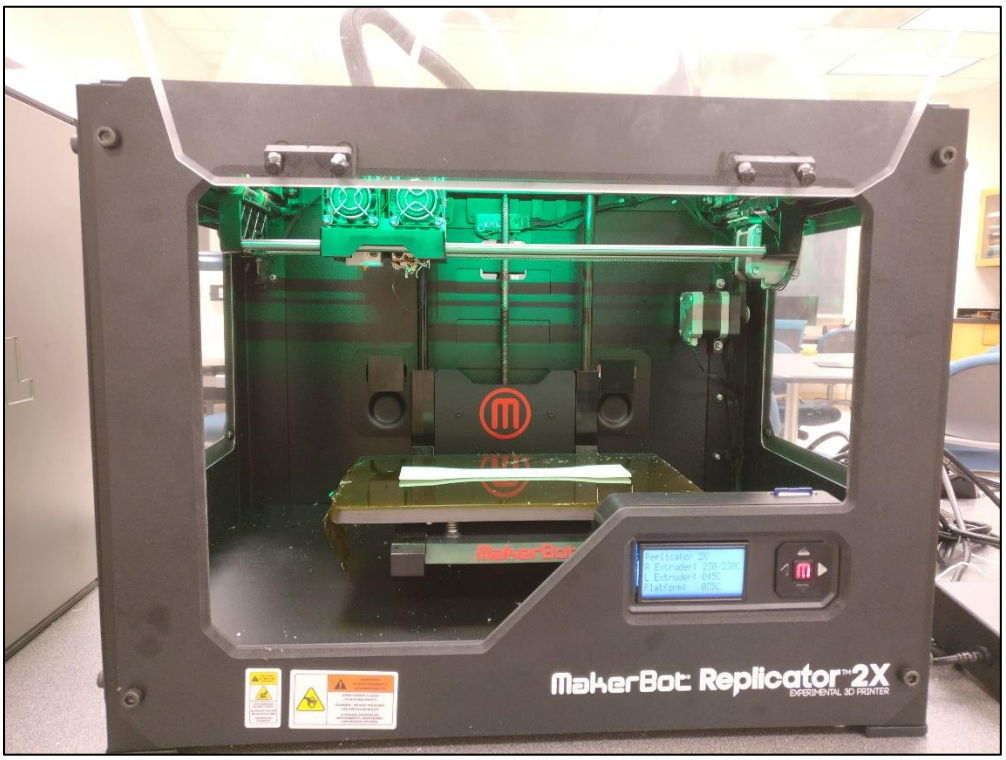

Figure 27: MakerBot© Replicator 2X used for printing.

The next task was to search a different slicer that would slice the model convincingly and write it to an .x3g file format. The next slicer sought to was 'Slic3r©'.

With the firmware of the slicer set to MakerWare (MakerBot) © settings, it was effectively able to slice even the thin walled features in the model. 'Slic3r©' stored this data in a G-code format. Therefore, 'Replicator G©' (another slicing software) was used to convert the G-code files to '.x3g' format. This produced effective results.

3.1.4 Printer Parameters.

The MakerBot© Replicator 2X has a heated bed. The material used in this study was white ABS (Acrylonitrile Butadiene Styrene). The extruder temperature for ABS was set to 230º C. Whereas, the bed temperature was set to 130º C. This avoided warping and ensured that the part would stay on the bed firmly during the entire build. As discussed earlier, the 3D print settings have a huge impact on the strength, structure and the finish of the specimen. Therefore, the settings for each of the model were decided such that they would result in the best possible specimen. The HI specimens were printed with a layer height of 0.2 mm whereas the CS specimens were printed with a layer height of 0.4 mm. At a particular layer height, the slicer automatically sets the filament width. The continuous models on the other had to be modeled with a layer height of 0.4 mm and a filament extrusion width of 0.4 mm. This was because the printer extruder was not able to print the continuous infills consistently and resulted in a discontinuous fill. Since all the infill patterns had already been modelled in CAD, the infill percentage used for each of the model is 100%, i.e. a solid rectangular infill to represent the continuous solid part. Each of the specimen was printed without a raft to enable the bottom layer of the parts to bond adequately resulting in a stronger part. Another reason that the parts were printed without

the raft was that the process of removing the raft also strains some of the bottom fibers and may damage the parts. Initial tests also revealed that the parts printed without a raft were stronger than the ones printed with a raft.

The continuous specimens had a continuous area in the gage length, which was suspended along the length exactly midway in height of specimen. Hence, this region needed a support structure to avoid sagging of the suspended area. Default support settings were used for this region i.e. 0.42 mm filament thickness and 0.4 mm layer height. The support structure was later scrapped off using carving knives. The completely continuous (C) sample used for deriving the material properties had the same print settings; 0.2 mm layer height and 45º/-45º solid infill. The printing parameters are summed up in Table 5.

Table 5: Printing Parameter for the dogbone geometries.

	Layer Height (mm)	Filament Width (mm)	Required Support
Continuous (C)	0.2	0.67	No
Hexagonal Infill (HI)	0.2	0.67	No
Hexagonal Continuous(HC)	0.35	0.4	Yes
Circular Infill (CI)	0.4	0.42	No
Circular Continuous (CC)	0.4	0.42	Yes

3.1.5 Tensile Tests

In order to test the strength and compare the material properties with the simulation results, tensile test was performed on the test specimens. The tests were performed on 'Modular under Microscope Mechanical Test System – μTS' by Psylotech©. Figure 28 shows the tensile test frame with a specimen attached with grips. As the specimen geometry did not fit the slotted grips, clamping grips were used to hold the specimen. A displacement controlled tensile test was performed. A displacement of 10 mm was applied at a uniform velocity of 50 μ/s. This ensured that the specimens elongated plastically and finally fractured. Similar settings were used for the corresponding continuous parts as well. The test data file records the displacement and the corresponding force applied at every time step of 0.05 seconds. Therefore, for every specimen, approximately 1000 data points are collected per test. This data is further post processed to obtain the effective modulus of the specimens. The displacement is used to obtain the average strain throughout the specimen. The force applied is used to calculate the stress in the least cross-sectional area as shown in Eq. 11.

$$\sigma = \frac{F}{A} \tag{11}$$

σ = Stress,

F = Force applied,

A = Area of cross-section

$$\varepsilon = \frac{\delta L}{L} \tag{12}$$

ε = Strain,

δL = Change in length,

L = Length (Gage length),

The strain calculation is given by Eq. 12. The stress and stress are used to calculate the effective elastic modulus. The elastic modulus is calculated using Eq. 13,

$$E = \frac{\delta \sigma}{\delta \varepsilon} \tag{13}$$

E = Young's Modulus (Effective elastic modulus in case of this study),

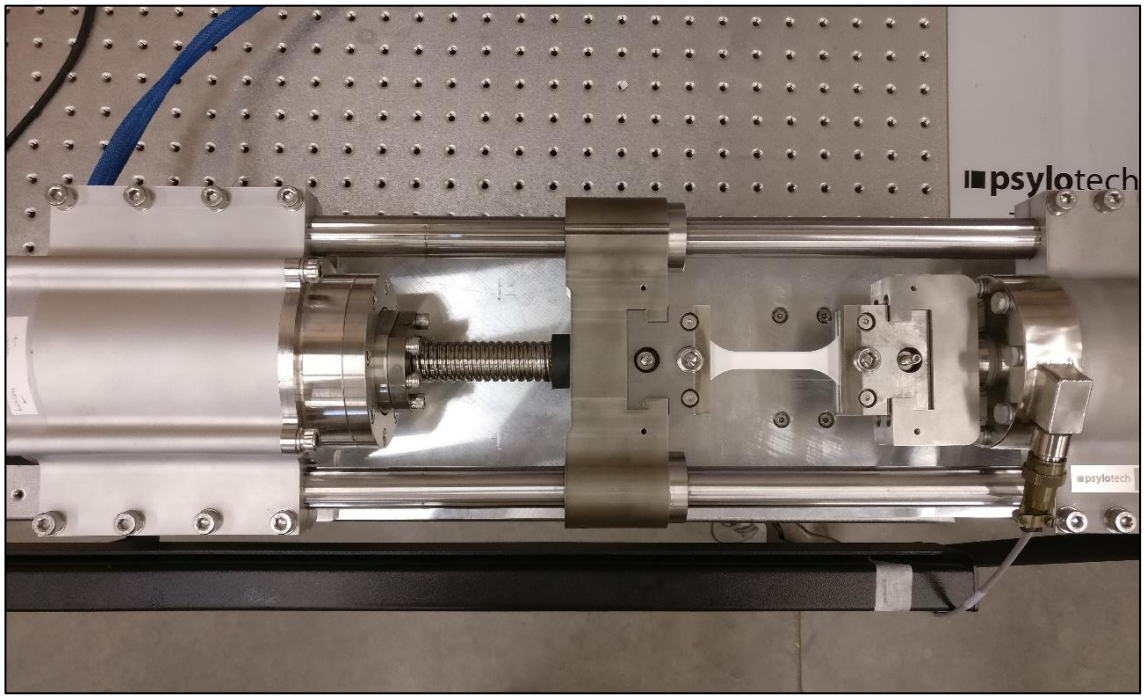

Figure 28: Psylotech© Tensile Test frame used in the study.

3.1.6 FEA Simulations

Once the specimens are printed, each of the specimen is compared with their corresponding CAD models for each of the dimension of the gage length. An average of the length, width and height of the gage section is calculated for each set of 20 samples. A new CAD model is designed considering the change in the dimensions, so that the specimens are modelled as-built. The only difference is that these models are designed as continuous geometries and not as discrete fibers closely bonded to each other. This CAD model is the as-built model.

The next step is to analyze these specimens with an FEA solver. The solvers used for this were ANSYS© and Abaqus©. A Transient Structural Analysis is conducted on the as-built CAD models. Two approaches are followed in the initial part of study. First, an analysis is carried out using the material properties of bulk ABS [65]. Since bulk ABS is isotropic, an isotropic model is used with the bulk material properties. This approach is called as Bulk Isotropic Model (BIM).

For the second approach, the material properties for the test specimens of ABS are derived from the completely continuous (C) samples. An isotropic model along with these properties is used. This approach is called as a Derived Isotropic Model (DIM) at this stage of the study. This would enable us to compare the FEA simulations using bulk and derived properties with the experimental results.

Since the patterned specimens have thin walled structures, a refined mesh is used and displacement controlled uniaxial tensile test is simulated. The mesh statistics are tabulated in Table 6. Quadratic tetrahedral elements were used in ANSYS© and Abaqus©

simulations. Table 6 shows the mesh statistics for the specimens. Figures 29 through 32 show the meshes for different geometries using ANSYS©. Since the mesh plots in Abaqus© are similar they have not been presented; they can be found in Appendix A. The end of one of the shoulders is set as a fixed support. The displacement results from the tensile test are inputted in as the displacement, applied at the opposite shoulder end. However, since the study is comparing only the linear FEA results, displacements until yield are used. The specimen data is ensured to remain in the elastic region. The stress and strain are calculated as outputs in the results section.

Table 6: Mesh statistics from FEA solvers.

	ANSYS©		Abaqus©	
	Nodes	Elements	Nodes	Elements
Continuous (C)	15209	7344	2400	1092
Hexagonal Infill (HI)	19522	9397	103885	62493
Hexagonal Continuous (CHI)	13341	6582	18765	9667
Circular Infill (CS)	26840	13026	44840	13026
Circular Continuous (CCS)	13280	6515	17520	9572

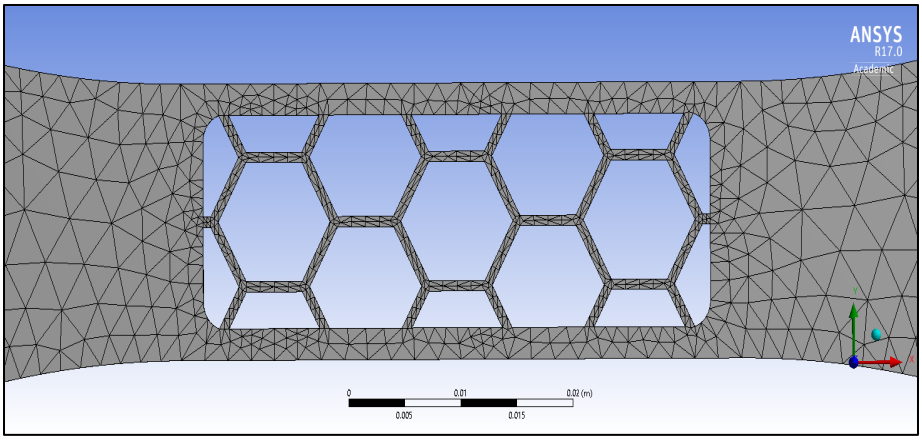

Figure 29: Mesh model for Hexagonal Infill (HI).

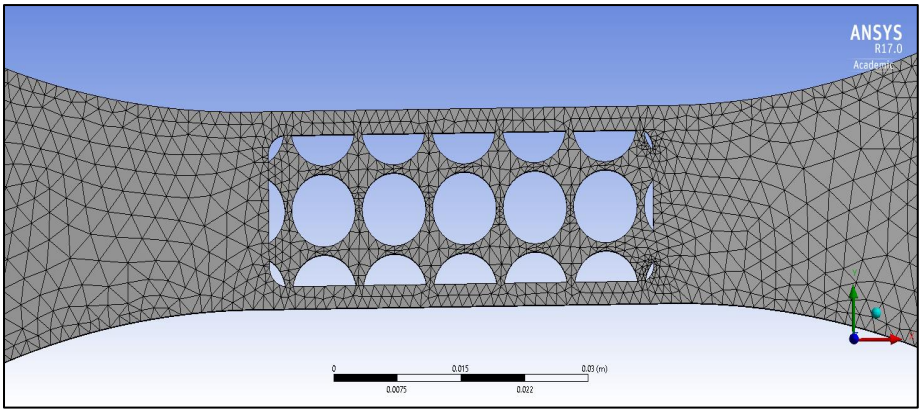

Figure 30: Mesh model for Circular Infill (CS).

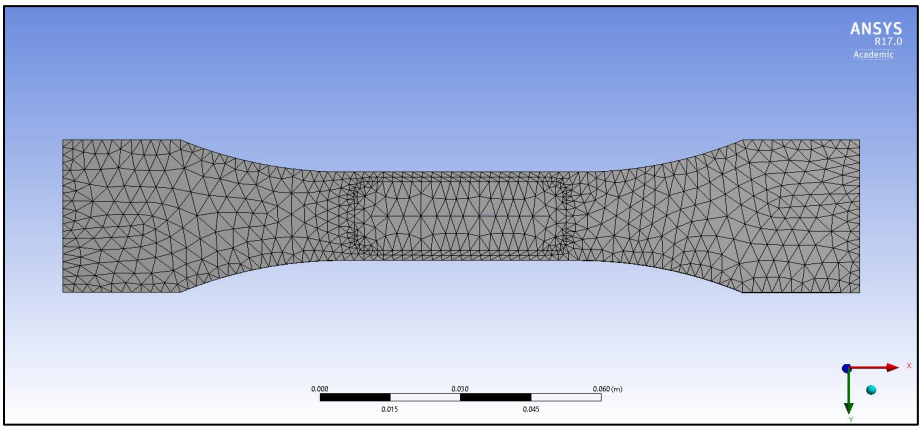

Figure 31: Mesh model for Hexagonal continuous (CHI).

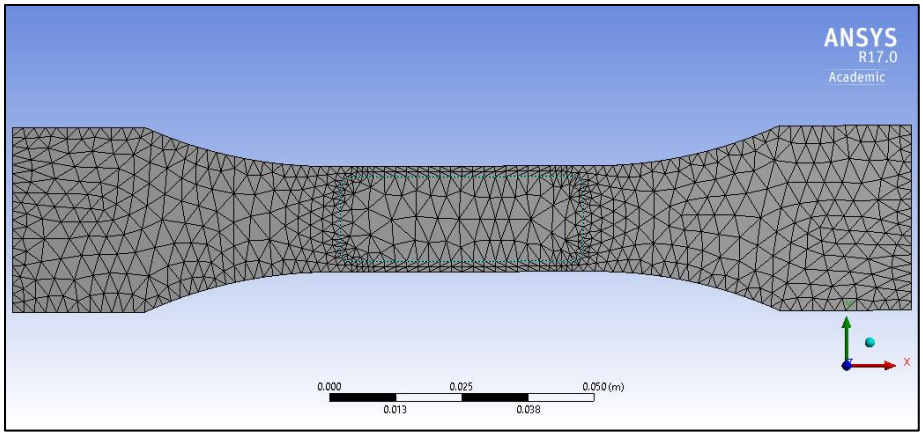

Figure 32: Mesh model for Circular continuous (CCS).

Similarly, FEA is also conducted on a different solver i.e. ABAQUS©. Since ABAQUS© does not accept Solidworks© files, each of the CAD files are converted to a '.step' format. A similar displacement controlled analysis is carried out with this solver as well. Stress and strain are obtained as results. Since the Elastic Modulus is already an input in the solver, only the stress and strain values of each of the patterned and continuous specimens are compared.

3.2 Results and Discussions

The final prints of each of the geometries are shown in the Figure 33. The dimensions of the printed parts in a given set varied by ± 0.1 mm. These parts were tested on a tensile test bed; the results of the tensile test are discussed below.

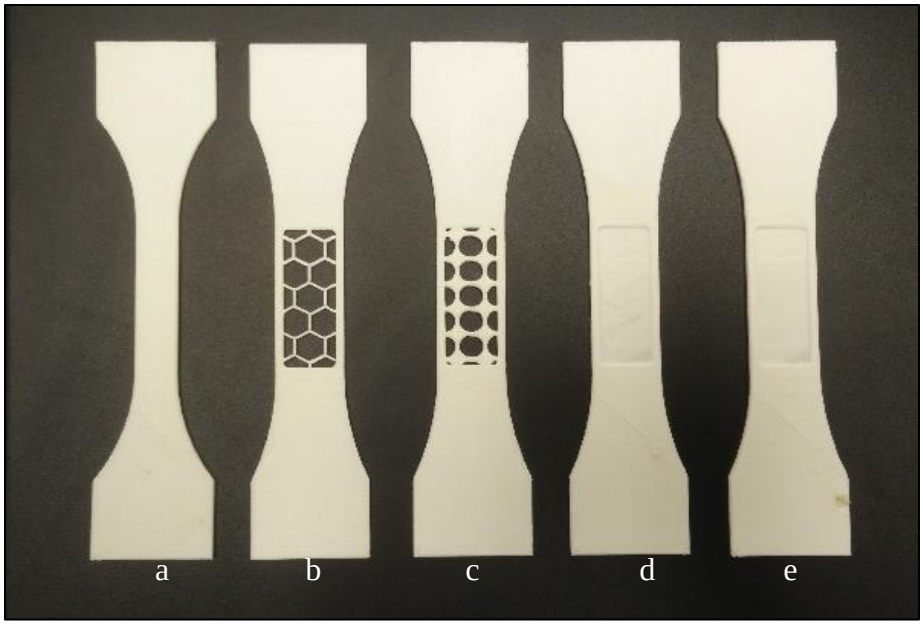

Figure 33: Printed specimens: (a) Continuous (C), (b) Hexagonal Infill (HI), (c) Circular Infill (CS), (d) Circular Continuous (CCS), (e) Hexagonal Continuous (CHI).

3.2.1 Tensile Tests

The Tensile tests generated a series of data to analyze. For each specimen, a Stress vs Strain and Force vs Displacement curve is plotted. The continuous (C) sample data is post processed to calculate the material properties for the study. The stress-strain curve for this sample is shown in Figure 34. The derived elastic modulus is 1±0.1 GPa. The continuous (C) parts typically fractured in the center of the gage sections transversely. The fractured part is shown in Figure 40. This modulus calculated was used in FEA simulations.

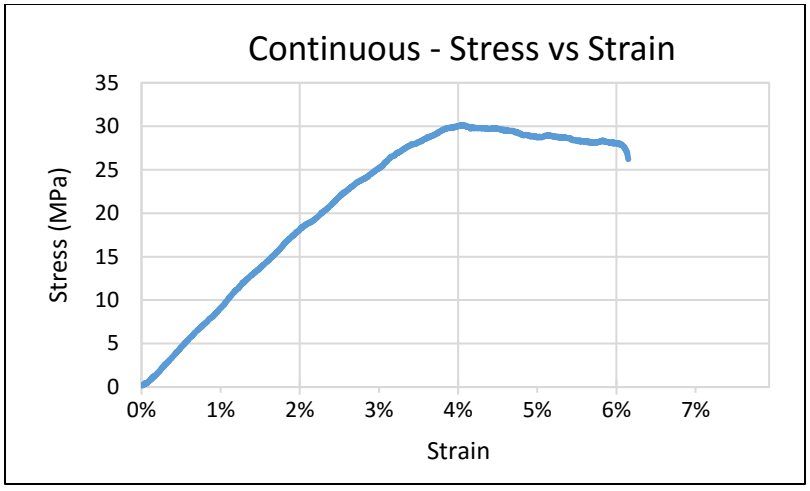

Figure 34: Stress-Strain curve for Continuous (C) samples.

As mentioned earlier, effective modulus is calculated for each of the specimens. Consider the results of the Hexagonal Patterned specimens. Stress is calculated across the least cross sectional area. For the 20 hexagonal patterned specimens (HI) the average effective elastic modulus was 1.25±0.25 GPa. The actual elastic modulus of a continuous ABS specimen ranges from 2 GPa to 2.4 GPa and that of the 45/-45 FDM ABS specimen is 1±0.1 GPa. Comparing these results with the corresponding set of equivalent volume continuous (CHI) specimens, the elastic modulus ranged from 1±0.1 GPa. This meant that the continuous specimens of equal volume of infill showed a lower effective modulus. The test results have been tabulated in this section to aid comparison. A stress-strain plot for the patterned and continuous specimens in Figure 35 illustrates the elastic and plastic region before fracture. The ultimate strength of Hexagonal infill (HI) patterns was 28.1 MPa at 4.5% strain and the ultimate tensile strength of its corresponding continuous (CHI) sample is 16.7 MPa at 7.3% strain. The equivalent continuous patterns withheld a lesser force than the infill specimens withheld. The Force vs Displacement diagram in Figure 36

depicts the forces applied during the tensile test. The continuous (CHI) model had a single layer of diagonally oriented fibers and hence were weaker than the infill specimens (HI).

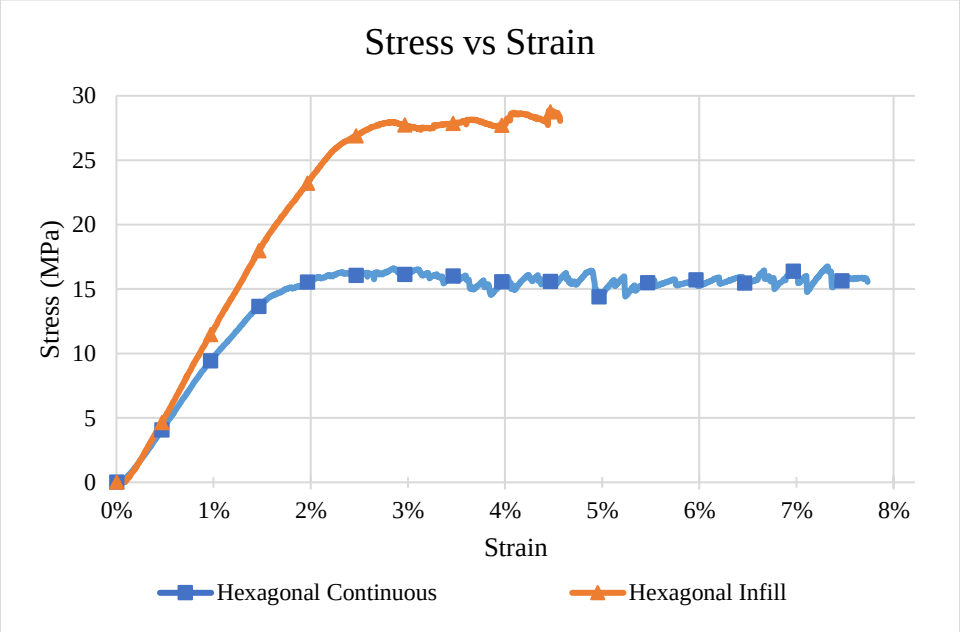

Figure 35: Stress-Strain curve for Hexagonal specimens.

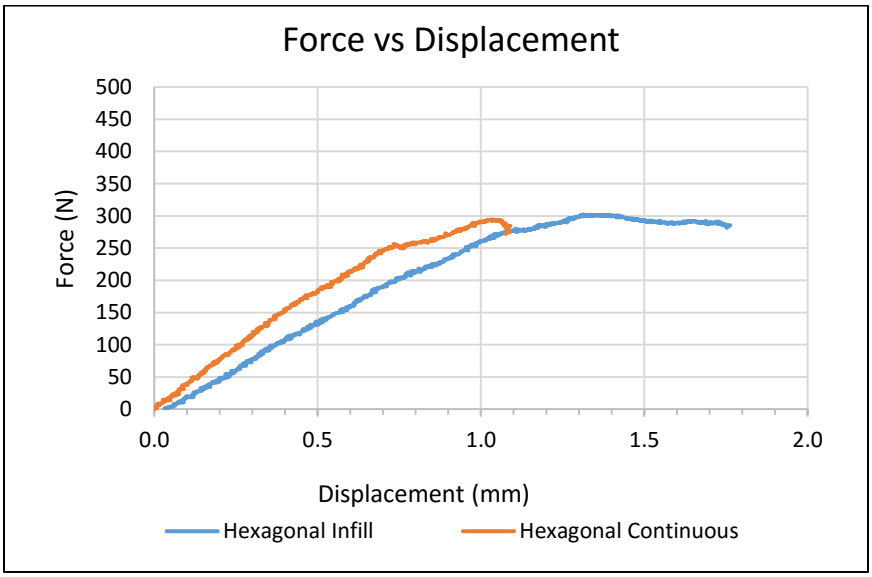

Figure 36: Force-Displacement curve for Hexagonal set.

The circular infill specimens had an average effective elastic modulus of 1.6±0.2 GPa, whereas the corresponding continuous (CCS) specimen set had an average effective elastic modulus of 0.99±0.1 GPa. The maximum force applied during the test for samples was around 400 N as shown in Figure 37. However, in contrast to the previous case, the equivalent volume continuous (CCS) samples failed at a similar value of strain as that of the infill specimens. Figure 38 shows the stress-strain plots for CS and CCS specimen set. Even though both the geometries failed at a similar value of displacement, the maximum stress for CS specimens is more than the CCS set.

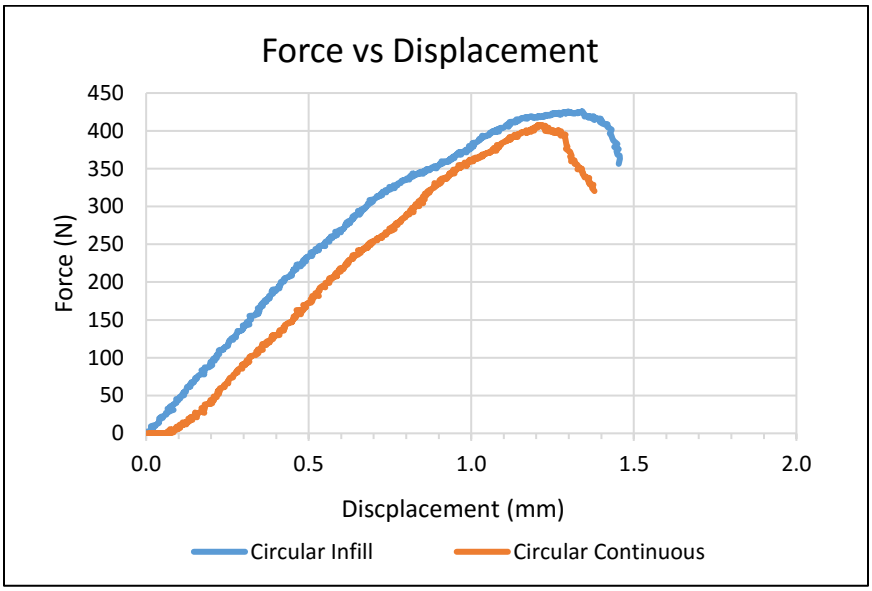

Figure 37: Force-Displacement curve for Circular Patterns.

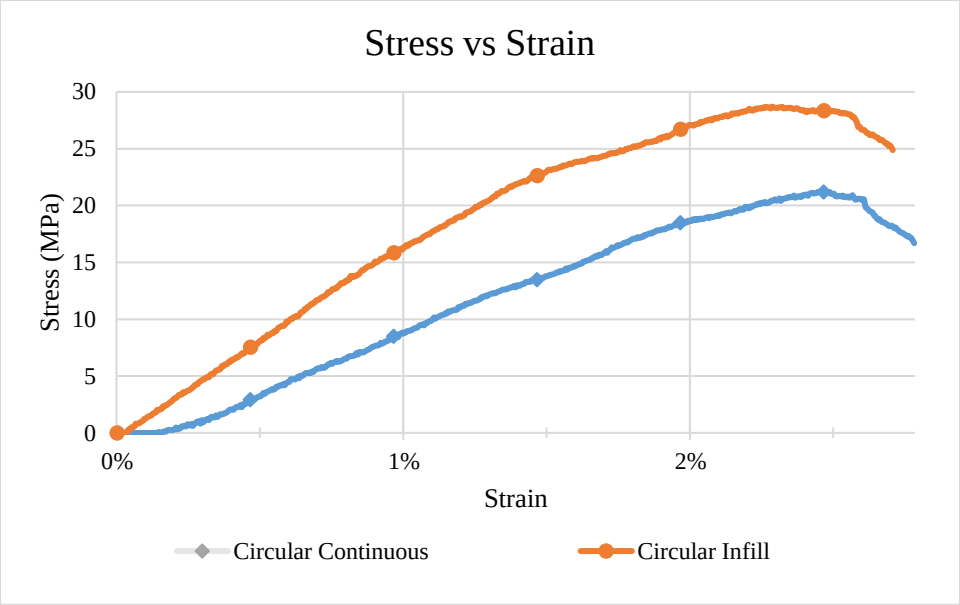

Figure 38: Stress-Strain curve for Circular samples.

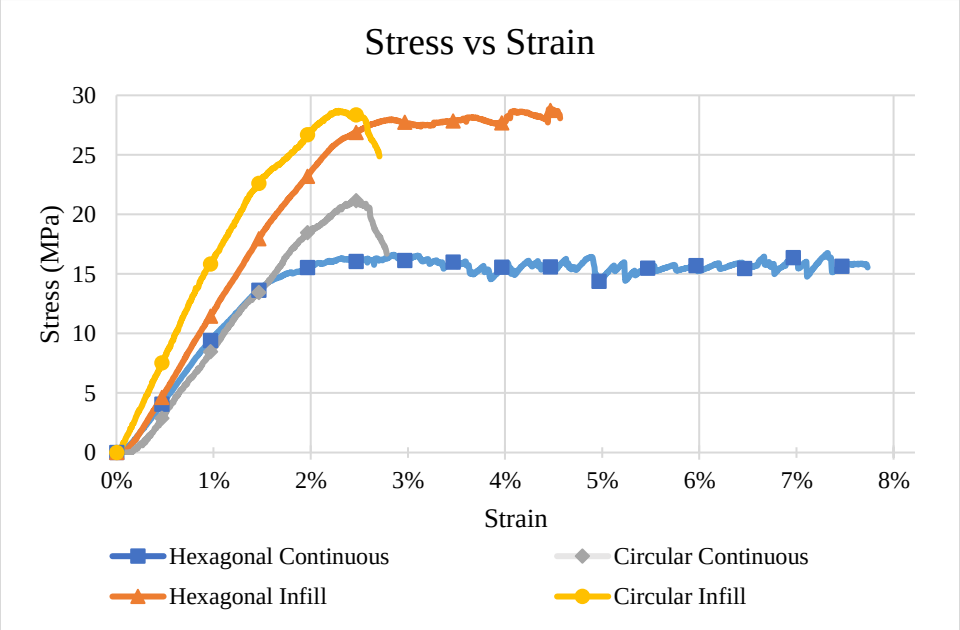

Figure 39: Comparison of Stress-Strain curves.

It is important to note that even though the hexagonal infill and corresponding continuous samples had considerable plastic region. The circular infill and continuous

samples did not have a plastic region on the stress-strain curve suggesting brittle behavior. Figure 39 shows a comparison of the stress-strain curves of all the specimens. The infill geometries (CHI and HI) are stiffer (higher effective modulus) than their corresponding continuous geometries (CS and CCS) and withstand higher values of stresses. Table 7 summarizes the test data for all of the tested samples. CS samples had highest effective modulus and showed similar tensile strength as that of the HI samples.

Table 7: Comparison of test data for different samples.

	Maximum Force Applied (N)	Ultimate Strength (σ_{ut}) (MPa)	Ultimate Strain (ε_{ut})	Effective Modulus (GPa)
Continuous (C)	724	27	0.06	1 ± 0.1
Hexagonal Infill (HI)	301	28.1	0.045	1.26 ± 0.25
Hexagonal Continuous (CHI)	285	16.7	0.0726	1 ± 0.1
Circular Infill (CI)	426	24.9	0.027	1.6 ± 0.2
Circular Continuous (CC)	407	16.9	0.027	0.99 ± 0.1

Analyzing the fracture of the specimens during the test showed stress whitening in the load carrying features and eventual fracture. Further examination of the crack and fracture pattern suggested that the patterned parts fractured at intersection or junction points in the infill pattern. Since the path followed by the extruder while printing the pattern is a time-optimized path and not a continuous path, whenever the extruder joins one end of the filament to another feature of the pattern, a junction or intersection is created. Since

this point is not a continuous point, the bonding of the filament over both the features may not be perfect while the part solidifies. This imperfect bonding creates discontinuities. In case of the hexagonal pattern, junction points are where one side of the hexagon meets another hexagon, where the fracture occurred. In addition, primary fractures occurred in sides of the gage length. This section though continuous has a diagonal infill pattern, which is not the strongest orientation [23] since its direction is not parallel to the stress axis. Another reason for the fracture was imperfect interlayer bonding. The fractured specimens are shown in Figure 40. Since the hexagonal specimen did not break completely, the fracture points are marked with a line in Figure 40.

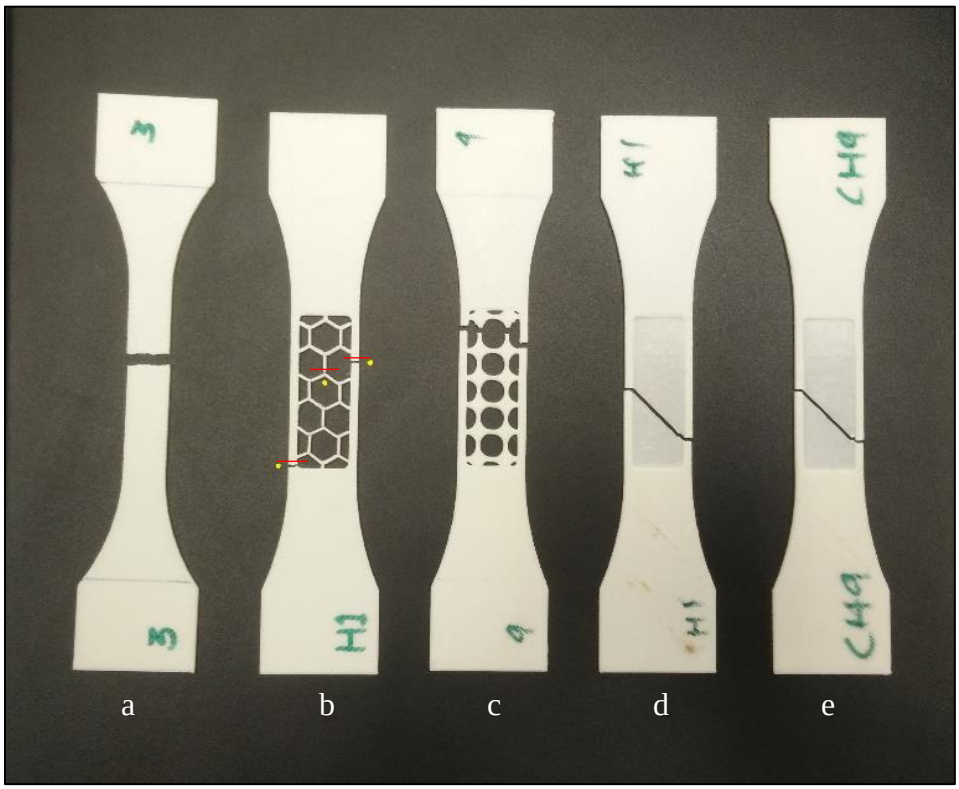

Figure 40: Fractured Specimens: (a) Continuous (C), (b) Hexagonal Infill (HI), (c) Circular Infill (CI), (d) Circular Continuous (CC), (e) Hexagonal Continuous (HC).

The continuous specimens on the other hand fractured along a 45º line (same direction as the infill). The gage section consisted of only a single layer of material and hence the fracture was governed by the direction of the fibers. However, the continuous specimens had imperfections in them, namely small areas where inter-filaments delamination occurred. This manufacturing defect was present in almost all specimens. All the continuous specimens broke along these delaminations (which represented imperfect bonding) and the crack propagated along the direction of the infill causing a lateral separation between the adjacent filaments. Further fractures occurred along the sides of the geometry. Since the region representing the continuous volume consists of only a single layer of material in a 45º direction, the inter-filament strength is weakened and therefore the continuous specimens failed at lower value of force. One noteworthy observation is that for all the continuous specimens, for all the samples, the failure and failure mode was governed by defects. The fracture mode of the continuous (CCS) specimens was similar to those mentioned earlier i.e. along the 45º direction. For the circular infill (CS) specimens, the part failed transversely across the least cross-sectional area.

3.2.2 Finite Element Analyses

The final post-print dimensions were recorded and a new CAD model was designed for each set based on these new dimensions. These as-built models were analyzed in ANSYS© and Abaqus©. Since normal stresses were obtained from the experimental calculations, normal stresses were considered in the analyses. The stress results from both the FEA solvers, were similar, such that the stress-strain curves from both FEA solvers

were coincidental, therefore, only the results from ANSYS are presented, unless otherwise necessary. The stress plots are also truncated to limit the stress comparison in the elastic region. Consider the continuous (C) specimen used for deriving material properties. The stress at 1.5% strain from the tensile test was calculated to be 13.9 MPa. Using the BIM, the yield stress calculated in Abaqus© and ANSYS© was 21% and 24% more than the experimental value. Figure 41 shows the stress strain plot of FEA simulations and experimental results. Using DIM in this analysis led to a negative error of 45% with the experimental values. The normal stress plot from ANSYS© and Abaqus© for (C) model is shown in Figure 42 and Figure 43 respectively. The stress plots depicted stress concentration in areas where actual failure occurred.

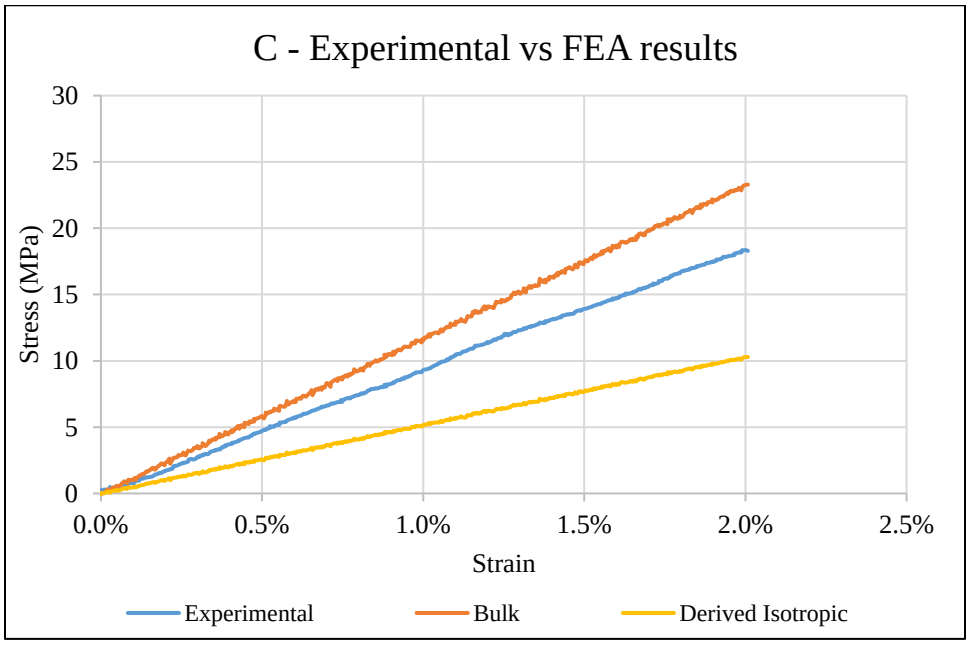

Figure 41: Stress-strain plot for C samples: Experimental and Simulated

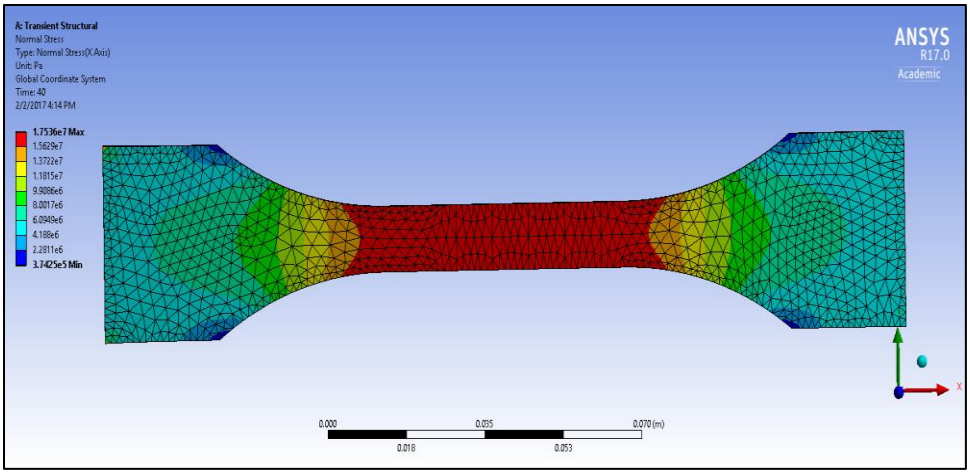

Figure 42: Normal stress plot of continuous (C) sample from ANSYS©.

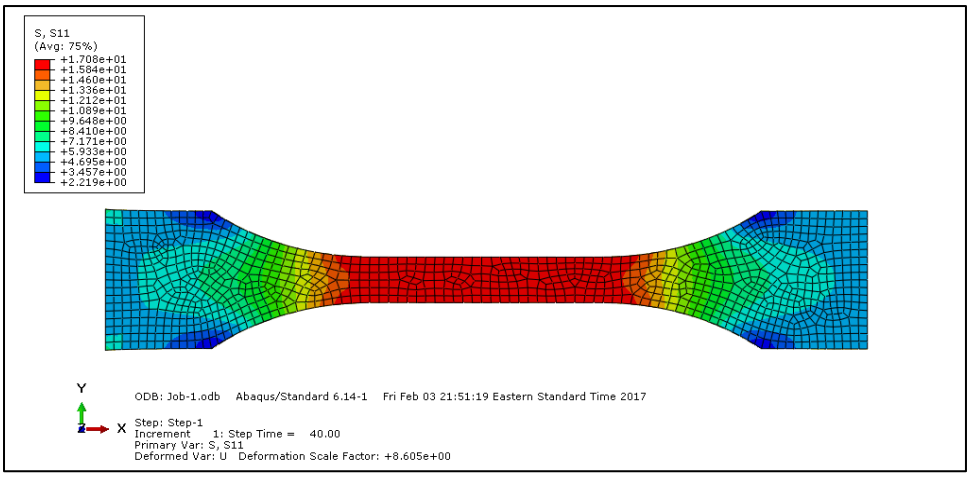

Figure 43: Normal stress plot of continuous (C) sample from Abaqus©.

For the as-built hexagonal infill geometry, the stress at 1.5% strain from FEA is 11.9 MPa from ANSYS© and 11.2 MPa from Abaqus© using the DIM. This is lesser than the corresponding stress from experimental results. The stress at 1.5% strain using BIM is 23.8 MPa from ANSYS© and 22.7 MPa from Abaqus©, which is more than the corresponding experimental results. Therefore, FEA predicts that specimen can withstand higher values of stresses than actual while using BIM and that the specimen can withstand

lesser stress values than actuality when used with DIM. Thus, FEA is not able to predict the yield stress values reliably, with bulk or derived material properties models. Similar is the case for stress at 1% strain. Figure 44 shows the stress-strain curves for experimental and simulation results. For the results of yield strain, the errors in values of strain though present, were considerably small. The stress contour plots from the FEA solvers can be used to visualize the position of maximum stress, which is in accordance with the experimental values. The normal stress plots for HI samples from both the solvers using derived properties are shown in Figures 45 and 46.

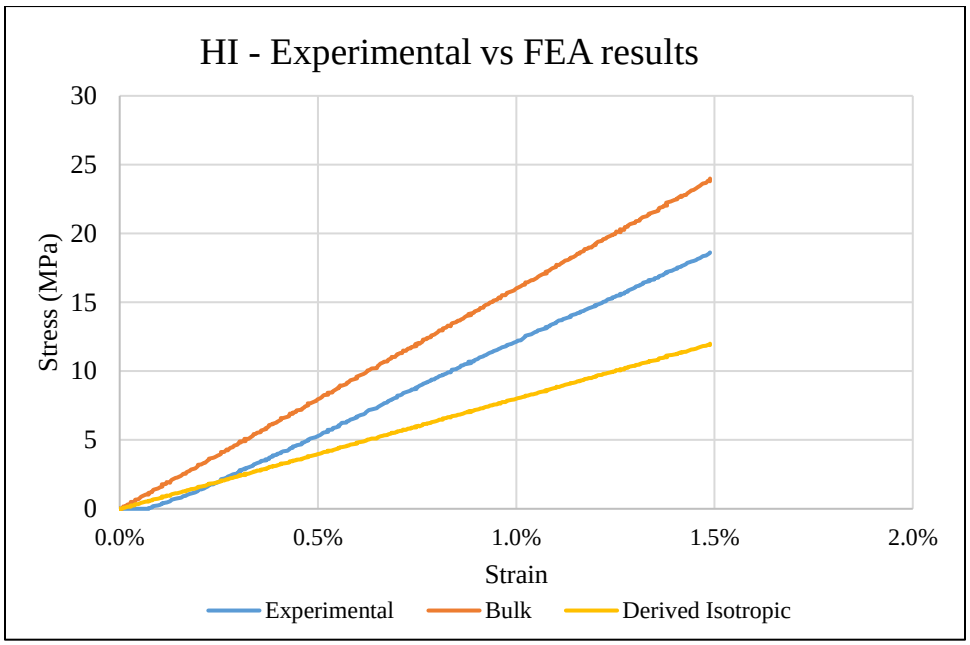

Figure 44: Stress-strain plot for HI samples: Experimental, BIM and DIM.

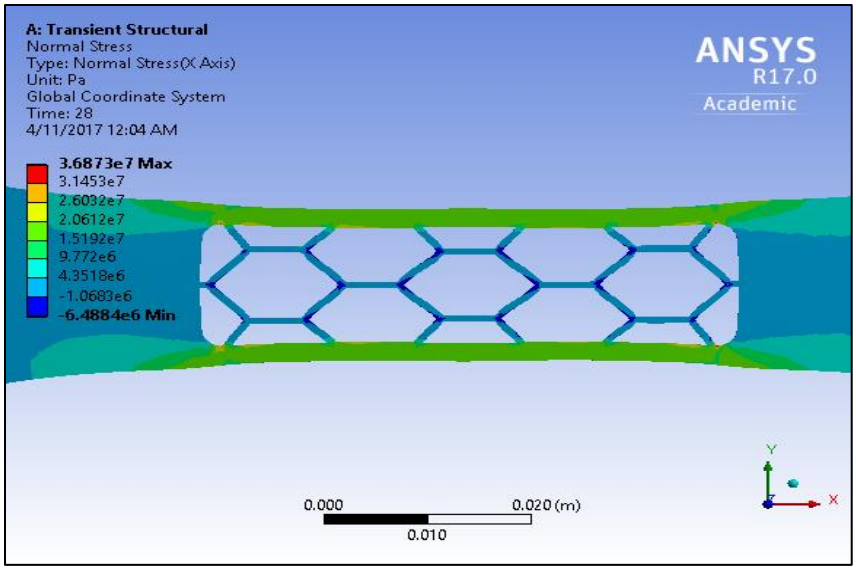

Figure 45: Normal stress plot of HI sample from ANSYS©.

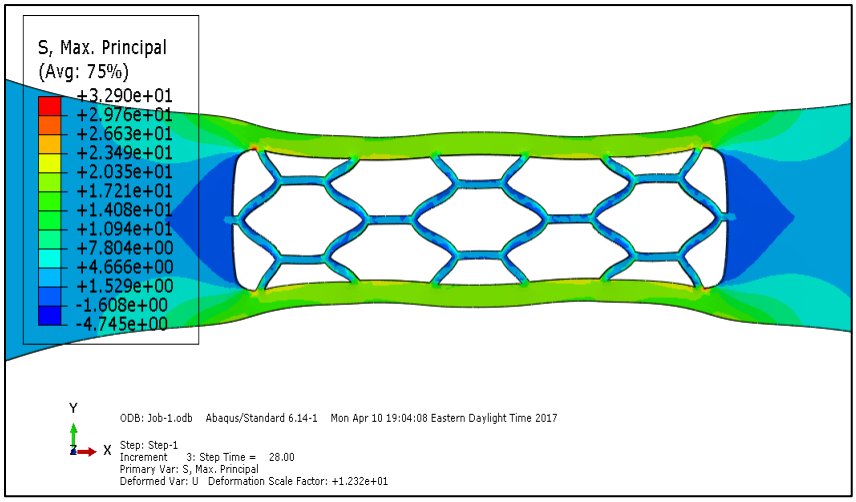

Figure 46: Normal stress plot of HI sample from Abaqus©.

In case of the equivalent volume (hexagon) continuous (CHI) samples, FEA from both the solvers over predicted the stresses when bulk properties were used. Nevertheless, the yield stress values using the derived material properties were within a close range of the experimental values. Figure 47 shows the stress-strain curves; the results using DIM

are close to experimental results. It can be seen from the figures that the stresses are concentrated in the center of the gage section, where the fracture occurs. However, FEA may not be able to depict the failure mode unless further intensive analysis is conducted. The stress plots using derived properties are shown in Figures 48 and 49.

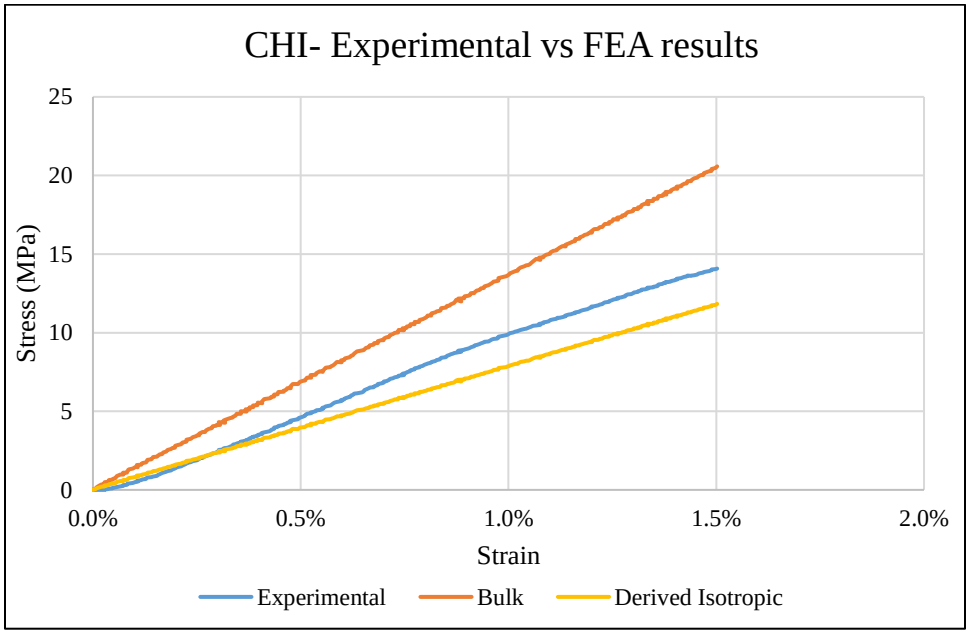

Figure 47: Stress-strain plot for CHI samples: Experimental, BIM and DIM.

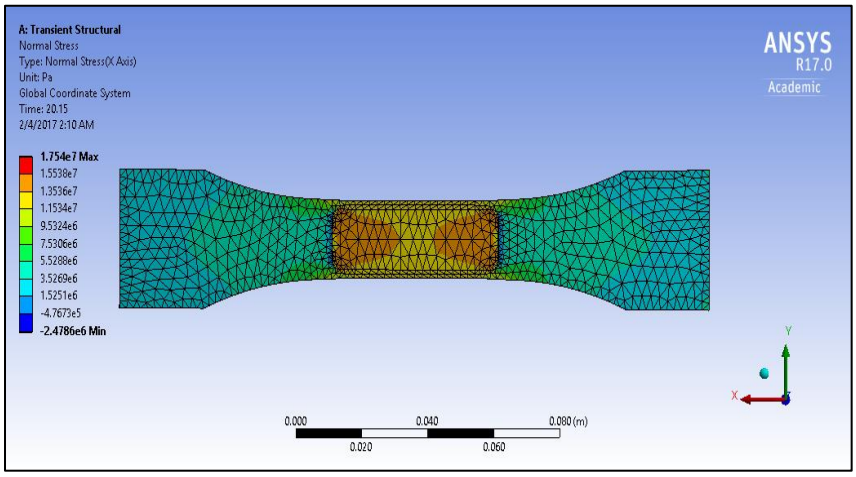

Figure 48: Normal stress plot of CHI sample from ANSYS©.

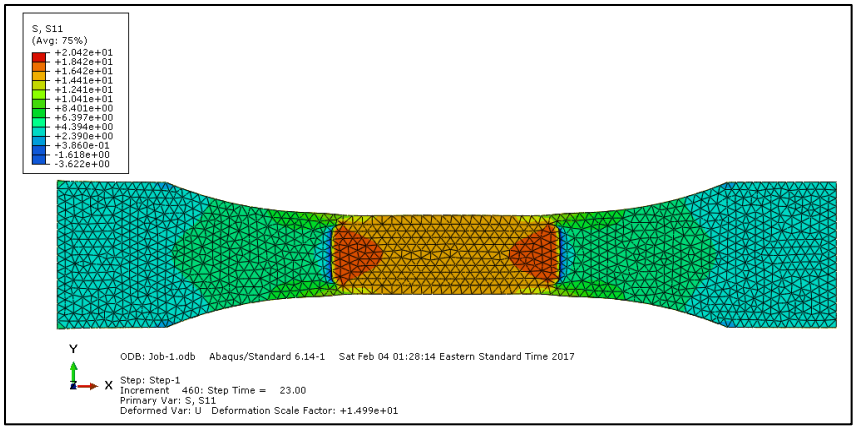

Figure 49: Normal stress plot of CHI sample from Abaqus©.

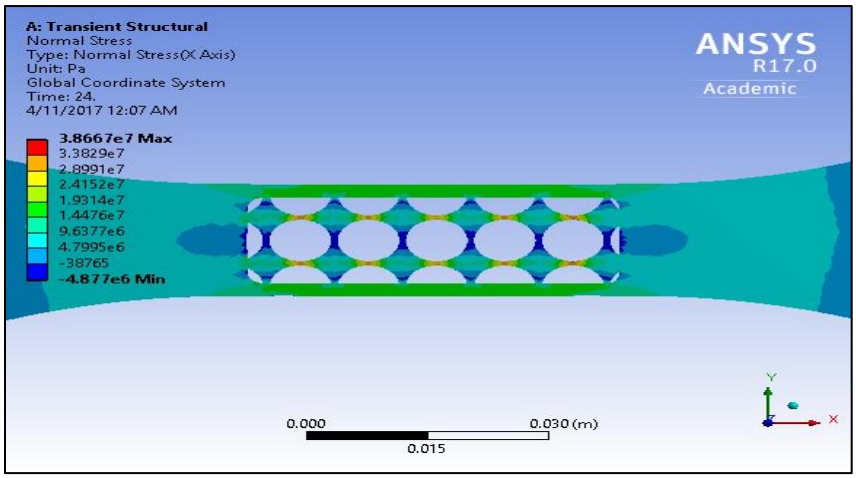

Figure 50: Normal stress plot of CS sample from ANSYS©.

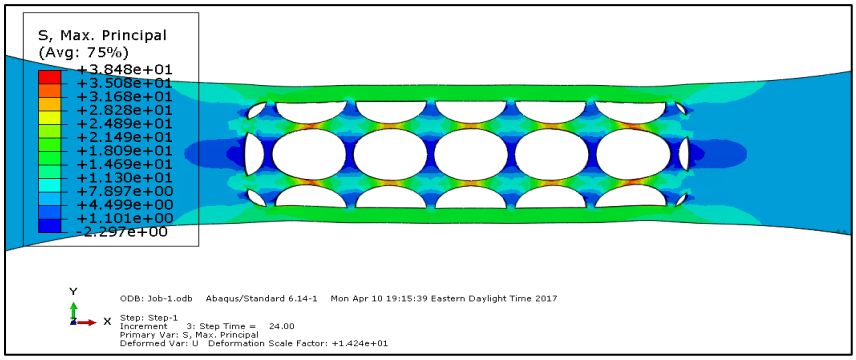

Figure 51: Normal stress plot of CS sample from Abaqus©.

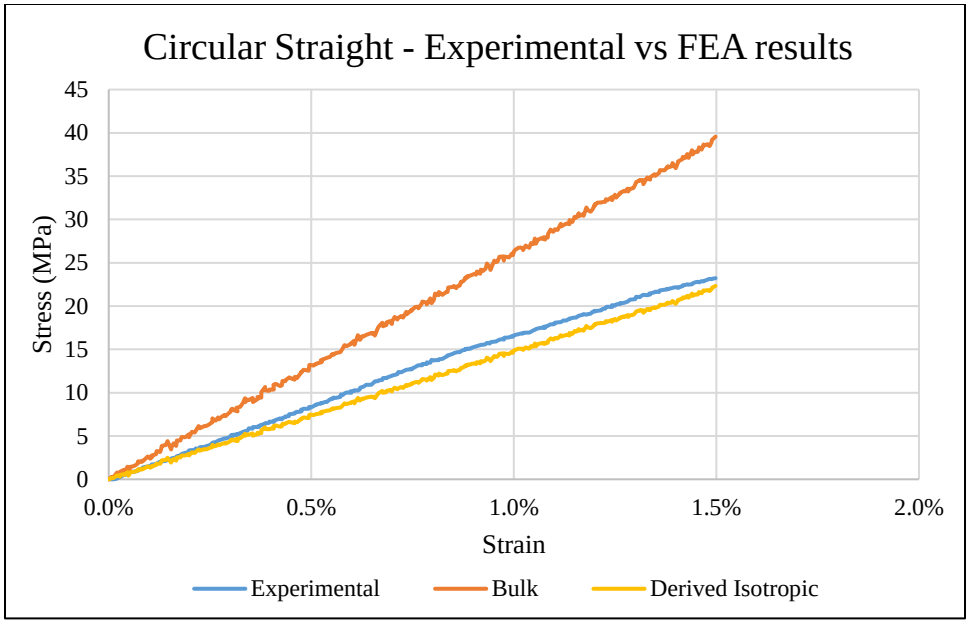

Figure 52: Stress-strain plot for CS samples: Experimental, BIM and DIM.

In case of Circular-straight (CS) samples as well, using BIM, FEA over-predicted the results by as much as 70%. The difference in stresses at 1% strain, of experimental and simulation results was about 55%; BIM results showing 25.8 MPa and experimental results showing 16.6 MPa. However, the DIM results were in excellent agreement with the experimental results until 1.5% strain. The stress-strain curve using DIM model strong adhered to the experimental data. Errors between experimental and simulation results were as low as 4%, can be found in Figure 52. From the FEA stress plots in Figure 50 and Figure 51, we can see that, stress concentration occurs in areas of least cross-section, which is where the fracture initiated. Thus, stress plots accurately depict the stress concentrations in the specimen.

With the equivalent volume continuous (CCS), yield stress is about 20% less than the experimental results when DIM is used. An error of 30% is seen when bulk material

properties are used. Since the facture in the continuous samples is governed by cracks along the 45º fibers, the FEA stress plot cannot be used to visualize the failure in case of continuous specimens. Figures 53 and 54 give the FEA stress plots for CCS specimens. All the stress and strain results from the FE analyses are listed in Table 8 alongside the experimental results. Since the stress plots of FEA using bulk properties are similar to the ones obtained using derived properties, they have not been presented in this section.

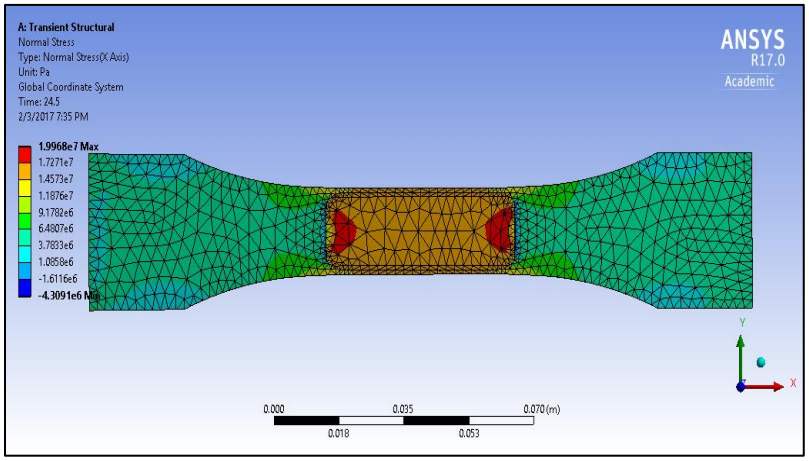

Figure 53: Normal stress plot of CCS sample from ANSYS©.

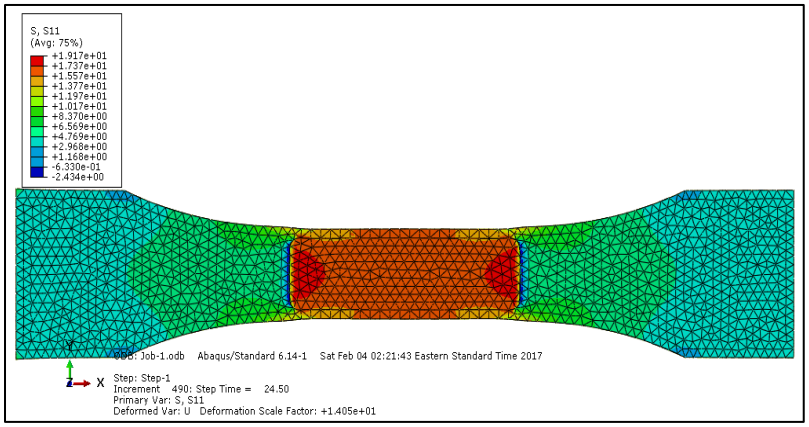

Figure 54: Normal stress plot of CCS sample from Abaqus©.

Table 8: Comparison of FEA stress results with experimental results.

		Experi-mental (MPa)	DIM			BIM		
			ANSYS© (MPa)	Abaqus© (MPa)	Error	ANSYS© (MPa)	Abaqus© (MPa)	Error
C	$\sigma_{1.5\%}$	13.9	7.6	7.1	45%	17.3	16.9	24%
	$\sigma_{1\%}$	9.4	5.3	4.9	43%	11.5	11.1	18%
HI	$\sigma_{1.5\%}$	18.6	11.9	11.2	35%	23.8	22.7	28%
	$\sigma_{1\%}$	12.1	8	7.5	33%	16.1	15.8	33%
CHI	$\sigma_{1.5\%}$	14.1	11.8	12.7	16%	20.6	21.5	45%
	$\sigma_{1\%}$	10	7.9	8.7	20%	13.8	15.1	38%
CS	$\sigma_{1.5\%}$	23.2	22.3	22.1	3%	39.5	38.2	70%
	$\sigma_{1\%}$	16.6	14.6	13.5	12%	25.8	24.5	55%
CCS	$\sigma_{1.5\%}$	14	10.5	11.5	6%	18.2	18.9	30%
	$\sigma_{1\%}$	8.8	6.2	7.1	19%	11.1	12	26%

Table 8 compares all the results of the simulations with the experimental results. $\sigma_{n\%}$ represents stress (σ) at n% strain. The experimental results are considered as benchmark and represented as neutral, uncolored cells. The results of simulations that are in acceptable range of the experimental results are colored in green. The results with large errors with respect to experimental values are colored in a shade of red.

To summarize, the results predicted by FEA were not entirely in accordance with the experimental results. Using the DIM, FEA from both the solvers under predicted the stress and strain values for different samples, namely the continuous, hexagonal and circular patterns. It is important to note that for the hexagonal continuous (CHI) samples, FEA results were close to the experimental results (6% error). The FEA results for the circular infill samples were under predicted by 4% - 12%. This indicates that geometry plays a role in the observed errors. On the other hand, using BIM, the stress results of FEA were consistently larger than the experimental results with large errors percentages (30% to 70%). The continuous samples' FEA results were the least erroneous with about 15% of error. These errors in results of stress decreased at smaller displacements i.e. at 1% strain.

The Hexagonal Infill specimens failed at the junction point first, as shown in Figure 40, shortly before fracturing on the sides. FEA could not predict the failure within the infill pattern for this specimen. On basis of the stress plot, the hexagonal infill pattern, should have failed only in the sides, which is not the case. For the hexagonal continuous and the circular continuous sample, at even though the stress concentration is in the gage section, the current analysis could not predict failure along the 45º fiber direction. Nevertheless, the completely continuous and the circular infill sample failed at points where stress concentration was maximum in the FEA stress plots. Thus, FEA was able to predict failure modes in samples having continuous geometries. The current analysis is not entirely reliable when compared with the experimental results of different FDM samples.

From the above analyses, we can conclude that the FEA simulations that were carried out were unpredictable and therefore unreliable. One could propose that if all the

results were over predicted or if all the results were under predicted a certain correction factor could be used in simulations. However, this was not the case while using BIM or DIM. This analysis paves us a way to quantify the error in simulation results and experimental values when basic simulations are performed. An intensive research is required to effectively analyze FDM parts using FEA or other methods of analysis. The next step is to develop a material model to account for the anisotropy of the FDM model. Another approach that can be studied is to use the composite layer representation in the FEA solvers to represent the layers of a FDM part. This can enable to represent the layer orientation of the FDM parts and analyze them. Chapter 4 discusses these approaches and the results of performing these analyses. Four different infill patterns are also included in the chapter for a more extensive analysis.

CHAPTER 4: FEA SIMULATIONS WITH ADVANCED MATERIAL MODELS

A better FEA model is needed to accurately represent the behavior of FDM parts. Isotropic FEA models used in the precious chapters were not reliably in agreement with the experimental values. Therefore, as-built models of additional infill patterns are also conducted, along with analyses of a completely solid model. A need arises to conduct a detailed analysis that would be decisive to validate results of the FEA simulations of AM parts. FEA using isotropic model is performed on these geometries. Since the FDM parts behave as anisotropic materials, FEA using an orthotropic model is conducted and eventually compared to the experimental results. A composite analysis is also conducted for all the different geometries; with the view that a composite layup might better predict the layered FDM part. The methodology used is similar to that followed in Chapter 3; to design geometry, print, develop FEA model, analyze, and validate with experimental results. The following sections talk about the specimen development, analyses methodologies, comparison metrics and the results of the study.

4.1 Methodology

As mentioned earlier, the methodology followed in this section is similar to the one followed in Chapter 3. A 3D CAD model is created for each of the infill pattern, such that the geometry accommodates the infill pattern and can be subjected to tensile testing. Along with hexagonal, circular straight and their corresponding continuous specimens, 'Linear (Straight and Cross-Hatch)', 'Circular Packed', 'Hilbert Curve infill', and 'Infill-less' patterns are designed. These geometries are printed with the same MakerBot© printer. The

data is post-processed to be compared with the simulation results. Since G-code based models were prohibitive, solid continuous models depicting the infill were used. The two analysis-approaches used in Chapter 3 were applied to the new geometric specimens:

1. Isotropic model using properties of bulk ABS material (BIM).
2. Isotropic model using derived properties from experimental tests (DIM).

However, the representation does not completely adhere with the structure or mechanical behavior of FDM parts, therefore an anisotropic approach is adopted. A set of tensile test samples is used to derive the orthotropic properties, by printing the sample in three mutually perpendicular orientations. Further directional material properties are calculated and used as input to perform an FEA using orthotropic material model. Next approach includes using a composite analysis with orthotropic properties. These analyses are performed on all of the specimens. Results are compared with the experimental data, normal stresses being metric of comparison.

4.1.1 Geometry

In addition to the four geometries developed earlier, five new specimens as mentioned are designed. Each pattern type has an infill specimen and a corresponding equivalent volume continuous specimen. Therefore, the final list of the specimens is as follows:

1. Hexagonal – Infill (HI) and Continuous (CHI)
2. Hilbert Curve – Infill (HC) and Continuous (CHC).

3. Circular: Straight Arrangement – Infill (CS) and Continuous (CCS).
4. Circular: Packed Arrangement – Infill (CP) and Continuous (CCP).
5. Linear: Straight Arrangement – Infill (LS) and Continuous (CLS).
6. Linear: Cross-Hatch Arrangement – Infill (LC) and Continuous (CLC).
7. Infill-less (I)
8. Completely continuous (C)

Since these specimens will be subjected to tensile testing, a typical tensile-test dogbone geometry is used. The dogbone is designed similar to the specifications stated in ASTM D638. These geometries were designed in Solidworks© as solid continuous models. The maximum dimensions of the dogbones were 170 × 35 × 2 mm and the gage dimensions are 50 × 20 × 2 mm, decided on basis of properly accommodating the infill features. The design process for these specimens is similar to the one followed in Chapter 3. To ensure repeatability a sample set of 20 specimens for each pattern was selected. The continuous geometries were designed so as the gage section would have a continuous infill, which would be equivalent in volume with the corresponding infill pattern. The infill pattern accounted to 20% to 30% of the volume in the gage section; this resulted in the continuous section being only a layer thick. The continuous patterns designed for the new infill pattern, taking into account the printing abilities of the printer, turned out to be similar to the two corresponding samples printed earlier. Hence, these samples would not be printed again. In addition to these geometries, another set of dogbones was designed to derive orthotropic

properties. A set of 10 parts each were printed in three different orientations: X, Y and Z to evaluate the properties in these directions. Figure 55 to Figure 60 depict the geometries.

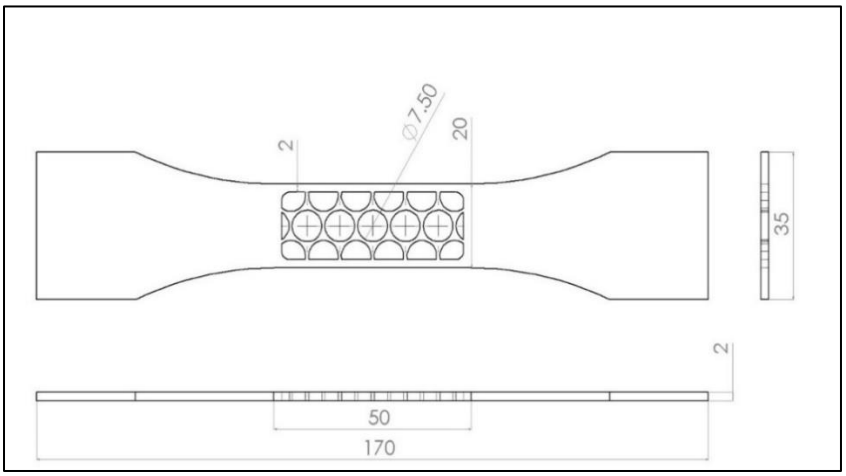

Figure 55: Circular – Packed Infill (CP) specimen.

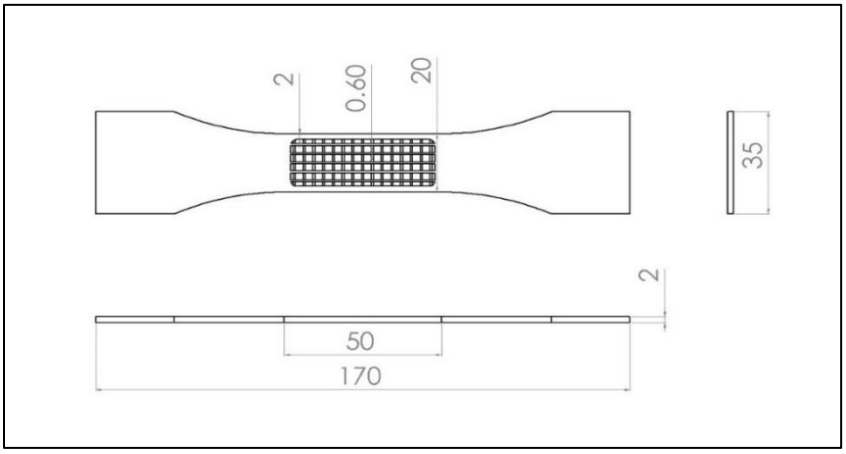

Figure 56: Linear – Straight Infill (LS) specimen.

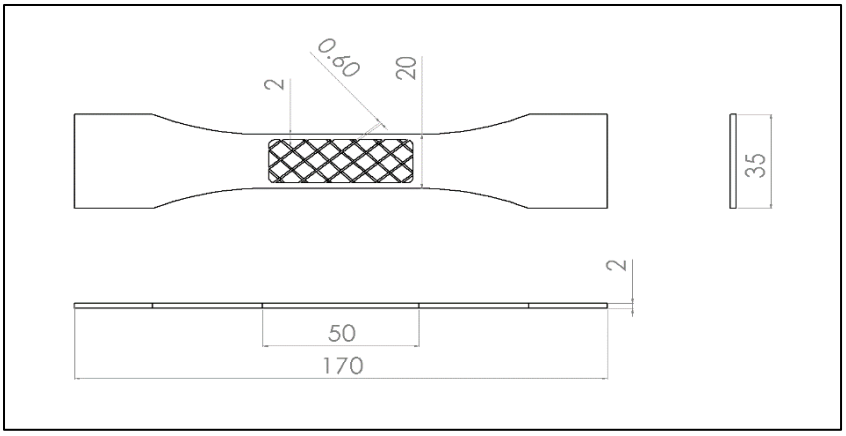

Figure 57: Linear – CrossHatch Infill (LC) specimen.

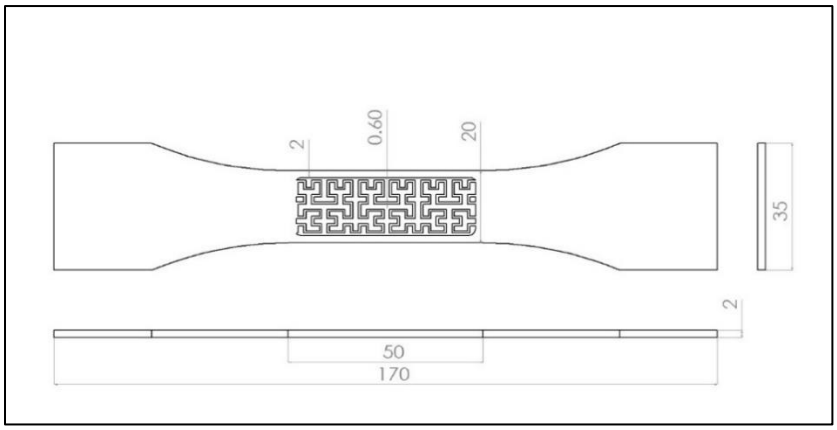

Figure 58: Hilbert Curve Infill (HC) specimen.

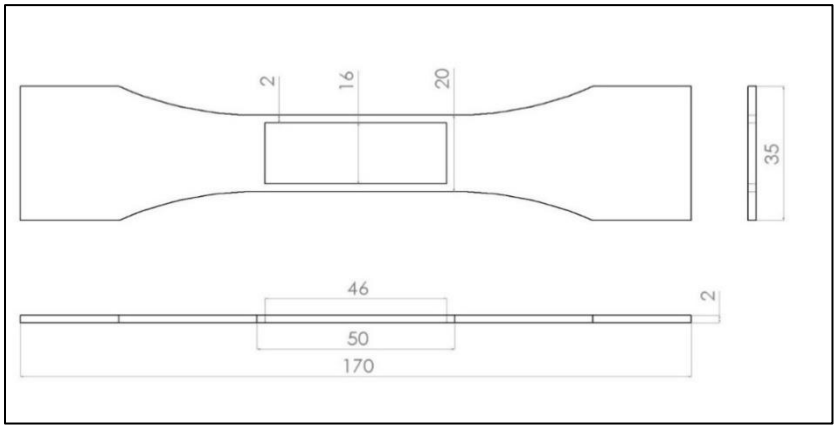

Figure 59: Infill-less (I) specimen.

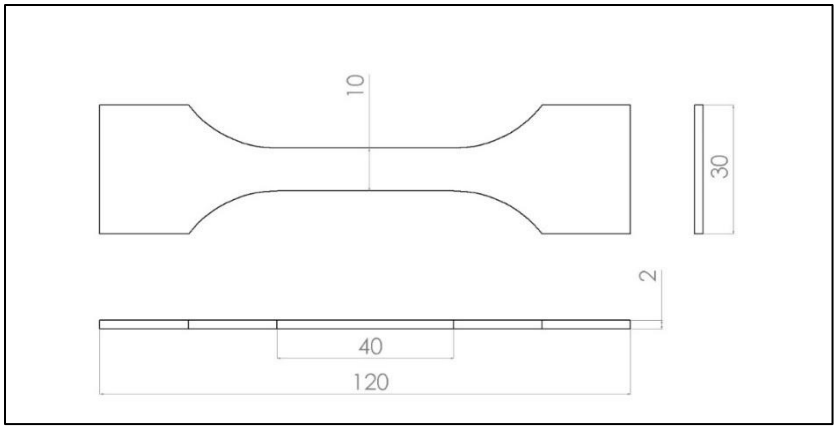

Figure 60: Orthotropic (Printed in three directions: CX, CY, CZ) specimen.

4.1.2 Printing Parameters

These CAD models were converted into 'STL' file format for the printer. The MakerBot© Replicator 2X printer was used, along with 'Slic3r©' as the slicing software. The material used in this part of the study was white ABS (Acrylonitrile Butadiene Styrene) as well. The printing parameters for all the parts is provided in Table 9. All the corresponding continuous parts had geometries similar to those designed in Chapter 3 and hence they were not printed again. The parts were printed with a 100% infill with a rectangular fill pattern without a raft. The orthotropic part was printed in X direction with the fibers aligned in X direction to obtain CX parts; the same part was printed with the fiber orientation being in the Y direction to get CY. Similarly, the orthotropic dogbone was printed vertically with fiber orientation along the width to get CZ parts. The orientation of parts is shown in Figure 61. For the CZ samples, which were built in Z direction, support material had to be printed to enable efficient prints.

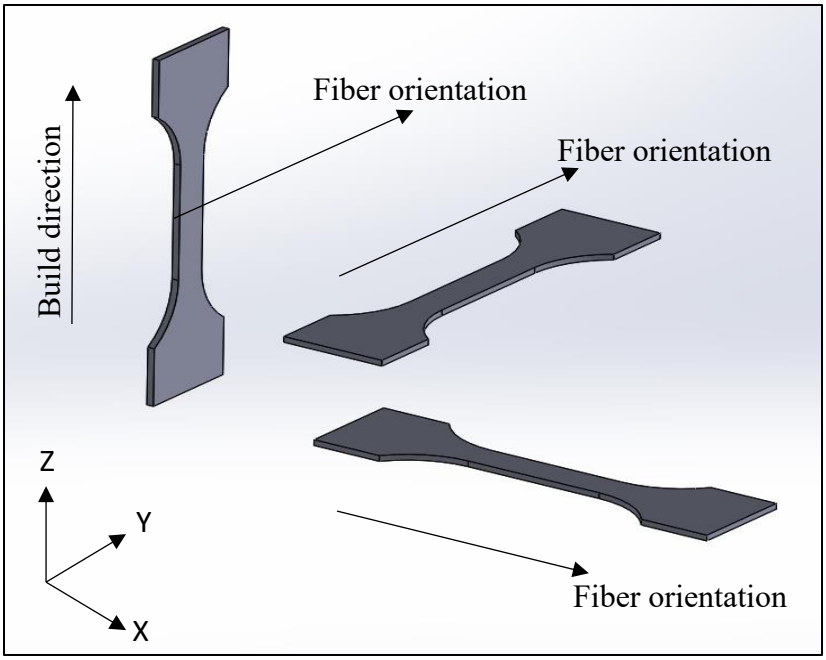

Figure 61: Orthotropic samples printed in three orientations.

Table 9: Printing Parameters for dogbone geometries.

	Layer Height (mm)	Filament Width (mm)	Required Support
Hilbert Infill (HI)	0.2	0.67	No
Circular Packed Infill (HI)	0.4	0.42	No
Linear Straight Infill	0.2	0.67	No
Linear CrossHatch Infill	0.2	0.67	No
Infill-less	0.2	0.67	No
Continuous X	0.2	0.67	No
Continuous Y	0.2	0.67	No
Continuous Z	0.2	0.67	Yes

4.1.3 Tensile tests

The tensile tests were performed on 'Modular under Microscope Mechanical Test System – μTS' by Psylotech©. The samples were subjected to a displacement controlled tensile loading at a constant speed of 50 μ/s until fracture. The data from the orthotropic samples provided material properties for the orthotropic model, whereas the data from test samples was used to validate the simulation results.

4.1.4 FEA Simulations

Once these specimens were printed, as-built CAD models are developed that take into account the dimensional changes of the final part. Since analyses using the isotropic models are already completed for C, HI, CS, CCS and CHI, isotropic analyses are carried out on the new infill patterns only. The first being FEA using isotropic properties of bulk ABS material properties (BIM) and the second approach being, analysis using isotropic model using experimentally derived properties (DIM). These properties were derived in Chapter 3. The third approach is using an orthotropic material model to simulate the tensile loading. This model should better represent the anisotropic behavior of FDM parts. The engineering constants required for the material model are derived from the experimental test samples (CX, CY, and CZ). Since these are derived properties, this approach is referred to as orthotropic derived model (ODM) henceforth. These analyses are performed in both ANSYS© and Abaqus©. A refined mesh was defined using the adaptive mesh feature in ANSYS© to mesh the fine features of the infill effectively. This mesh was recreated in Abaqus© using locally governed mesh tool. Quadratic tetrahedral elements were used in

both the solvers. The tensile test is simulated similar to that described in Chapter 3. Figure 62 and Figure 63 depict the meshes for two of the new infills. Rest of the meshes can be found in Appendix A.

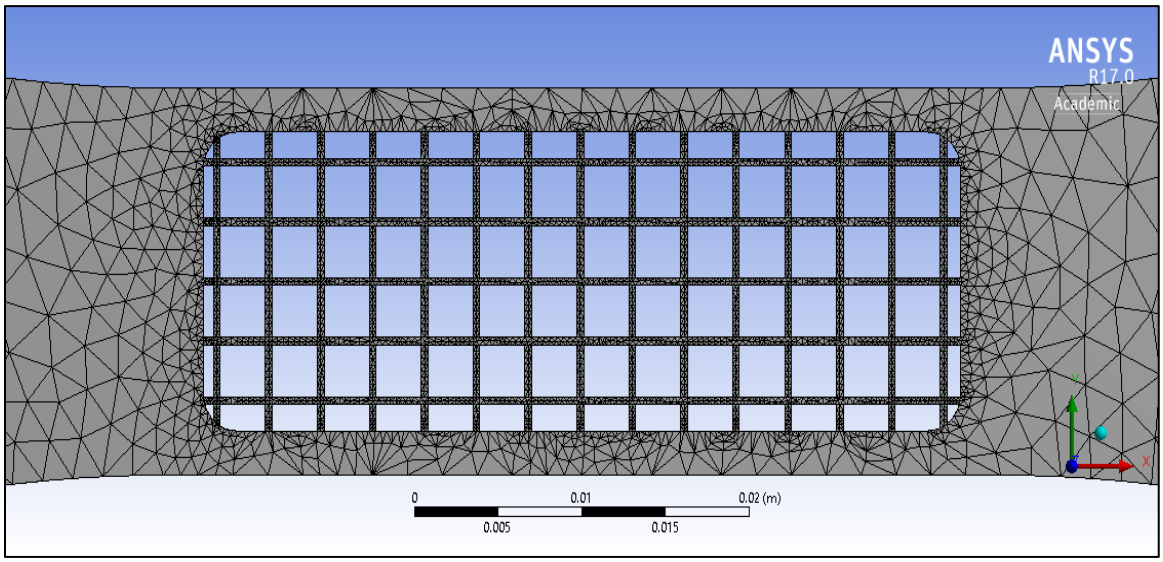

Figure 62: Mesh model for Linear Straight infill.

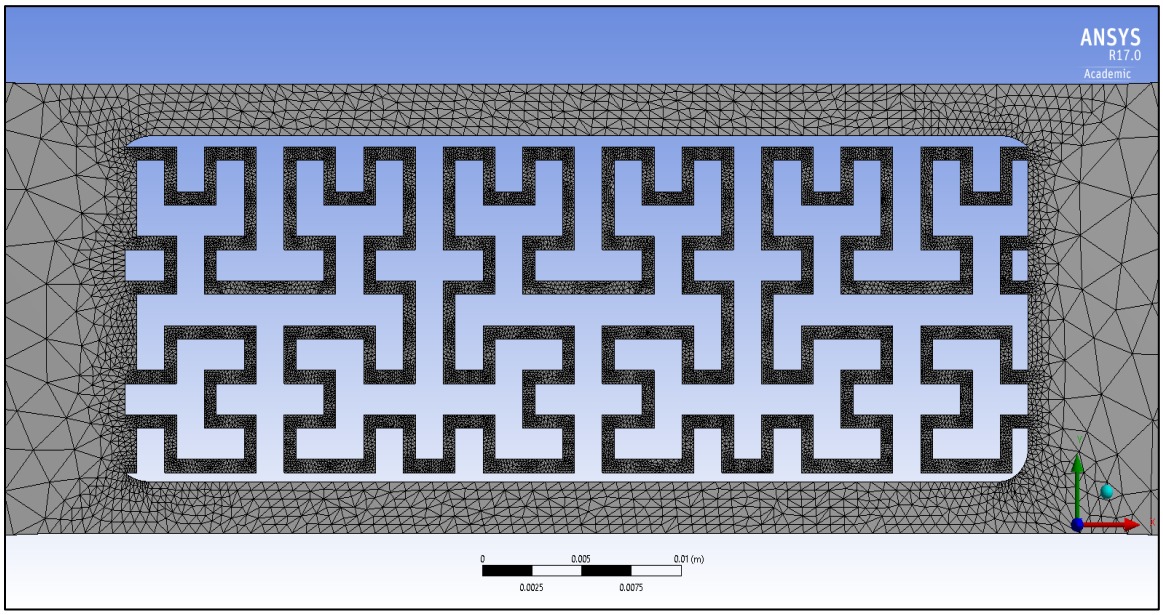

Figure 63: Mesh model for Hilbert infill.

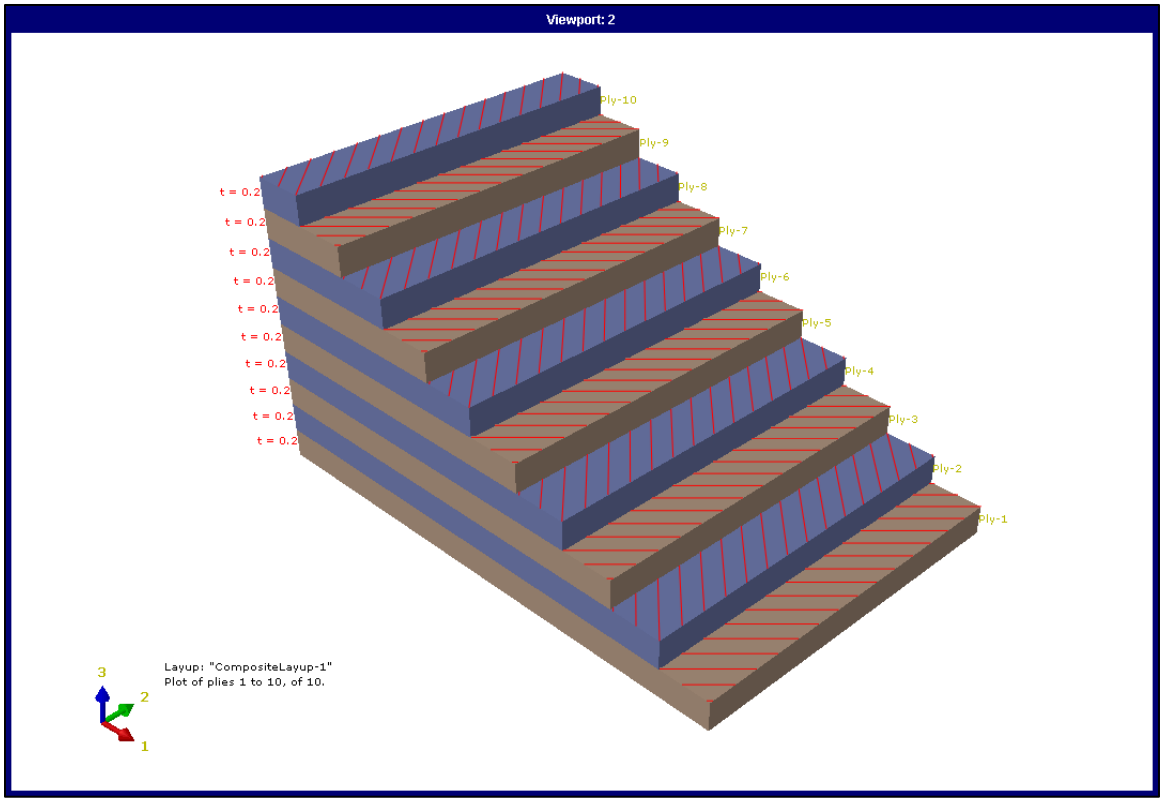

Figure 64: Ply-stack plot for composite analysis of HI specimen.

The fourth approach uses a composite layup to define the finite element model for the part. In a composite analysis, the part is divided into a set of plies or lamina, stacked together to form a composite. This analysis enables us to set up fiber orientations within each lamina, so that the directional layup of fibers is taken into account while analyzing the part. Since the FDM parts are built in layers (analogical to laminae), a composite analysis is conducted on as-built parts to examine if such an analysis can accurately predict behavior of FDM parts. The as-built models are divided into the appropriate number of composite plies while specifying the thickness of each ply. The models built with 0.2 mm layer height have a ply thickness of 0.2 mm with 10 layers stacking up to the 2 mm height

of the part. Similarly, 0.4 mm layer height parts have a ply thickness of 0.4 mm. The fiber directions are specified as 45º/-45º every alternate layers, just as the actual parts. A solid composite model is selected. Figure 64 shows the ply-stack plot for 10-ply HI specimen. In addition to this, in a composite analysis, tetrahedral elements cannot be used for meshing the geometry (as each ply is treated as a 2D lamina), but only brick elements can be used. The parts that were not automatically meshed as brick elements are partitioned to achieve a brick meshing. Since the equivalent volume, continuous specimens are completely similar with only dimensional differences, only CHI is analyzed and discussed. The composite analyses are however performed only in Abaqus©, since ANSYS© only permits using shell models for composite analysis.

4.1.5 Dimensional Sensitivity of FEA simulation.

The dimensional accuracy of the FDM printer used is 0.1 mm. The standard deviation of the dimensions of the set of parts were within ±0.1 mm. In order to check the sensitivity of the FEA simulations of these changes in dimensions, a sensitivity check was performed. The FEA was performed using a DIM model, on HI sample set. Two models were developed representing the maximum dimensional change in the infill features (the filament width and the polygon size). The original filament width was 0.7 ± 0.1 mm. and the polygon size was 10 ± 0.1 mm. However, the FEA simulations did not show any considerable differences in the results of the two models used as compared to the base model. Table 10 summarizes the parameters if this analysis.

Table 10: Dimensional sensitivity analysis.

	Original model (HI)	Model 1	Model 2
Filament width (mm)	0.7	0.8	0.6
Polygon size (mm)	10	10.1	10.2
Error in results (%)	-	< 2%	< 1%

4.2 Results

The final specimens and infill patterns are depicted in Figure 66. The orthotropic parts built in the Z orientation were built with supports, which were removed by sawing, with no damage to the part. Figure 65 shows the parts used for deriving orthotropic properties. The behavior of the parts is discussed in brief along with the comparison of the infill patterned parts with the corresponding continuous parts.

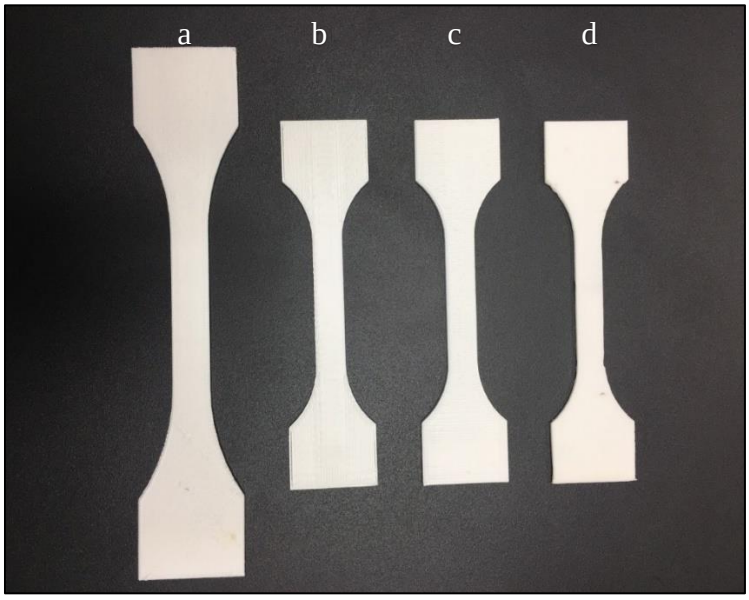

Figure 655: Final printed parts: CC (a), CX (b), CY(c), CZ (d).

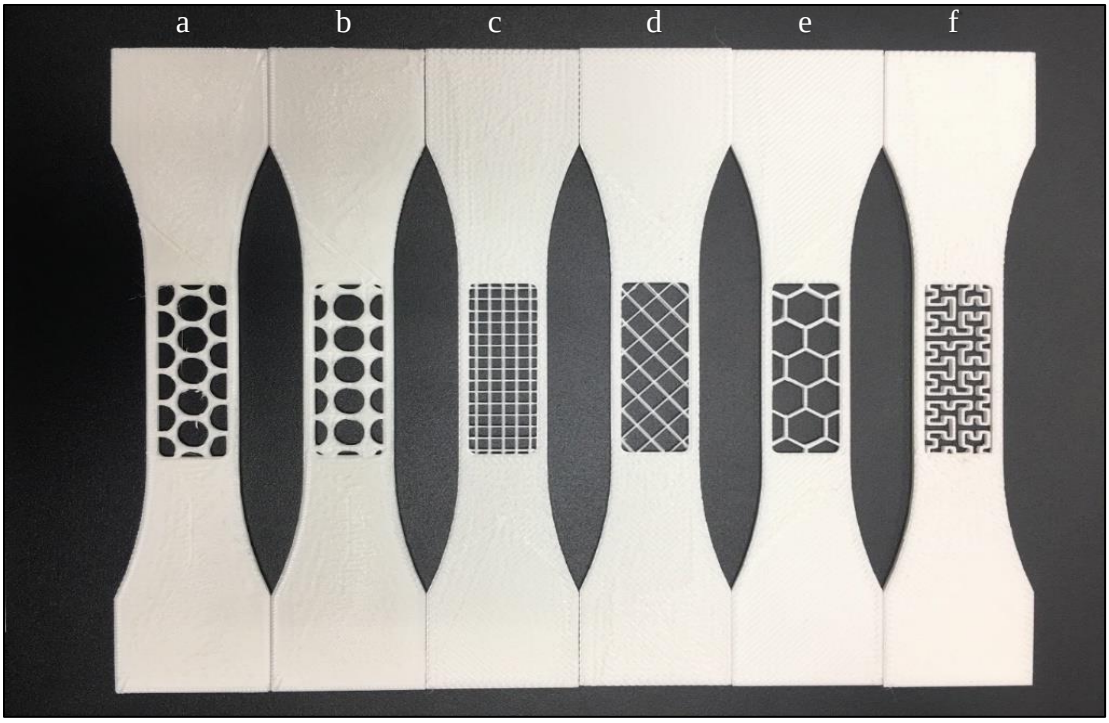

Figure 666: Final printed parts: Circular Packed (a), Circular Straight (b), Linear Straight (c), Linear Cross-Hatch (d), Hexagonal (e), Hilbert Curve (f).

4.2.1 Experimental Results.

Similar to the previous analyses, the tensile test data was post processed; force-displacement curves, stress-strain curves and effective moduli are evaluated for each part as average of the 20 samples for that part. The stress-strain data for each of new infill pattern and their corresponding continuous samples are presented below. Figure 67 shows the stress-strain curve for the orthotropic parts; this is used for deriving the orthotropic material properties.

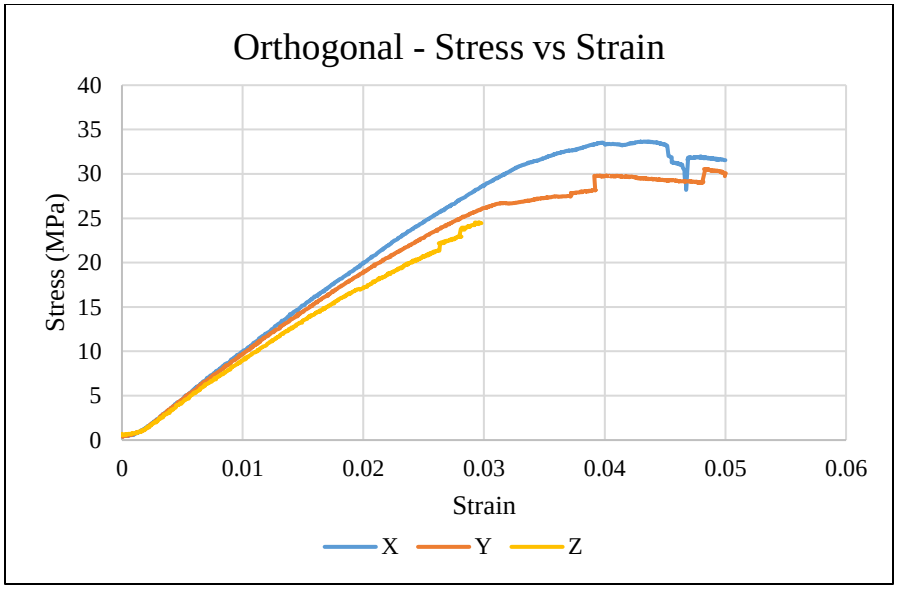

Figure 67: Stress-Strain curve for Orthogonal Samples.

It is evident from Figure 67 that the CX part has a higher strength followed by CY and CZ. The elastic moduli are calculated as the slope of each of the curves. The derived engineering constants are presented in Table 11. Density was not derived; Young's Modulus was calculated by Eq. 14,

$$E = \frac{\delta\sigma}{\delta\varepsilon} \tag{14}$$

σ = Stress,

ε = Strain,

E = Young's Modulus,

ν = Poisson's Ratio.

Shear modulus (G) was calculated using Eq. 15.

$$G = \frac{E}{2(1+\nu)} \tag{15}$$

Table 11: Orthotropic material properties derived from experimental testing.

Material Property of ABS	Value
Young's Modulus in X (E_x)	1.1 GPa
Young's Modulus in Y (E_y)	0.9 GPa
Young's Modulus in Z (E_z)	0.88 GPa
Poisson's Ratio ($\nu_{xy} = \nu_{xy} = \nu_{xy}$)	0.394
Shear Modulus (G_{xy})	0.39 GPa
Shear Modulus (G_{yz})	0.32 GPa
Shear Modulus (G_{xz})	0.31 GPa
Density	1020 kg/m^3

These properties were used as input to the material model in FEA simulations. The stress-strain data for rest of the samples is provided below from Figure 68 to Figure 71.

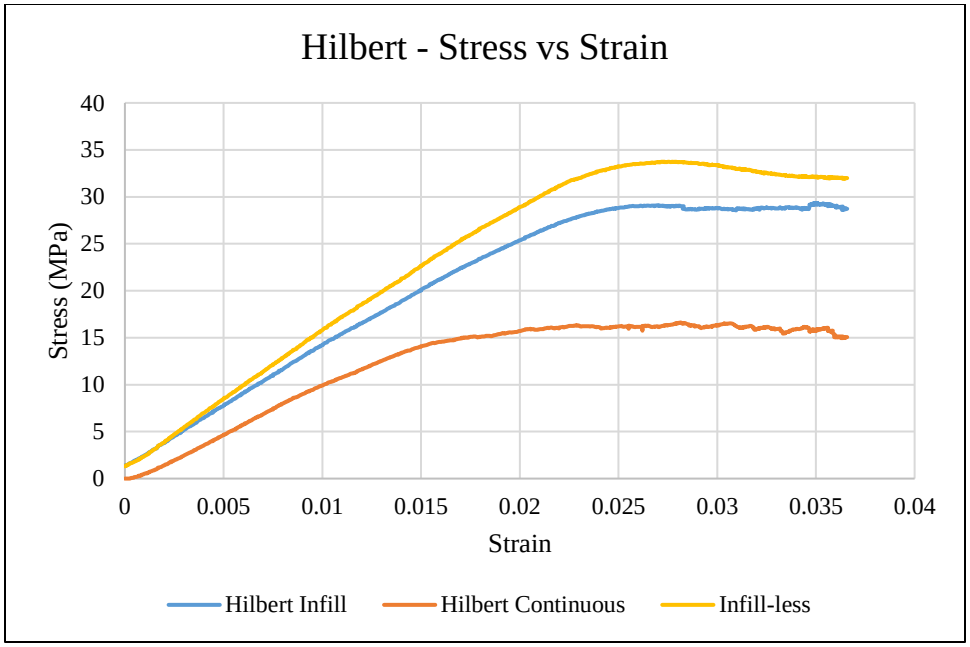

Figure 68: Stress-Strain curve for Hilbert Curve (HC & HCI) and Infill-less (I).

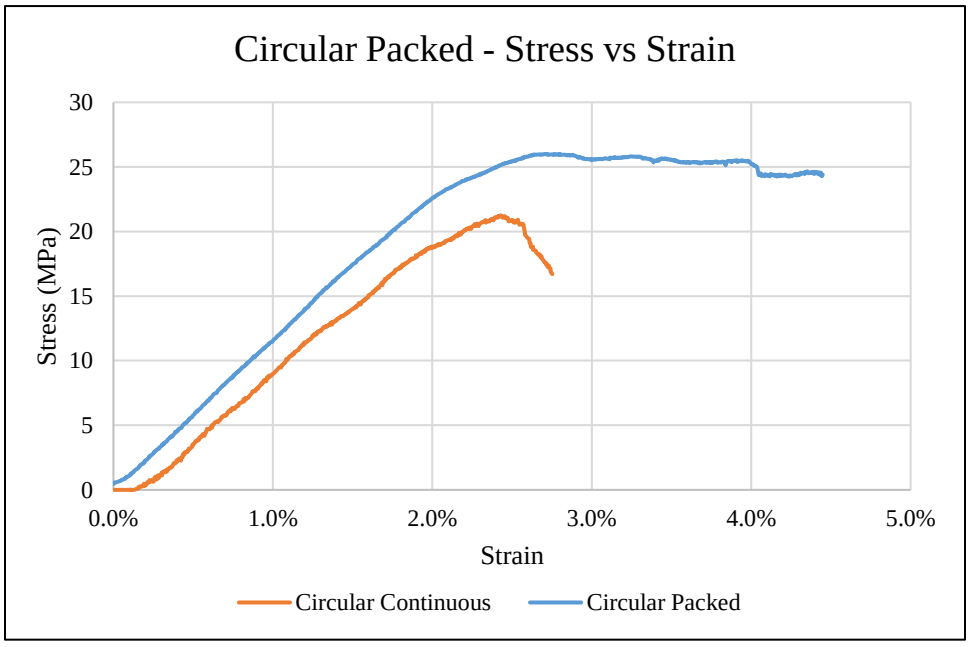

Figure 69: Stress-Strain curve for Circular Packed Infill (CP) Pattern.

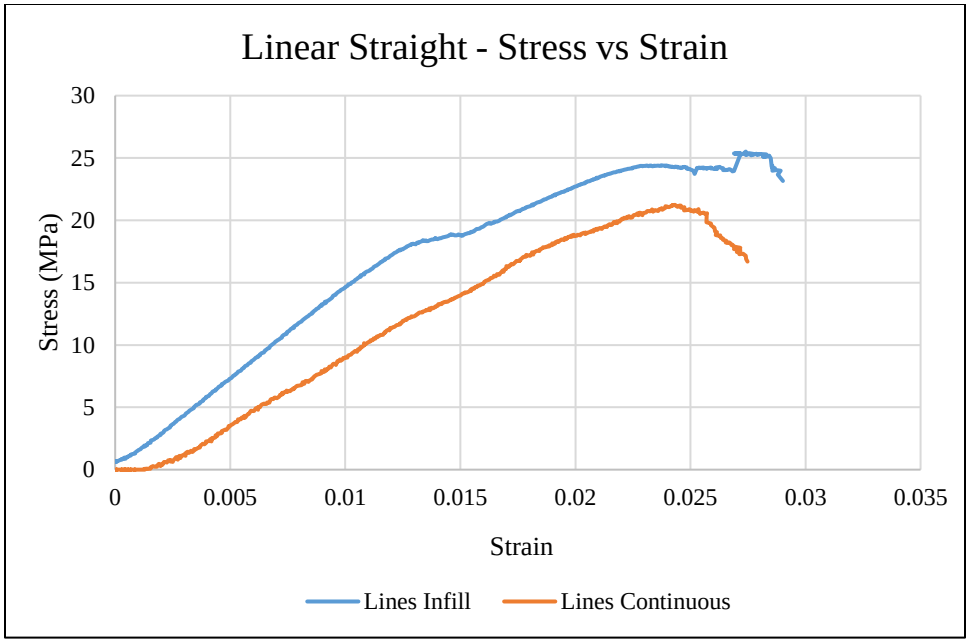

Figure 70: Stress-Strain curve for Linear Straight Infill (LS) Pattern.

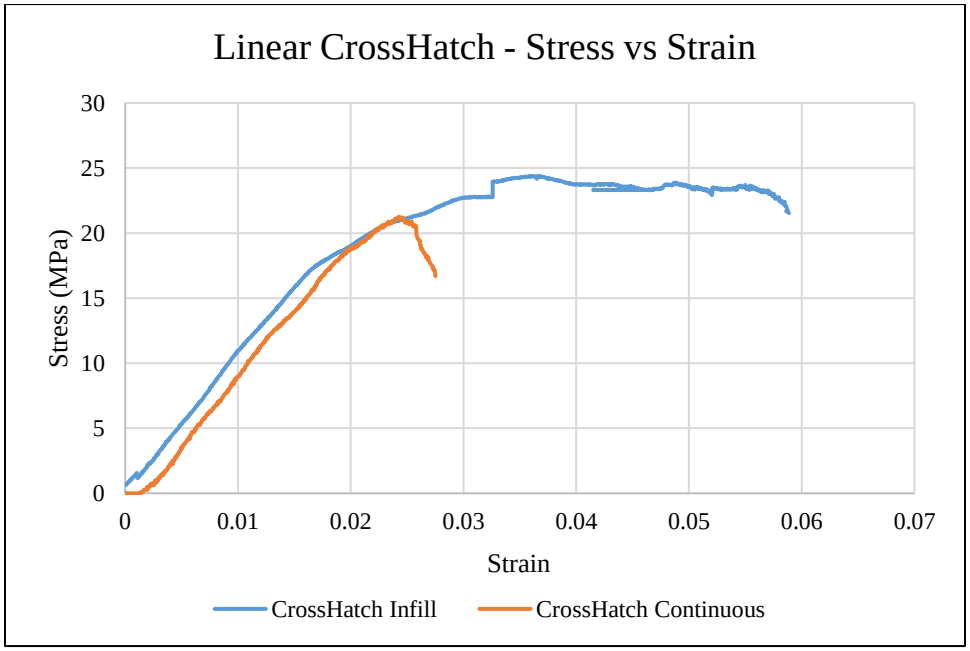

Figure 71: Stress-Strain curve for Linear Cross-Hatch Infill (LC) Pattern.

It is evident from the results that the infill specimens withstood higher amounts of stress than their corresponding equivalent volume samples; even though both the samples of a pattern set behaved similarly in the elastic region. Stress values were calculated based on the least cross-sectional area for all the samples. The infill specimens also sustained higher strains before fracture, as compared to their equivalent continuous samples. It is important to note that the LS specimens showed brittle behavior, as opposed to the other infill specimens, which showed considerable plastic deformation as well. The LS and LC specimens were equally strong, but were weaker than HC, CP and I specimens.

Table 12: Comparison of test data for different samples.

		Ultimate Strength (σ_{ut}) (MPa)	Ultimate Strain (ε_{ut})	Stress at 2 % strain ($\sigma_{2\%}$) (MPa)	Effective Modulus (GPa)
Hilbert Curve	(HC)	28.7	0.036	25.3	1 ± 0.1
	(CHC)	15.1	0.036	15.7	-
Circular Packed	(CP)	25.1	0.04	22.7	1.26 ± 0.25
	(CCP)	16.7	0.027	18.9	-
Linear Straight	(LS)	25	0.029	22.6	1 ± 0.1
	(CLS)	16.7	0.027	18.9	-
Linear CrossHatch	(LC)	18.85	0.06	21.7	1.6 ± 0.2
	(CLC)	16.7	0.027	18.9	-
Infill-less	(I)	32	0.036	29	0.99 ± 0.1

Table 12 summarizes the experimental data as per the respective specimens. The continuous samples for each of the samples shared the same dimensions as the continuous samples printed for Chapter 3. Therefore, the test data from the Chapter 3 is reused for comparison. It is important to analyze and discuss the fracture patterns of different geometries, to compare the results from FEA simulations. Figure 72 presents the fractured specimens. Every fracture point for each specimen is marked by red line.

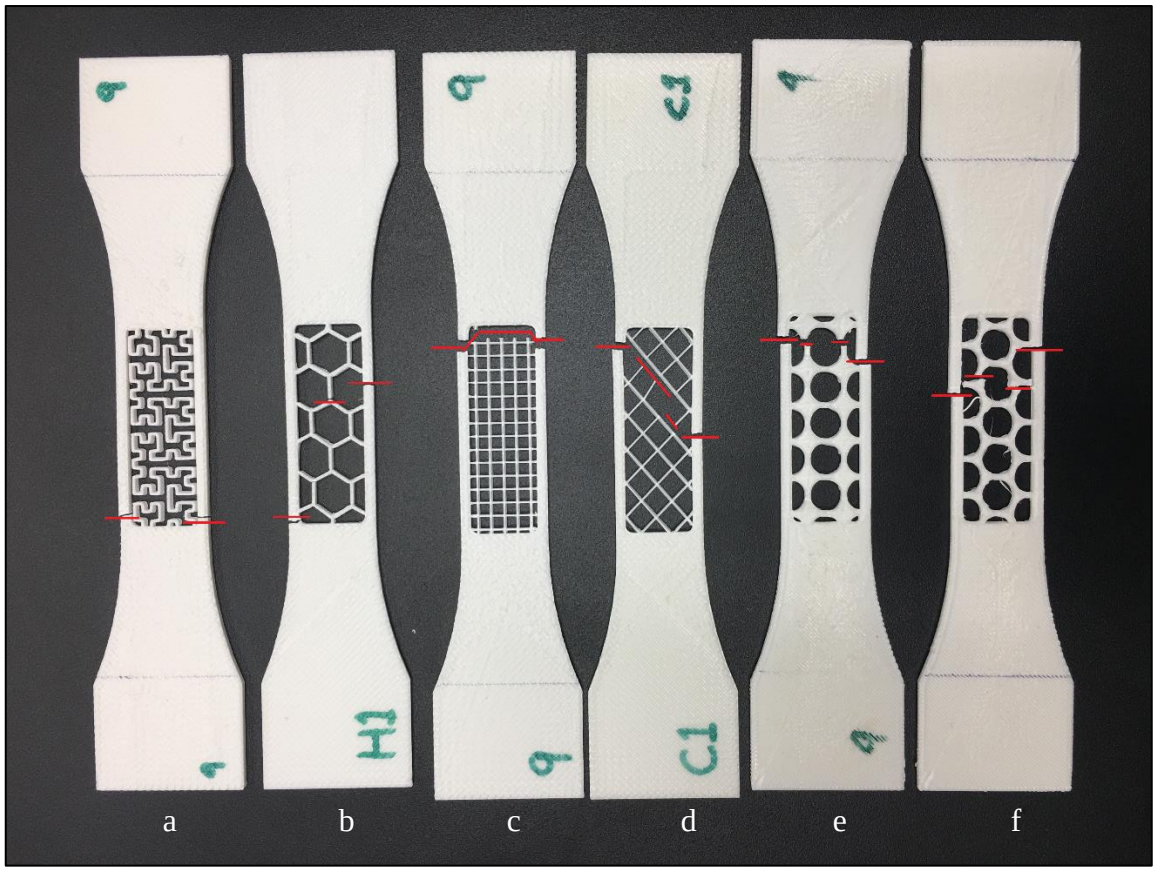

Figure 72: Final printed parts: Hilbert Curve (a), Hexagonal (b), Linear Straight (c), Linear Cross-Hatch (d), Circular Straight (e), Circular Packed (f).

Consider the HC specimen, which fractured only on the side structures; the infill feature was elastic as a whole and did not fracture. In case of LS pattern, first, the infill pattern fractured at the joints between ends of the infill fibers and the solid part; eventually fracturing at the sides as well. The LC specimens fractured in a complex way, with the infill pattern fracturing first along the fibers and later the sides fracturing with opposite sides fracturing at a 45º pattern. The CP specimens fractured in the infill region at the least cross-sectional area first and later along the sides. The I specimens fractured with opposite sides fracturing along a 45º line. FEA simulations should be able to predict such behaviors.

4.2.2 FEA Simulations – Isotropic Models

This sections talks about the FEA results of simulations performed using the isotropic material model. Since the HI and CS and the continuous specimens have already been analyzed under isotropic models, only the new specimens have been analyzed and discussed in this section. The as-built models of these specimens were analyzed in Abaqus© and ANSYS© and normal stresses were considered for comparison. Stress plots have been truncated since only elastic region is compared. Since the stress plots from both the solvers are similar, only stress plots from ANSYS© analyses have been shown. Stress plots from Abaqus© can be found in Appendix D. Additional, ANSYS© stress plots can also be found in Appendix C. Considering the Hilbert Curve (HC) results from Figure 73; it is evident that the BIM analyses over-predicted whereas the DIM under-predicted (by a huge margin). Stress results using the BIM are closer to the experimental data as compared to the DIM.

Using BIM, we see an 8% - 15% of error, with strong adherence in the initial half of the stress-strain curve; the DIM results present a 40% - 45% error throughout the curve.

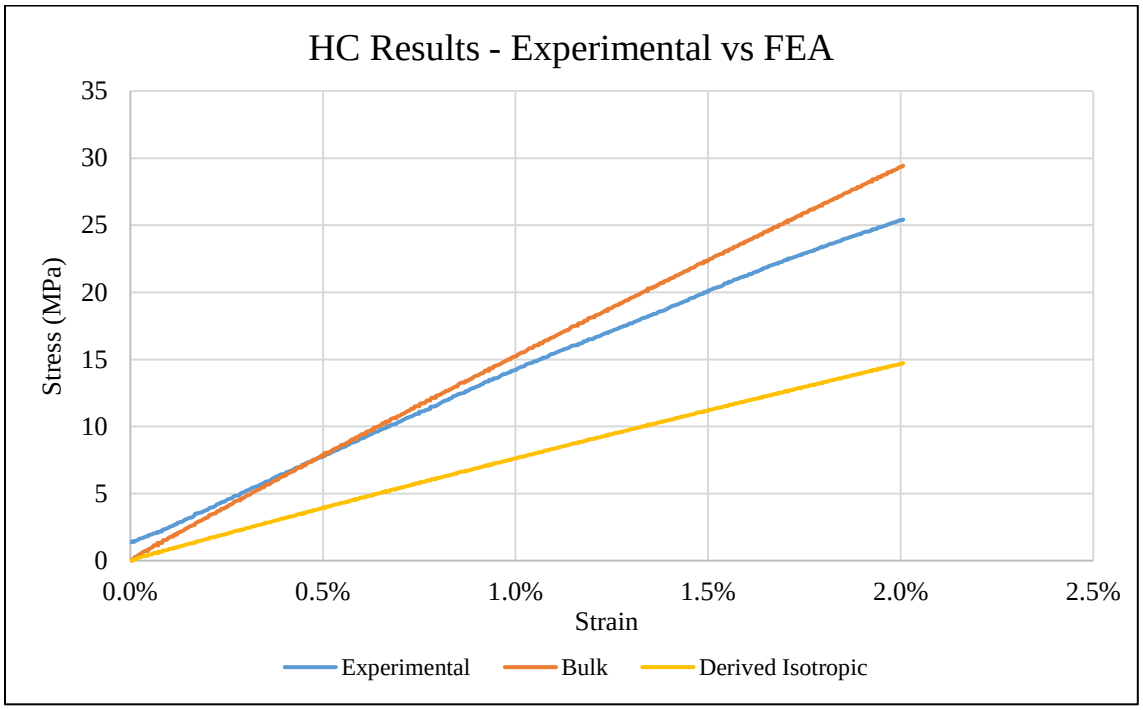

Figure 73: Stress-strain plot for HC: Experimental, BIM and DIM results.

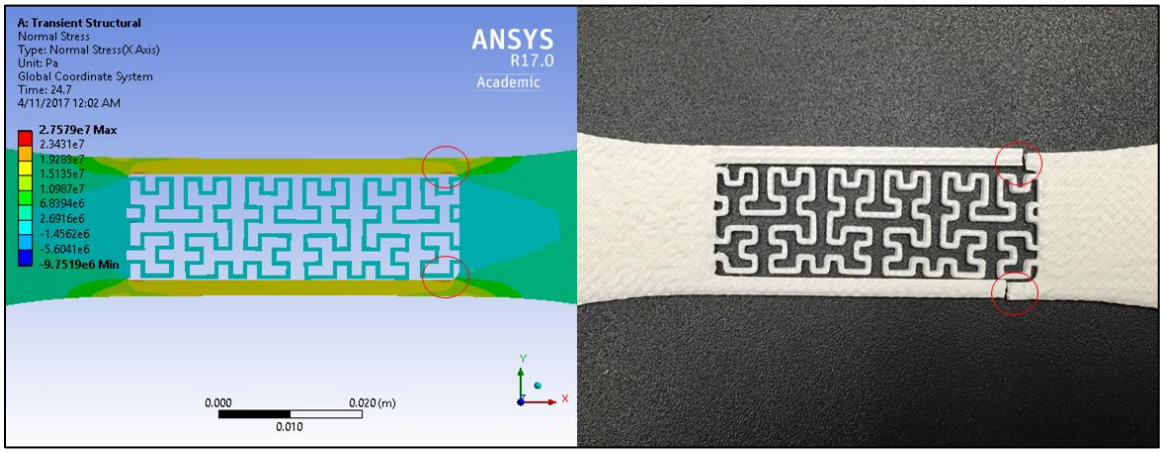

Figure 74: Stress plot for HC: left – FEA contour plot, right – actual fractured part.

Figure 74 shows the stress contour plot and the actual fractured specimen. It is evident that maximum stress occurs in the side members, where the fracture actual happened and that the infill features carry very little stresses, which in physical testing did not break either. The fracture points are circled in Figure 74. The stress plots from both the models is similar with only difference being the magnitude of stress. Hence, only the stress plot from DIM is shown. This is applicable for all the specimens. Similarly, with the I specimens, BIM agrees strongly with the experimentally data (4% - 9% error). Nevertheless, DIM under predicted the data by about 50% as seen in Figure 75. The stress plot in Figure 76 also shows high stress concentrations in the shoulders, however, it is not possible to say if FEA would predict the exact point of fracture (like opposite shoulders fracture along the inclined line) without further analysis.

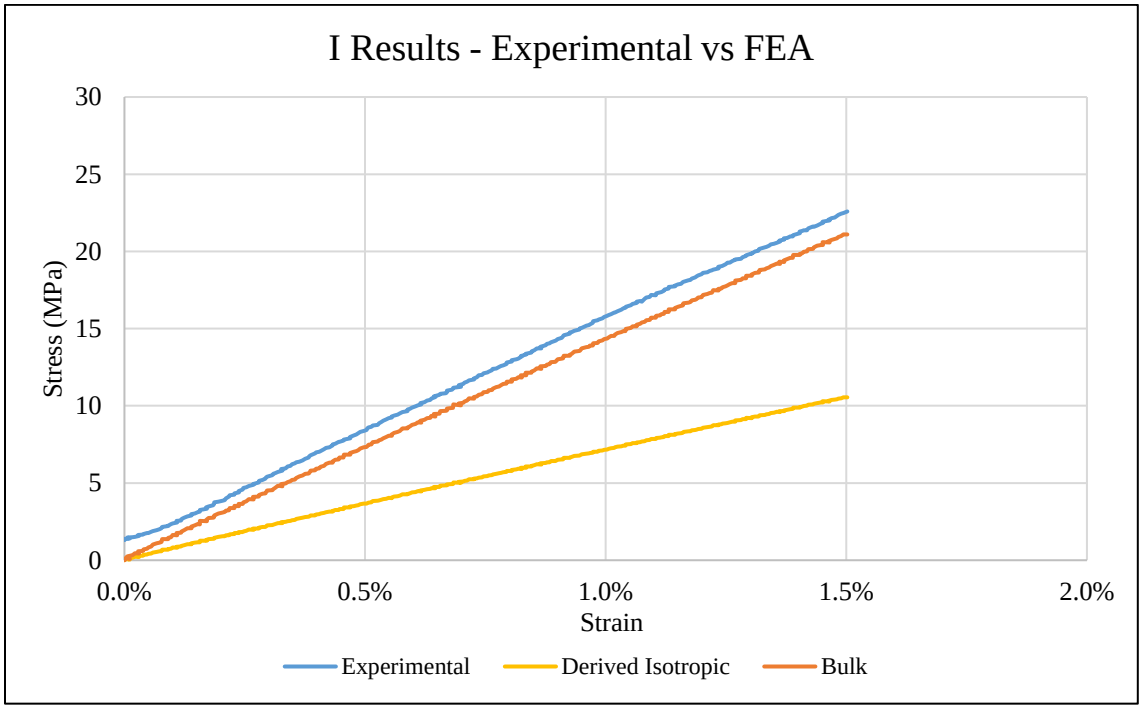

Figure 75: Stress-strain plot for I: Experimental, BIM and DIM results.

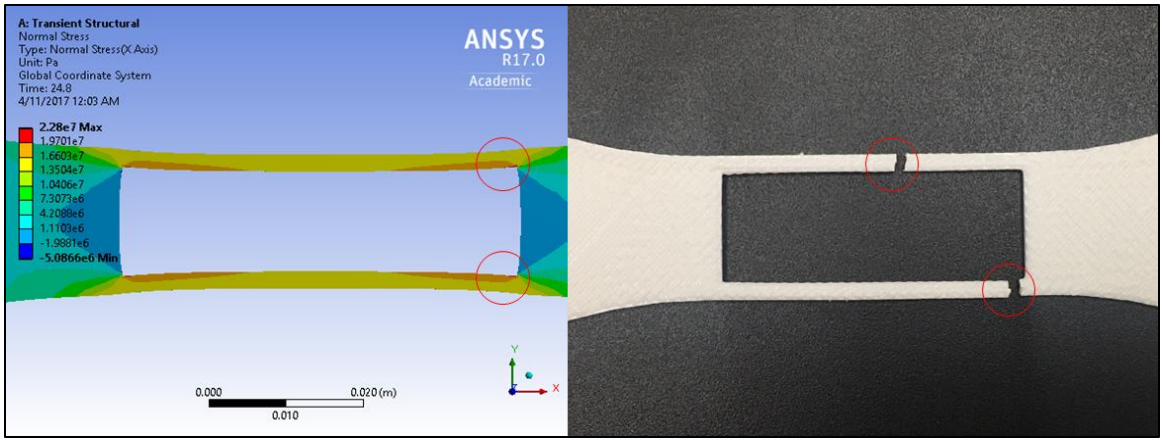

Figure 76: Stress plot for I: left – FEA contour plot, right – actual fractured part.

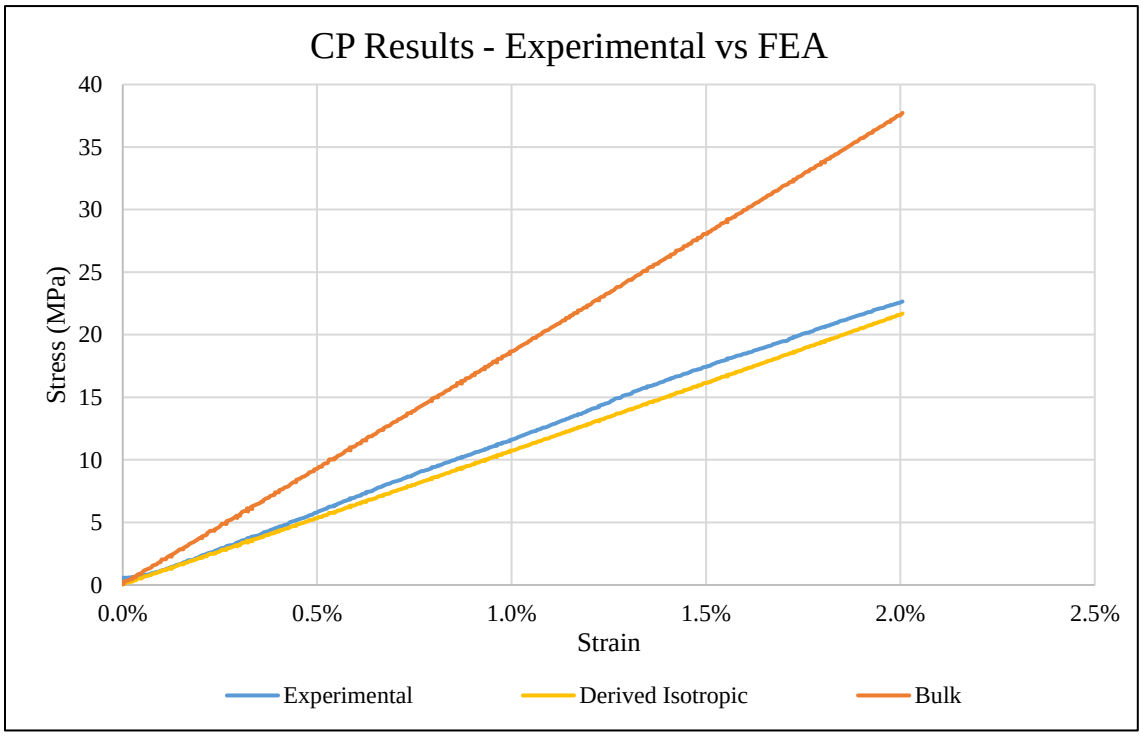

Figure 77: Stress-strain plot for CP: Experimental, BIM and DIM results.

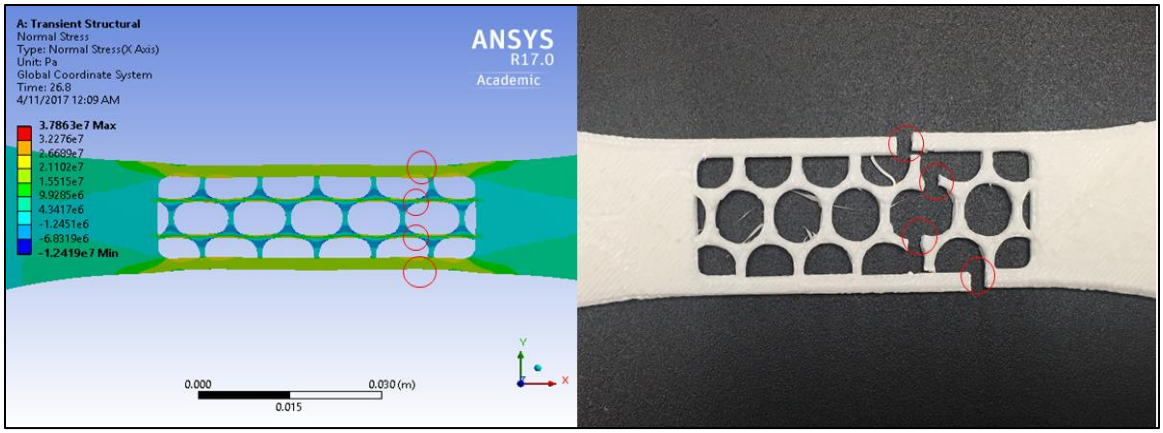

Figure 78: Stress plot for CP: left – FEA contour plot, right – actual fractured part.

The CP results are shown in Figures 77 and 78. The stress-strain plot in Figure 77 shows that results from DIM are in close agreement with the experimental data. The DIM results stand in agreement throughout the stress-strain curve with a 1% to 6% of error; which considering the fact that a non-homogeneous FDM part is being analyzed, are acceptable results. Similarly, the stress plot shows high stress concentrations in areas of least cross-section, which is where the fracture initiated in physical tests. We can see in Figure 78 that the FEA model has high stress concentrations in areas where the fracture actually occurred, leading us to infer that FEA can be used as a stress visualization tool. The BIM model however, deviated highly from the actual results by as much 65%.

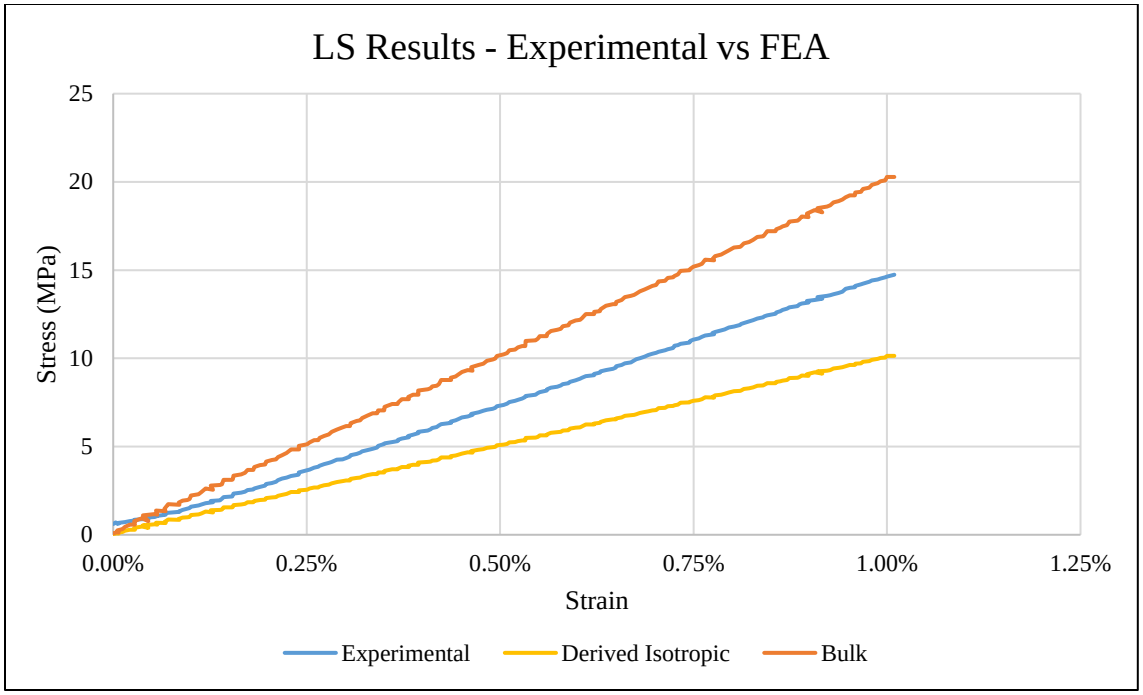

Figure 79: Stress-strain plot for LS: Experimental, BIM and DIM results.

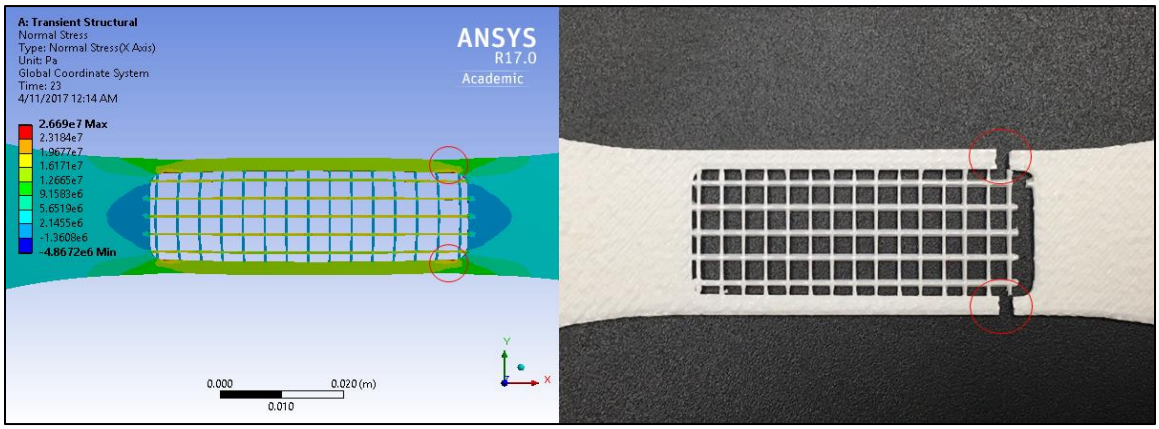

Figure 80: Stress plot for LS: left – FEA contour plot, right – actual fractured part.

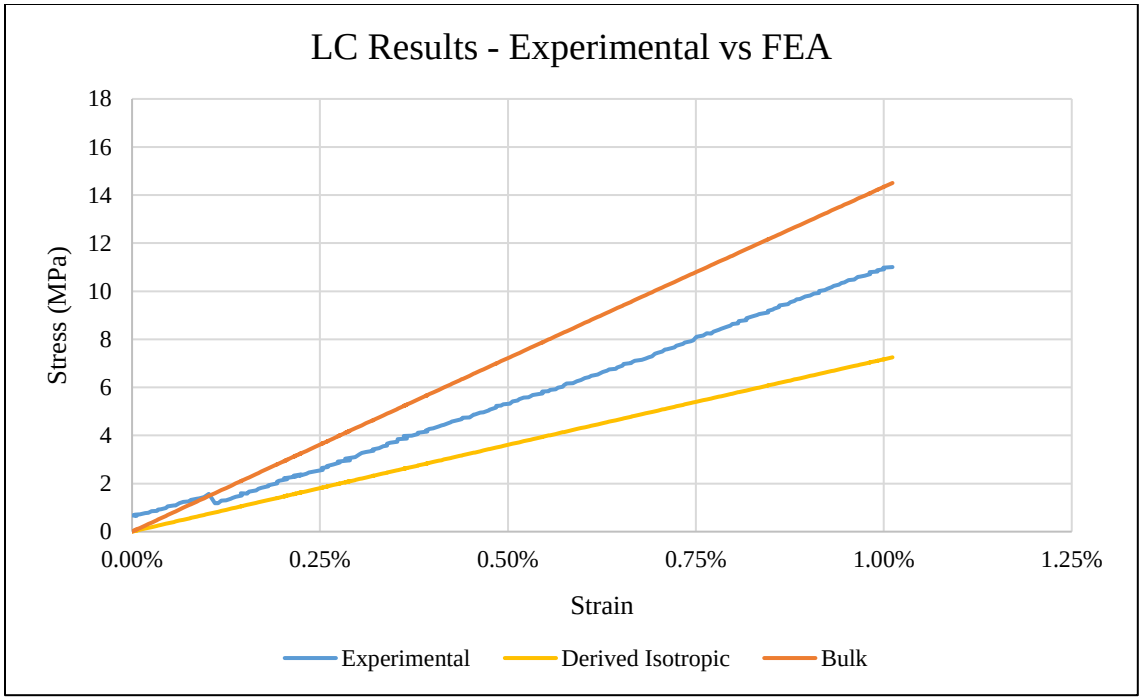

Figure 81: Stress-strain plot for LC: Experimental, BIM and DIM results.

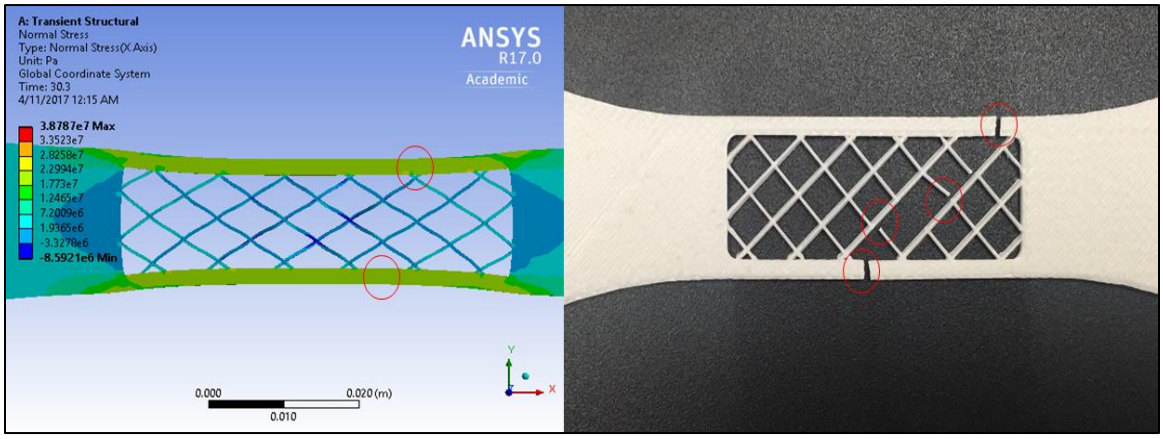

Figure 82: Stress plot for LC: left – FEA contour plot, right – actual fractured part.

In case of both LS and LC specimens, the error between DIM results and experimental data was higher as compared to the CP specimen. For both LS and LC specimens, BIM over-predicted and DIM under-predicted the results. BIM in both cases

showed 30% - 40% error. DIM on the other hand showed 20% to 30% error as seen in Figure 79. Figure 80 shows the stress plots and the actual fractured LS part. The actual part fractured at the junction points at the ends of the infill pattern and later broke at the shoulders. However, the junction points in the stress plots have minimal stress concentrations. This is likely an artifact of the inadequacy to represent imperfect bonding at junction points in the FEA model. Similarly, for the LC specimens, the infill features are predicted to have low stress concentrations, but we can see from the fractured parts the infill patterns also fractured. Figure 81 shows comparison of experimental and FEA results for LC specimens. Figure 82 shows stress plots for LC specimen. Table 13, summarizes the stress values for each specimen for FEA and the errors with respect to (wrt) experimental results. Stresses at 1% and 2% strain, are presented.

Table 13: Summary of FEA results.

	DIM			BIM		
	Stress at 1% strain (MPa)	Stress at 2% strain (MPa)	Error wrt Experimental results	Stress at 1% strain (MPa)	Stress at 2% strain (MPa)	Error wrt Experiment results
HC	7	15	40%	15.2	29	8%
I	8.7	-	50%	14.4	-	5%
CP	10.8	21.8	< 1%	18.7	37	75%
LS	10.1	-	30%	20.3	-	40%
LC	7.3	-	32%	14.3	-	30%

It is evident from results that, even though FEA simulations are in accordance with some of the samples, they deviated from actual results in most of the cases. BIM consistently over-predicted and DIM consistently under-predicted; some simulations were in agreement using BIM whereas others were in accordance while using DIM. The following subsections discuss the results of the orthotropic and the composite models.

4.2.3 FEA Simulations – Orthotropic and Composite Models

The orthotropic analyses take into consideration the anisotropy of the FDM parts to an extent. Even though a complete anisotropic model is not derived, an orthotropic analysis should predict results better than the previous FEA models. On the other hand, the composite analysis should take into the effects of the layered structure of FDM parts. The results from both the FEA models: ODM and CLM are discussed simultaneously for a given specimen. The results from ODM of both ANSYS© and Abaqus© are similar and hence only ANSYS© results are presented (Stress-Strain curves coincide for most specimens, stress plots are identical), unless in cases where there are considerable differences in results from both the solvers. Separate results are presented wherever necessary. The stress contour plots from FEA simulation using both the models are similar to the ones discussed in the previous section. Therefore, they are not presented in this section but can be found in Appendix C and Appendix D.

The first specimen is the C specimen; Figure 83 shows a cone of results from the FEA simulations, including ODM and CLM results. ODM under-predicted the results just like DIM. Even though they were slightly better than the DIM results, were far off from

the experimental data. CLM also failed to give accurate results with higher error values than ODM results. The ODM show considerable differences in results from both the solvers as well. The stress plots however, of both the models show stress concentration in areas where the actual fracture occurs. However, whether or not these simulations can predict the zigzag nature of the fracture is difficult to state without further analysis.

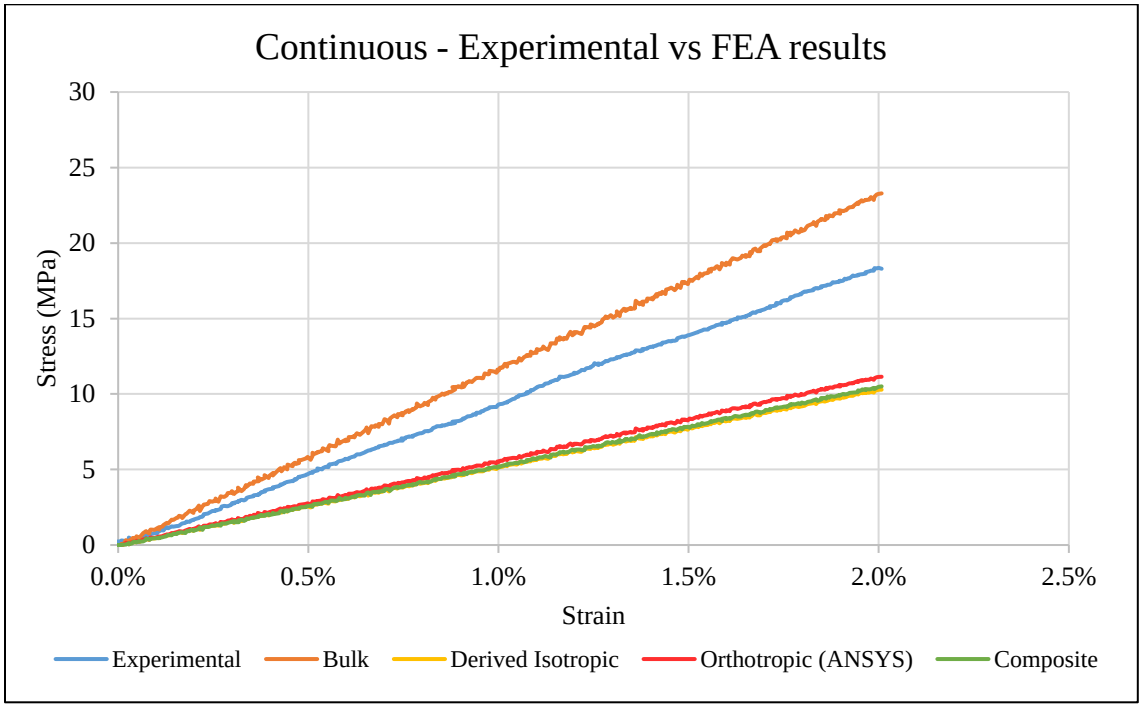

Figure 83: Stress-strain plot for C: Experimental and Simulated results.

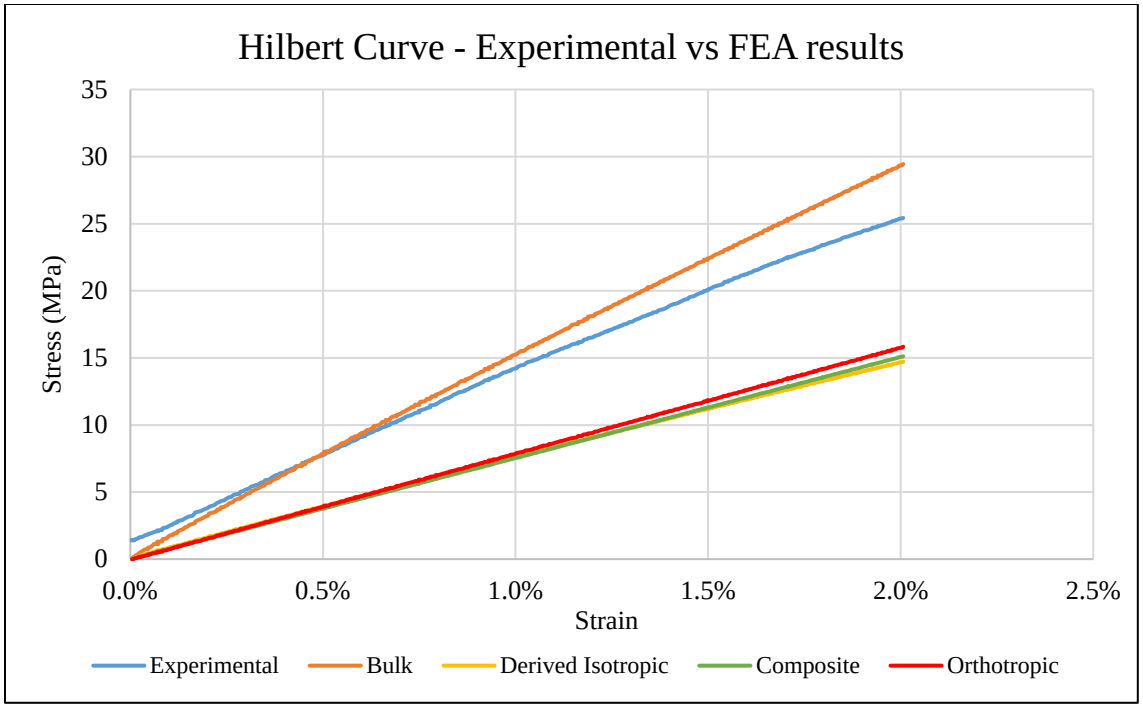

Figure 84: Stress-strain plot for HC: Experimental and Simulated results.

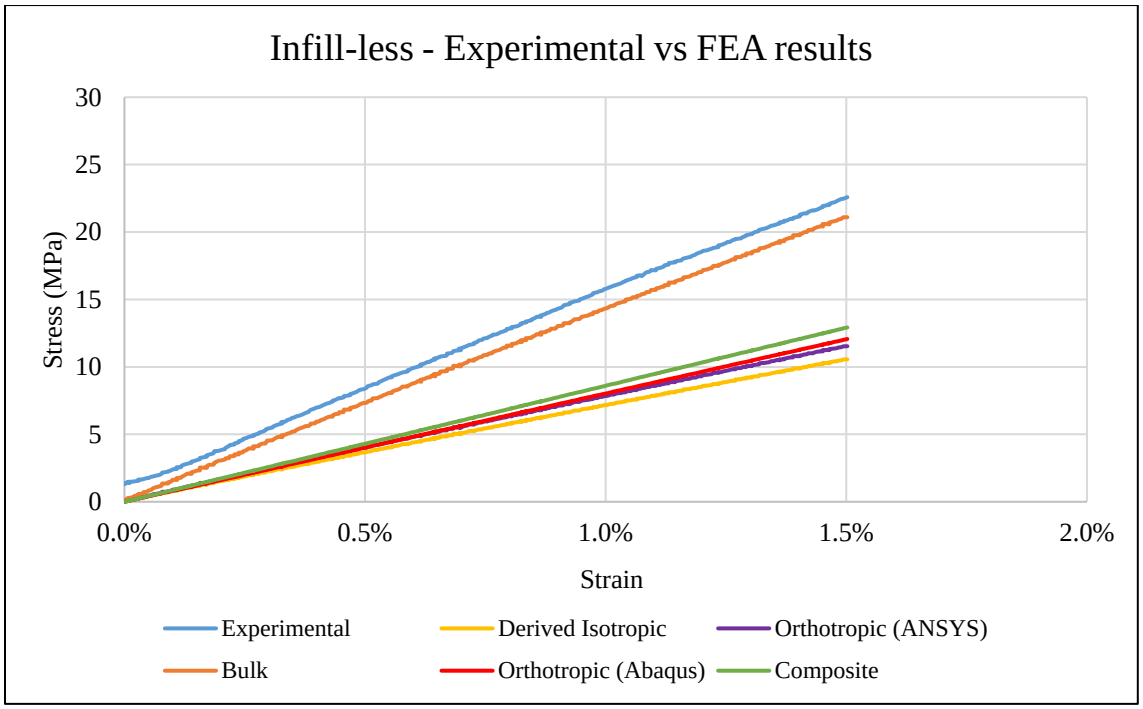

Figure 85: Stress-strain plot for I: Experimental and Simulated results.

The HC and I specimen results are similar as well, ODM and CLM results being better than DIM results however, still way off from the actual results. Both the models under-predict the results, the stress plots being similar to the previous models. Figures 84 and 85 show the stress-strain results of simulations and experimental results for HI and I specimens respectively.

In case of HI samples, even though the ODM under-predicted the results, the model resulted in better accuracy as compared to the DIM results. The errors between the experimental values reduced to about 26% for ODM results. CLM however did not result in improvement of the stress values, but were very similar to the ODM results. The stress strain results can be found in Figure 86. The stress plot is similar to Figure 45 presented in Chapter 3, i.e. it did not account for the fracture in the infill feature or junction points.

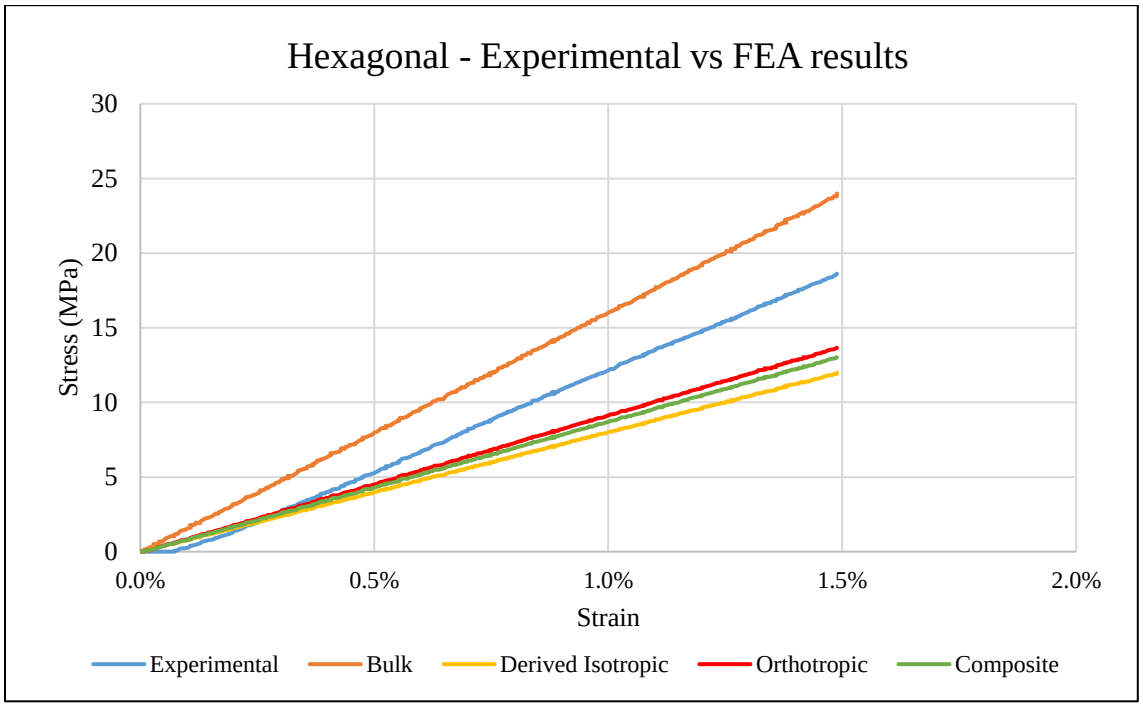

Figure 86: Stress-strain plot for HI: Experimental and Simulated results.

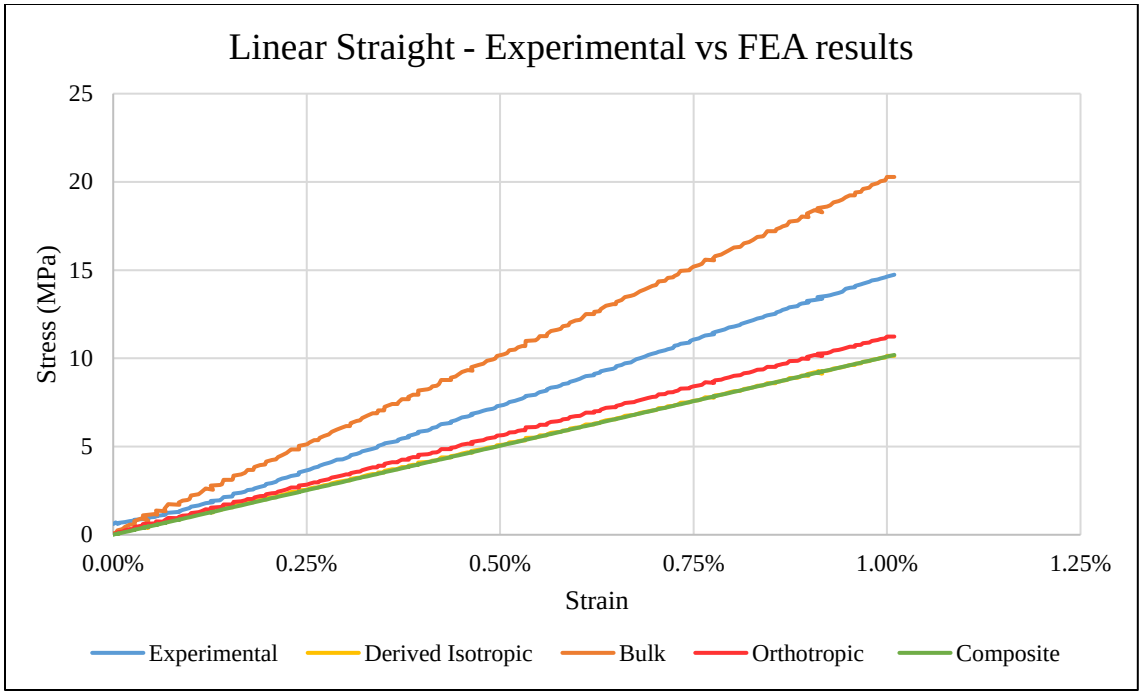

Figure 87: Stress-strain plot for LS: Experimental and Simulated results.

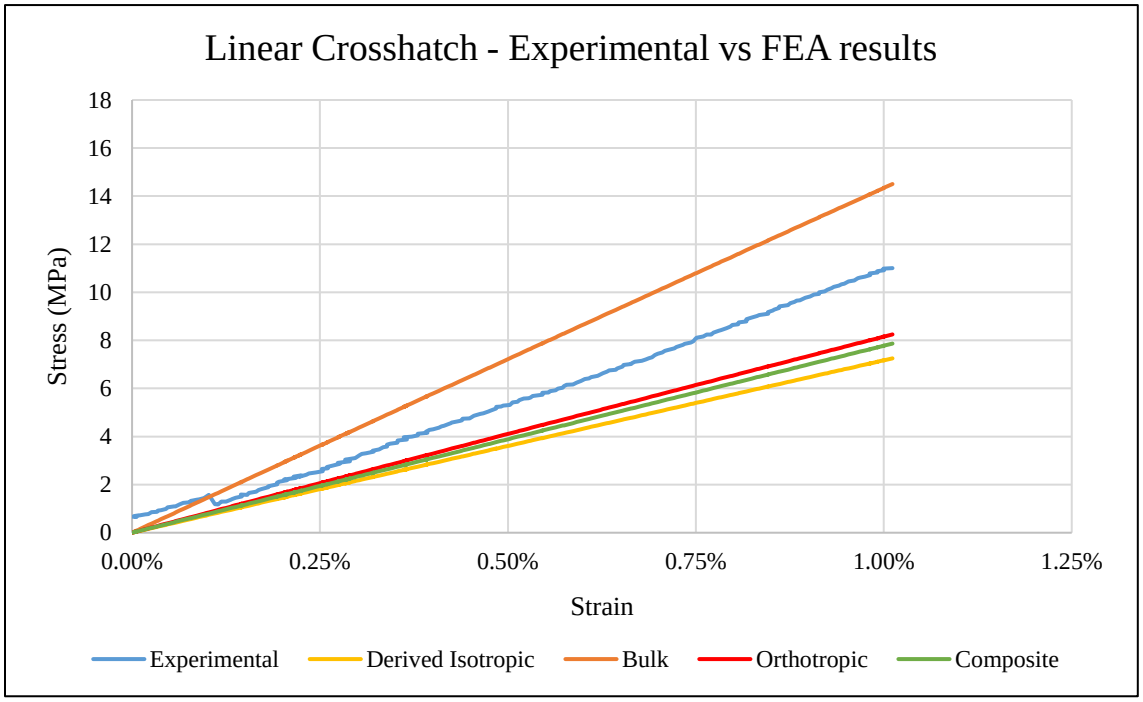

Figure 88: Stress-strain plot for LC: Experimental and Simulated results.

Similar is the case with the LS and LC specimens, as shown in Figure 87 and Figure 88 respectively, with ODM, the stress-strain curve from simulations moves closer to the experimental curve. There is a reduction in the percentage error, with the orthotropic model even though the errors are not within acceptable range. Around the 2% strain, the ODM results for LS coincide with the experimental results. The stress plots are similar to the ones as discussed in section 4.2.3. The CLM results however, deviated from the experimental and ODM values in a negative direction.

In case of the CS and CP samples, the DIM results were quite close to the experimental results. The ODM results were even closer for both the samples as seen from Figures 89 and 90. The ODM stress-strain curve was within acceptable deviances of about 1% to 8% from the experimental results for CS. It can be seen from Figure 90 that the ODM results were almost entirely similar in case of CP samples, such that the ODM stress-strain curve from ANSYS© almost entirely coincided with the experimental results curve. However, the Abaqus© results using ODM showed higher deviations. Thus, we see a considerable difference between the results from different solvers (in this case, error between the solvers is more than the error between simulation and experimental results). The CLM results deviated farther away from the experimental results showing more percentage deviation than even the DIM results. The stress plots are similar to previous results hence the earlier discussions remain valid. The stress plots for CS specimen is similar to the plot shown in Figure 50, whereas the stress plots for CP specimens is similar to the plot shown in Figure 78. Additionally, the stress plots can also be found in Appendix C and Appendix D.

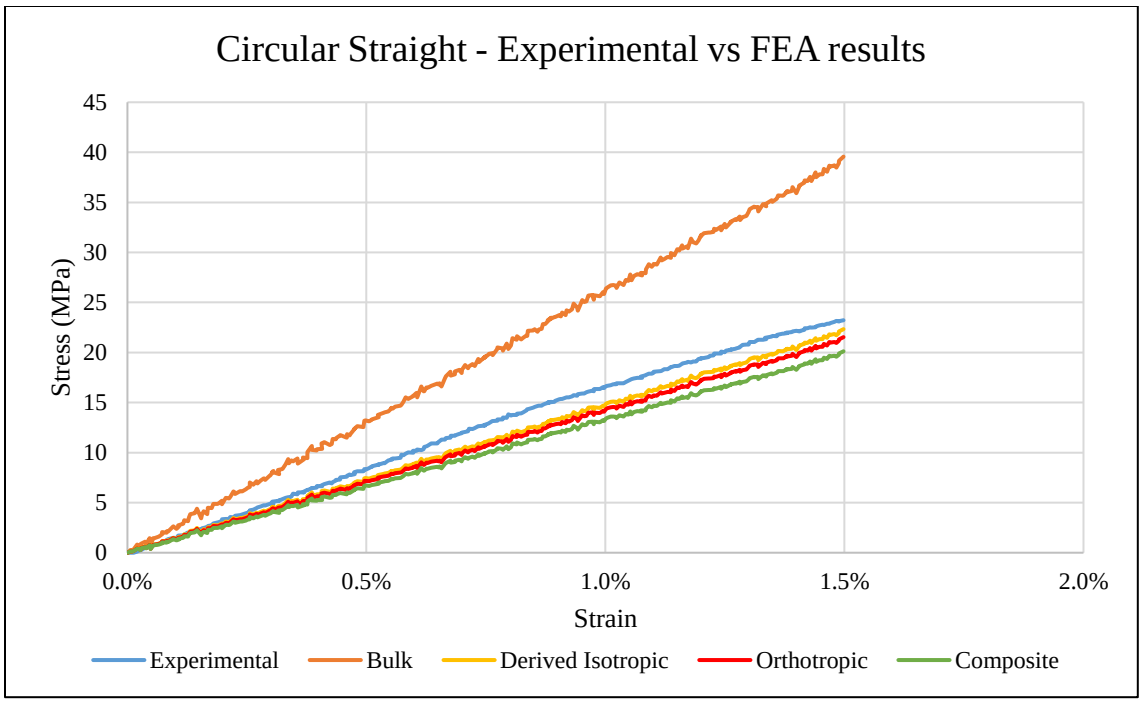

Figure 89: Stress-strain plot for CS: Experimental and Simulated results.

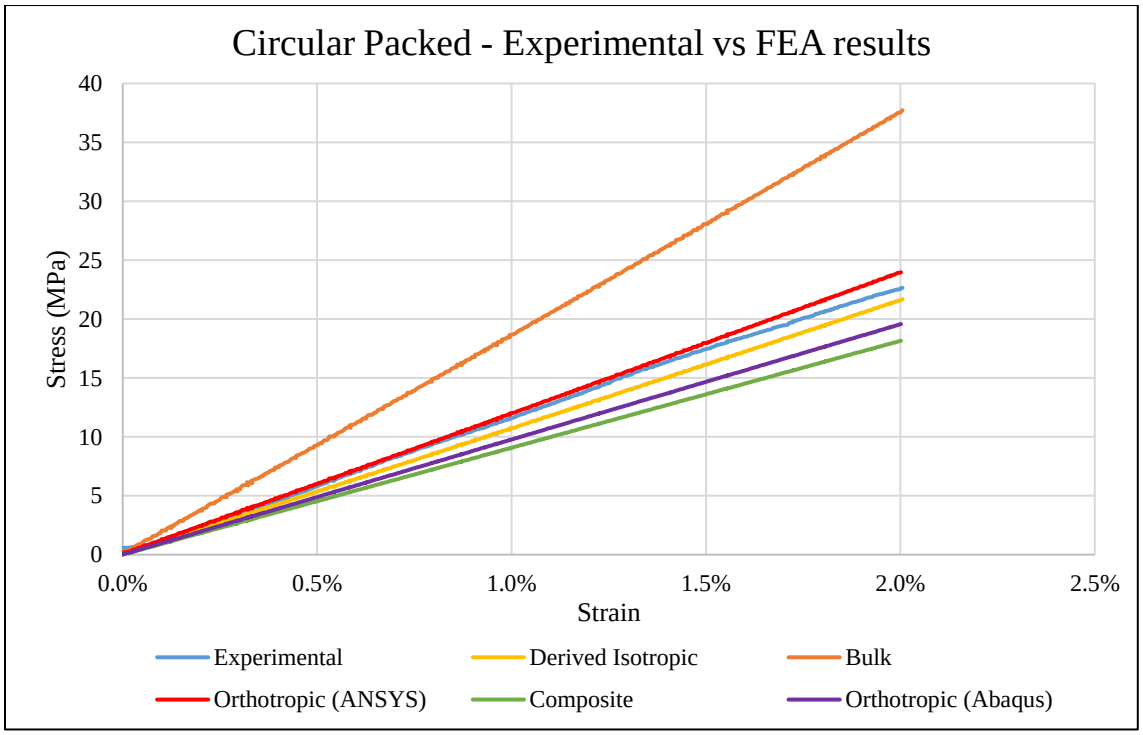

Figure 90: Stress-strain plot for CP: Experimental and Simulated results.

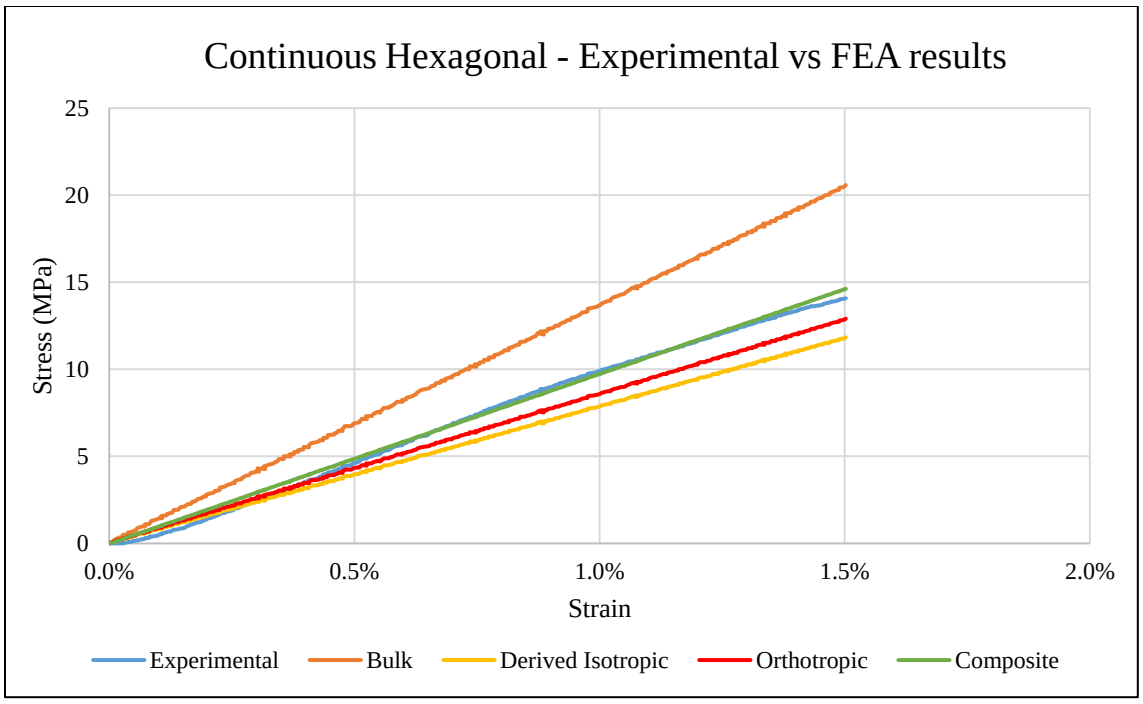

Figure 91: Stress-strain plot for CHI: Experimental and Simulated results.

In case of the CH samples, from Figure 91, CLM results show strong agreement with the experimental data, with the simulation based stress-strain curve completely coinciding with the experimental data until 1.5% strain. However, ODM results deviate from experimental data. Thus, this is the experiment predicting the model that predicts the experiment. This is the only case where CLM predicted more accurate results as compared to ODM. The stress plot shows similar stress concentration as shown in Figure 72, but might not be able to predict the angled fracture as seen in actual tests, until further analysis is conducted.

Table 14 summarizes the results from simulations with the errors. Figure 92 describes the error from the simulations with respect to the experimental data at 1.5% strain.

Table 14: Summary of FEA results.

	ODM			CLM		
	Stress at 1% strain (MPa)	Stress at 1.5% strain (MPa)	Error wrt Experiment	Stress at 1% strain (MPa)	Stress at 1.5% strain (MPa)	Error wrt Experiment
C	5.3	8.6	38%	5.3	7.9	43%
HI	9	13.7	26%	8.6	13	30%
CHI	9	12.9	10%	10	14.6	0%
HC	7.8	11.8	41%	7.8	11	45%
I	8	12.3	45%	8.6	12.9	42%
CS	14.8	21.5	8%	13.3	20.1	14%
CP	12.3	17.6	0%	8	13.6	28%
LS	11.2	-	23%	10.2	-	30%
LC	8.3	-	22%	7.7	-	29%

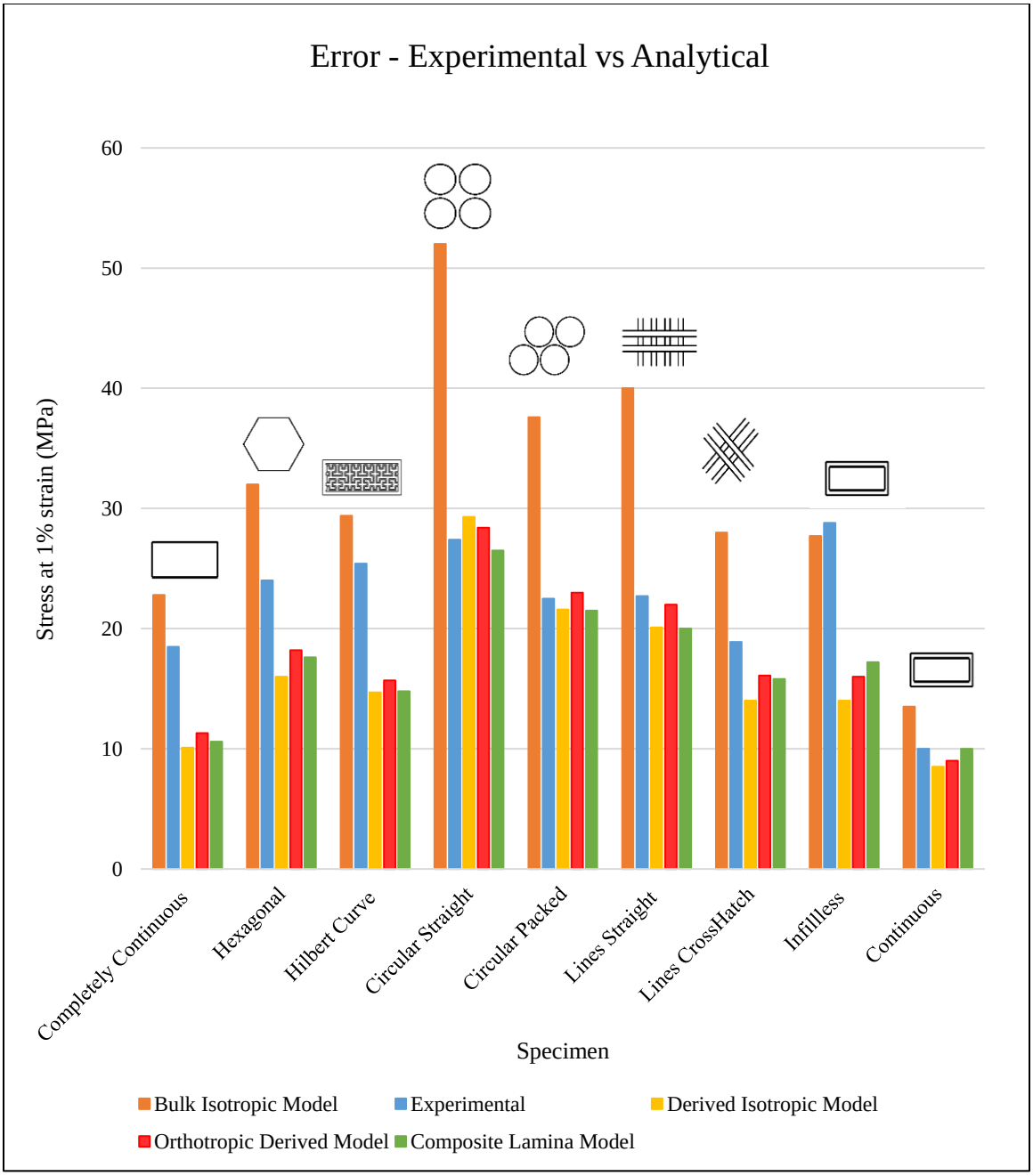

Figure 92: Summary of errors between FEA simulations and experimental results.

From Figure 92, we can see that in most of the cases, FEA simulation results deviated from the experimental results. We can see from the figure that BIM consistently

over-predicted the results, meaning FEA predicted the part to be stronger than it actually was in physical tests (except in case of I specimen). BIM model showed huge deviations in most of the specimens, especially the infill specimens. The only cases when BIM model results were within acceptable regions were in case of HC and I samples. BIM results in case of HC and I models were more accurate than the rest of the models. In addition to these samples, the C sample was the only other case in which BIM were gave better results as compared with other models.

On the other hand, DIM constantly under-predicted the results. DIM results for CP and CS were the closest to experimental values with deviations within the acceptable limit. In case of HI, LS, LC and CH samples, the stress-strain curve deviated from the experimental data up to 30%. Similar was the case of ODM, with results being under-predicted throughout all samples expect CS, CP and CH. The ODM model results seemed like an improvement in DIM results, but still exhibited significant prediction errors in case of C, HC and I samples. However, in case of CS, CP and CH samples, the respective ODM stress-strain curves almost completely adhered to their respective experimental stress-strain curves, thus, stating that and orthotropic FEA model is accurate with experimental values. From an overall perspective, we see that errors reduced with an orthotropic model in most cases, since the orthotropic model took the effects of anisotropy of the parts into consideration. However, a complex ODM resulted in only a slight improvement in results as compared to DIM. This can be associated with the fact that only a uniaxial tensile test was simulated. Therefore, Young's Modulus in direction of loading (E_x) was the dominant property from the orthotropic matrix. It can be hypothesized that with a complex loading

scenario, ODM would provide far better results as compared to DIM. It is also important to note that in case of CP models, ANSYS© results were completely in agreement with the experimental data, however Abaqus© results of the same model deviated considerably. Similarly, Abaqus© results in case of CHI samples were more accurate as compared to ANSYS results. Thus, a difference between the results of different solvers is observed.

The CLM results however, were generally inferior to ODM results, i.e. they showed more divergence from experimental data as compared to ODM results. Again, this was consistent throughout, with deviations being acceptable only in case of CS and CP (worse than ODM) but not in case of other specimens. In addition to this, CLM analysis showed large deformation which can be attributed to element meshing errors. CLM also takes a longer time to complete the analysis as compared to ODM and other models, yet fails to predict the results as accurately as ODM. The composite layup was employed with a view that it would take into consideration the layered structure and fiber orientation of FDM parts, therefore, predicting accurate results; but ODM provided better results. One explanation can be due to the type of analysis. In case of ODM analyses, the model is considered as a solid model with orthotropic material properties and assigned a particular material orientation. In composite layup, each ply (or layer) is considered as a lamina or a planar surface. The mesh elements are created on this surface and extruded with a finite thickness equal to the thickness of the ply. The results are depicted in a laminar sense; since a laminar representation is not an appropriate representation of the solid structure of FDM parts, we see an error in the results as compared to the ODM analysis. Laminar theory also

assumes perfect bonding between each layer of composite; however, this is not the case in actual scenario and can be a reason for the divergence from experimental data.

As far as the stress contour plots are concerned, since the FEA simulation for a given sample stayed the same, with changes in only material models, the stress plots for a sample geometry were very similar, the only difference being the magnitude of the stresses developed. It was evident that FEA was able to predict the stress concentrations in most of the parts, be it continuous or infill samples. However, in case of more intricate infill samples, like HI, LS, LC, even though FEA predicted the stress concentrations in shoulders, it failed to depict the stresses developed in the infill features. The joints were the first to break in physical tests, whereas FEA simulations showed least stress concentrations in these areas. In addition, in case of CH and C where fracture occurred along the fiber direction, FEA cannot be used to predict such a fracture, until further analysis is conducted. The stress plots from all the analyses can in found in Appendix C and Appendix D

Observing the data in Figure 92, we can see that ODM results in case of CP, CHI and CS specimens are highly accurate. This is true in case of DIM results as well. ODM results for HI, LS and LC specimens show deviations from experimental data. This leads us to believe whether ODM predictions are accurate in geometries with continuous load bearing areas (CP, CS, and CHI). However, ODM results deviate heavily in case of C specimens, and hence the previous statement is refuted. Similarly, with BIM, the accuracy of prediction changes with geometries as evident in Figure 92.

We see that some FEA models predict the behavior of FDM parts accurately (with acceptable deviations), whereas in most of the cases, FEA simulations fail to predict the normal stresses in a typical uniaxial tensile test accurately. We observe that a given FEA model predicts the same test differently, and hence there is no certainty to propose a correction factor for these errors. Over-prediction in some models and under-prediction in others renders us to state that FEA is unreliable in case of simulating FDM parts under uniaxial loading. In addition to the type of FEA analysis, the accuracy of the results in some cases were also dependent on the FEA solvers. We also observe that the accuracy of the predictions of results also depends on the geometry of the part. Some infill pattern results were more accurate than others with the same FEA model were. It is necessary to look into this data to enable us to analyze FDM parts accurately. Chapter 5 lays down the conclusions based on the results from these studies. These conclusions are based on results from both Chapter 3 and Chapter 4. Chapter 5 also discusses the scope of future work in addition to the conclusions of this study.

CHAPTER 5: CONCLUSIONS AND FUTURE WORK

5.1 Conclusion

A comparative study of FEA simulations and experimental data is performed. In order to compare this data, a set of different specimen geometries were designed and printed. These sets of parts were tested and these tests were simulated using different FEA models. The goal of this study was to compare FEA simulations of as-built models of FDM dogbone specimens with experimental test results. The conclusions from the results of this study are two fold and listed below.

1. Higher Fidelity Material Models provide better results.

   As mentioned earlier, FDM parts exhibit anisotropy, therefore, considering this while simulating an FDM part is necessary. It is evident from the results that the Orthotropic Material Model consistently provided better results than both the Isotropic (derived) Material Models (with an exception in BIM for the I specimen). It is also seen that ODM also consistently produced better results than CLM. The orthotropic properties were also used in composite model, along with specifying the fiber orientation for each layer. However, CLM results were poorer than a simple orthotropic model. In addition to this, CLM analyses showed meshing errors, large deformations and consistently took longer time as compared to ODM analyses. Therefore, there is no need to resort to a complex composite model while analyzing FDM parts. It can be concluded that, from the four models used, the

higher fidelity Orthotropic Material Model (ODM) best represents the non-isotropic FDM parts.

2. FEA results are inconsistent and therefore, unreliable.

   The inconsistency of FEA of FDM parts can be discussed in three parts.

   a. Stress-strain curve results.

      The stress-strain results from the FEA simulations were plotted along with the experimental results. It is evident from the results that, BIM consistently over-predicted the results (with errors up to 75%), whereas the derived material models consistently under-predicted the results. BIM provided acceptable results only in case of the I specimens. Even though, the ODM model better represented the non-isotropic behavior of FDM parts, the accuracy of this model was not consistent with all the specimens. Errors using ODM were lesser than 2% for the CHI, CP and CS specimens but were as high as 30% in case of the HC and I specimens. FEA results were accurate in certain simulations and inaccurate in others. Therefore, it can be concluded that the stress-strain curve results from FEA simulations are inconsistent and therefore, may not be reliable.

   b. Stress contour plots.

      Stress contour plots were similar for the different FEA models used, the only difference being the magnitude of stresses developed. The stress plots enabled us to compare the areas of stress concentration (and ultimately fracture) in FEA models with the actual areas of fracture. We can see that in case of the CP, CS,

C, I and HC, the FEA stress plots accurately predicted the areas of fracture. However, in case of the HI, LS and LC, FEA failed to depict the stress concentrations at the junction points in the infill features. In addition, current FEA models cannot predict the fracture along the fiber orientations seen in the CHI specimens. Therefore, we can conclude that in cases where geometries have a continuous load bearing area, like in case of the C, CP and CS, FEA can be used as visualization tool for stress concentrations. However, in cases of intricate infill patterns with junction points, like the HI, LS and LC FEA cannot be relied upon. Stress concentrations may be identifiable from FEA, but junction points are often sources of inaccuracy.

c. Type of geometry.

From the results discussed in the previous chapter, it is clear that the ODM results were very accurate only in case of the CP, CHI and CS specimens. In addition, the DIM results for these specimens were within acceptable deviations. However, ODM results showed considerable deviations in case of rest of the specimens. Similarly, BIM results were accurate for the I and HC specimens, and were way off in case of other specimens. This leads us to conclude that even when the parts are modeled as-built, the accuracy of FEA simulations depends upon the geometry of the part. One explanation for this can be the effect of bonding on the final material properties of the part. The quality of bonding and in turn the material properties, depend upon the time between the laying the adjacent fibers within the layer and the time between each

successive layers. This determines the quality of bond formation between adjacent and successive layers. The time between laying adjacent fibers and layers is dependent on the path of the extruder, which in turns depends on the geometry of the part, and the path derived from the slicer. Therefore, the properties of the part become a geometry and slicer (toolpath) dependent function. So in addition to the material model, lack of accurate representation of as-built microstructure causes errors as well.

To summarize, due to material model infidelities and geometric dependencies (leading to a bonding dependency), the FEA simulations performed in this study are not a reliable means for analyzing FDM parts.

5.2 Future Scope

It is important to address these problems; this would enable us to tie the material model problems with the toolpath dependencies to obtain a high fidelity FEA model, to accurately analyze FDM parts. The study also had some limitations that are needed to be addressed. The future scope is listed below:

1. Perform and Simulate different loading conditions.

   The FDM parts in this study are only subjected to uniaxial tensile tests. However, the real loading conditions of end use FDM parts are more complex than unidirectional loading. Future research can include testing and simulating the FDM parts in complex multiple loading scenarios. This includes compressive tests, bending tests, impact tests. A multi-dimensional test system would enable us to

compare the accuracy of FEA simulations for FDM parts in complex loading situations. Using ODM lead to only a small improvement in results as compared to DIM. The reason being that only uniaxial tensile tests were simulated. An ODM used in combined loading (e.g. bending and tensile loading) might results in a larger improvement as compared to DIM results.

2. Higher fidelity material models and FEA models.

   With FDM parts exhibiting anisotropy, an anisotropic material model with 21 independent elastic constants, may best represent these parts. However, deriving all the 21 independent constants is a tedious process. Owing to the anisotropy, non-homogeneous and non-linear behavior of FDM samples, multi-axial testing of may samples is required to fully characterize the response of FDM parts [66]. Using a data-driven characterization strategy that employs an automated six degree of freedom test apparatus as stated in [67], would enable us to characterize the real response of FDM parts.

3. Microstructure representation of FDM parts.

   We can say from the study, that representing FDM parts as homogeneous solid entities leads to errors within the results. With the toolpath and fiber-to-fiber bonding playing an important role in the behavior of FDM parts, it is necessary to take the microstructure of FDM parts into consideration while simulating them. The fiber-to-fiber bonding can be represented in the model by specifying the fiber-to-fiber overlap in the CAD model. This can be done in two ways.

a. Using a toolpath from G-code to correctly generate a CAD model without errors.
b. To analyze microscopic images of FDM parts to create voids (pertaining to different orientations) in the CAD to replicate the non-homogeneous FDM part. A similar void analysis can be found in [45]

It is necessary to look into such a method to represent FDM parts, since a change in the geometry of the infill pattern, will ultimately lead to a change in the bonding between adjacent and successive filaments. Therefore, in addition to the material model, a model that accurately represents the microstructure is also required.

4. Extend for different AM technologies.

   Similar studies can and should be conducted by using samples from different AM technologies. With parts from different AM technologies increasingly being used in end use applications, research in this direction is needed.

5. Discrete Element Analysis.

   FEA represents a CAD model as a continuum of smaller finite elements, a contradicting idea for non-homogeneous FDM parts. Another interesting method of analysis that could be used is Discrete Element Analysis, which is based on Discrete Element Method (DEM). DEM is a numerical approximation method for mechanics of continuous and discontinuous models, which is based on an interacting system of particles [68]. The material is modelled as an assembly of rigid particles and the interaction between each particle is explicitly considered to evaluate the stress-strain results. Steuben *et al* [68] discusses a Discrete Element

Method to analyze the particle based AM methods. Such a system of discrete rigid particles might be better able to link the material model and the toolpath dependencies associated with an FDM part.

There is potential to investigate and develop better means to relate the microstructure and material behavior of FDM (or AM) parts. An ample amount of research would be needed. With the increasing use of AM parts for functional applications, research regarding simulating these parts under the actual loading condition is necessary.

5.3 Summary

Numerous research tasks were performed in this study. These are summarized below.

- Designed specimen geometries for the study.
- Printed the specimens with the optimum quality.
- Tested specimens on uniaxial tensile test bed to obtain experimental results.
- Derived material models (isotropic and orthotropic) from experimental data for simulations.
- Modeled ‘As-built’ specimen geometries of FDM parts with:
    - A fiber model approach
    - A solid model approach.
- Performed FEA simulations of as-built geometries using continuum material models:
    - Isotropic model.

- Orthotropic model.
- Composite model.

  Derived properties (from experiments) were used to achieve higher fidelity for each of the material models.

- Compared FEA results with the corresponding experimental data.

Recalling the design statement, **FEA simulations of tensile loading of as-built geometries using experimentally derived material models predict actual behaviors of FDM parts verified with experimental testing.** From this research, we conclude that FEA results of as-built geometries using experimentally derived material models are not always accurate or reliable means of predicting behavior of FDM parts due to both geometric dependencies (which lead to bonding dependencies) and material model inaccuracies.

Further research is necessary to solve the issues pertaining to the material model inaccuracies as well as microstructure (bonding) representations. Developing and validating approaches that answer these issues can lead to a better representation of FDM parts for their effective analyses.

REFERENCES

[1] Gibson, Ian, David W. Rosen, and Brent Stucker, 2010, Additive manufacturing technologies. New York: Springer.

[2] T. Wohlers, "U.S. Manufacturing Competitiveness Initiative Dialogue," presented at the Council on Competitiveness, Oak Ridge, TN, 18-Apr-2013.

[3] https://www.eos.info/additive_manufacturing/for_technology_interested

[4] http://www.3epd.com/services/additive-manufacturing/

[5] Ziemian, C., Sharma, M., & Ziemian, S. (2012). Anisotropic mechanical properties of ABS parts fabricated by fused deposition modelling. *INTECH Open Access Publisher*.

[6] http://www.avid3dprinting.com/fdm/

[7] Hashmi, S., Batalha, G.F., Tyne, C.V. and Yilbas, B. S. (2014), "Comprehensive Materials Processing", Elsevier, Amsterdam, pp. 338.

[8] Mani, M., Lane, B., Donmez, A., Feng, S., Moylan, S., & Fesperman, R. (2015). Measurement science needs for real-time control of additive manufacturing powder bed fusion processes. *National Institute of Standards and Technology, Gaithersburg, MD, Standard No. NISTIR, 8036*.

[9] Zhang, Y., & Chou, Y. K. (2006). Three-dimensional finite element analysis simulations of the fused deposition modelling process. *Proceedings of the Institution of Mechanical Engineers, Part B: Journal of Engineering Manufacture*, *220*(10), 1663-1671.

[10] Vasiliev, V., and Evgeny V. Morozov, Advanced Mechanics of Composite Materials (Third Edition), *Elsevier, Boston, 2013, Page iii,* ISBN 9780080982311.

[11] Sayre III, R. (2014). *A Comparative Finite Element Stress Analysis of Isotropic and Fusion Deposited 3D Printed Polymer* (Doctoral dissertation, Rensselaer Polytechnic Institute).

[12] Koruche, U. S., & Patil, S. F. (2015), "Application of Classical Lamination Theory and Analytical Modeling of Laminates*." International Research Journal of Engineering and Technology, Volume: 02 Issue: 02.*

[13] Reddy, J.N. (2006). An Introduction to the Finite Element Method (Third Ed.). *McGraw-Hill*. ISBN 9780071267618.

[14] http://www.padtinc.com/blog/the-focus/fused-deposition-modeling-fdm-properties-a-micromechanics-perspective

[15] http://www.padtinc.com/blog/the-focus/constitutive-modeling-of-3d-printed-fdm-parts-part-2-approaches

[16] Mamadapur, M. S. (2007). *Constitutive modeling of fused deposition modeling acrylonitrile butadiene styrene (ABS)* (Doctoral dissertation, Texas A&M University).

[17] Hopkinson, N., & Dicknes, P. (2003). Analysis of rapid manufacturing—using layer manufacturing processes for production. *Proceedings of the Institution of Mechanical Engineers, Part C: Journal of Mechanical Engineering Science*, *217*(1), 31-39.

[18] https://www.stratasysdirect.com/solutions/fused-deposition-modeling/

[19] http://proto3000.com/fused-deposition-modeling-solutions-fdm-3d-printing-applications.php

[20] http://www.stratasys.com/resources/case-studies/defense

[21] Lee, C. S., Kim, S. G., Kim, H. J., & Ahn, S. H. (2007). Measurement of anisotropic compressive strength of rapid prototyping parts. *Journal of materials processing technology*, *187*, 627-630.

[22] Upadhyay, K., Dwivedi, R., & Singh, A. K. (2017). Determination and Comparison of the Anisotropic Strengths of Fused Deposition Modeling P400 ABS. In *Advances in 3D Printing & Additive Manufacturing Technologies* (pp. 9-28). Springer Singapore.

[23] Es-Said, O. S., Foyos, J., Noorani, R., Mendelson, M., Marloth, R., & Pregger, B. A. (2000). Effect of layer orientation on mechanical properties of rapid prototyped samples. *Materials and Manufacturing Processes*, *15*(1), 107-122.

[24] Li, L., Sun, Q., Bellehumeur, C., & Gu, P. (2002). Composite modeling and analysis for fabrication of FDM prototypes with locally controlled properties. *Journal of Manufacturing Processes*, *4*(2), 129-141.

[25] Gajdoš, I., & Slota, J. (2013). Influence of printing conditions on structure in FDM prototypes. *Technical Gazette*, *20*(2), 231-236.

[26] Bellehumeur, C., Li, L., Sun, Q., & Gu, P. (2004). Modeling of bond formation between polymer filaments in the fused deposition modeling process. *Journal of Manufacturing Processes*, *6*(2), 170-178.

[27] Sun, Q., Rizvi, G. M., Bellehumeur, C. T., & Gu, P. (2008). Effect of processing conditions on the bonding quality of FDM polymer filaments. *Rapid Prototyping Journal*, *14*(2), 72-80.

[28] Bagsik, A., Schöppner, V., & Klemp, E. (2010, September). FDM part quality manufactured with Ultem* 9085. In *14th International Scientific Conference on Polymeric Materials* (Vol. 15, pp. 307-315).

[29] Ahn, S. H., Montero, M., Odell, D., Roundy, S., & Wright, P. K. (2002). Anisotropic material properties of fused deposition modeling ABS. *Rapid prototyping journal*, *8*(4), 248-257.

[30] Montero, M., Roundy, S., Odell, D., Ahn, S. H., & Wright, P. K. (2001). Material characterization of fused deposition modeling (FDM) ABS by designed experiments. *Society of Manufacturing Engineers*, *10*(13552540210441166).

[31] Domingo-Espin, M., Borros, S., Agullo, N., Garcia-Granada, A. A., & Reyes, G. (2014). Influence of building parameters on the dynamic mechanical properties of polycarbonate fused deposition-modeling parts. *3D Printing and Additive Manufacturing*, *1*(2), 70-77.

[32] Baich, L., & Manogharan, G. (2015). Study of infill print parameters on mechanical strength and production cost-time of 3D printed ABS parts. In *International Solid Freeform Fabrication Symposium, Austin, TX* (pp. 209-2018).

[33] Rodríguez, J. F., Thomas, J. P., & Renaud, J. E. (2001). Mechanical behavior of acrylonitrile butadiene styrene (ABS) fused deposition materials. Experimental investigation. *Rapid Prototyping Journal*, *7*(3), 148-158.

[34] Dutta, D. (1999). Deposition strategies and resulting part stiffnesses in fused deposition modeling. *Ann Arbor*, *1050*, 48109.

[35] Huang, B., Masood, S., Nikzad, M., Venugopal, P. R., & Arivazhagan, A. (2016). Dynamic Mechanical Properties of Fused Deposition Modelling Processed Polyphenylsulfone Material. *American Journal of Engineering and Applied Sciences*, *9*(1), 1-11.

[36] Anitha, R., Arunachalam, S., & Radhakrishnan, P. (2001). Critical parameters influencing the quality of prototypes in fused deposition modelling. *Journal of Materials Processing Technology*, *118*(1), 385-388.

[37] Zaldivar, R. J., Witkin, D. B., McLouth, T., Patel, D. N., Schmitt, K., & Nokes, J. P. (2017). Influence of processing and orientation print effects on the mechanical and thermal behavior of 3D-Printed ULTEM® 9085 Material. *Additive Manufacturing*, *13*, 71-80.

[38] Lanzotti, A., Grasso, M., Staiano, G., & Martorelli, M. (2015). The impact of process parameters on mechanical properties of parts fabricated in PLA with an open-source 3-D printer. *Rapid Prototyping Journal*, *21*(5), 604-617.

[39] Khan, S. A., Fahad, M., & Khan, M. A. (2016). Evaluation of the Effect of Infill Pattern on Mechanical Strength of Additively Manufactured Specimen. *Professor Dr. Muhammad Tufail Convener*, *356*, 356.

[40] Wu, W., Geng, P., Li, G., Zhao, D., Zhang, H., & Zhao, J. (2015). Influence of layer thickness and raster angle on the mechanical properties of 3D-printed PEEK and a comparative mechanical study between PEEK and ABS. *Materials*, *8*(9), 5834-5846.

[41] Syamsuzzaman, M., Mardi, N. A., Fadzil, M., & Farazila, Y. (2014). Investigation of layer thickness effect on the performance of low-cost and commercial fused deposition modelling printers. *Materials Research Innovations*, *18*(sup6), S6-485.

[42] Zou, R., Xia, Y., Liu, S., Hu, P., Hou, W., Hu, Q., & Shan, C. (2016). Isotropic and anisotropic elasticity and yielding of 3D printed material. *Composites Part B: Engineering*, *99*, 506-513.

[43] Casavola, C., Cazzato, A., Moramarco, V., & Pappalettere, C. (2016). Orthotropic mechanical properties of fused deposition modelling parts described by classical laminate theory. *Materials & Design*, *90*, 453-458.

[44] Bertoldi, M., Yardimci, M. A., Pistor, C. M., Guceri, S. I., & Sala, G. (1998). Mechanical characterization of parts processed via fused deposition. In *Proceedings of the 1998 solid freeform fabrication symposium* (pp. 557-565).

[45] Magalhães, L. C., Volpato, N., & Luersen, M. A. (2014). Evaluation of stiffness and strength in fused deposition sandwich specimens. *Journal of the Brazilian Society of Mechanical Sciences and Engineering*, *36*(3), 449-459.

[46] Alaimo, G., Marconi, S., Costato, L., & Auricchio, F. (2017). Influence of meso-structure and chemical composition on FDM 3D-printed parts. *Composites Part B: Engineering*, *113*, 371-380.

[47] Dutta, D. (1999). Deposition strategies and resulting part stiffnesses in fused deposition modeling. *Ann Arbor*, *1050*, 48109.

[48] Liu, X., & Shapiro, V. (2016). Homogenization of material properties in additively manufactured structures. *Computer-Aided Design*, *78*, 71-82.

[49] Croccolo, D., De Agostinis, M., & Olmi, G. (2013). Experimental characterization and analytical modelling of the mechanical behaviour of fused deposition processed parts made of ABS-M30. *Computational Materials Science*, *79*, 506-518.

[50] Gurrala, P. K., & Regalla, S. P. (2014). Part strength evolution with bonding between filaments in fused deposition modelling: This paper studies how coalescence of filaments contributes to the strength of final FDM part. *Virtual and Physical Prototyping*, *9*(3), 141-149.

[51] Hambali, R. H., Celik, H. K., Smith, P. C., Rennie, A. E. W., & Ucar, M. (2010, September). Effect of build orientation on FDM parts: a case study for validation of deformation behaviour by FEA. In *IN: Proceedings of iDECON 2010—international conference on design and concurrent engineering, Universiti Teknikal Malaysia Melaka, Melaka* (pp. 224-228).

[52] Hambali, R. H., Smith, P., & Rennie, A. E. W. (2012). Determination of the effect of part orientation to the strength value on additive manufacturing FDM for end-use parts by physical testing and validation via three-dimensional finite element analysis. *International Journal of Materials Engineering Innovation*, *3*(3-4), 269-281.

[53] Domingo-Espin, M., Puigoriol-Forcada, J. M., Garcia-Granada, A. A., Llumà, J., Borros, S., & Reyes, G. (2015). Mechanical property characterization and simulation

of fused deposition modeling Polycarbonate parts. *Materials & Design*, *83*, 670-677.

[54] Bellini, A., & Güçeri, S. (2003). Mechanical characterization of parts fabricated using fused deposition modeling. *Rapid Prototyping Journal*, *9*(4), 252-264.

[55] Rodríguez, J. F., Thomas, J. P., & Renaud, J. E. (2003). Mechanical behavior of acrylonitrile butadiene styrene fused deposition materials modeling. *Rapid Prototyping Journal*, *9*(4), 219-230.

[56] Cuan-Urquizo, E., Yang, S., & Bhaskar, A. (2015). Mechanical characterisation of additively manufactured material having lattice microstructure. In *IOP Conference Series: Materials Science and Engineering* (Vol. 74, No. 1, p. 012004). IOP Publishing.

[57] Villalpando, L., Eiliat, H., & Urbanic, R. J. (2014). An optimization approach for components built by fused deposition modeling with parametric internal structures. *Procedia CIRP*, *17*, 800-805.

[58] Villalpando, L. (2013). Characterization of parametric internal structures for components built by fused deposition modeling. *Electronic Theses and Dissertations: University of Windsor*.

[59] El-Gizawy, A. S., Corl, S., & Graybill, B. (2011, July). Process-induced properties of fdm products. In *Proceedings of the ICMET, International Conference on Mechanical Engineerings and Technology Congress & Exposition*.

[60] Rezayat, H., Zhou, W., Siriruk, A., Penumadu, D., & Babu, S. S. (2015). Structure–mechanical property relationship in fused deposition modelling. *Materials Science and Technology*, *31*(8), 895-903.

[61] Garg, A., & Bhattacharya, A. (2017). An insight to the failure of FDM parts under tensile loading: finite element analysis and experimental study. *International Journal of Mechanical Sciences*, *120*, 225-236.

[62] Ajoku, U., Hopkinson, N., & Caine, M. (2006). Experimental measurement and finite element modelling of the compressive properties of laser sintered Nylon-12. *Materials Science and Engineering: A*, *428*(1), 211-216.

[63] Martínez, J., Diéguez, J. L., Ares, E., Pereira, A., Hernández, P., & Pérez, J. A. (2013). Comparative between FEM models for FDM parts and their approach to a real mechanical behaviour. *Procedia Engineering*, *63*, 878-884.

[64] Davis, J. R. (Ed.). (2004). *Tensile testing*. ASM international.

[65] https://plastics.ulprospector.com/generics/1/c/t/acrylonitrile-butadiene-styrene-abs-properties-processing

[66] Steuben, J. C., Iliopoulos, A. P., & Michopoulos, J. G. (2016). Implicit slicing for functionally tailored additive manufacturing. *Computer-Aided Design*, *77*, 107-119.

[67] Michopoulos, J. G., Hermanson, J. C., & Iliopoulos, A. (2014). Advances on the constitutive characterization of composites via multiaxial robotic testing and design

optimization. *Advances in computers and information in engineering research*, *1*, 73-95.

[68] Steuben, J. C., Iliopoulos, A. P., & Michopoulos, J. G. (2016). Discrete element modeling of particle-based additive manufacturing processes. *Computer Methods in Applied Mechanics and Engineering*, *305*, 537-561.

APPENDIX A: MESH STATISTICS

All the specimens were meshed taking into account an optimum mesh quality according to the geometry of the specimens. As every geometry had its unique infill features, each specimen was meshed differently depending on the geometry. A refined mesh is used on intricate geometry details using the adaptive mesh control in ANSYS©. However, due to differences in automatic meshing between solvers, in Abaqus©, local control was used to assign mesh properties to the geometry to match those of ANSYS©. This was done to ensure that both the solvers have similar mesh statistics. The mesh statistics and mesh plots from both the solvers is presented in the following sections.

A.1: Mesh Properties

Quadratic elements are used throughout all the simulations. However, due to meshing errors in some geometries in case of Abaqus©, linear hexahedral elements are used instead of tetrahedral elements. For example, composite model necessarily needed hexahedral elements. The mesh statistics from both the solvers are tabulated in Table A - 1.

Table A - 1: Mesh statistics for specimens

	ANSYS©			Abaqus©		
	Type	Nodes	Elements	Type	Nodes	Elements
Continuous (C)	Tetrahedral	36961	18762	Tetrahedral	33776	19455
Hexagonal Infill (HI)	Tetrahedral	19522	9397	Tetrahedral	50054	28285
Hexagonal Continuous (CHI)	Tetrahedral	13341	6582	Tetrahedral	18765	9667
Circular Straight Infill (CS)	Tetrahedral	26840	13026	Tetrahedral	39358	22276
Circular Continuous (CCS)	Tetrahedral	13280	6515	Tetrahedral	18141	9248
Circular Packed (CS)	Tetrahedral	237364	147796	Hexahedral	253152	217305
Linear Straight (LS)	Tetrahedral	321630	152453	Tetrahedral	235015	132826
Linear Crosshatch (LC)	Tetrahedral	148474	70412	Tetrahedral	198523	114529
Hilbert Curve (HC)	Tetrahedral	424719	212611	Tetrahedral	196970	119300
Infill less (I)	Tetrahedral	60437	36631	Hexahedral	24745	18448

Since composite analysis required the geometry to be meshed in hexahedral elements only, each of the specimens' geometries were manually partitioned and assigned a hexahedral element meshing. Further, each region was manually meshed, since automatic meshing could not be used. The mesh statistics for composite analyses are shown in Table A-2.

Table A - 2: Mesh statistics for geometries used in CLM analysis.

	Abaqus©		
	Type	Nodes	Elements
Continuous (C)	Hexahedral	50732	44020
Hexagonal Infill (HI)	Hexahedral	96140	81110
Hexagonal Continuous (CHI)	Hexahedral	72251	62366
Circular Straight Infill (CS)	Hexahedral	39282	30005
Circular Packed Infill (CS)	Hexahedral	61852	49248
Linear Straight Infill (LS)	Hexahedral	70397	51392
Linear Crosshatch Infill (LC)	Hexahedral	61205	45044
Hilbert Curve (HC)	Hexahedral	73953	56790
Infill less (I)	Hexahedral	15005	10800

A.2: Mesh Plots

Figures A-1 to A-10 depict the mesh plots used in ANSYS©.

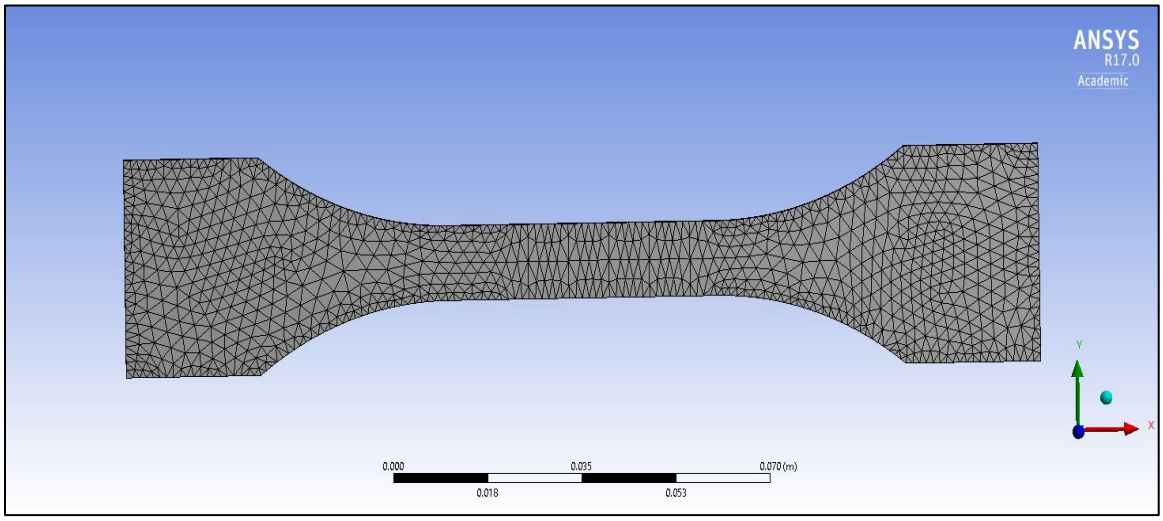

Figure A - 1: ANSYS© mesh plot for C specimen.

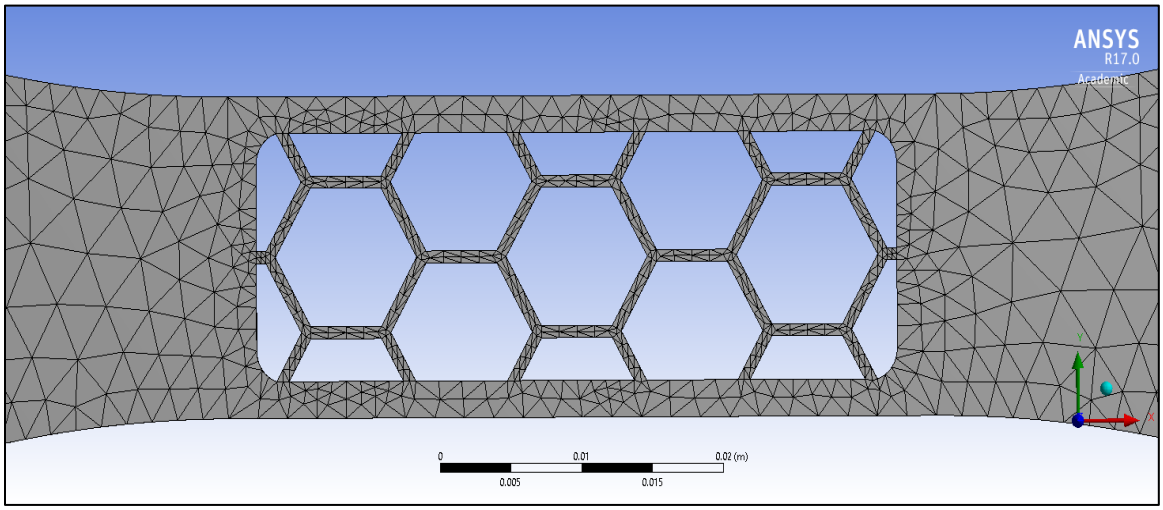

Figure A - 2: ANSYS© mesh plot for HI specimen.

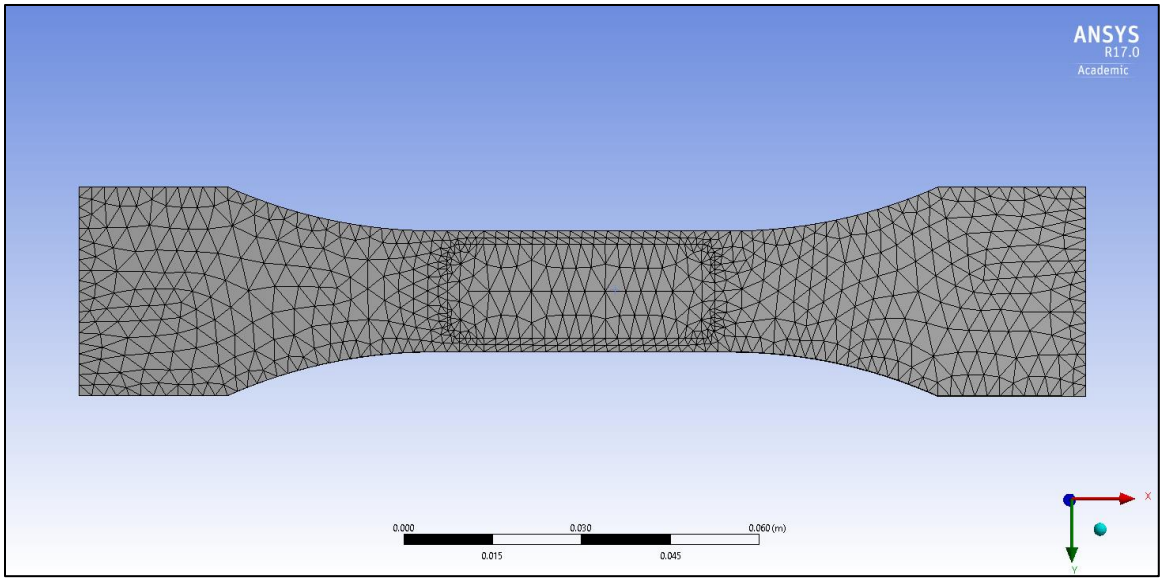

Figure A - 3: ANSYS© mesh plot for CHI specimen.

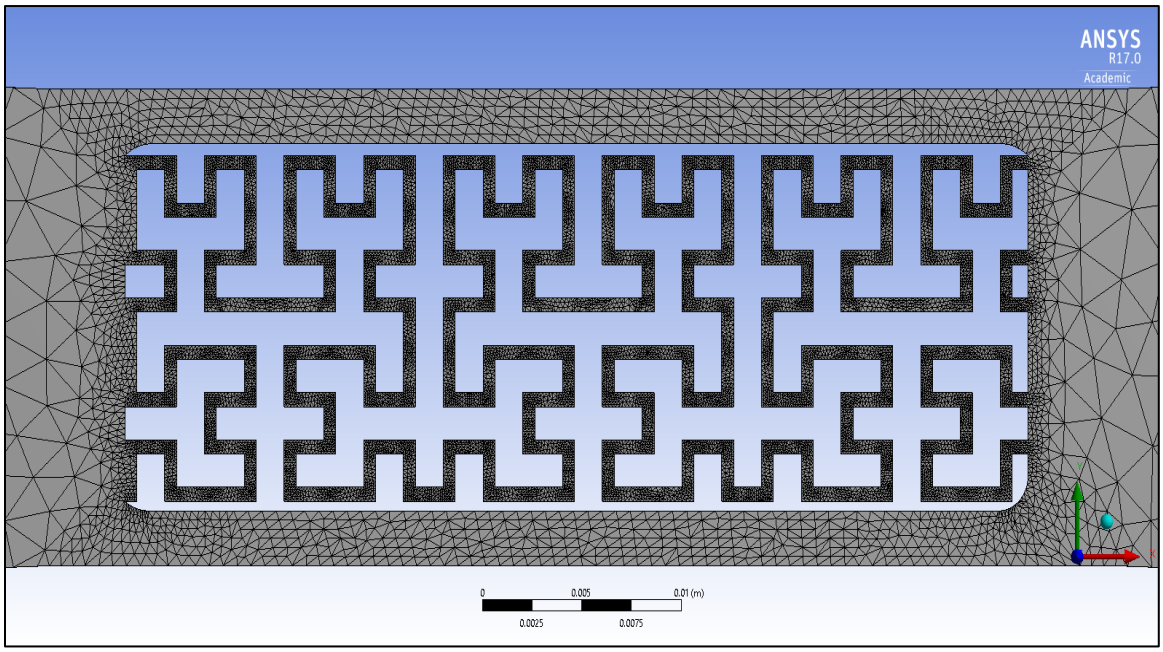

Figure A - 4: ANSYS© mesh plot for HC specimen.

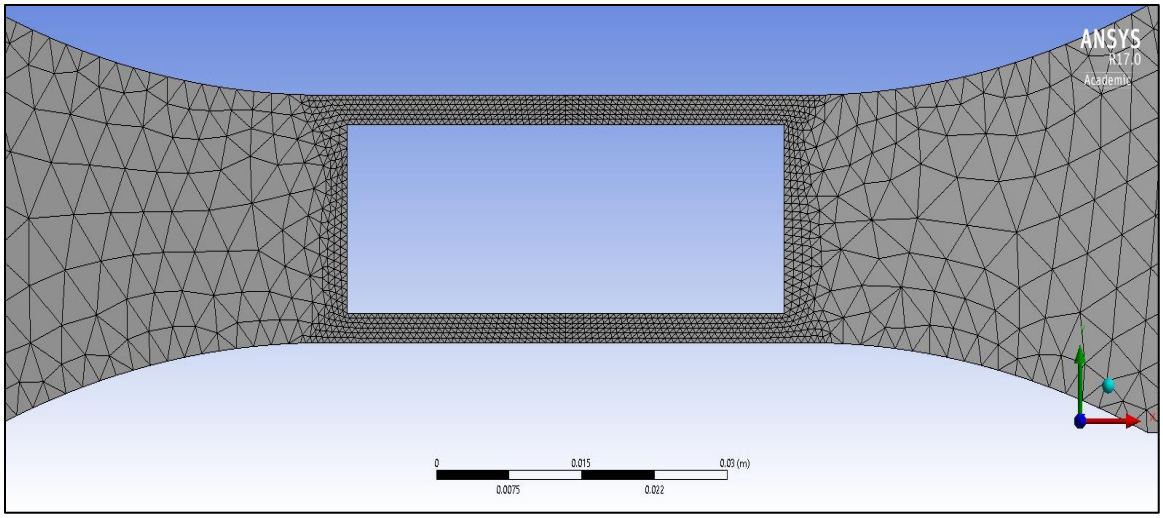

Figure A - 5: ANSYS© mesh plot for I specimen.

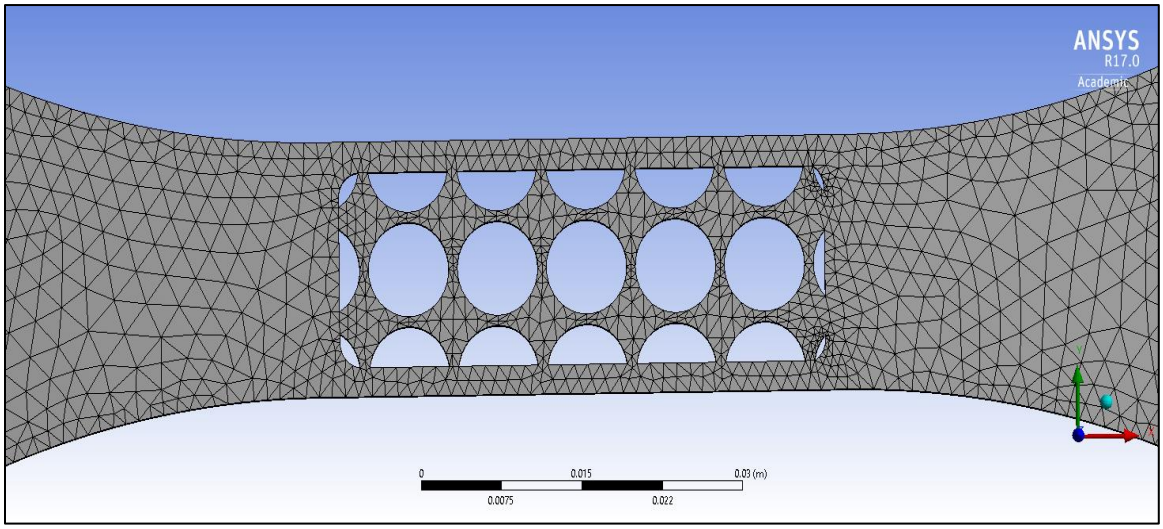

Figure A - 6: ANSYS© mesh plot for CS specimen.

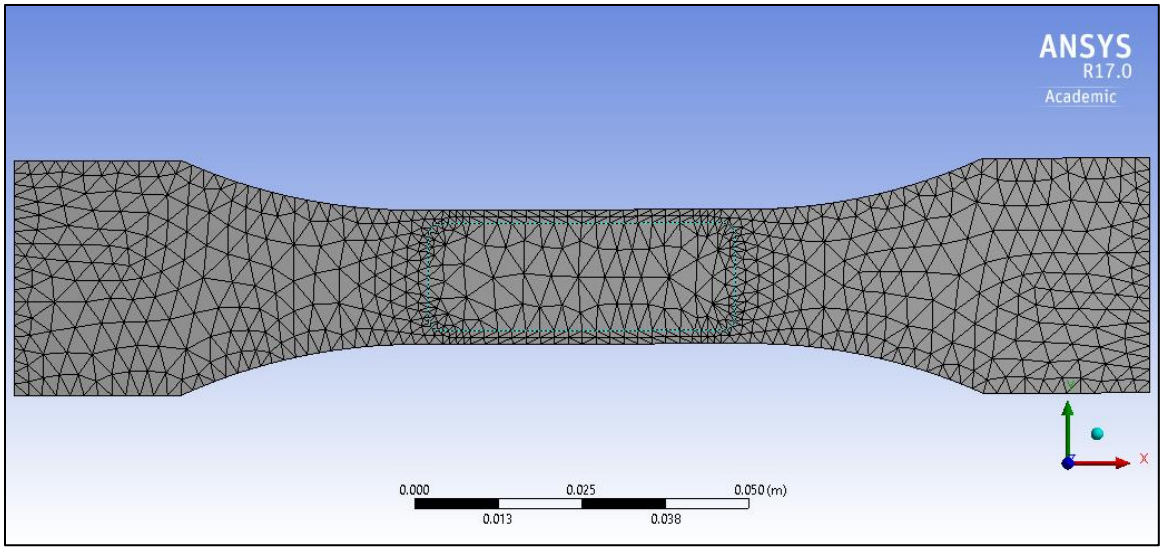

Figure A - 7: ANSYS© mesh plot for CCS specimen.

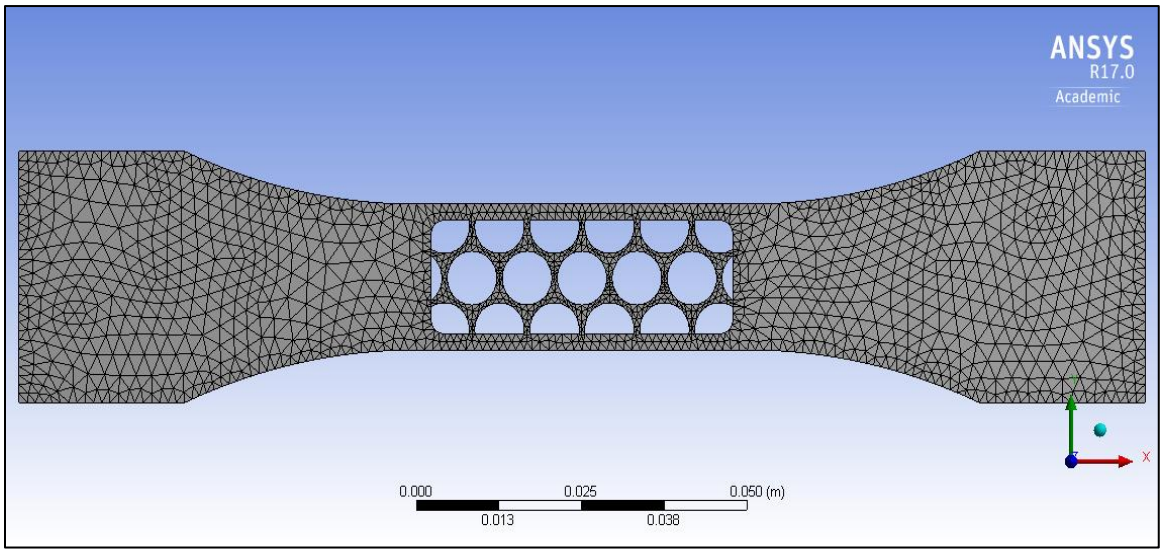

Figure A - 8: ANSYS© mesh plot for CP specimen.

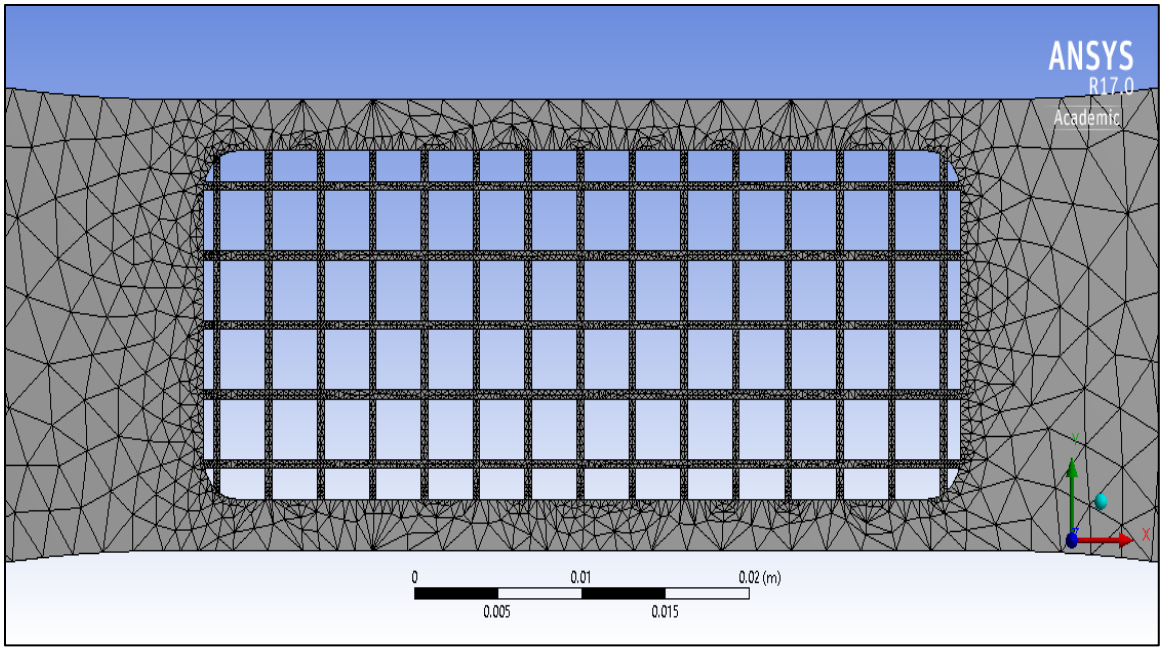

Figure A - 9: ANSYS© mesh plot for LS specimen.

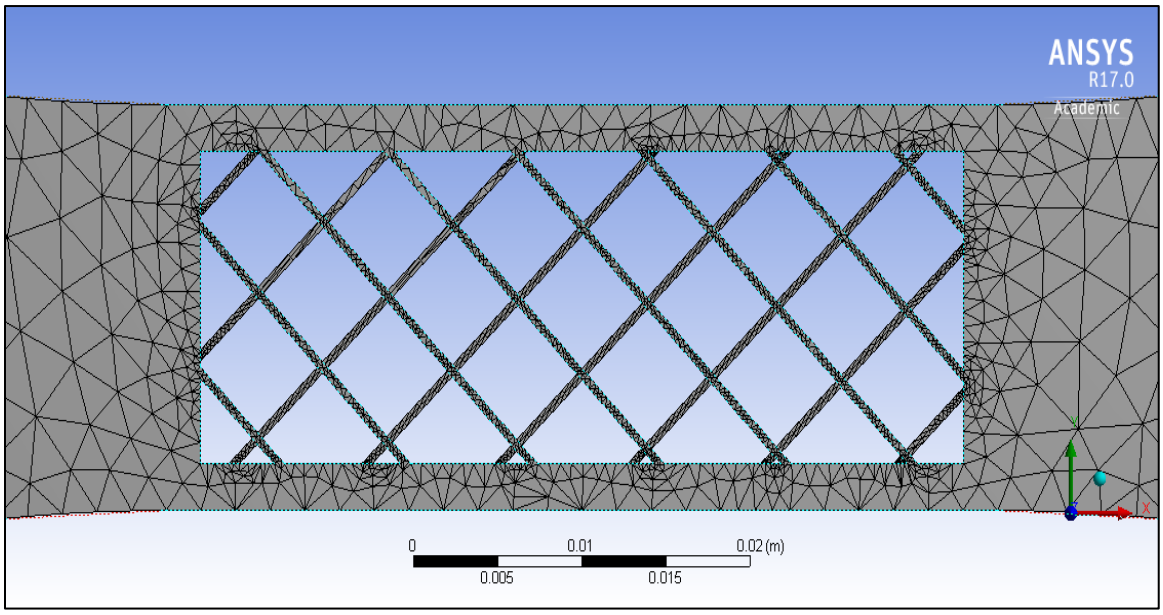

Figure A - 10: ANSYS© mesh plot for LC specimen.

Figures A-11 to A-29 depict the mesh plots used in Abqaus©.

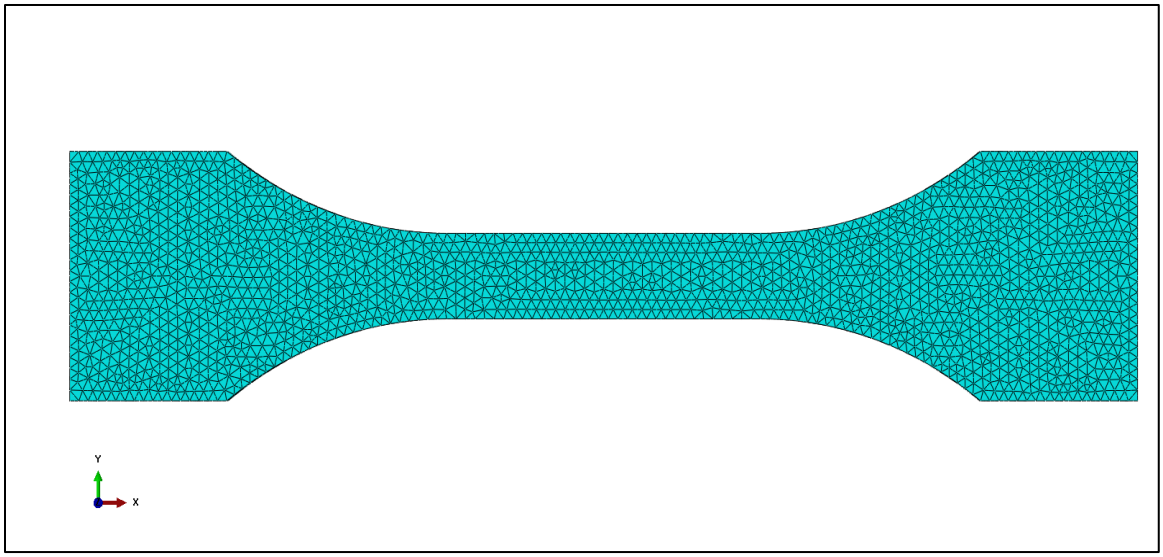

Figure A - 11: Abaqus© mesh plot for C specimen.

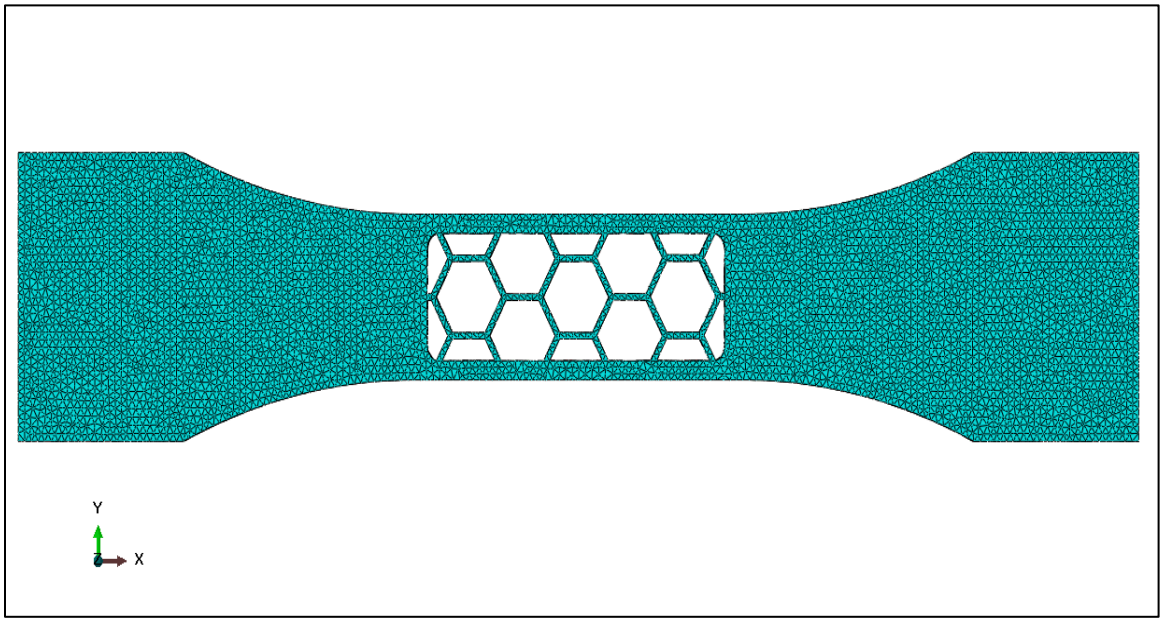

Figure A - 12: Abaqus© mesh plot for HI specimen.

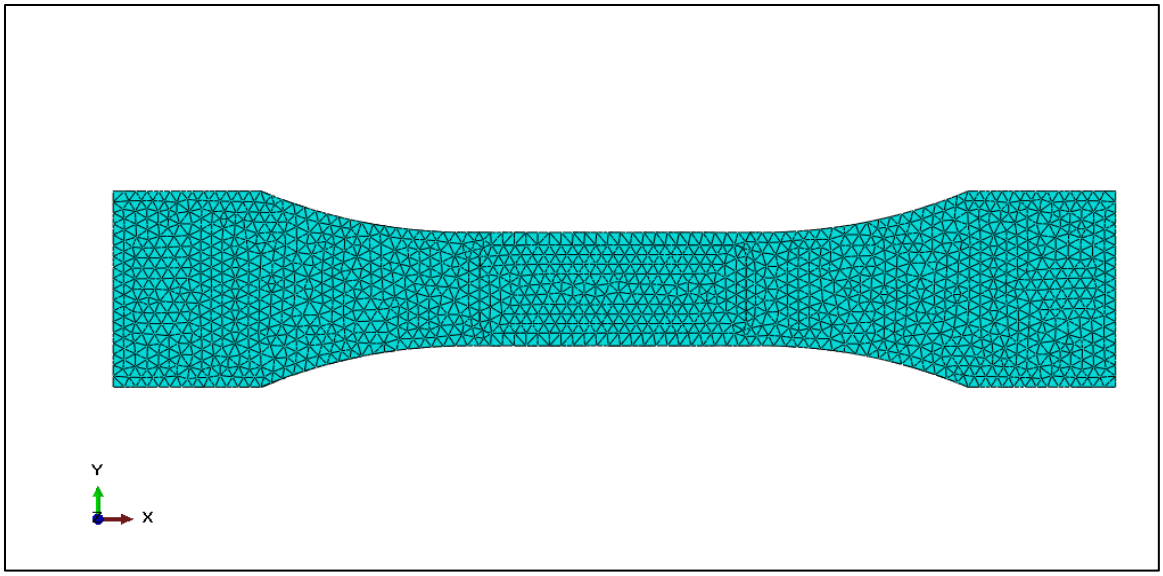

Figure A - 13: Abaqus© mesh plot for CHI specimen.

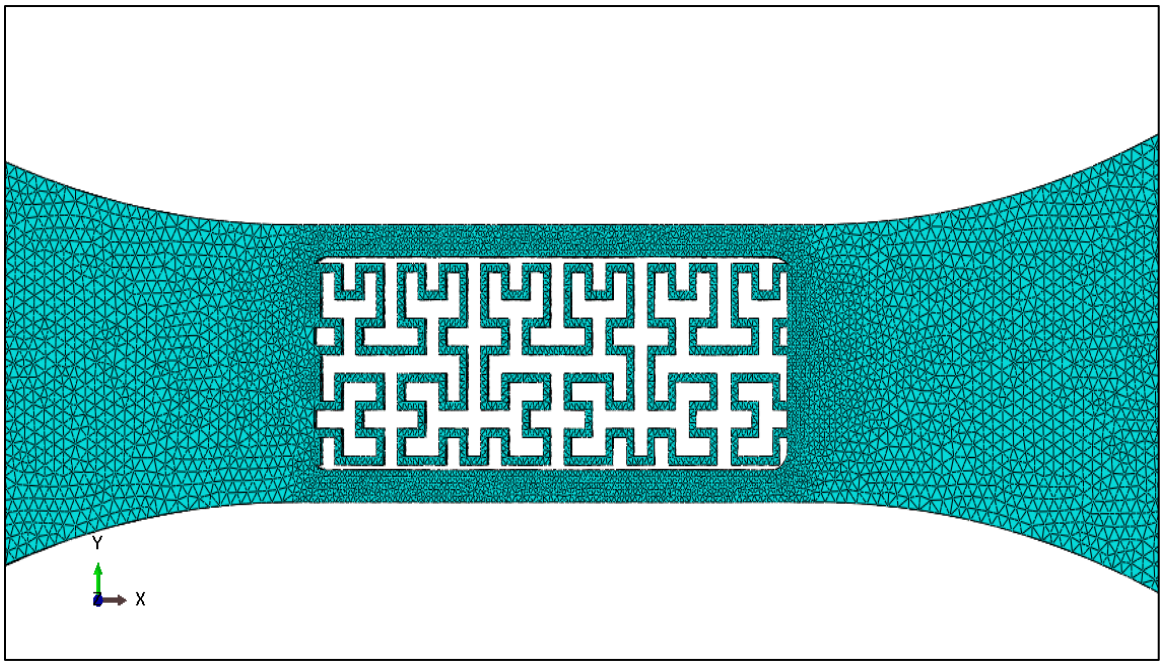

Figure A - 14: Abaqus© mesh plot for HC specimen.

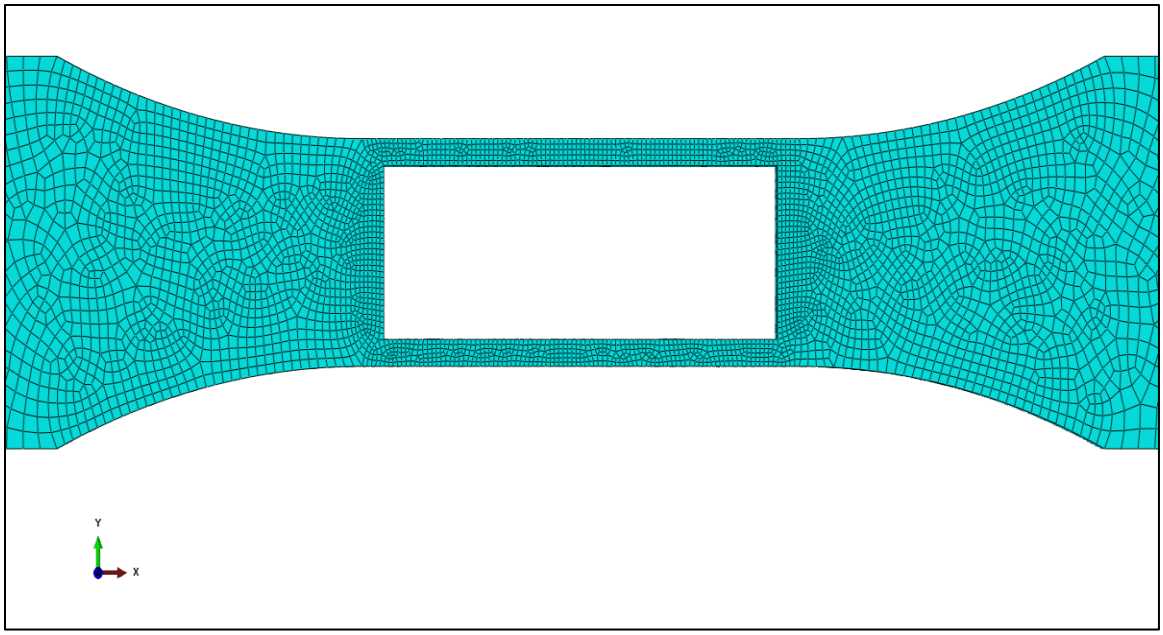

Figure A - 15: Abaqus© mesh plot for I specimen.

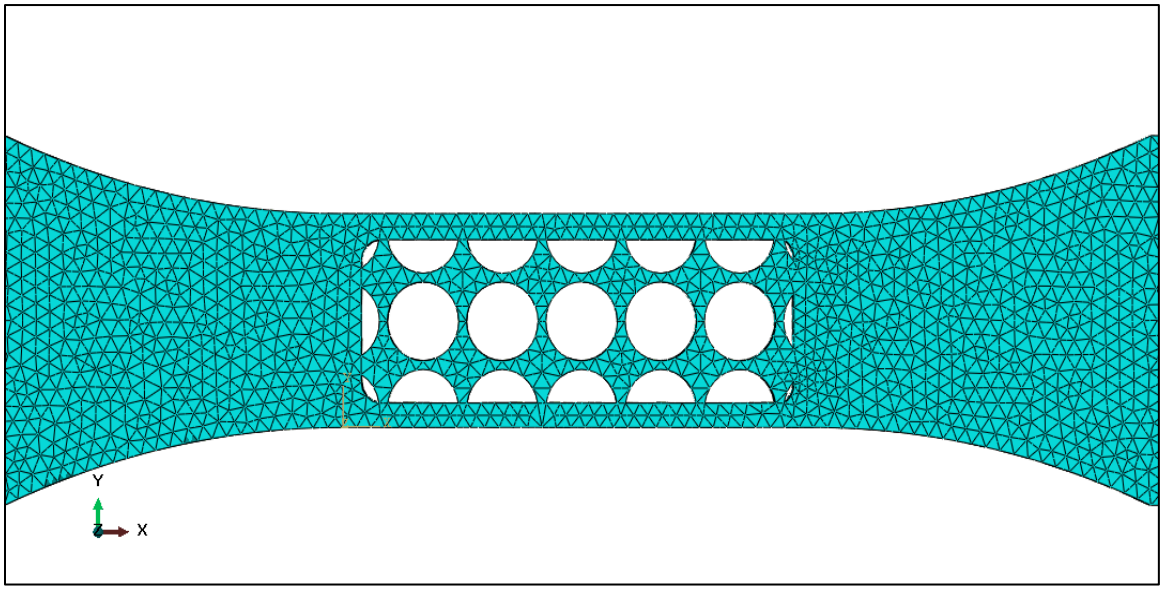

Figure A - 16: Abaqus© mesh plot for CS specimen.

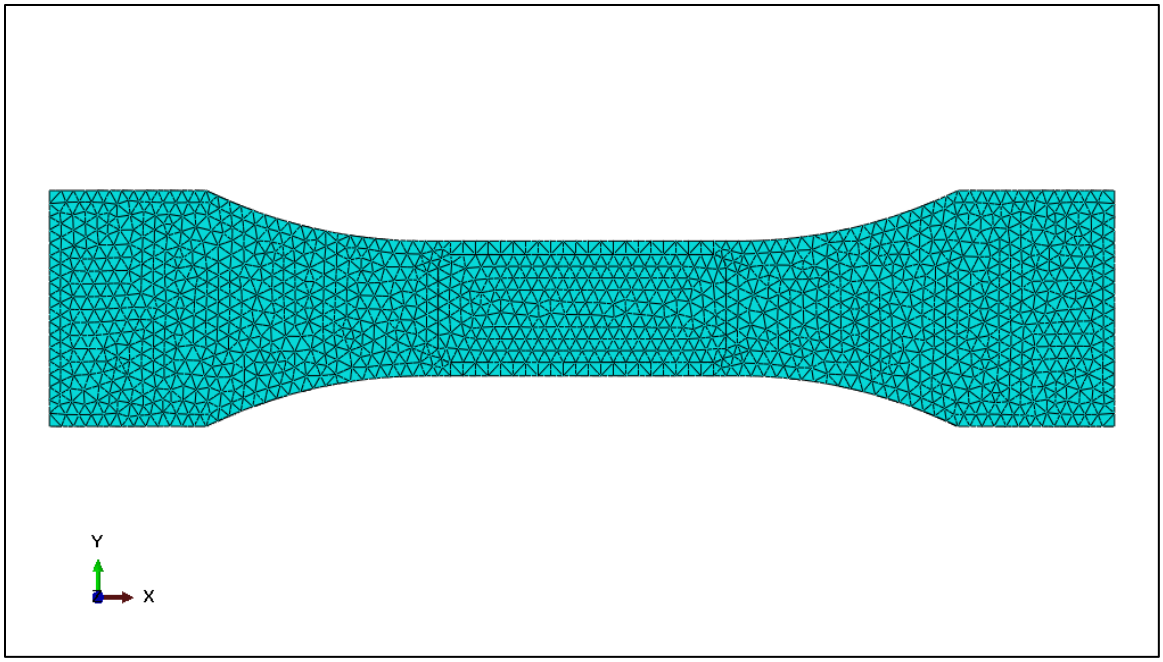

Figure A - 17: Abaqus© mesh plot for CCS specimen.

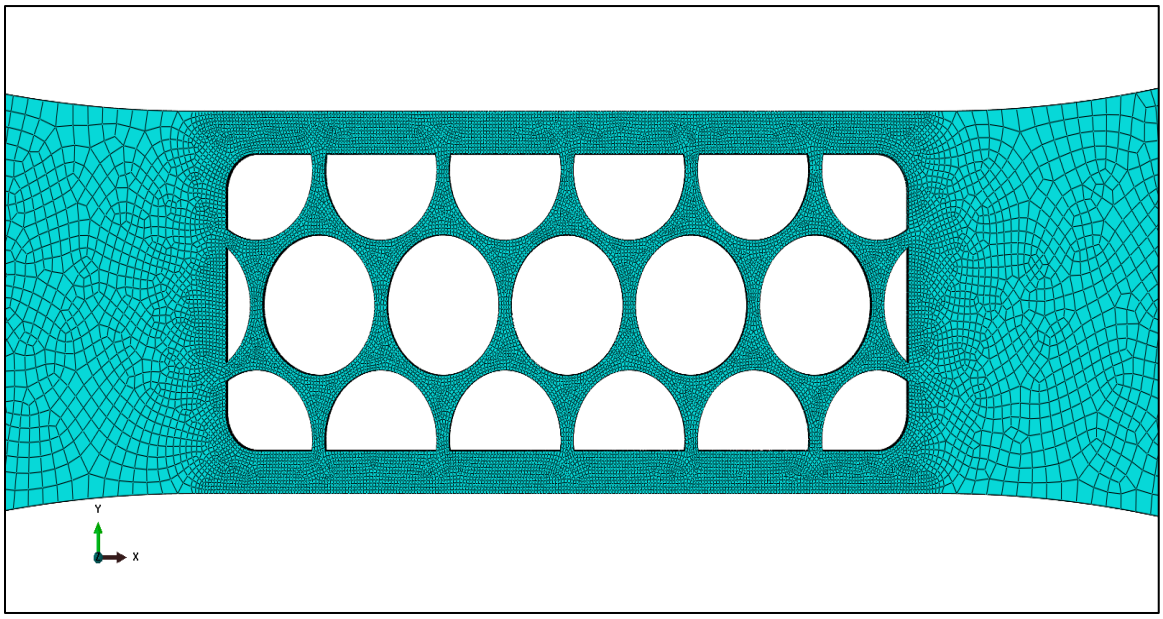

Figure A - 18: Abaqus© mesh plot for CP specimen.

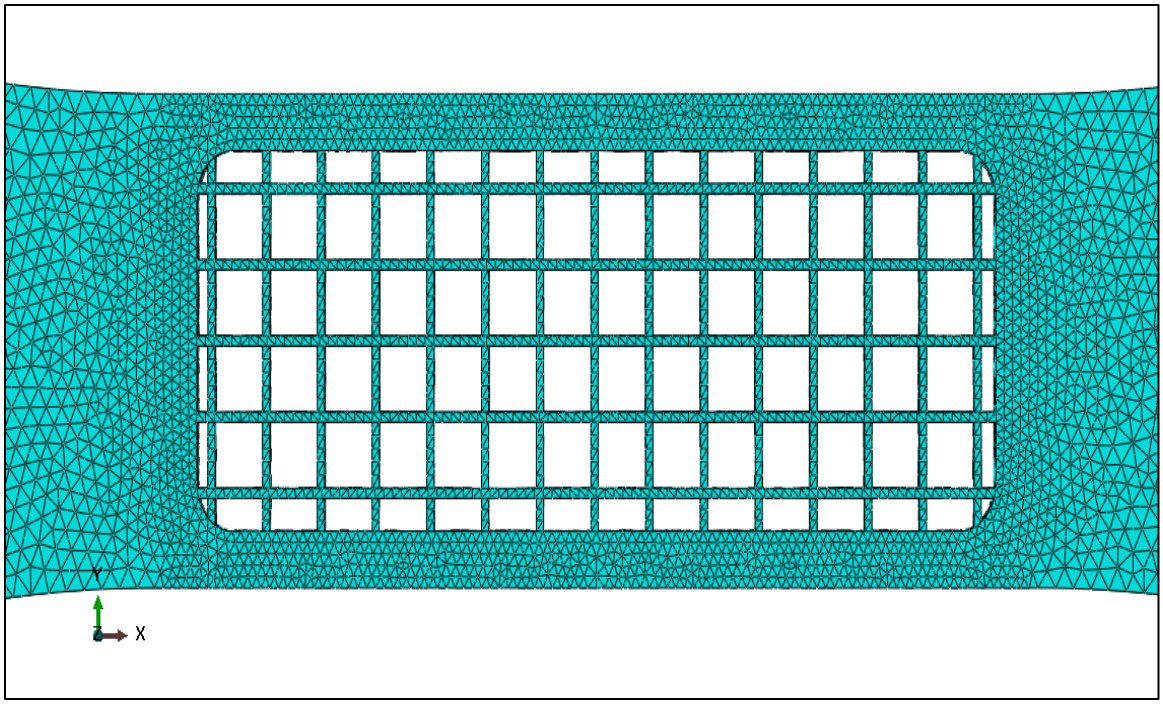

Figure A - 19: Abaqus© mesh plot for LS specimen.

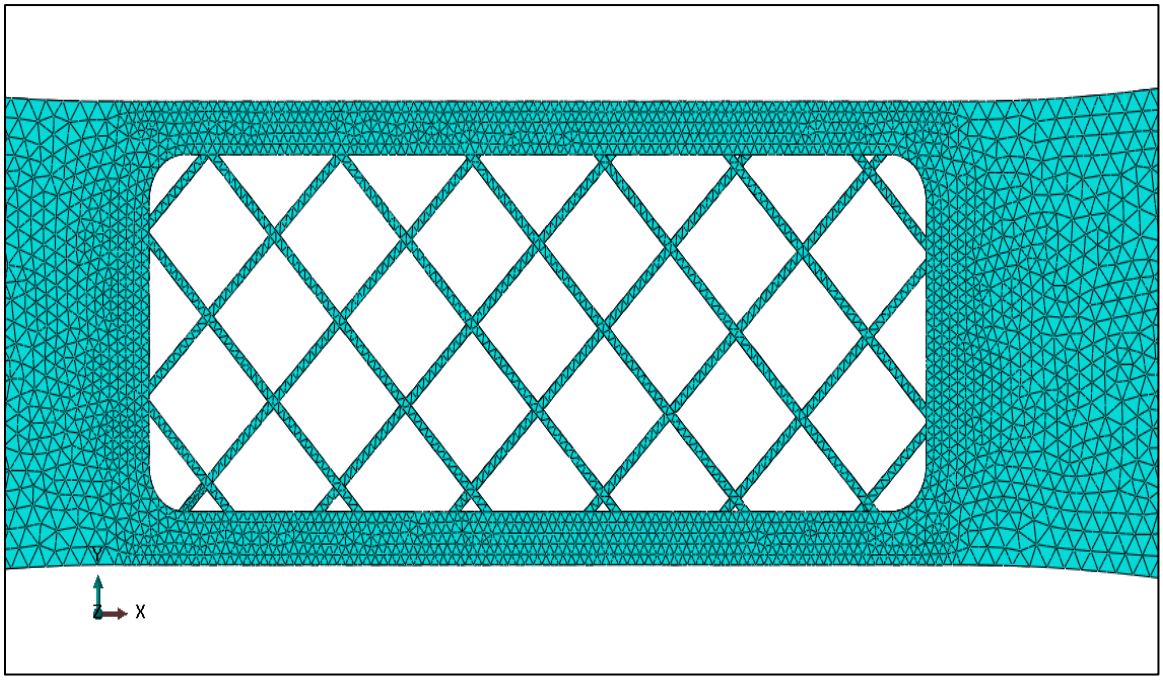

Figure A - 20: Abaqus© mesh plot for LC specimen.

Since CLM required, a hexahedral mesh, the geometries were manually mesh with hexahedral elements. Figures A-21 to A-29 show the mesh plots used with CLM.

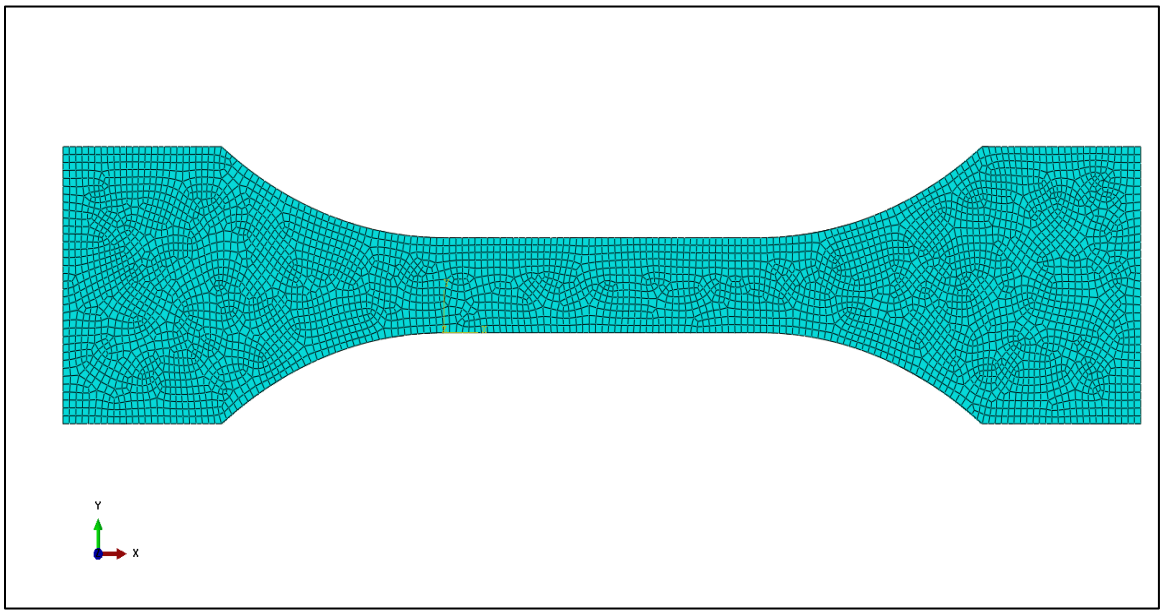

Figure A - 21: Abaqus© mesh plot for C specimen for CLM analysis.

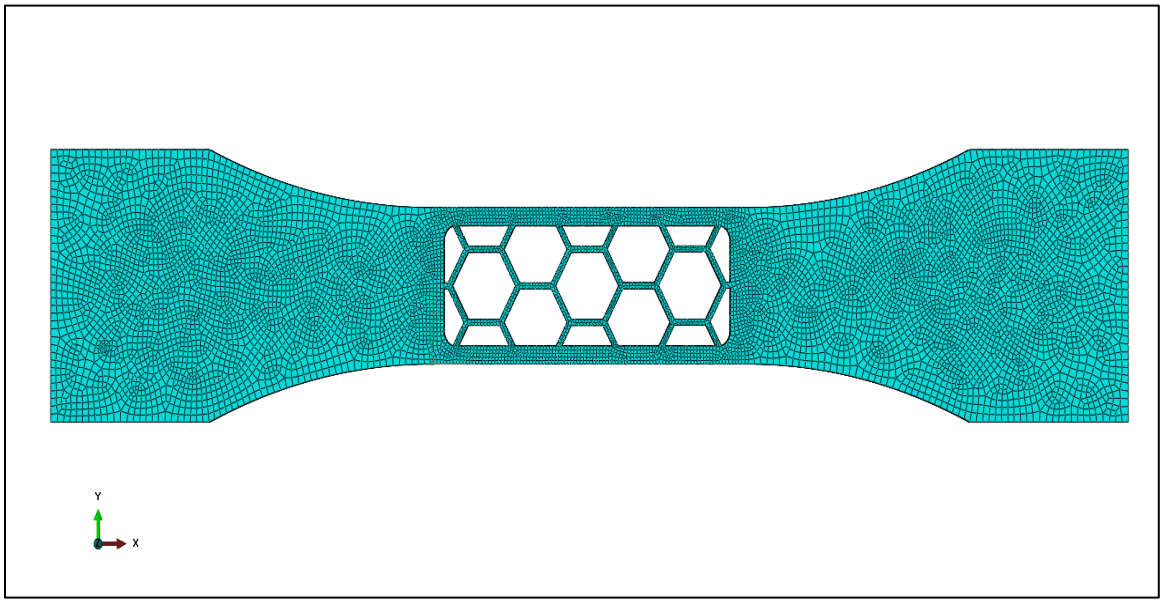

Figure A - 22: Abaqus© mesh plot for HI specimen for CLM analysis.

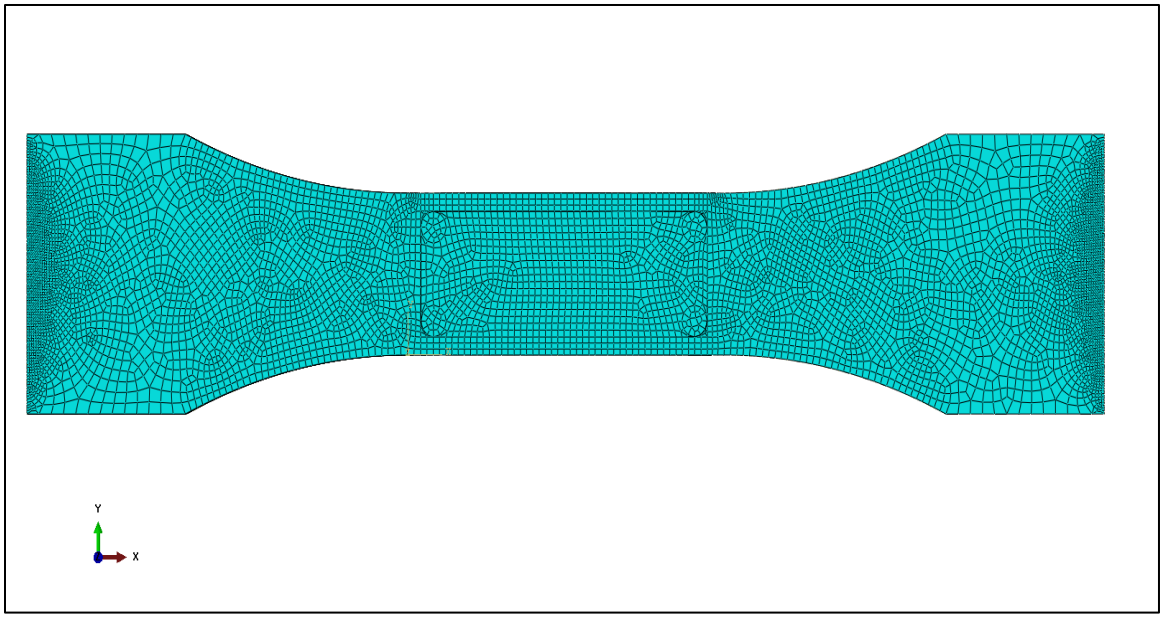

Figure A - 23: Abaqus© mesh plot for CHI specimen for CLM analysis.

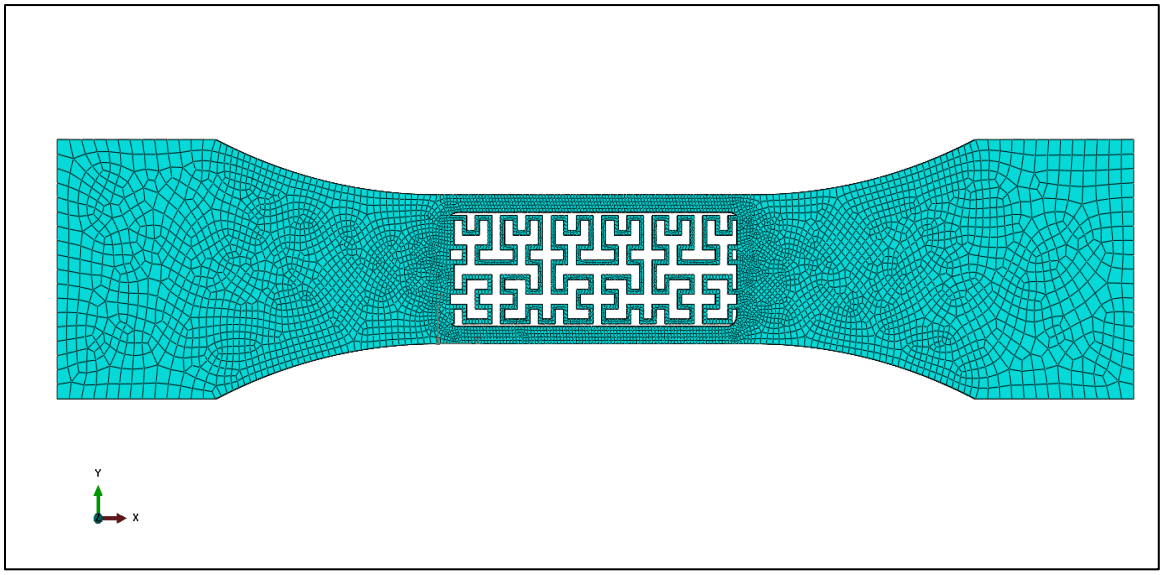

Figure A - 24: Abaqus© mesh plot for HC specimen for CLM analysis.

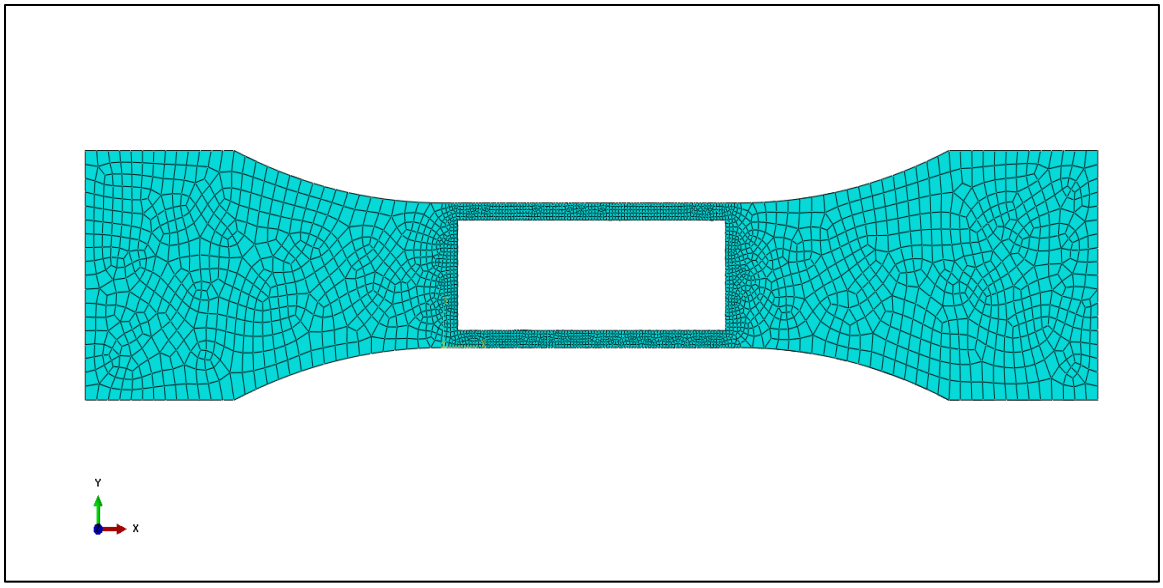

Figure A - 25: Abaqus© mesh plot for I specimen for CLM analysis.

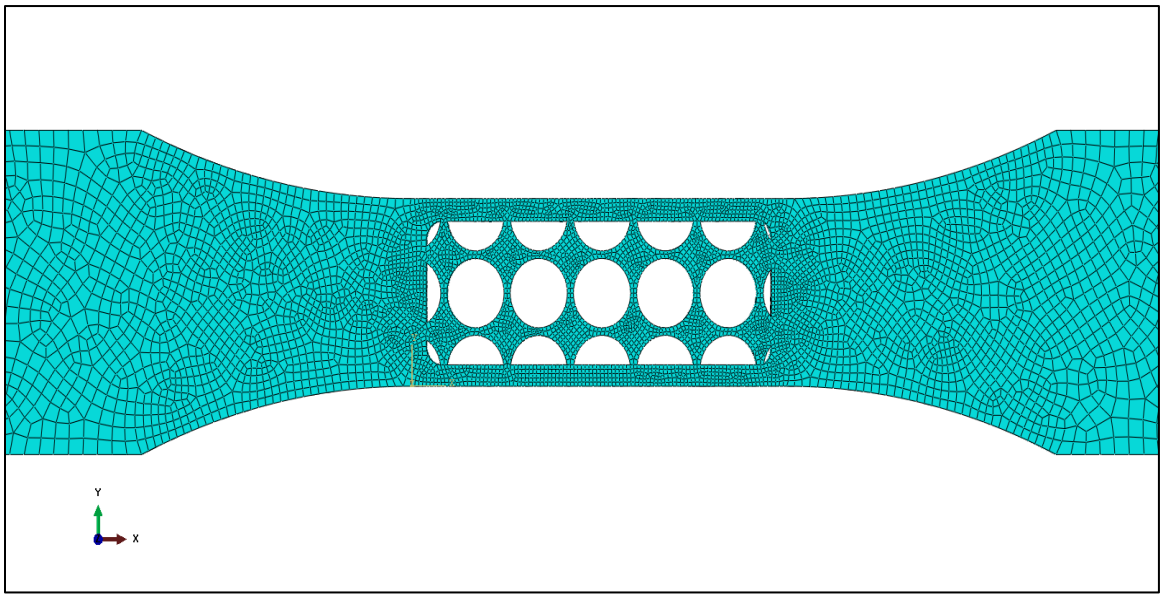

Figure A - 26: Abaqus© mesh plot for CS specimen for CLM analysis.

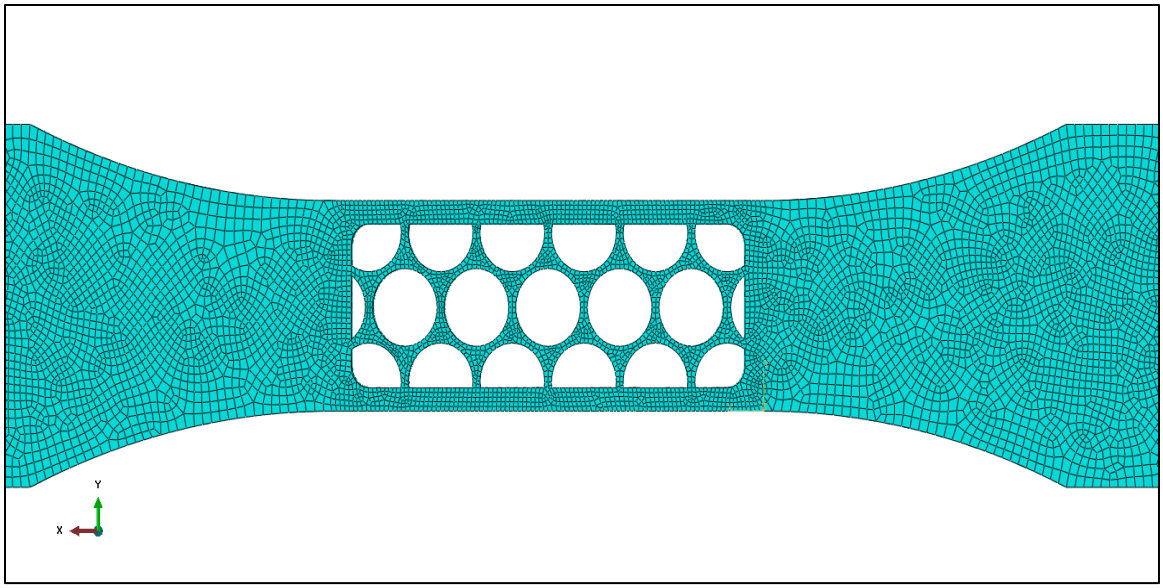

Figure A - 27: Abaqus© mesh plot for CP specimen for CLM analysis.

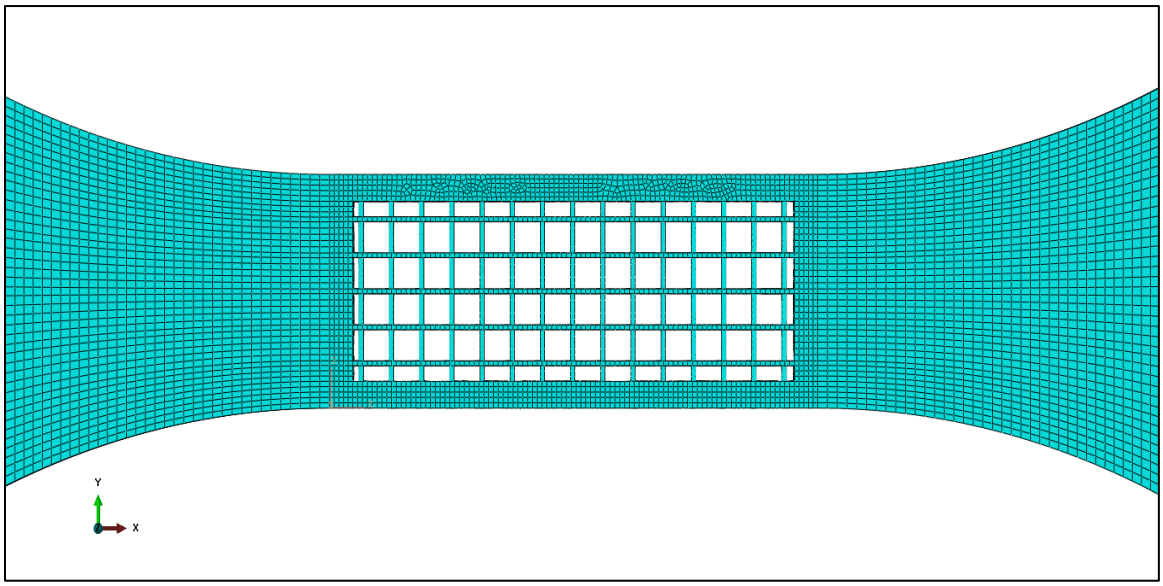

Figure A - 28: Abaqus© mesh plot for LS specimen for CLM analysis.

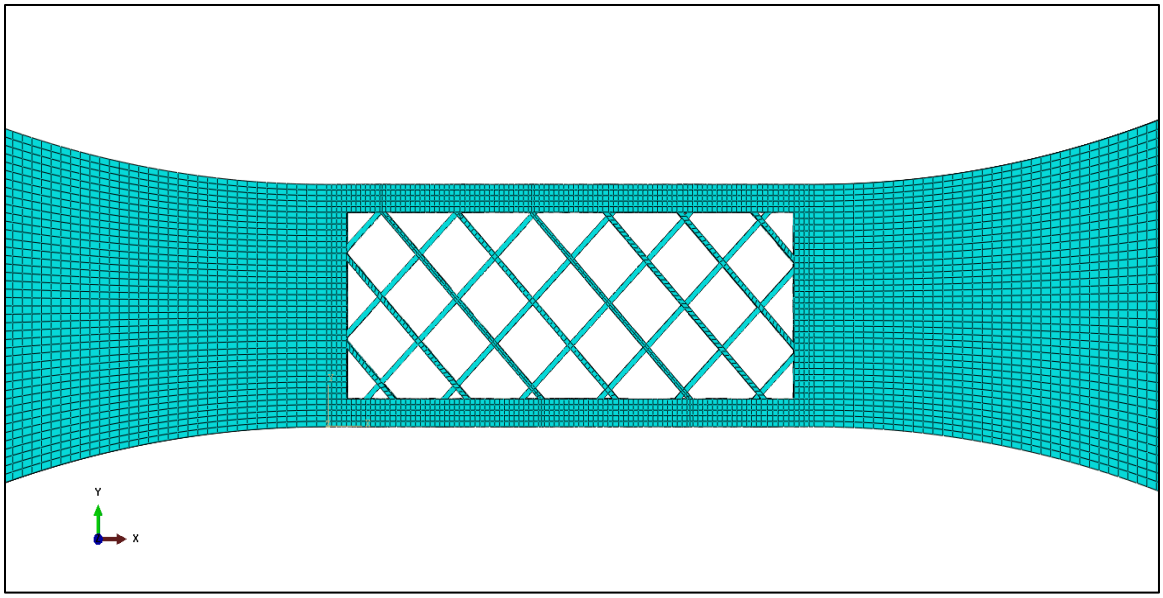

Figure A - 29: Abaqus© mesh plot for LC specimen for CLM analysis.

APPENDIX B: NORMAL STRESS RESULTS

This section presents the stress values from experimental data as well as different FEA simulations. The stress values at yield strain, at 2% strain and 1% strain are presented for experimental and FEA results. Table B-1 shows the stress values for BIM results. Table B-2 shows the stress values for DIM results. Table B-3 shows the stress values for ODM results. Table B-4 shows the stress values for CLM results.

Table B - 1: Normal Stress - Experimental and BIM results.

		Experimental	ANSYS©	ABAQUS©
Continuous (C)	Yield Stress (σ_y) (MPa)	30	45	43
	Stress at 2% strain ($\sigma_{2\%}$) (MPa)	18.5	22.8	22
	Stress at 1% strain ($\sigma_{1\%}$) (MPa)	9.6	12	11.9
Hexagonal Infill (HI)	Yield Stress (σ_y) (MPa)	27.9	44.4	43
	Stress at 2% strain ($\sigma_{2\%}$) (MPa)	24	32	32
	Stress at 1% strain ($\sigma_{1\%}$) (MPa)	12.1	15.9	16
Hexagonal Continuous (CHI)	Yield Stress (σ_y) (MPa)	16.2	23.3	26
	Stress at 2% strain ($\sigma_{2\%}$) (MPa)	15.7	21.5	23
	Stress at 1% strain ($\sigma_{1\%}$) (MPa)	9.9	13.8	14.2
Circular Straight (CS)	Yield Stress (σ_y) (MPa)	28.6	62.2	63.4
	Stress at 2% strain ($\sigma_{2\%}$) (MPa)	27.4	52.2	51
	Stress at 1% strain ($\sigma_{1\%}$) (MPa)	16.4	26.7	25.8
Circular Continuous (CCS)	Yield Stress (σ_y) (MPa)	21.2	27.8	28.5
	Stress at 2% strain ($\sigma_{2\%}$) (MPa)	18.9	20	22
	Stress at 1% strain ($\sigma_{1\%}$) (MPa)	8.2	12.5	11.9
Circular Packed (CP)	Yield Stress (σ_y) (MPa)	26.5	50	51
	Stress at 2% strain ($\sigma_{2\%}$) (MPa)	22.7	37.6	38
	Stress at 1% strain ($\sigma_{1\%}$) (MPa)	11.6	18.7	19.5
Hilbert Curve (HC)	Yield Stress (σ_y) (MPa)	29.1	35.2	35
	Stress at 2% strain ($\sigma_{2\%}$) (MPa)	25.3	29.4	30
	Stress at 1% strain ($\sigma_{1\%}$) (MPa)	14.2	15.2	15.5
Linear Straight (LS)	Yield Stress (σ_y) (MPa)	24.6	45.5	44.2
	Stress at 2% strain ($\sigma_{2\%}$) (MPa)	22.6	40	41.5
	Stress at 1% strain ($\sigma_{1\%}$) (MPa)	14.7	20.3	21.2
Linear CrossHatch (LC)	Yield Stress (σ_y) (MPa)	22.8	42	43
	Stress at 2% strain ($\sigma_{2\%}$) (MPa)	21.7	28	28.8
	Stress at 1% strain ($\sigma_{1\%}$) (MPa)	11	14.3	15
Infill-less (I)	Yield Stress (σ_y) (MPa)	32.9	33.7	34.8
	Stress at 2% strain ($\sigma_{2\%}$) (MPa)	29	27.7	28
	Stress at 1% strain ($\sigma_{1\%}$) (MPa)	15.8	14.3	14

Table B - 2: Normal Stress - Experimental and DIM results.

		Experimental	ANSYS©	ABAQUS©
Continuous (C)	Yield Stress (σ_y) (MPa)	30	17.5	17
	Stress at 2% strain ($\sigma_{2\%}$) (MPa)	18.5	9.6	8.6
	Stress at 1% strain ($\sigma_{1\%}$) (MPa)	9.6	5.3	6
Hexagonal Infill (HI)	Yield Stress (σ_y) (MPa)	27.9	22.8	21.8
	Stress at 2% strain ($\sigma_{2\%}$) (MPa)	24	16	15.8
	Stress at 1% strain ($\sigma_{1\%}$) (MPa)	12.1	8	7.9
Hexagonal Continuous (CHI)	Yield Stress (σ_y) (MPa)	16.2	15	16.4
	Stress at 2% strain ($\sigma_{2\%}$) (MPa)	15.7	14	14.4
	Stress at 1% strain ($\sigma_{1\%}$) (MPa)	9.9	8	8.5
Circular Straight (CS)	Yield Stress (σ_y) (MPa)	28.6	34.8	32
	Stress at 2% strain ($\sigma_{2\%}$) (MPa)	27.4	29	29.5
	Stress at 1% strain ($\sigma_{1\%}$) (MPa)	16.4	14.5	14.2
Circular Continuous (CCS)	Yield Stress (σ_y) (MPa)	21.2	15.8	16.9
	Stress at 2% strain ($\sigma_{2\%}$) (MPa)	18.9	13.5	14.4
	Stress at 1% strain ($\sigma_{1\%}$) (MPa)	8.2	7.1	7.6
Circular Packed (CP)	Yield Stress (σ_y) (MPa)	26.5	28.7	29.2
	Stress at 2% strain ($\sigma_{2\%}$) (MPa)	22.7	21.9	22.1
	Stress at 1% strain ($\sigma_{1\%}$) (MPa)	11.6	10.8	11.3
Hilbert Curve (HC)	Yield Stress (σ_y) (MPa)	29.1	17.5	17.2
	Stress at 2% strain ($\sigma_{2\%}$) (MPa)	25.3	14.8	15.4
	Stress at 1% strain ($\sigma_{1\%}$) (MPa)	14.2	7.7	8.1
Linear Straight (LS)	Yield Stress (σ_y) (MPa)	24.6	22.7	22.3
	Stress at 2% strain ($\sigma_{2\%}$) (MPa)	22.6	20.1	19.4
	Stress at 1% strain ($\sigma_{1\%}$) (MPa)	14.7	10.1	9.8
Linear CrossHatch (LC)	Yield Stress (σ_y) (MPa)	22.8	21.1	22.2
	Stress at 2% strain ($\sigma_{2\%}$) (MPa)	21.7	14.3	15.3
	Stress at 1% strain ($\sigma_{1\%}$) (MPa)	11	7.3	8.1
Infill-less (I)	Yield Stress (σ_y) (MPa)	32.9	22.8	21.1
	Stress at 2% strain ($\sigma_{2\%}$) (MPa)	29	18.2	17.3
	Stress at 1% strain ($\sigma_{1\%}$) (MPa)	15.8	8.9	7.8

Table B - 3: Normal Stress - Experimental and ODM results.

		Experimental	ANSYS©	ABAQUS©
Continuous (C)	Yield Stress (σ_y) (MPa)	30	21.9	22.5
	Stress at 2% strain ($\sigma_{2\%}$) (MPa)	18.5	11.4	11.9
	Stress at 1% strain ($\sigma_{1\%}$) (MPa)	9.6	5.8	6.1
Hexagonal Infill (HI)	Yield Stress (σ_y) (MPa)	27.9	25.4	25.6
	Stress at 2% strain ($\sigma_{2\%}$) (MPa)	24	18.3	18.9
	Stress at 1% strain ($\sigma_{1\%}$) (MPa)	12.1	9.5	9.6
Hexagonal Continuous (CHI)	Yield Stress (σ_y) (MPa)	16.2	19.3	19
	Stress at 2% strain ($\sigma_{2\%}$) (MPa)	15.7	17.2	17
	Stress at 1% strain ($\sigma_{1\%}$) (MPa)	9.9	8.7	8.5
Circular Straight (CS)	Yield Stress (σ_y) (MPa)	28.6	31.8	30.7
	Stress at 2% strain ($\sigma_{2\%}$) (MPa)	27.4	28	27.5
	Stress at 1% strain ($\sigma_{1\%}$) (MPa)	16.4	14.3	14
Circular Packed (CP)	Yield Stress (σ_y) (MPa)	26.5	31.7	25.9
	Stress at 2% strain ($\sigma_{2\%}$) (MPa)	22.7	23.9	19.2
	Stress at 1% strain ($\sigma_{1\%}$) (MPa)	11.6	12.2	9.7
Hilbert Curve (HC)	Yield Stress (σ_y) (MPa)	29.1	19.2	19.6
	Stress at 2% strain ($\sigma_{2\%}$) (MPa)	25.3	15.7	16.1
	Stress at 1% strain ($\sigma_{1\%}$) (MPa)	14.2	7.9	8.5
Linear Straight (LS)	Yield Stress (σ_y) (MPa)	24.6	25.1	25.9
	Stress at 2% strain ($\sigma_{2\%}$) (MPa)	22.6	22	22.7
	Stress at 1% strain ($\sigma_{1\%}$) (MPa)	14.7	11	11.9
Linear CrossHatch (LC)	Yield Stress (σ_y) (MPa)	22.8	23.9	23.5
	Stress at 2% strain ($\sigma_{2\%}$) (MPa)	21.7	16.5	16.1
	Stress at 1% strain ($\sigma_{1\%}$) (MPa)	11	8.3	7.7
Infill-less (I)	Yield Stress (σ_y) (MPa)	32.9	18.4	19.7
	Stress at 2% strain ($\sigma_{2\%}$) (MPa)	29	16.1	16.2
	Stress at 1% strain ($\sigma_{1\%}$) (MPa)	15.8	7.9	8

Table B - 4: Normal Stress - Experimental and CLM results.

		Experimental	ABAQUS©
Continuous (C)	Yield Stress (σ_y) (MPa)	30	20.7
	Stress at 2% strain ($\sigma_{2\%}$) (MPa)	18.5	10.4
	Stress at 1% strain ($\sigma_{1\%}$) (MPa)	9.6	5.2
Hexagonal Infill (HI)	Yield Stress (σ_y) (MPa)	27.9	24.2
	Stress at 2% strain ($\sigma_{2\%}$) (MPa)	24	17.5
	Stress at 1% strain ($\sigma_{1\%}$) (MPa)	12.1	8.8
Hexagonal Continuous (CHI)	Yield Stress (σ_y) (MPa)	16.2	22
	Stress at 2% strain ($\sigma_{2\%}$) (MPa)	15.7	19.6
	Stress at 1% strain ($\sigma_{1\%}$) (MPa)	9.9	9.8
Circular Straight (CS)	Yield Stress (σ_y) (MPa)	28.6	31.4
	Stress at 2% strain ($\sigma_{2\%}$) (MPa)	27.4	26.4
	Stress at 1% strain ($\sigma_{1\%}$) (MPa)	16.4	13.2
Circular Packed (CP)	Yield Stress (σ_y) (MPa)	26.5	24
	Stress at 2% strain ($\sigma_{2\%}$) (MPa)	22.7	18.2
	Stress at 1% strain ($\sigma_{1\%}$) (MPa)	11.6	9.2
Hilbert Curve (HC)	Yield Stress (σ_y) (MPa)	29.1	18.4
	Stress at 2% strain ($\sigma_{2\%}$) (MPa)	25.3	14.9
	Stress at 1% strain ($\sigma_{1\%}$) (MPa)	14.2	7.3
Linear Straight (LS)	Yield Stress (σ_y) (MPa)	24.6	22.8
	Stress at 2% strain ($\sigma_{2\%}$) (MPa)	22.6	20.3
	Stress at 1% strain ($\sigma_{1\%}$) (MPa)	14.7	10.3
Linear CrossHatch (LC)	Yield Stress (σ_y) (MPa)	22.8	23.3
	Stress at 2% strain ($\sigma_{2\%}$) (MPa)	21.7	15.7
	Stress at 1% strain ($\sigma_{1\%}$) (MPa)	11	7.8
Infill-less (I)	Yield Stress (σ_y) (MPa)	32.9	21.1
	Stress at 2% strain ($\sigma_{2\%}$) (MPa)	29	17.3
	Stress at 1% strain ($\sigma_{1\%}$) (MPa)	15.8	8.7

APPENDIX C: SIMULATION RESULTS – ANSYS©

C.1: BIM Results

This section presents the BIM analysis-normal stress plots of all the specimens from ANSYS©. The body of thesis has plots zoomed in on the infill patterns, the entire body stress plots are shown in this section. Figures C-1 to C-27 show the stress plots from the analyses. Figures C-1 to C-9 show ANSYS© normal stress plots using BIM.

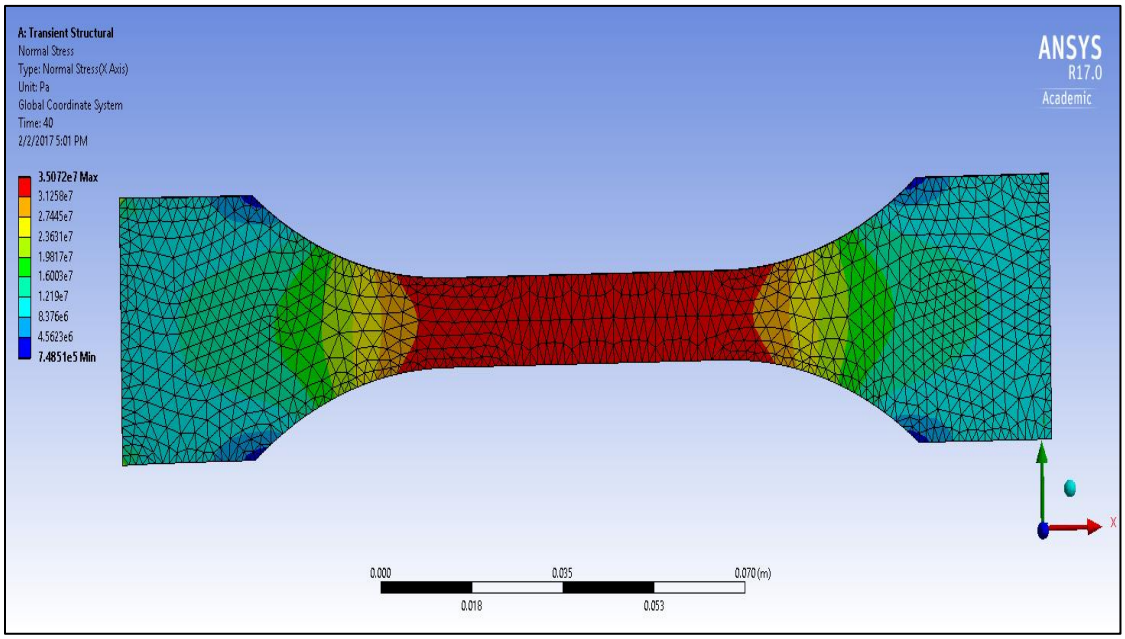

Figure C - 1: ANSYS© Normal Stress plot for C specimen using BIM.

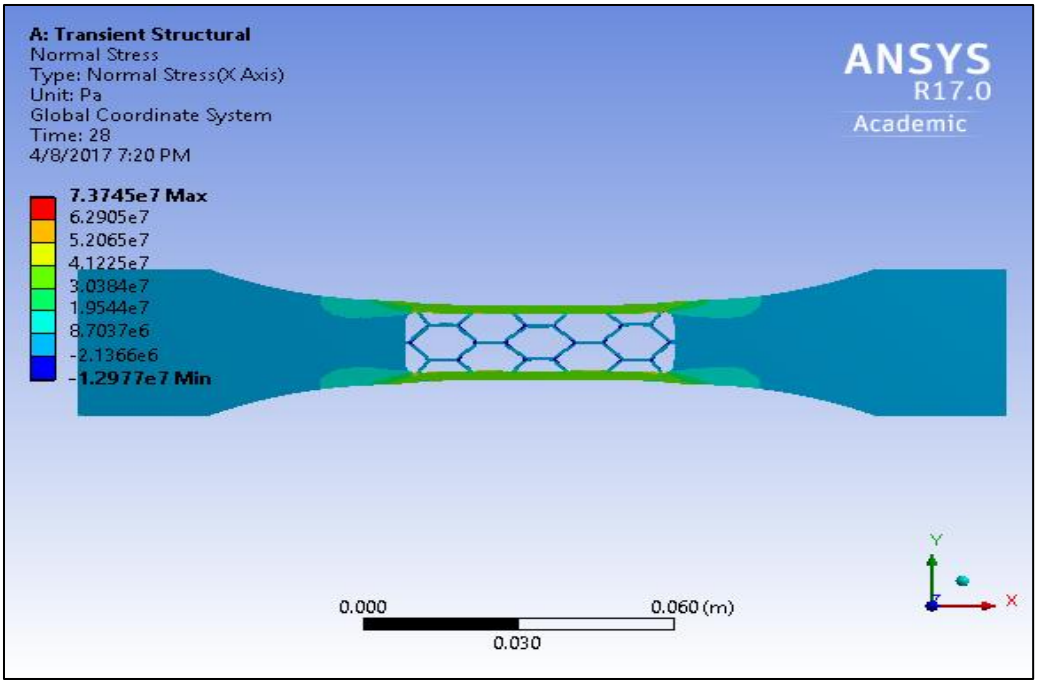

Figure C - 2: ANSYS© Normal Stress plot for HI specimen using BIM.

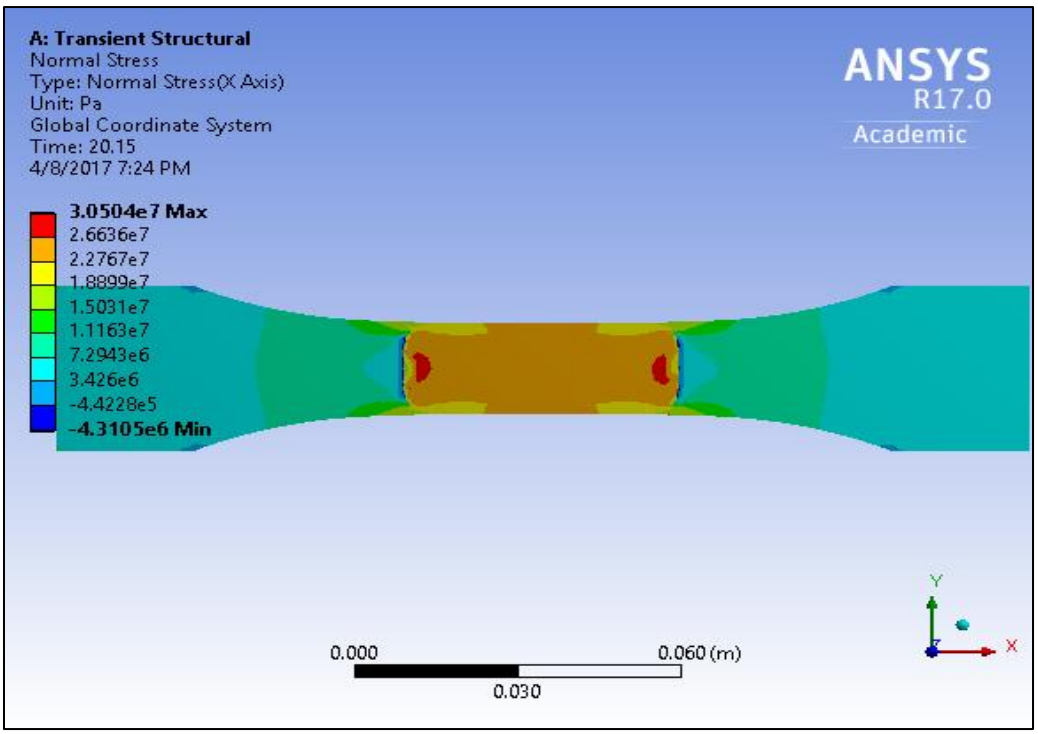

Figure C - 3: ANSYS© Normal Stress plot for CHI specimen using BIM.

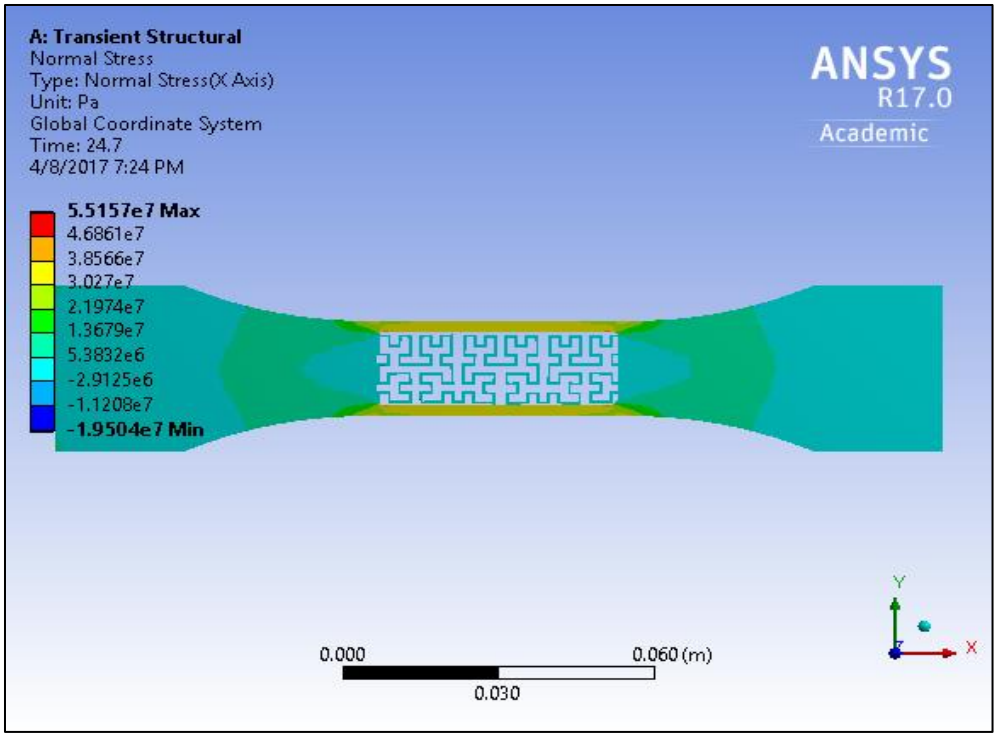

Figure C - 4: ANSYS© Normal Stress plot for HC specimen using BIM.

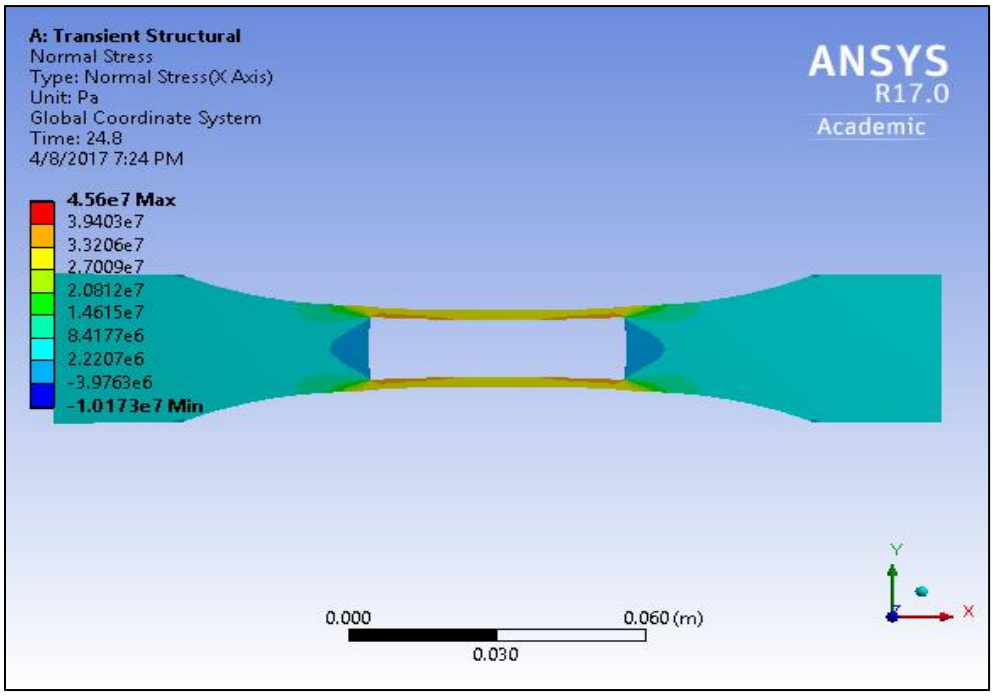

Figure C - 5: ANSYS© Normal Stress plot for I specimen using BIM.

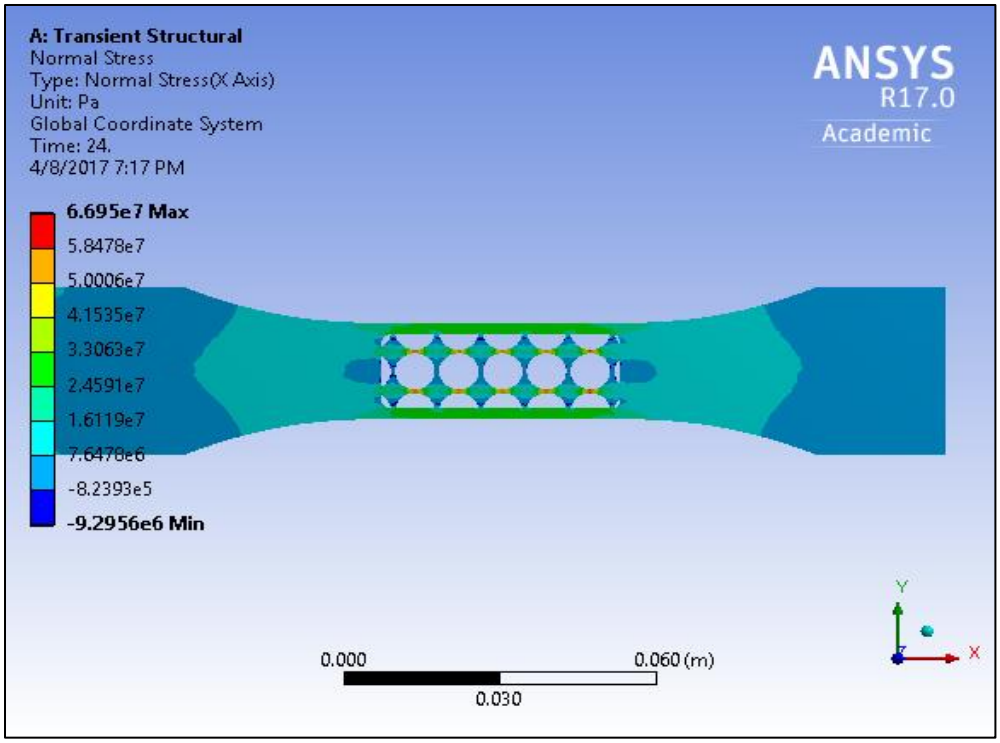

Figure C - 6: ANSYS© Normal Stress plot for CS specimen using BIM.

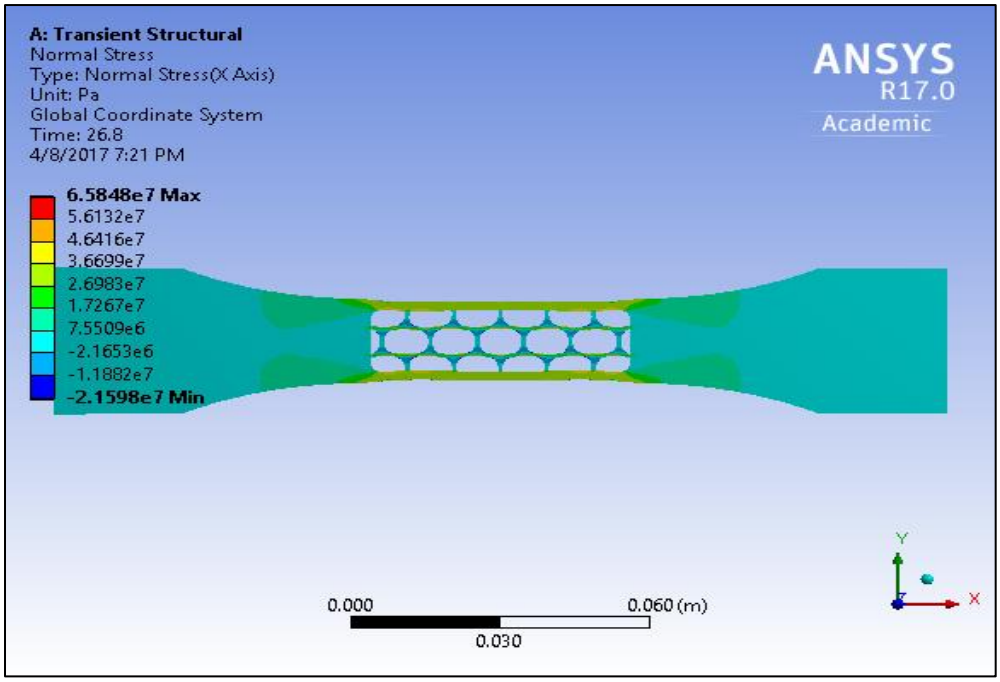

Figure C - 7: ANSYS© Normal Stress plot for CP specimen using BIM.

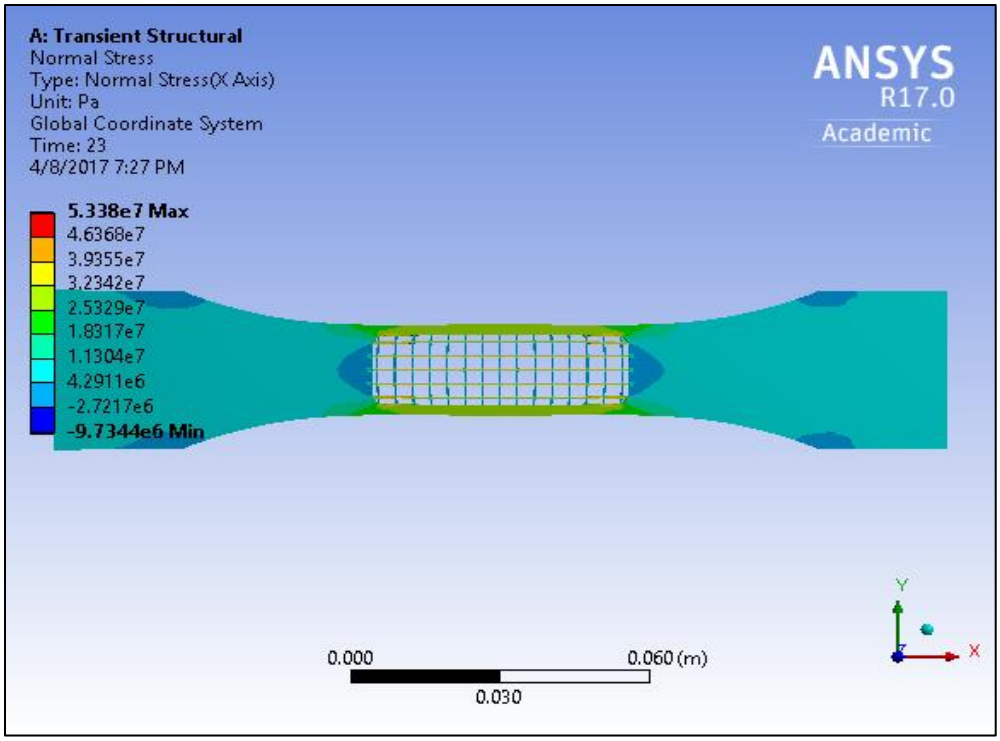

Figure C - 8: ANSYS© Normal Stress plot for LS specimen using BIM.

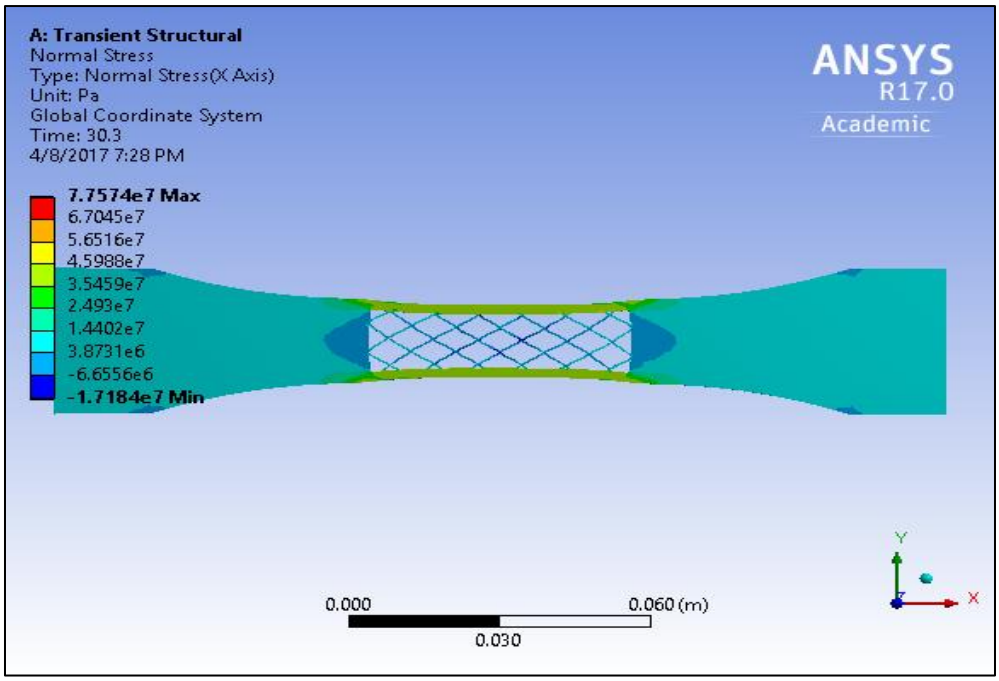

Figure C - 9: ANSYS© Normal Stress plot for LC specimen using BIM.

C.2: DIM Results

This section presents the DIM analysis normal stress plots for all the geometries using ANSYS©. Figures C-10 to C-18 show the normal stress plots.

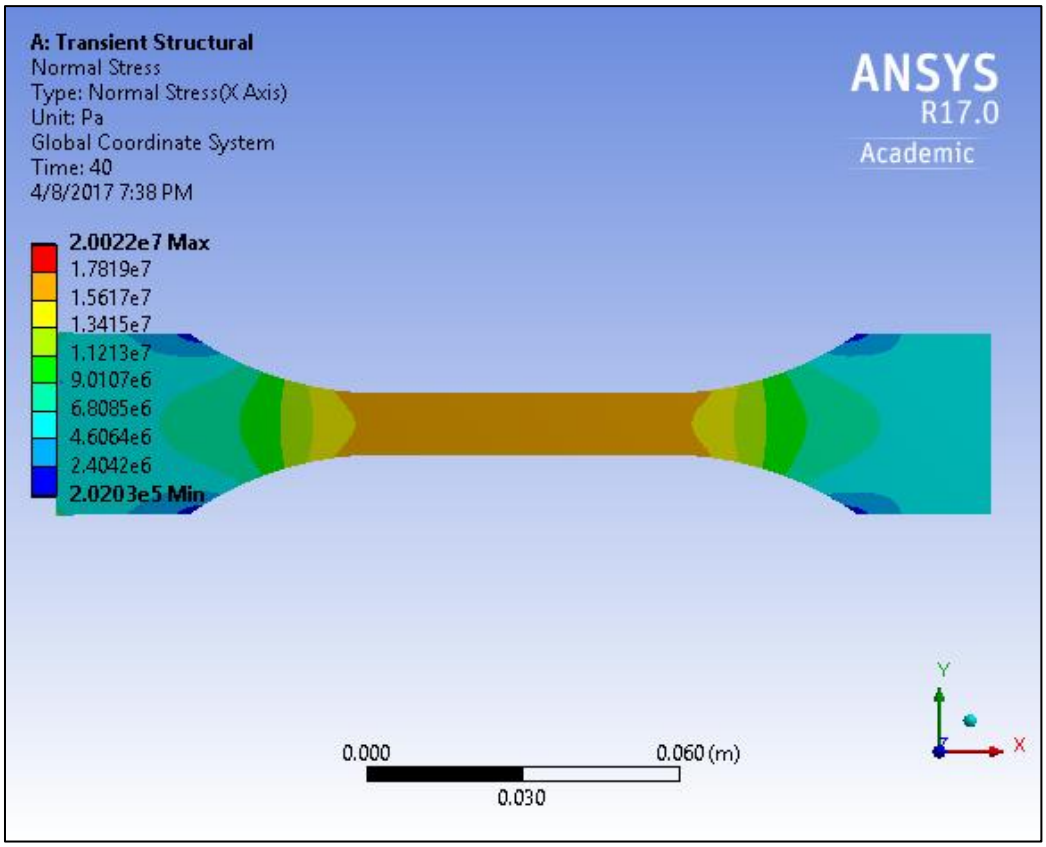

Figure C - 10: ANSYS© Normal Stress plot for C specimen using DIM.

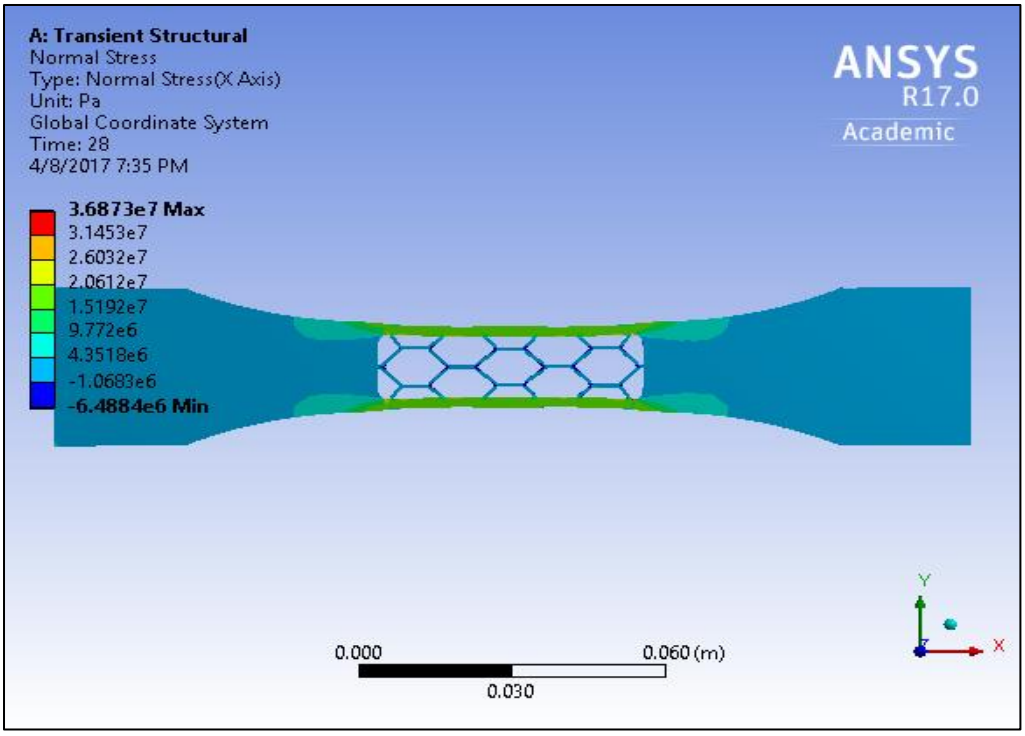

Figure C - 11: ANSYS© Normal Stress plot for HI specimen using DIM.

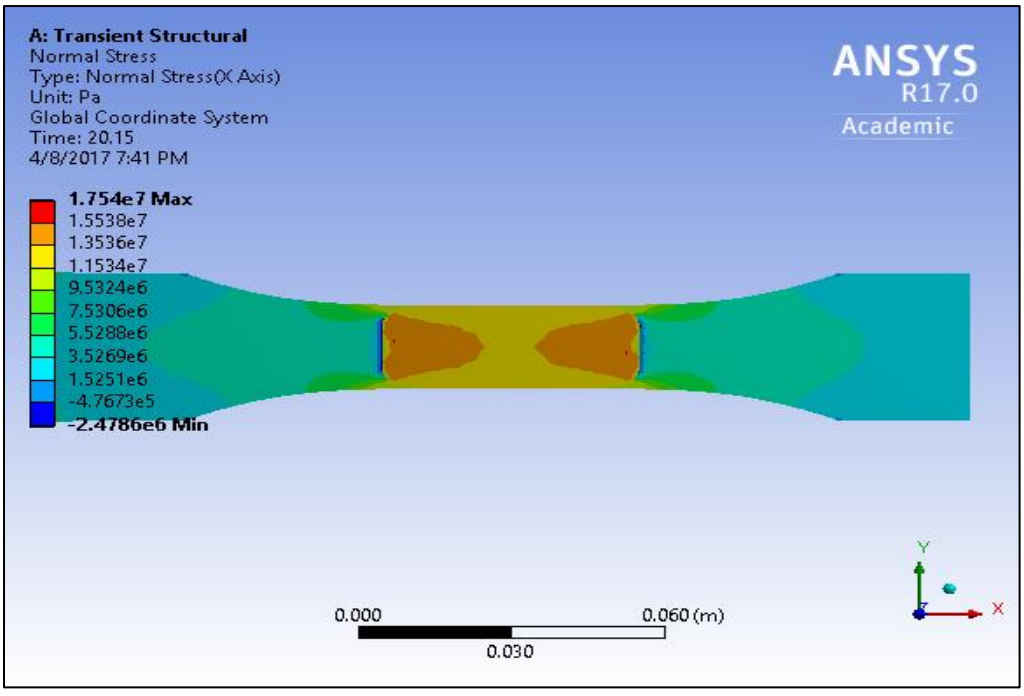

Figure C - 12: ANSYS© Normal Stress plot for CHI specimen using DIM.

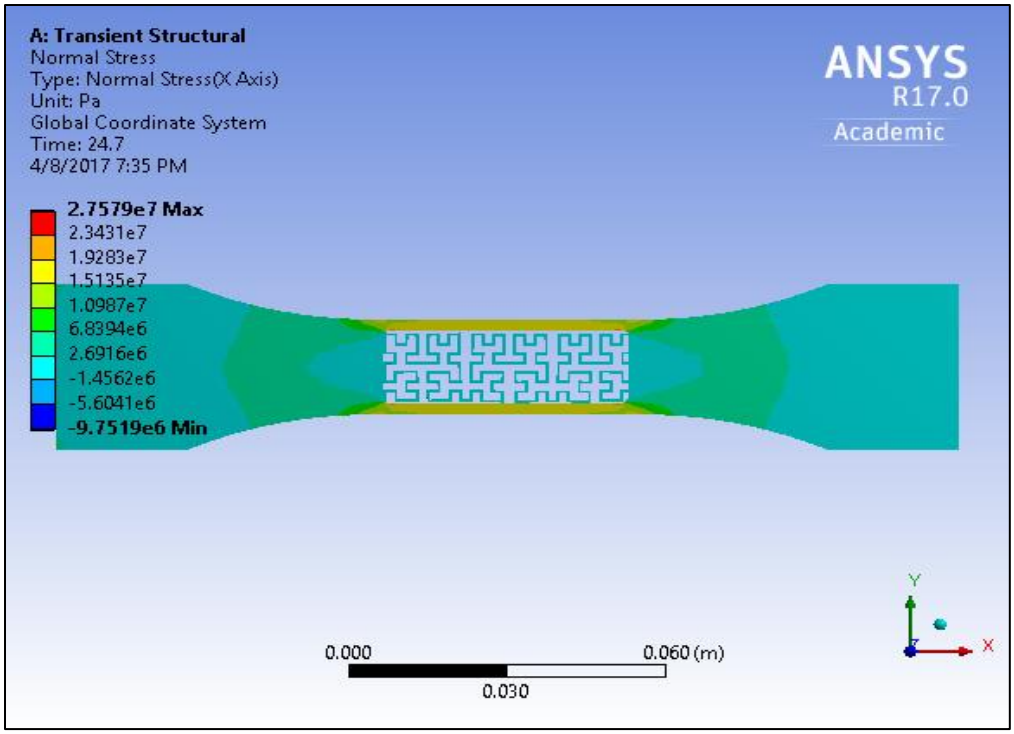

Figure C - 13: ANSYS© Normal Stress plot for HC specimen using DIM.

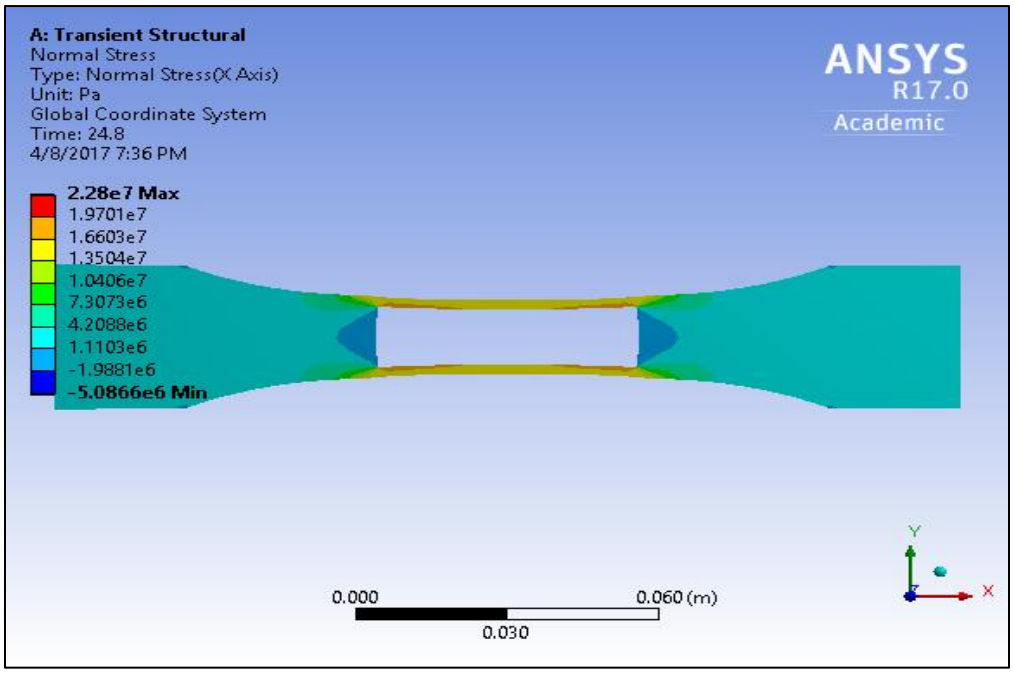

Figure C - 14: ANSYS© Normal Stress plot for I specimen using DIM.

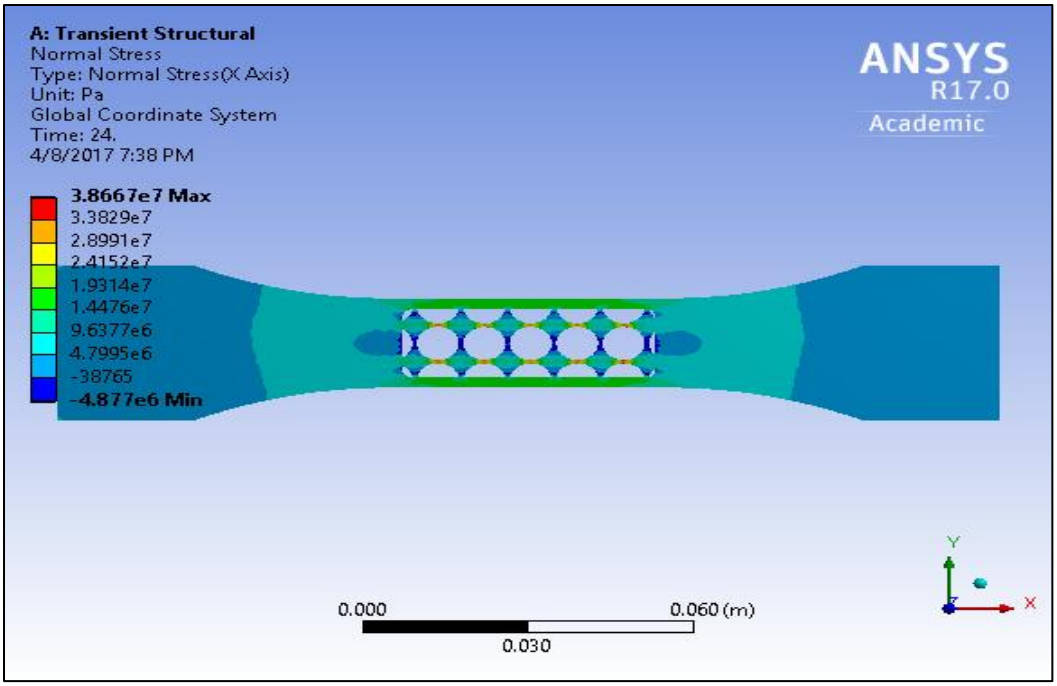

Figure C - 15: ANSYS© Normal Stress plot for CS specimen using DIM.

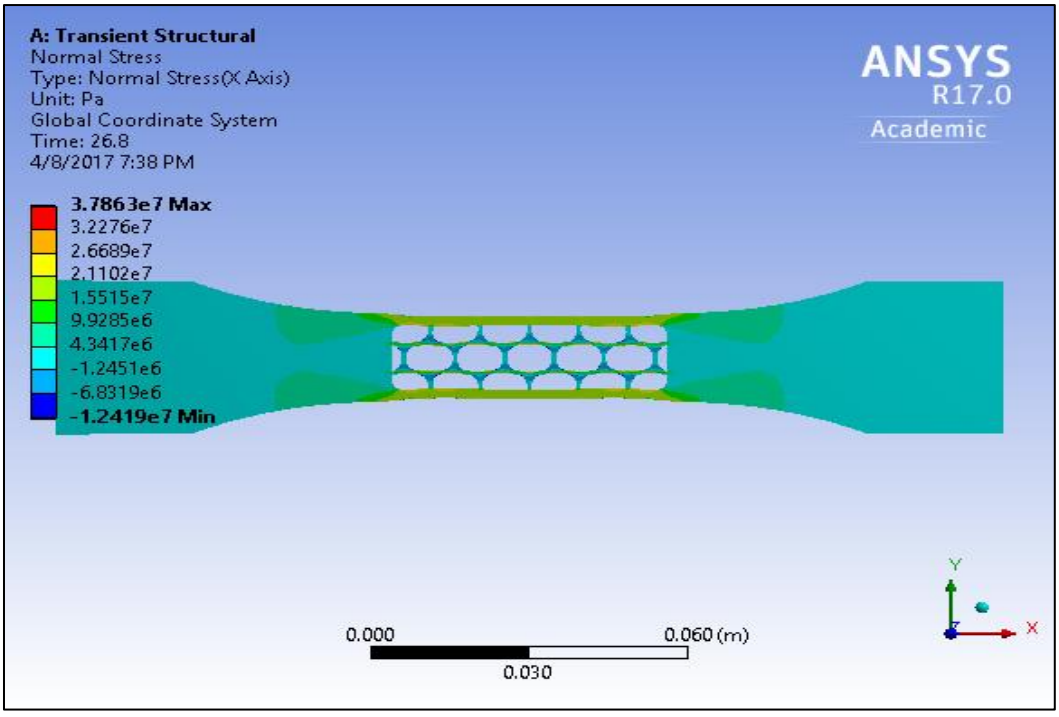

Figure C - 16: ANSYS© Normal Stress plot for CP specimen using DIM.

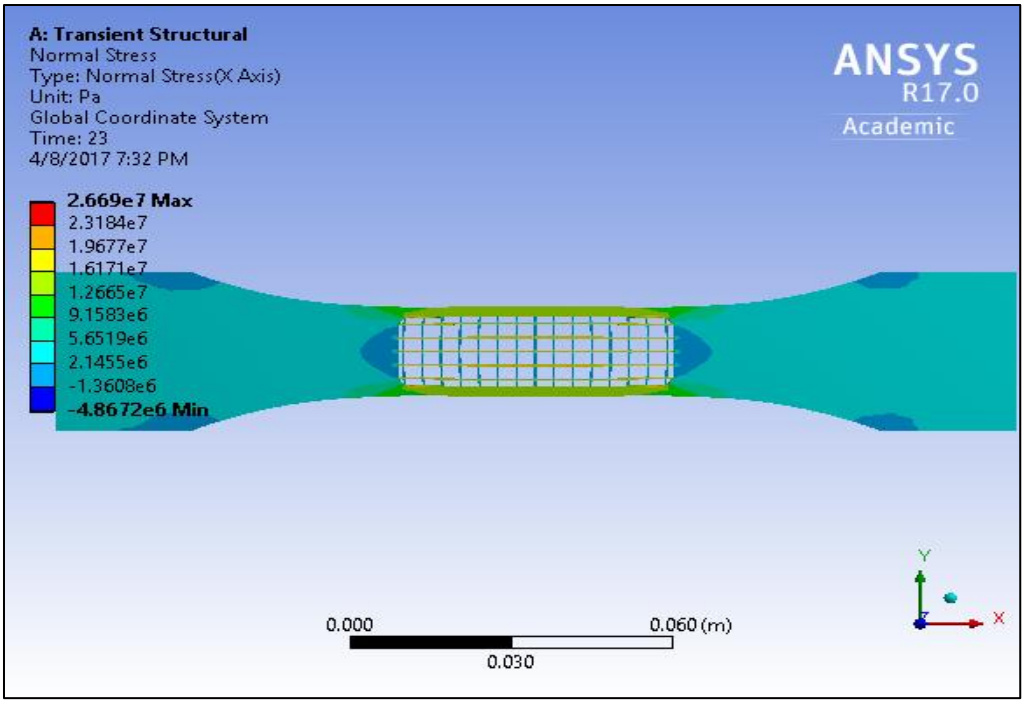

Figure C - 17: ANSYS© Normal Stress plot for LS specimen using DIM.

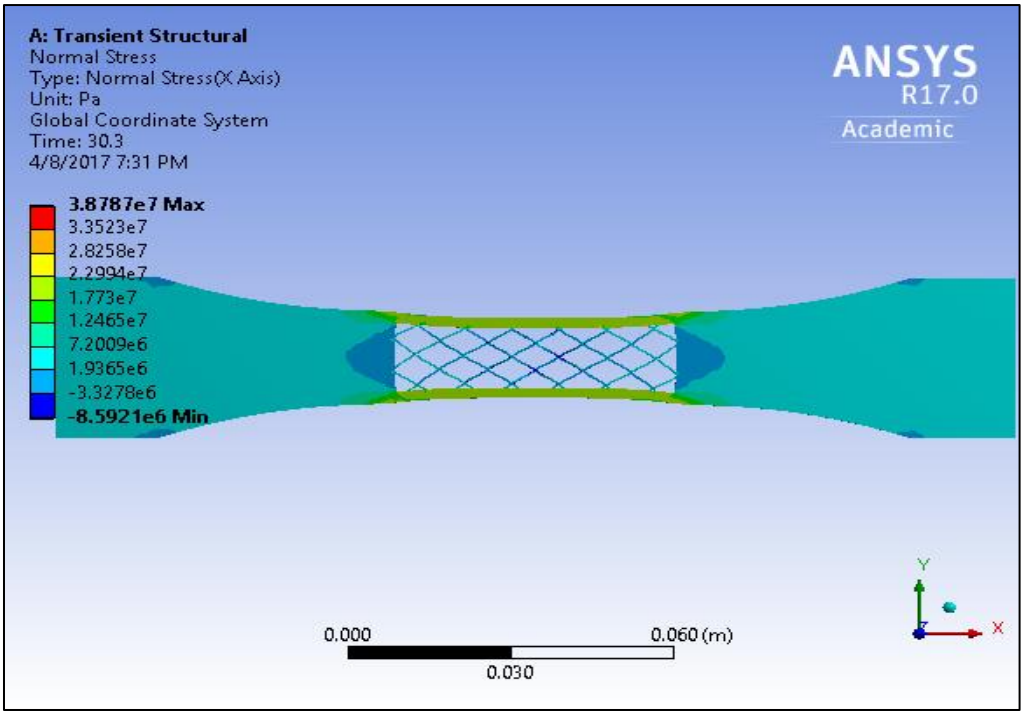

Figure C - 18: ANSYS© Normal Stress plot for LC specimen using DIM.

C.3: ODM Results

This section presents the ODM analysis normal stress plots for all the geometries using ANSYS©. Figures C-19 to C-27 show the normal stress plots.

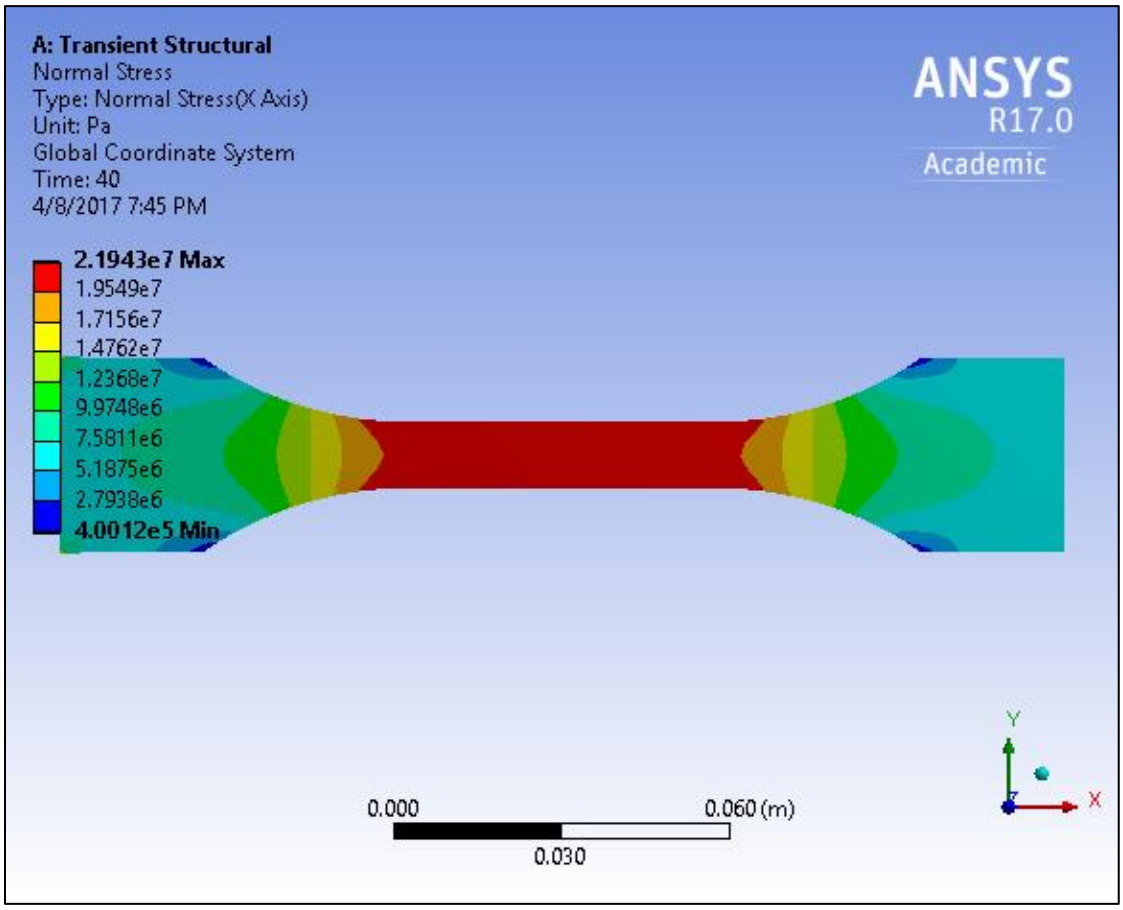

Figure C - 19: ANSYS© Normal Stress plot for C specimen using ODM.

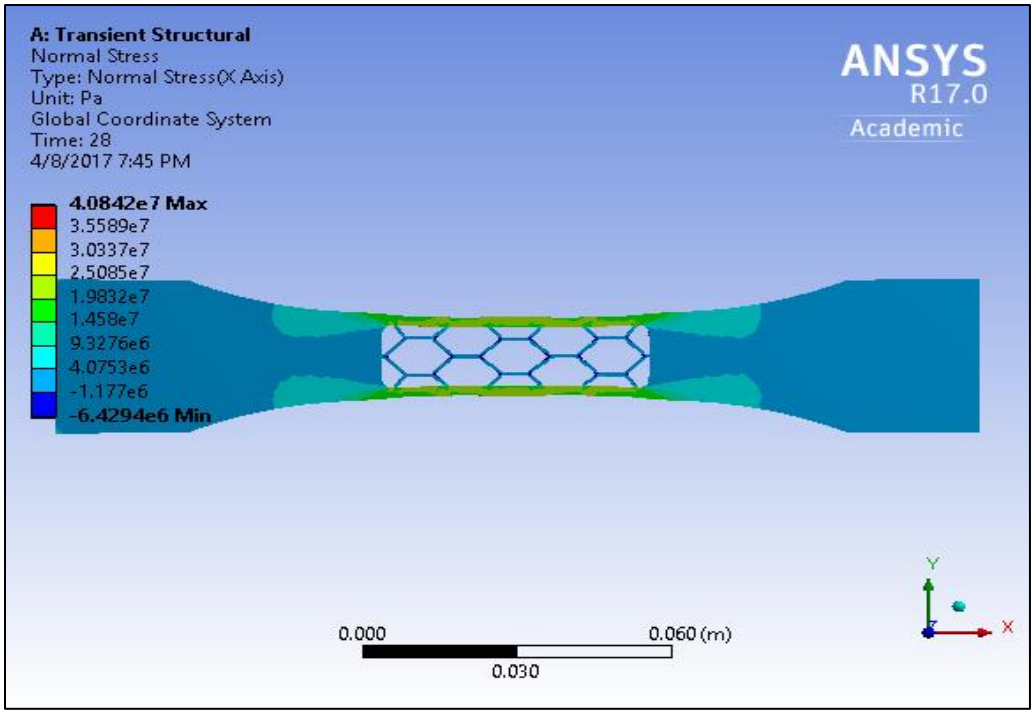

Figure C - 20: ANSYS© Normal Stress plot for HI specimen using ODM.

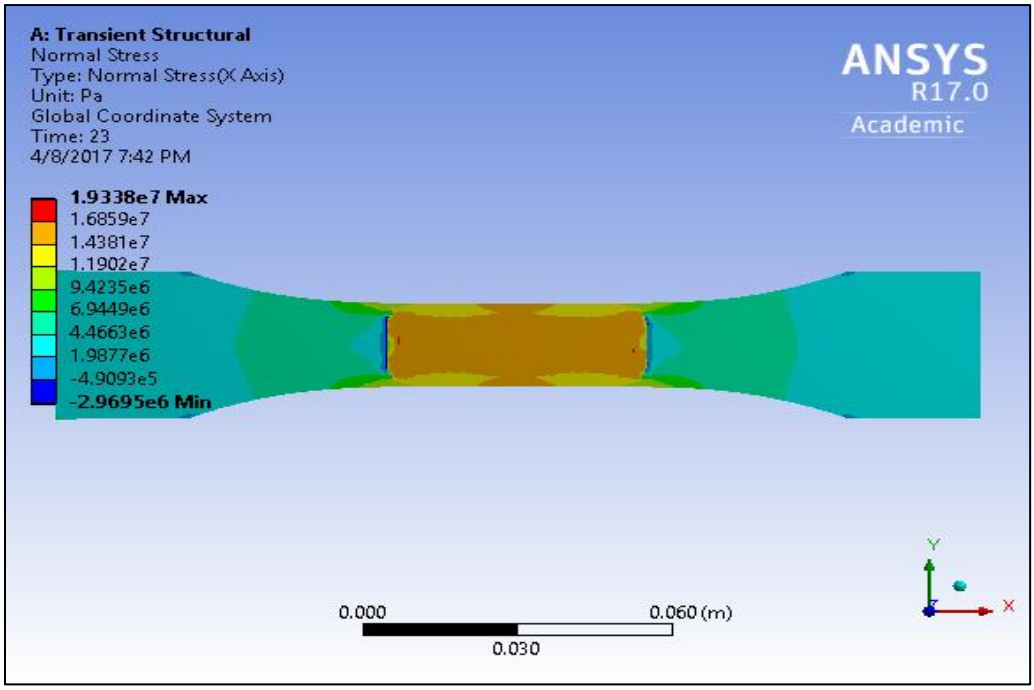

Figure C - 21: ANSYS© Normal Stress plot for CHI specimen using ODM.

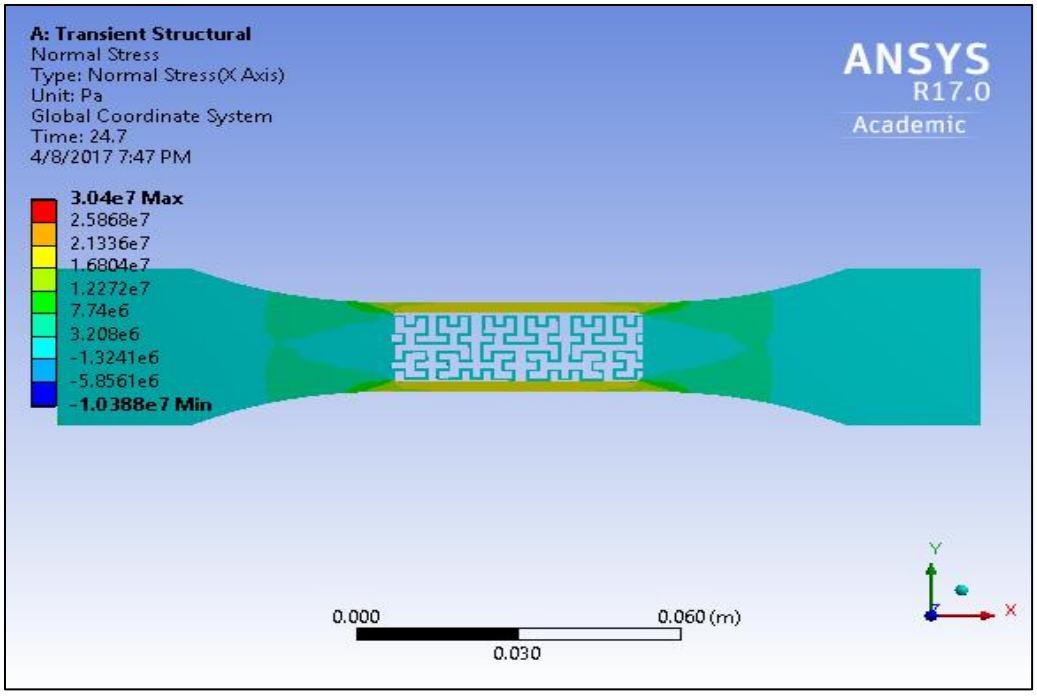

Figure C - 22: ANSYS© Normal Stress plot for HC specimen using ODM.

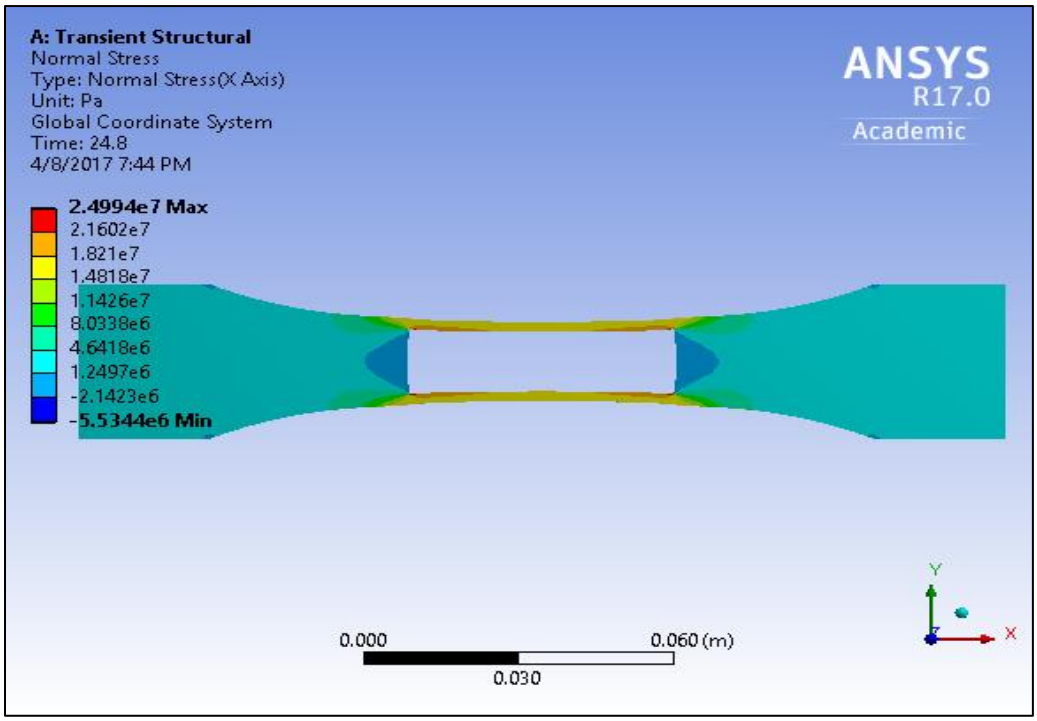

Figure C - 23: ANSYS© Normal Stress plot for I specimen using ODM.

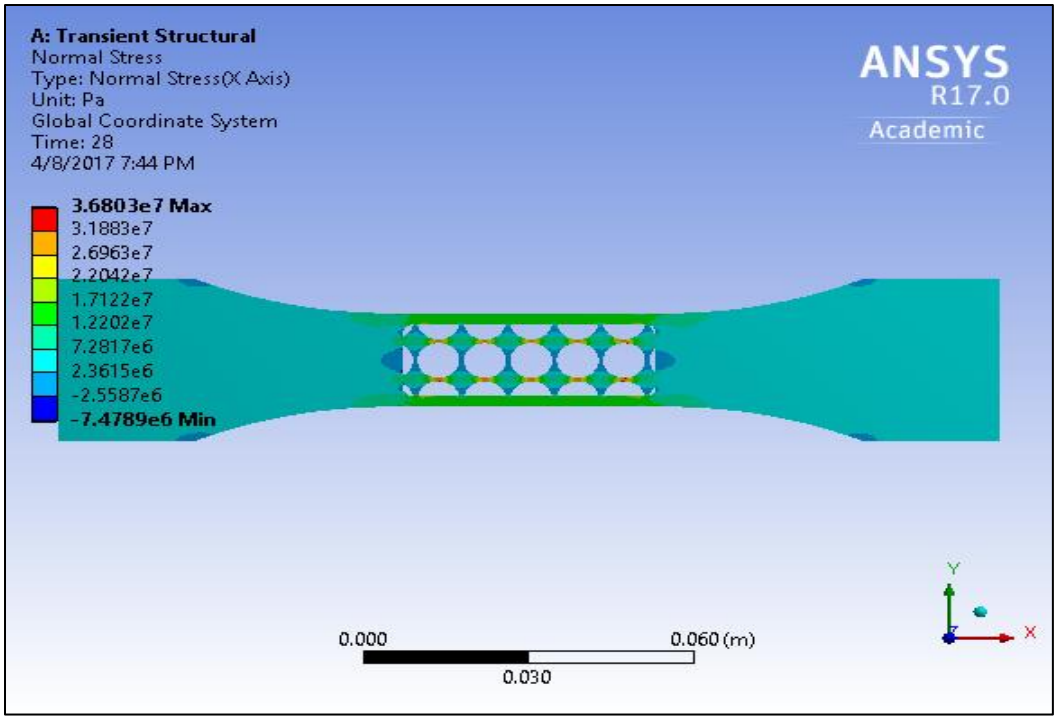

Figure C - 24: ANSYS© Normal Stress plot for CS specimen using ODM.

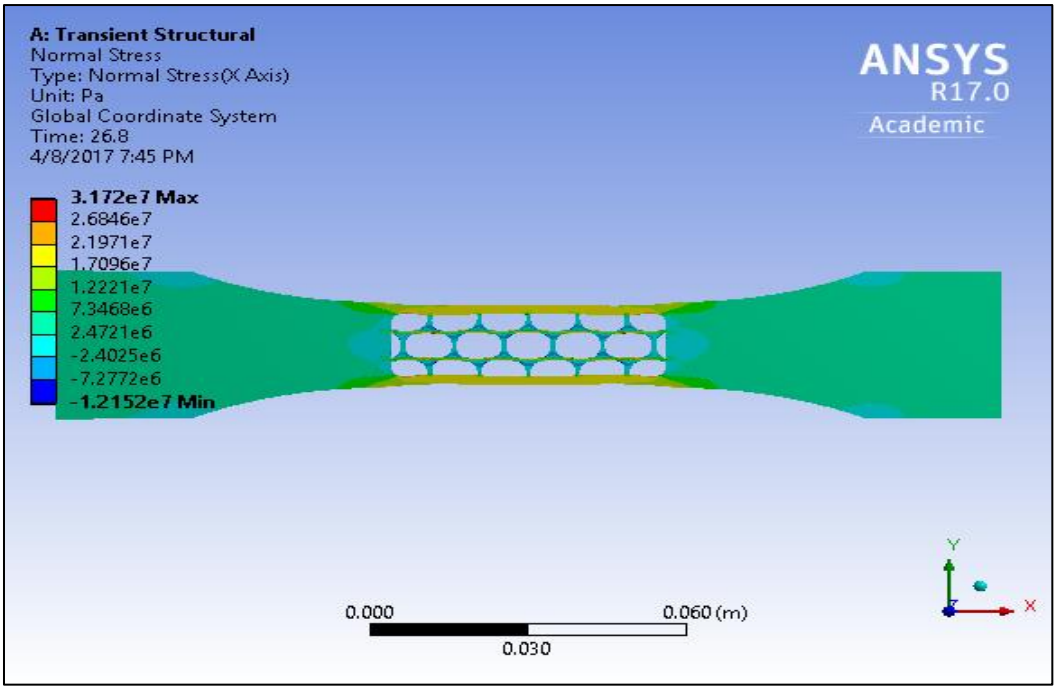

Figure C - 25: ANSYS© Normal Stress plot for CS specimen using ODM.

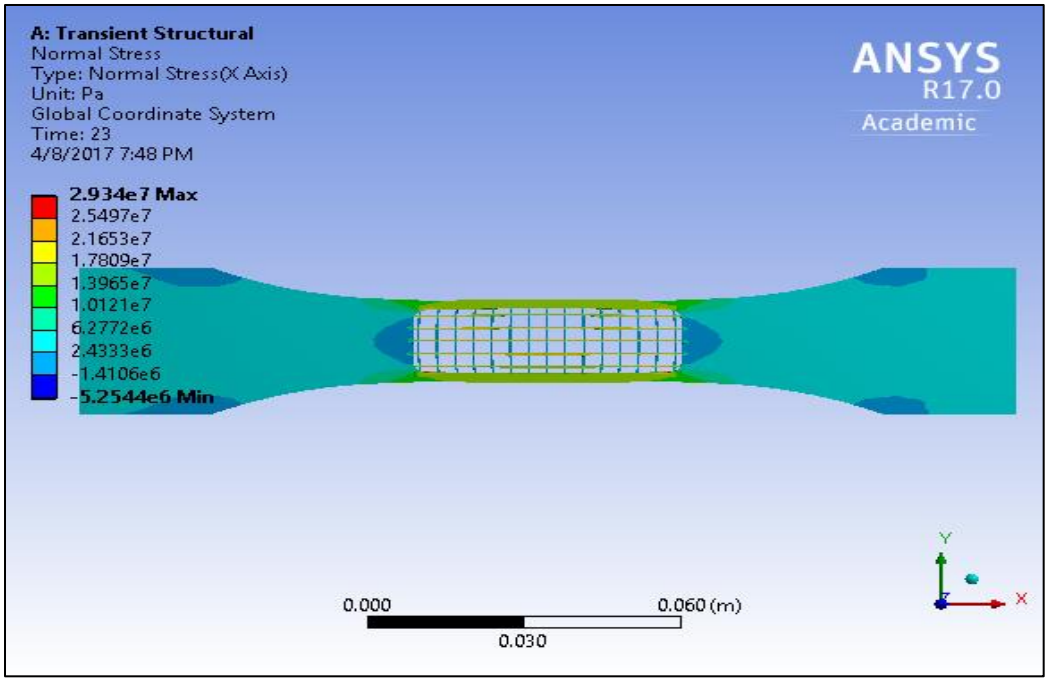

Figure C - 26: ANSYS© Normal Stress plot for LS specimen using ODM.

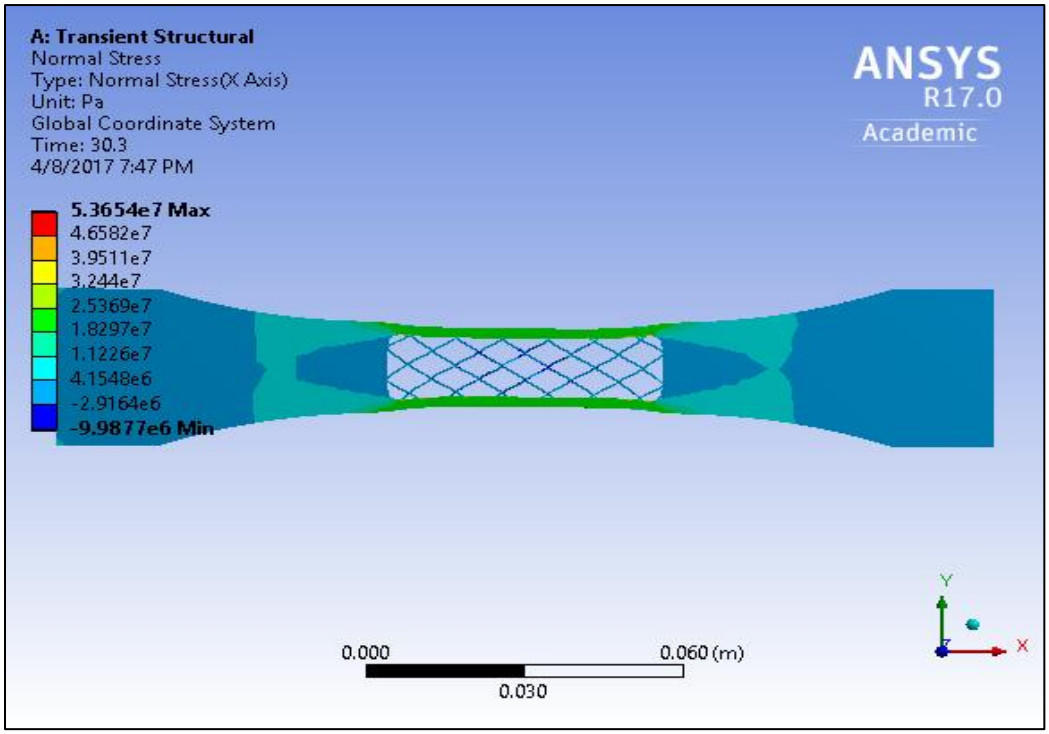

Figure C - 27: ANSYS© Normal Stress plot for LC specimen using ODM.

APPENDIX D: SIMULATION RESULTS – Abaqus©

D.1: BIM Results

This section presents the BIM analysis-normal stress plots of all the specimens from Abaqus©. The body of the thesis has plots zoomed in on the infill patterns, the entire body stress plots are shown in this section. Figures D-1 to D-9 show the stress plots from the BIM analyses.

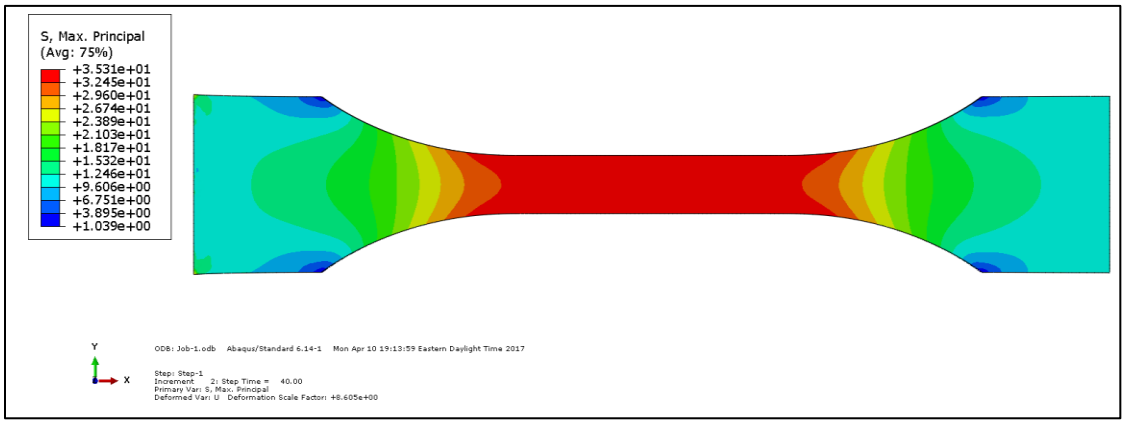

Figure D - 1: Abaqus© Normal Stress plot for C specimen using BIM.

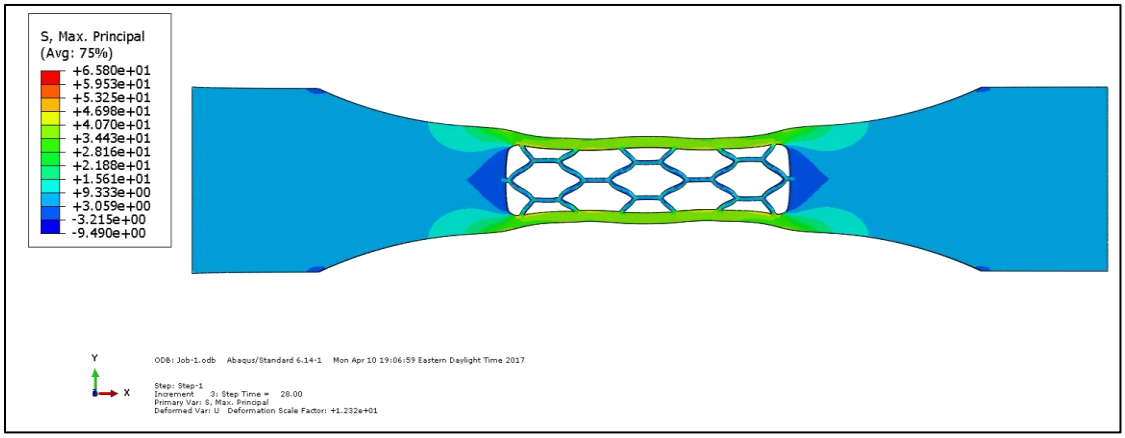

Figure D - 2: Abaqus© Normal Stress plot for HI specimen using BIM.

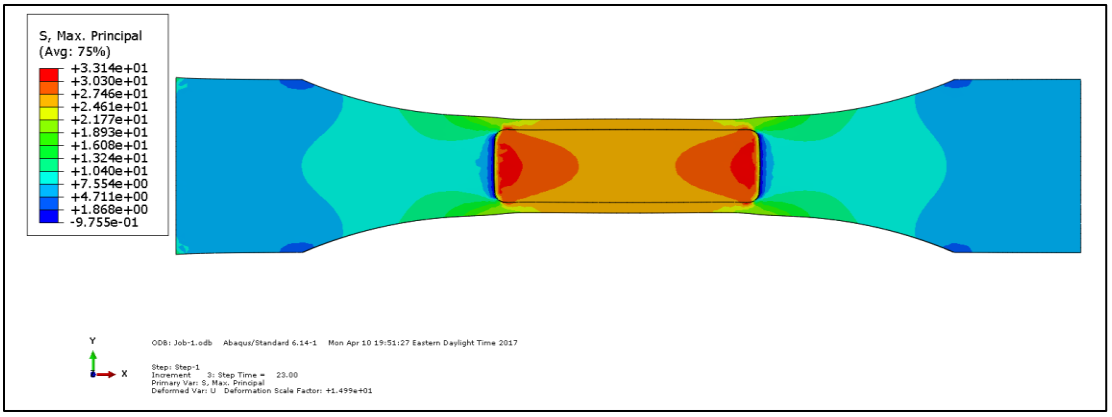

Figure D - 3: Abaqus© Normal Stress plot for CHI specimen using BIM.

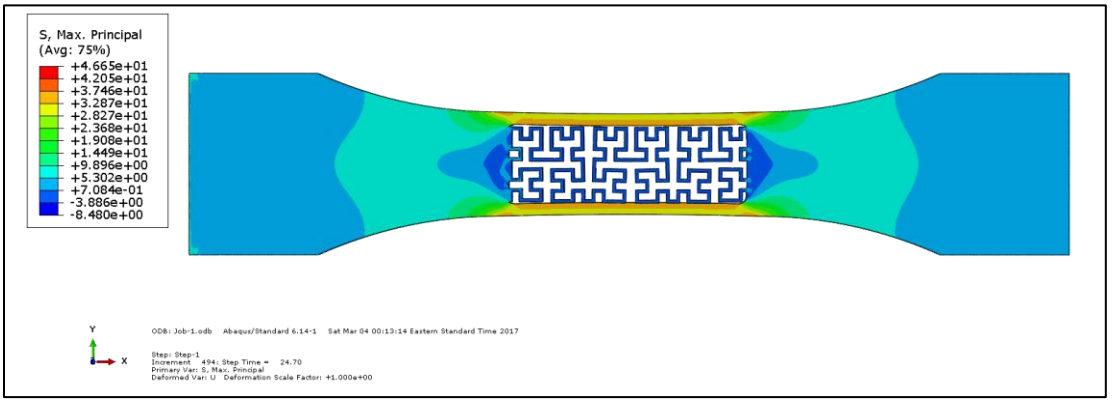

Figure D - 4: Abaqus© Normal Stress plot for HC specimen using BIM.

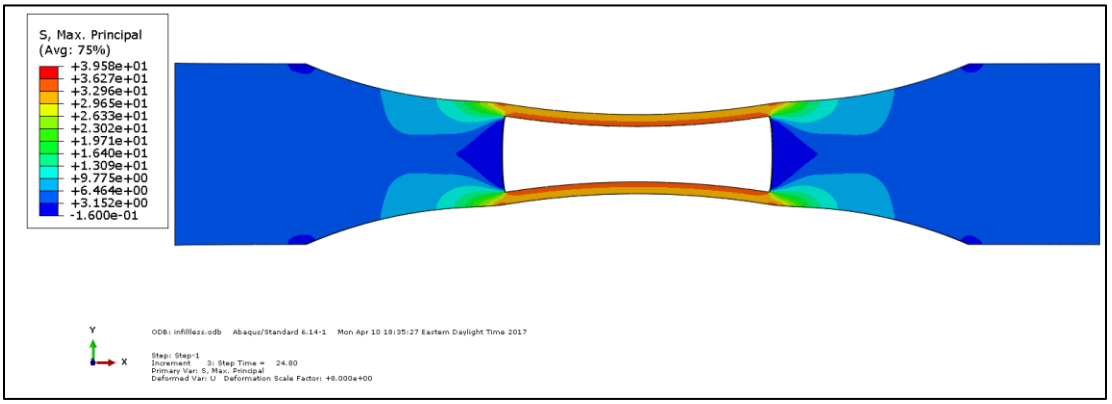

Figure D - 5: Abaqus© Normal Stress plot for I specimen using BIM.

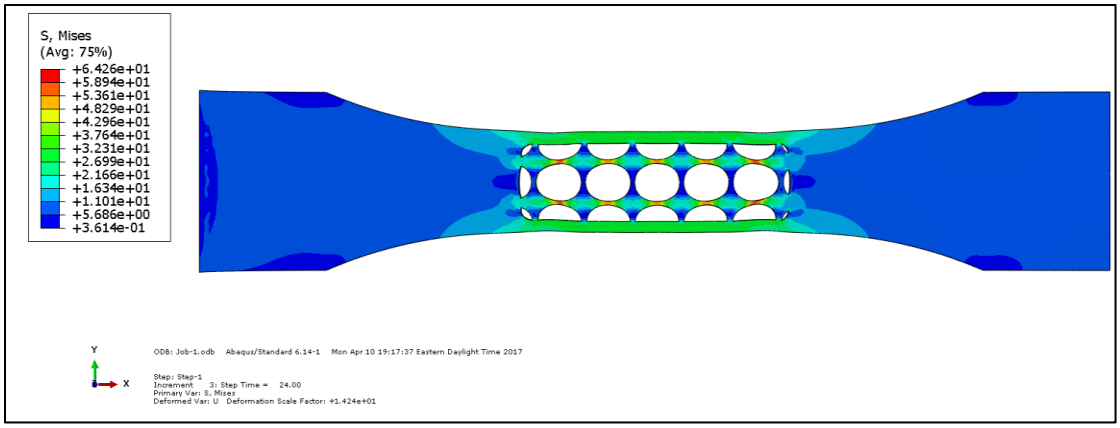

Figure D - 6: Abaqus© Normal Stress plot for CS specimen using BIM.

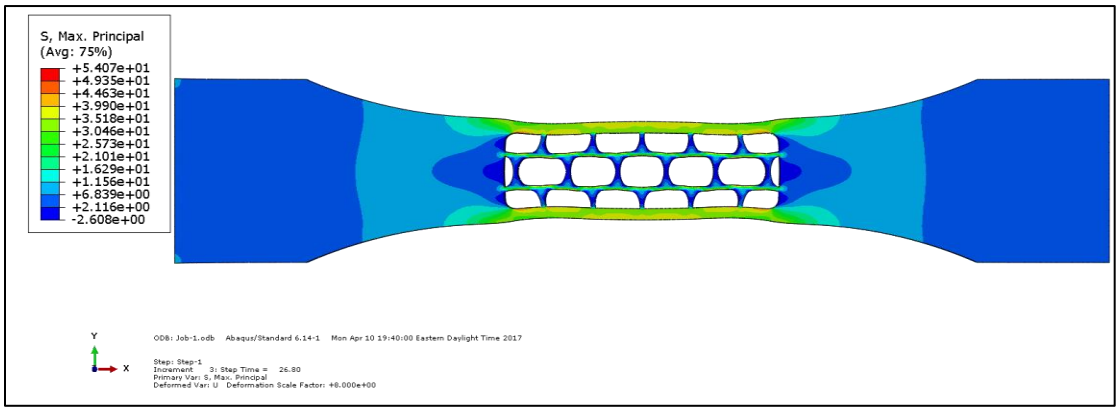

Figure D - 7: Abaqus© Normal Stress plot for CP specimen using BIM.

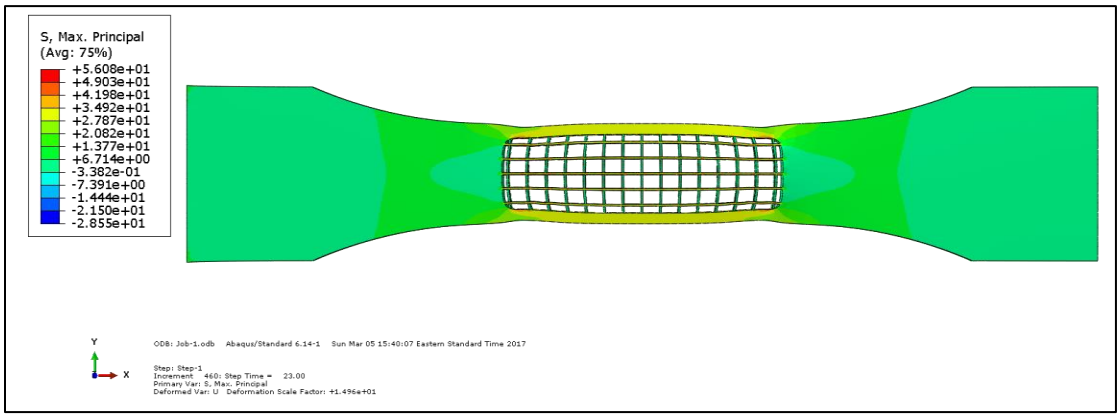

Figure D - 8: Abaqus© Normal Stress plot for LS specimen using BIM.

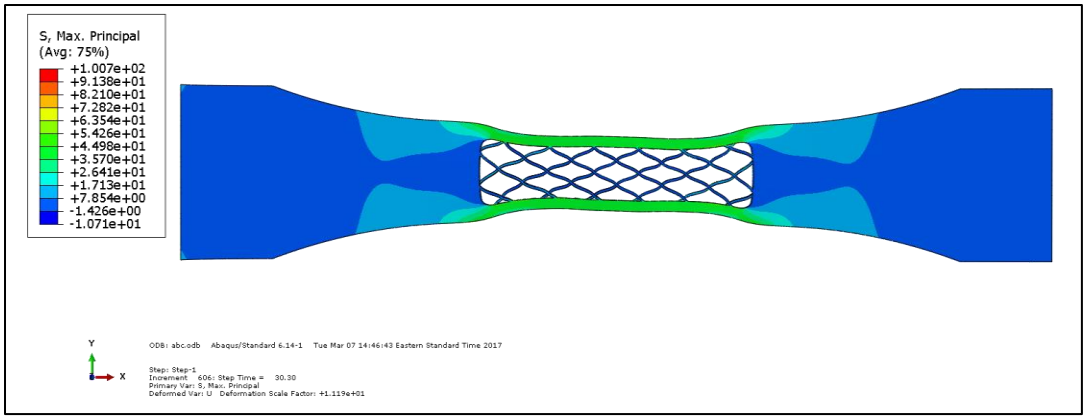

Figure D - 9: Abaqus© Normal Stress plot for LC specimen using BIM.

D.2: DIM Results

This section presents the DIM analysis-normal stress plots of all the specimens from Abaqus©. This the body of the thesis has plots zoomed in on the infill patterns, the entire body stress plots are shown in this section. Figures D-10 to D-18 show the stress plots from the DIM analyses.

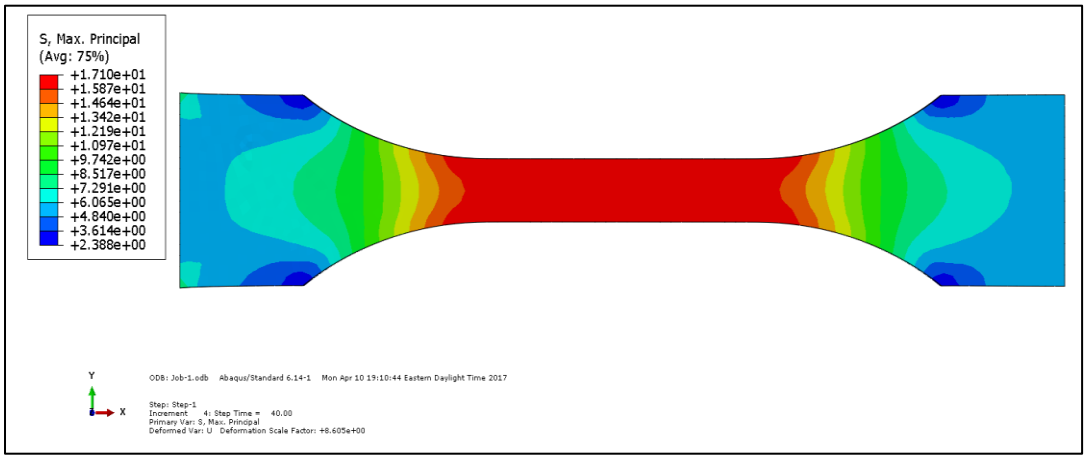

Figure D - 10: Abaqus© Normal Stress plot for C specimen using DIM.

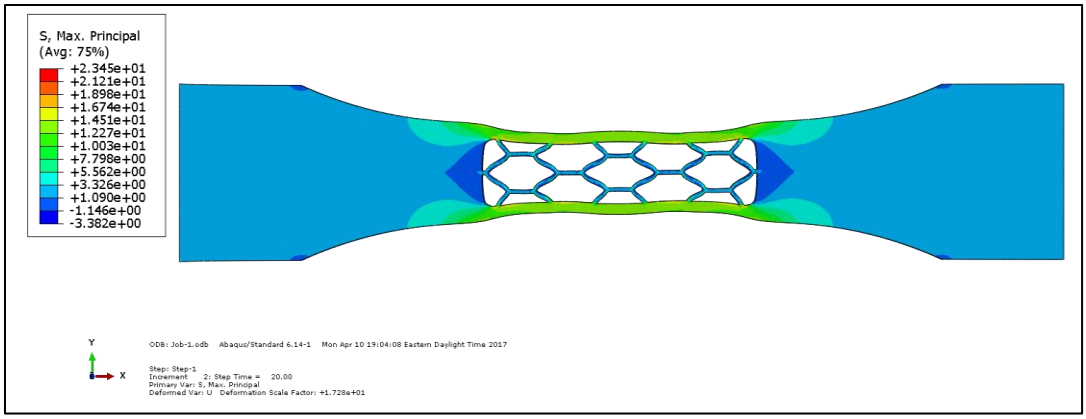

Figure D - 11: Abaqus© Normal Stress plot for HI specimen using DIM.

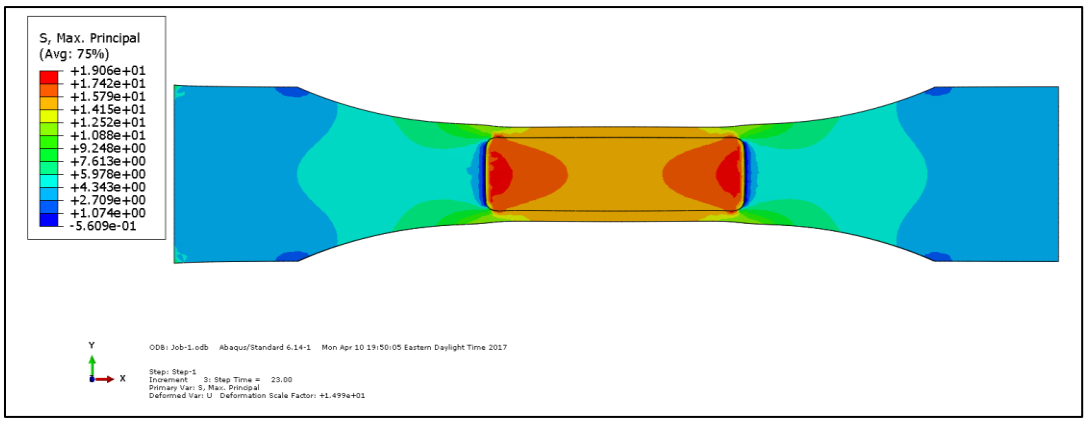

Figure D - 12: Abaqus© Normal Stress plot for CHI specimen using DIM.

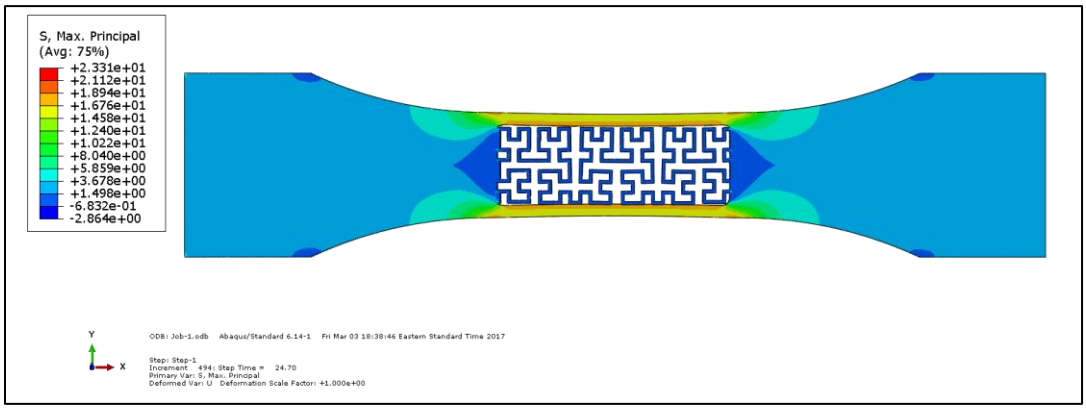

Figure D - 13: Abaqus© Normal Stress plot for HC specimen using DIM.

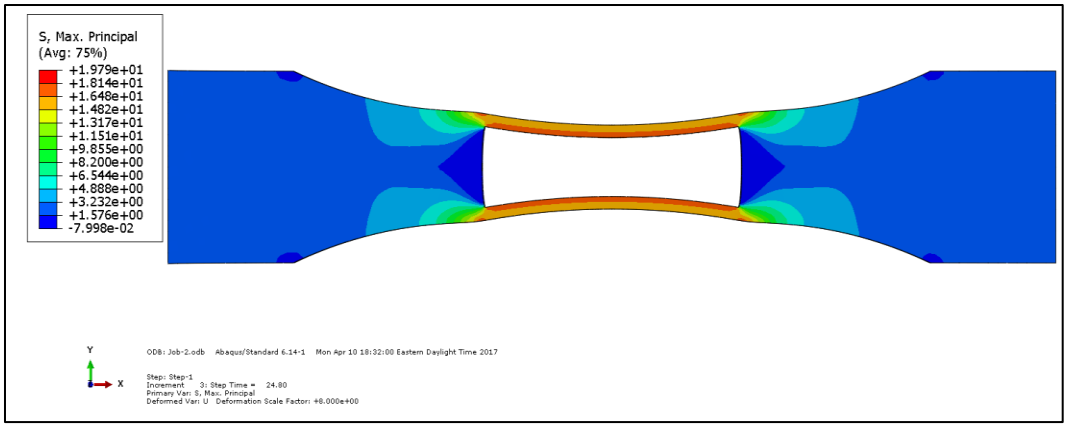

Figure D - 14: Abaqus© Normal Stress plot for I specimen using DIM.

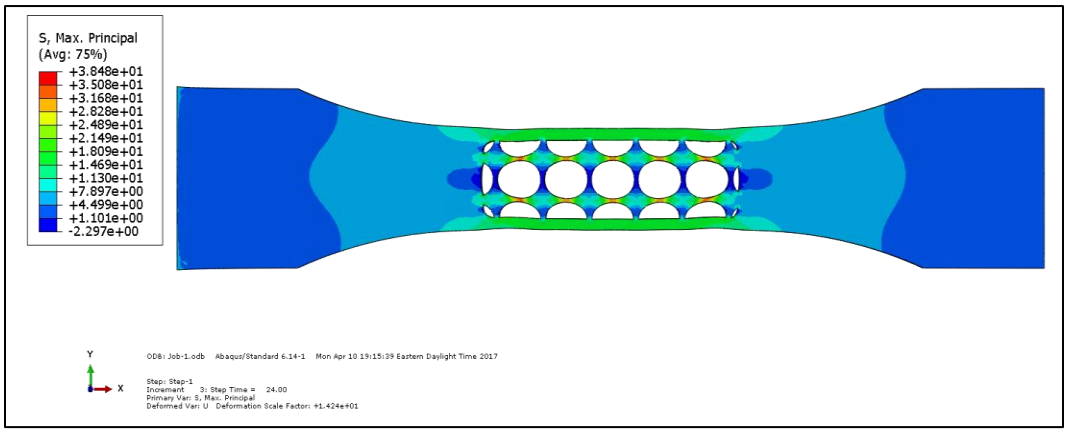

Figure D - 15: Abaqus© Normal Stress plot for CS specimen using DIM.

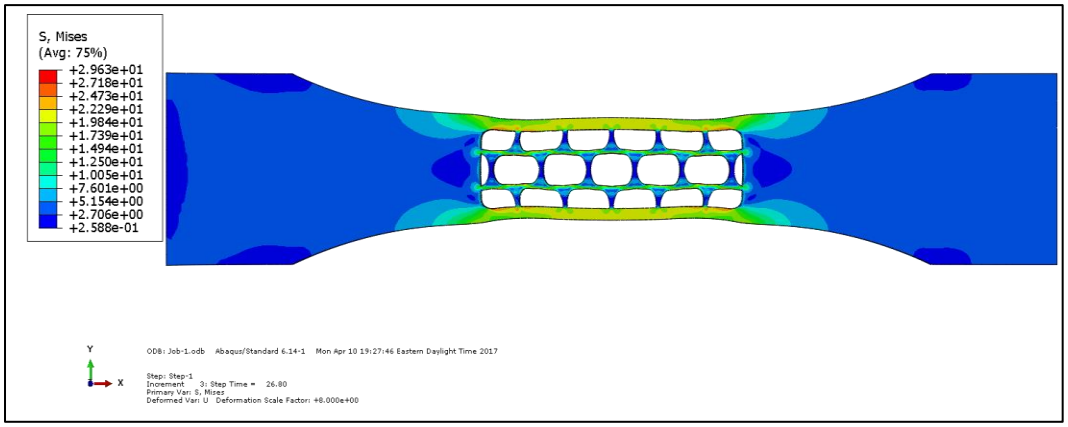

Figure D - 16: Abaqus© Normal Stress plot for CP specimen using DIM.

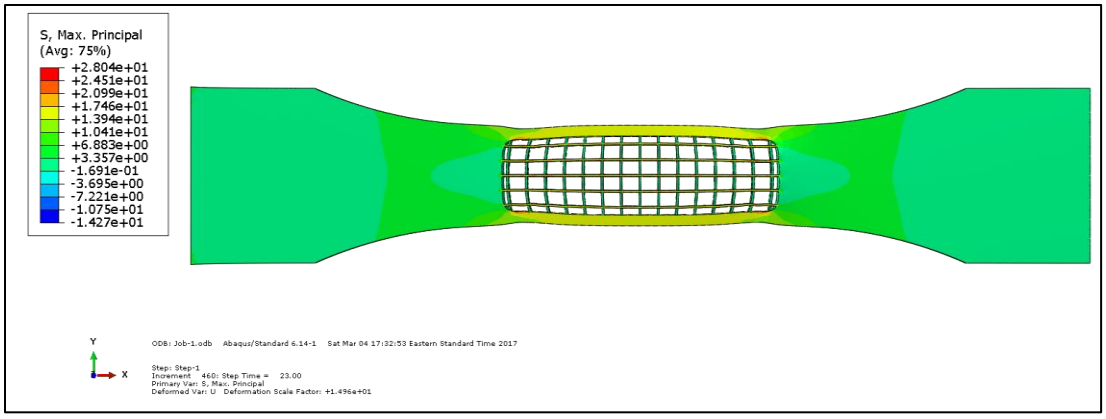

Figure D - 17: Abaqus© Normal Stress plot for LS specimen using DIM.

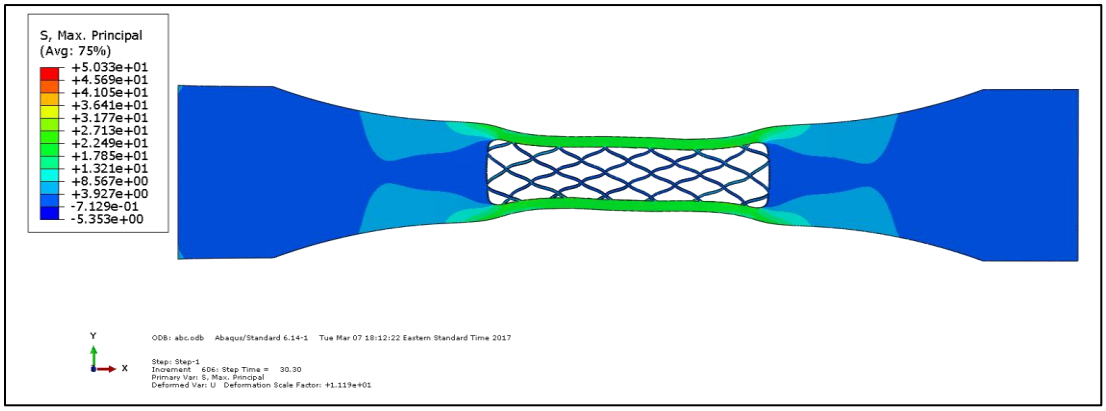

Figure D - 18: Abaqus© Normal Stress plot for LC specimen using DIM.

D.3: ODM Results

This section presents the ODM analysis-normal stress plots of all the specimens from Abaqus©. This the body of the thesis has plots zoomed in on the infill patterns, the entire body stress plots are shown in this section. Figures D-18 to D-27 show the stress plots from the ODM analyses.

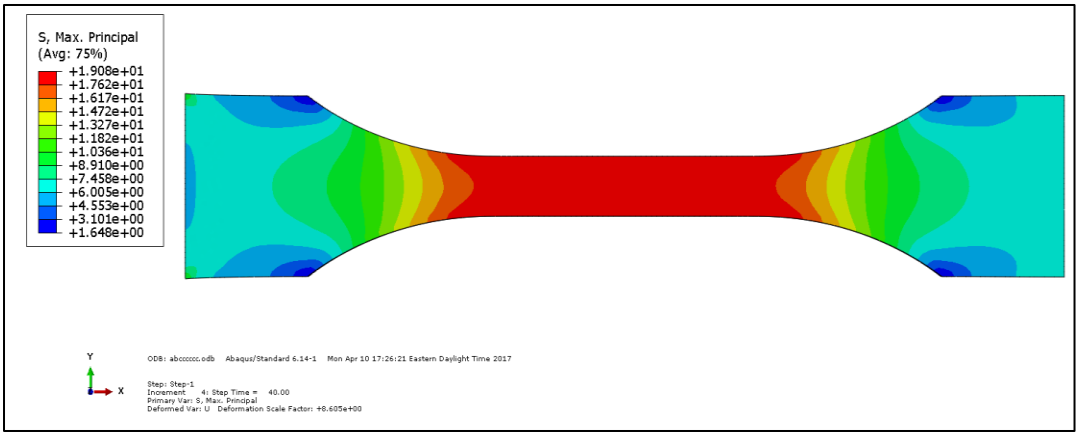

Figure D - 19: Abaqus© Normal Stress plot for C specimen using ODM.

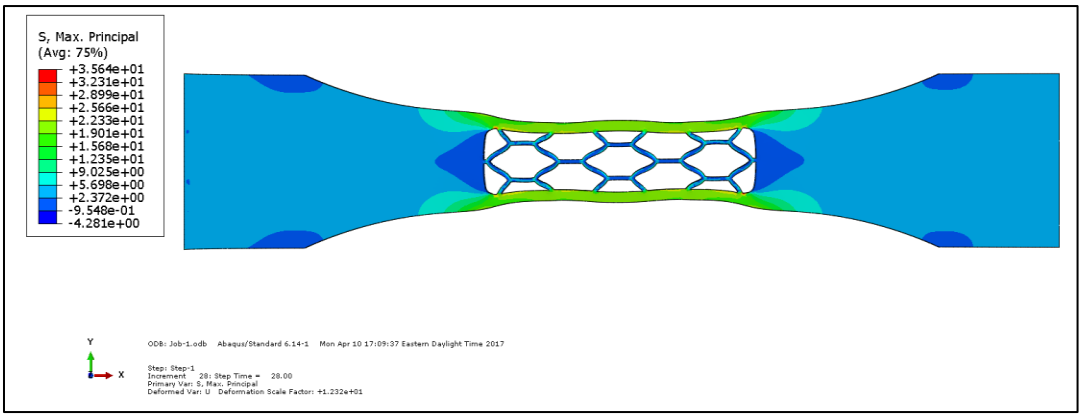

Figure D - 20: Abaqus© Normal Stress plot for HI specimen using ODM.

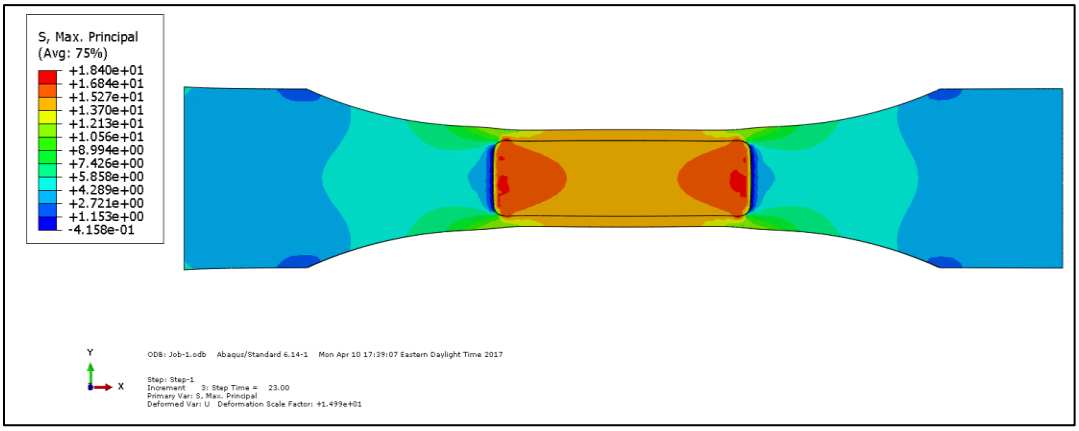

Figure D - 21: Abaqus© Normal Stress plot for CHI specimen using ODM.

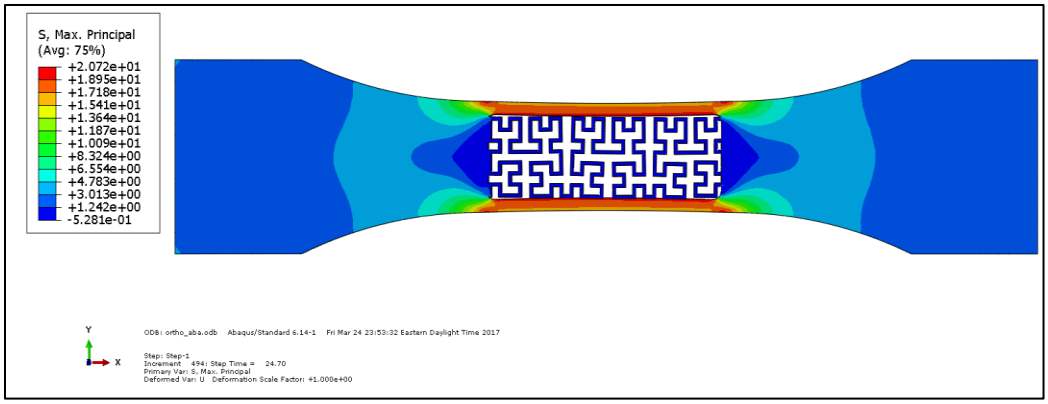

Figure D - 22: Abaqus© Normal Stress plot for HC specimen using ODM.

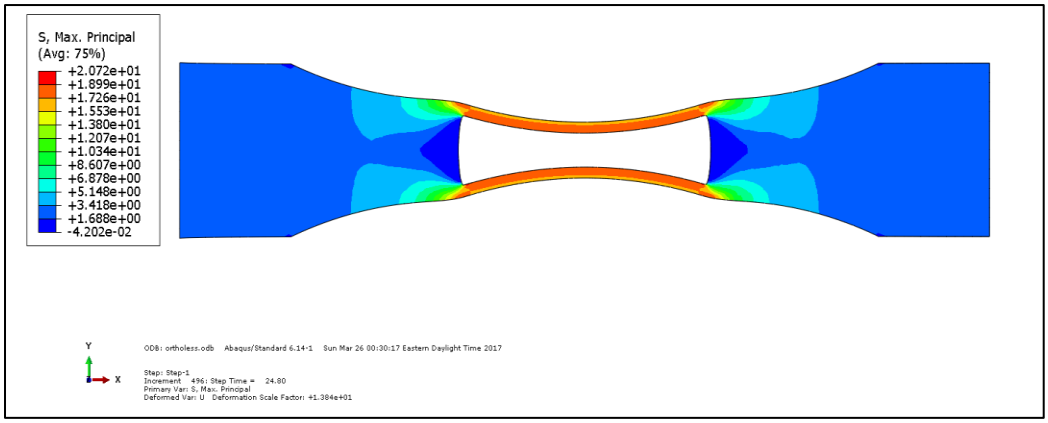

Figure D - 23: Abaqus© Normal Stress plot for I specimen using ODM.

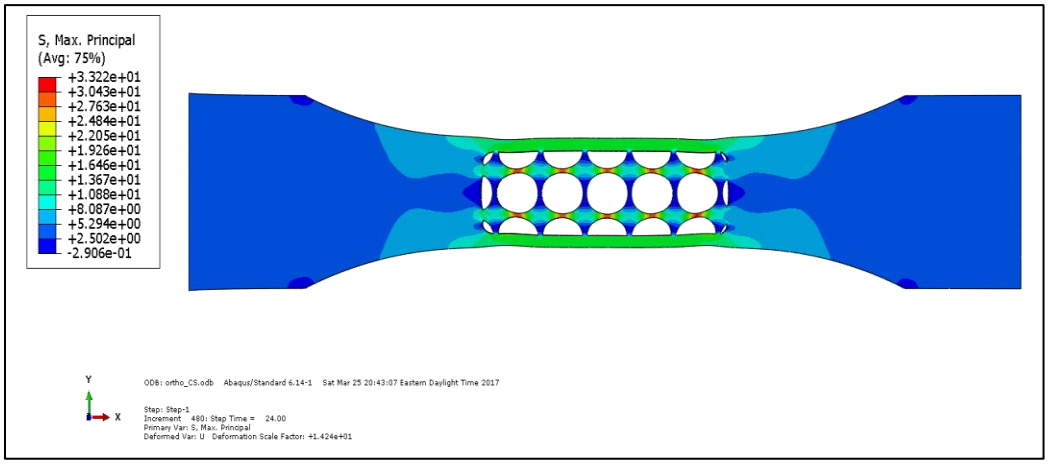

Figure D - 24: Abaqus© Normal Stress plot for CS specimen using ODM.

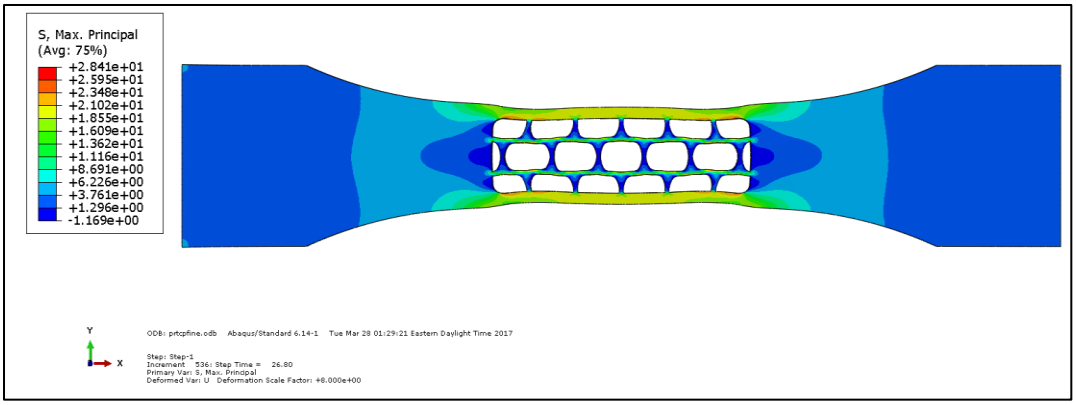

Figure D - 25: Abaqus© Normal Stress plot for CP specimen using ODM.

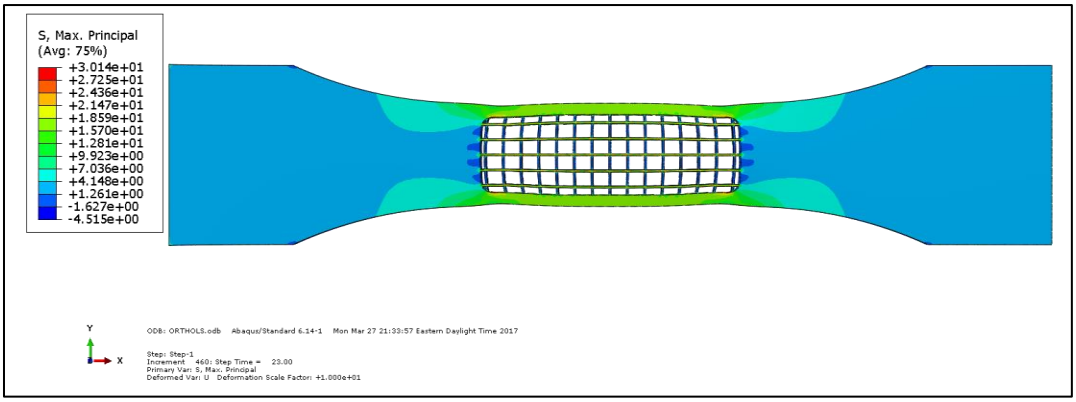

Figure D - 26: Abaqus© Normal Stress plot for LS specimen using ODM.

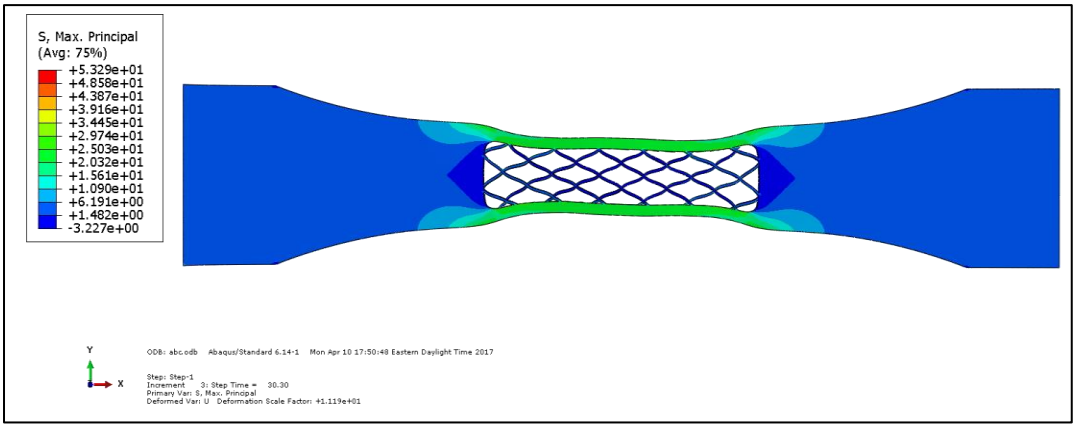

Figure D - 27: Abaqus© Normal Stress plot for LC specimen using ODM.

D.4: CLM Results

This section presents the CLM analysis-normal stress plots of all the specimens from Abaqus©. This the body of the thesis has plots zoomed in on the infill patterns, the entire body stress plots are shown in this section. Figures D-28 to D-36 show the stress plots from the CLM analyses.

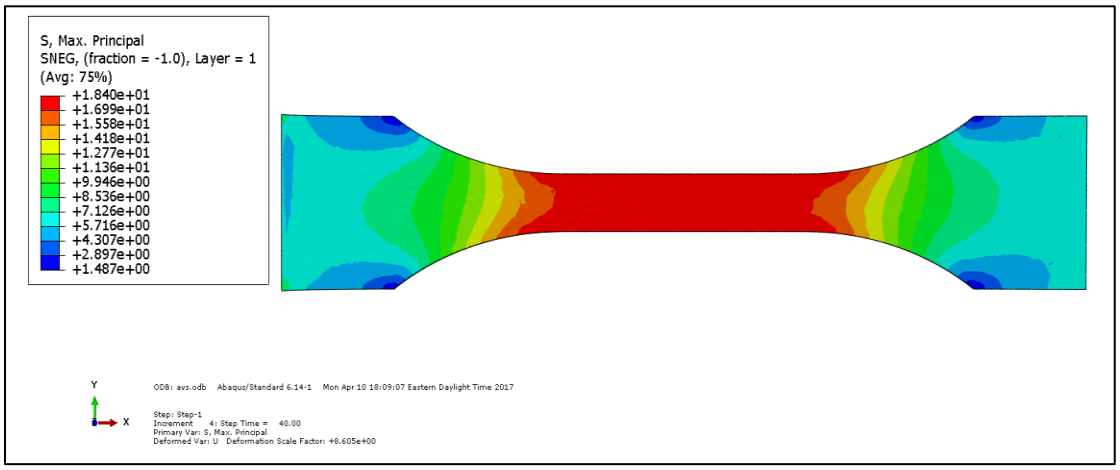

Figure D - 28: Abaqus© Normal Stress plot for C specimen using CLM.

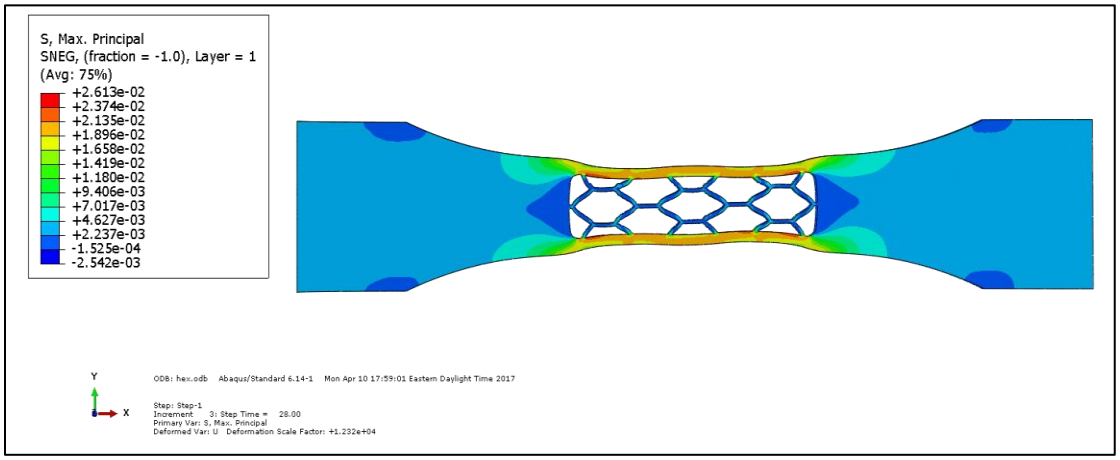

Figure D - 29: Abaqus© Normal Stress plot for HI specimen using CLM.

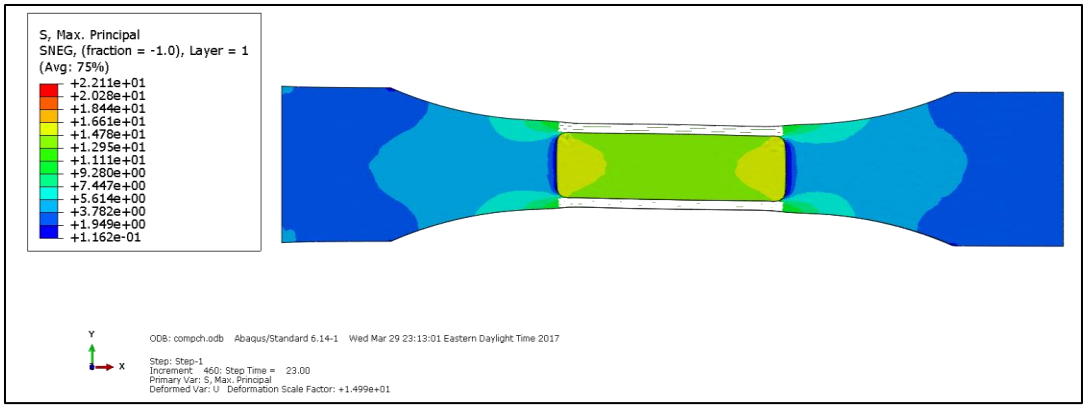

Figure D - 30: Abaqus© Normal Stress plot for CHI specimen using CLM.

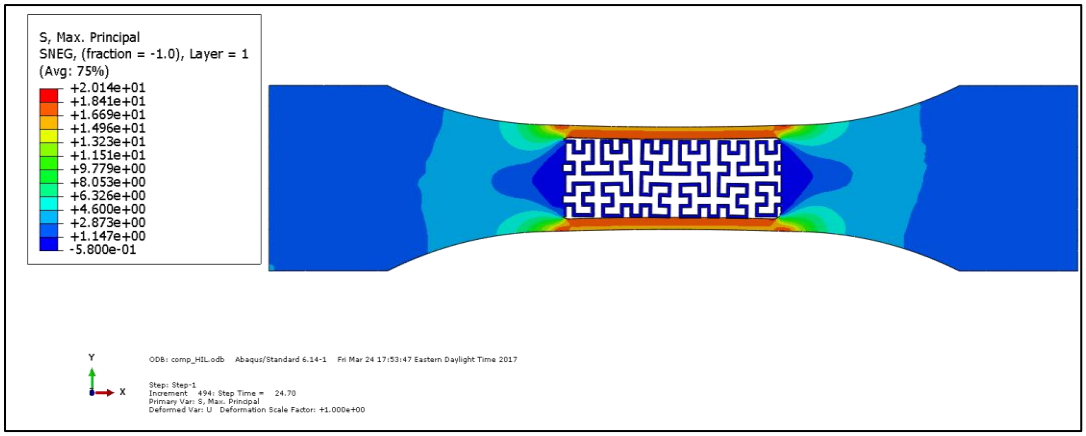

Figure D - 31: Abaqus© Normal Stress plot for HC specimen using CLM.

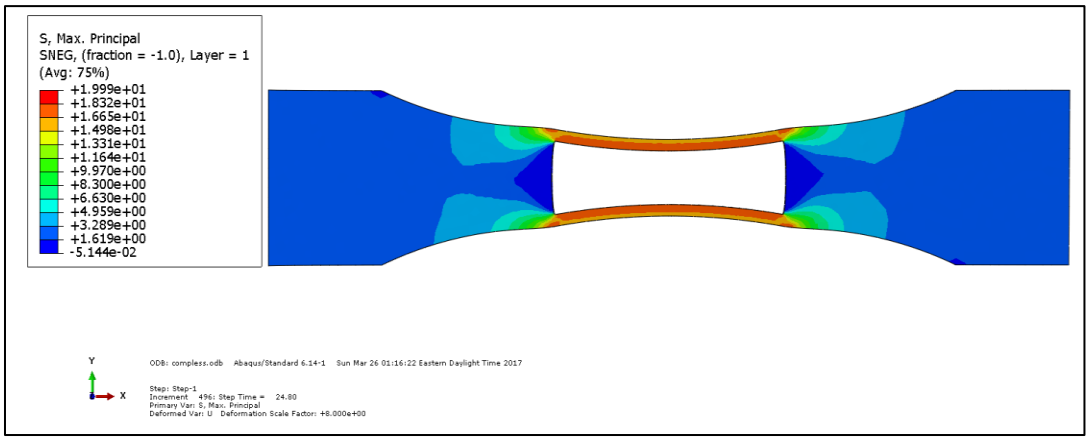

Figure D - 32: Abaqus© Normal Stress plot for I specimen using CLM.

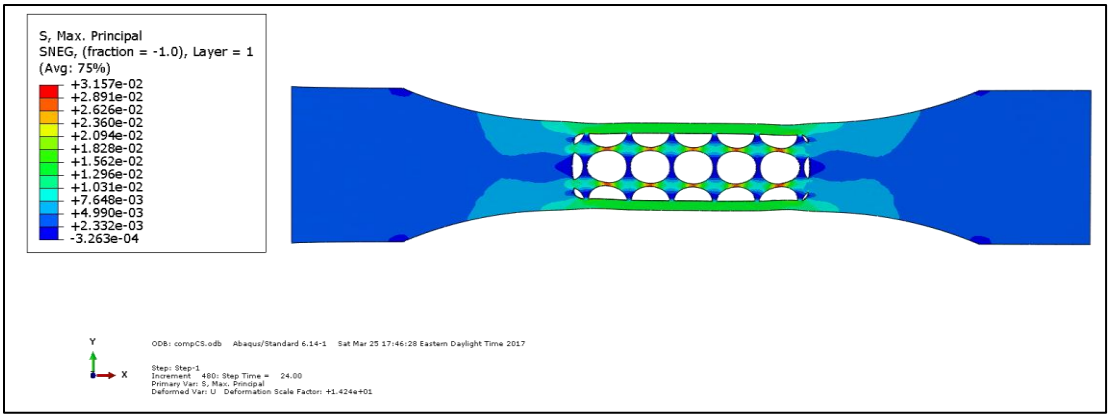

Figure D - 33: Abaqus© Normal Stress plot for CS specimen using CLM.

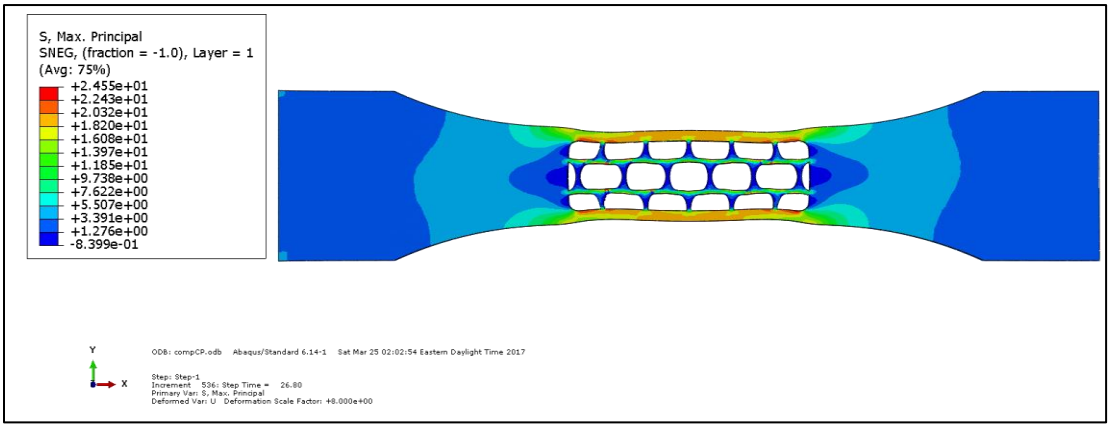

Figure D - 34: Abaqus© Normal Stress plot for CP specimen using CLM.

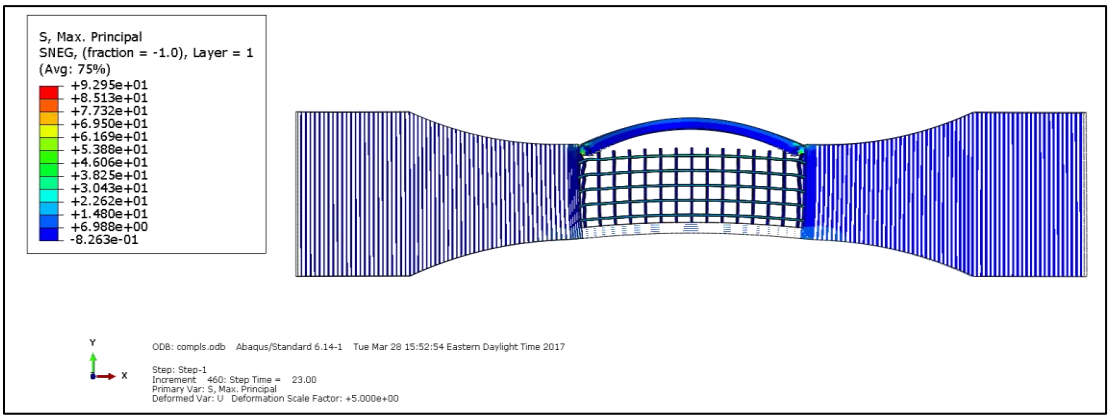

Figure D - 35: Abaqus© Normal Stress plot for LS specimen using CLM.

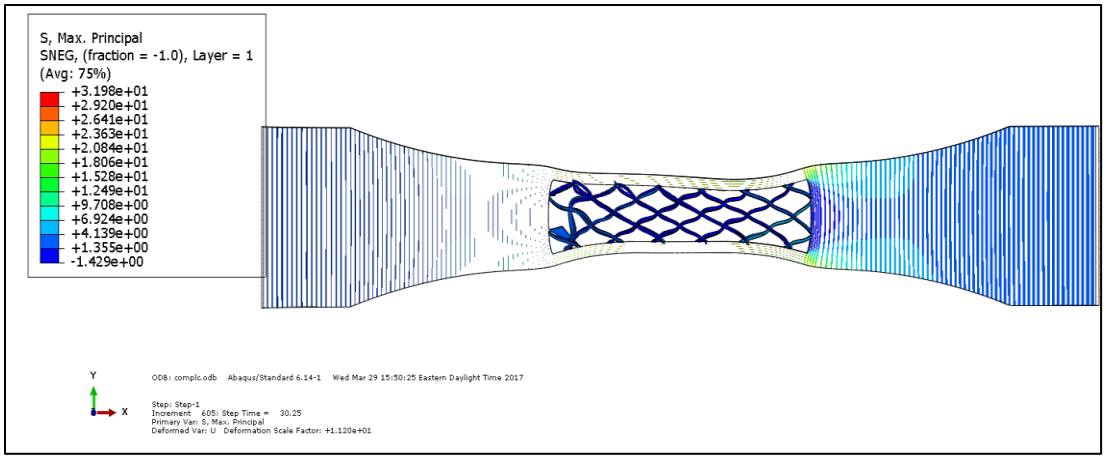

Figure D - 36: Abaqus© Normal Stress plot for LC specimen using CLM.

We can see from Figure D-35 and Figure D-36 that large out of plane deformations occur while using composite analysis. Composite analysis, considers a stack of 2D lamina, therefore, the forces in between the lamina, which are normal to the laminar plane, tend to cause this deformation. However, the stress in these regions are minimal.